

**NEAR-TARGET AND OTHER HEAVY RESIDUES IN THE
INTERACTION OF ^{12}C AND ^{16}O WITH ^{103}Rh**

E. Z. Buthelezi

**Dissertation presented for the Degree of Doctor of Philosophy
at the University of Stellenbosch**



Promoters:

Prof. A. A. Cowley

Dr. G. F. Steyn

Dr. T. N. van der Walt

DECLARATION

I, the undersigned, declare that the work contained in this thesis is my own original work and has not previously in its entirety or in part been submitted at any university for a degree.

Signature:.....

Date:.....

ABSTRACT

NEAR-TARGET AND OTHER HEAVY RESIDUES IN THE INTERACTION OF ^{12}C AND ^{16}O WITH ^{103}Rh

This study forms part of a larger investigation which has as a primary objective the development of a comprehensive theoretical description of all the processes which contribute to the continuum in the interaction of ^{12}C and ^{16}O with nuclei. Previous investigations of ^{12}C and ^{16}O induced reactions on targets with mass close to $A = 100$ have shown that the experimental excitation functions and recoil range distributions of heavy residues can be reproduced satisfactorily by means of a theoretical model which takes relatively few dominant reaction mechanisms into account. These include the complete fusion of the projectile with the target, the incomplete fusion of break-up α -type fragments (i.e. single α particles, ^8Be fragments and for the ^{16}O induced reactions also ^{12}C fragments) with the target and single-nucleon transfer at incident energies above about 15 MeV/nucleon. The mean-field interaction is mainly responsible for these interactions. The thermalization of the intermediate excited nuclei produced in this *first stage* of the reaction is described by an intranuclear interaction cascade, during which pre-equilibrium emission of particles and clusters may occur, followed by evaporation after statistical equilibrium has been attained. The model also included the probability that break-up α particles may escape with a large fraction of their initial energy after only a few interactions with individual target nucleons following their initial incomplete fusion. The theory also predicted an enhanced isobaric yield for residues with mass similar or near to that of the target.

The subsequent analysis of the emission spectra of intermediate mass fragments in these reactions, however, indicated that two additional aspects need to be considered as well in order to reproduce the experimental data. The first is that the projectile may lose a substantial amount of energy in an initial-state interaction before breaking up, which can be described as a friction dissipative process. The second is that several other incomplete fusion channels of “non- α -cluster”-type fragments should also be included in a more complete description of these reactions as their contributions are not negligible.

The present study has two main objectives. Firstly, to investigate the isobaric yield in the near-target mass region by measuring production cross sections for ^{103}Pd , $^{103\text{m}}\text{Rh}$ and ^{103}Ru . Previous studies only provided data for ^{103}Ag , which constitute only a few percent of the $A = 103$ isobaric yield. The new data constitute more than 80% of the $A = 103$ isobaric yield, which provide experimental confirmation of the enhanced isobaric yield in the near-target mass region. The second objective is to perform extensive new calculations of the excitation functions and recoil ranges in order to investigate the predictive power of the extended model in *a priori* calculations for the entire available data set.

SAMEVATTING

NABY-SKYF EN ANDER SWAAR RESKERNE IN DIE INTERAKSIE VAN ^{12}C EN ^{16}O MET ^{103}Rh

Hierdie studie maak deel uit van 'n meer omvattende ondersoek wat as 'n primêre doelwit die beskrywing van al die bydraende prosesse tot die kontinuum in die interaksie van ^{12}C en ^{16}O met kerne behels. In vorige ondersoeke van ^{12}C en ^{16}O geïnduseerde reaksies op skywe met massa naby $A = 100$ kon die eksperimentele opwekkrommes van swaar reskerne en reikwydte distribusies van terugslagkerne bevredigend gereproduseer word met behulp van 'n teoretiese model wat slegs enkele dominante reaksiemeganismes in berekening bring. Hierdie sluit in die volledige versmelting van die projektiel met die skyfkern, die onvolledige versmelting van opbreek α -tipe fragmente (d.w.s. α -deeltjies, ^8Be fragmente, en in die geval van ^{16}O geïnduseerde reaksies ook ^{12}C fragmente) met die skyfkern, en enkel-nukleon oordrag by invalsenergië wat hoër is as ongeveer 15 MeV/nukleon. Die gemiddelde-veld interaksie is hoofsaaklik verantwoordelik vir bogenoemde reaksie meganismes. Die oorgang na termiese ewewig van die opgewekte tussenkerne wat in hierdie *eerste stadium* van die reaksie gevorm word, word beskryf deur 'n intrakern interaksie kaskade wat gekenmerk word deur die voorewewigs emissie van deeltjies en klonte van deeltjies, gevolg deur verdamping nadat statistiese ewewig bereik is. Dié model sluit ook die waarskynlikheid in dat opbreek α -deeltjies kan ontsnap met 'n betekenisvolle fraksie van hul aanvanklike energie na slegs enkele interaksies met individuele skyfnukleone nadat hulle aanvanklik onvolledig versmelt het.

In latere studies van die emissiespektra van intermediêre massa fragmente in hierdie reaksies het dit egter geblyk dat twee addisionele aspekte ook in berekening geneem moet word om die eksperimentele data te reproduseer. Eerstens kan die projektiel 'n substansiële hoeveelheid energie verloor in 'n aanvangstoestand interaksie voordat dit opbreek, wat beskryf kan word as 'n wrywing-dissipatiewe proses. Tweedens kan verskeie ander onvolledige versmeltingskanale van fragmente met 'n nié- α -karakter ook betekenisvol bydra en kan hulle dus nie verwaarloos word in 'n meer volledige beskrywing van hierdie reaksies nie.

Die huidige studie het twee hoofdoelwitte. Eerstens word die isobariese opbrengs in die naby-skyfgebied ondersoek deur die produksie kansvlakke van ^{103}Pd , $^{103\text{m}}\text{Rh}$ en ^{103}Ru te meet. In vorige studies is slegs data verkry vir ^{103}Ag , wat net 'n klein persentasie van die $A = 103$ isobariese opbrengs verteenwoordig. Die nuwe data verteenwoordig meer as 80% van die $A = 103$ isobariese opbrengs, wat eksperimentele bevestiging verleen dat 'n verhoging in die isobariese opbrengs in die naby-skyfgebied bestaan. Die tweede doelwit is om 'n volledige stel nuwe *a priori* berekeninge te doen vir al die opwekkrommes van reskerne en reikwydte distribusies van terugslagkerne wat tans beskikbaar is om sodoende die voorspellings van die nuwe uitgebreide teoretiese model te toets.

ACKNOWLEDGEMENTS

Firstly, I would like to thank the Lord for making this a possible and a worthwhile journey.

My deepest gratitude goes to Dr. G.F. Steyn, Prof. E. Gadioli and Prof. A.A. Cowley for their support, motivation and patience. It has been a great pleasure and an honour to work with you. Your experience, wisdom and professionalism are quite remarkable.

I would also like to extend my thanks to my former boss, Dr. F.M. Nortier, who was there in the beginning. Also to Dr. Nico van der Walt and Dr. S.V. Förtsch for their help and involvement in the project.

Vorrei ringraziare questa gente seguente, Prof.sa E Gadioli Erba, Dott.sa. M. Cavinato, Prof.sa E. Fabrici, Prof. C. Birattari, Dott. Francesco Cerutti, il signori Roberto Bassini e Augusto Bassi. Esso é stato un grande piacere ed un privilegio lavorare con Loro in una maniera o nell'altra. Loro me ha fatto sente data in benvenuto e grazie così tanto!

Dr. Khosro Aardeneh, you are a remarkable chemist! It was a great privilege to work with someone with such expertise. It was tough going at times but you made it all look very simple and achievable.

Molto ringraziamenti al mia Francy amica il piú caro ed il ragazzi, Claudio, Vittorio, Antonio, Sara, Suzy, Andrea, Simone, Rita, Pamela, Chiara ed tutti alli. Voi me ha portato come un amico e ha fatto il mia sta in Milano molto piacevole, veramente. Tipi eravate grandi e non dimenticheró mai quello. La speranza di ritornare il favore un giorno!

Deidré Prince, Dawid de Villiers and J. M. Moeletsi, thank you guys so much. You are great and you have a special place in my heart!

Lencwadi iyisikhumbuzo sabazali bami asebadlula emhlabeni. Bongwiwe kanye nabantwana e KZN, akuve kuyisibusiso esikhulu kimina ukuba nomndeni ofana nani. Ngiyabonga kakhulu ngoxhaso lwenu lonke. Inkosi inibusise!!.

This is dedicated to my late parents and to you my precious, Sizwe.

CONTENTS

1	Introduction.....	1
1.1	Motivation.....	1
1.2	Objectives of the present study.....	7
1.2.1	New theoretical calculations.....	8
1.2.2	Isobaric yields of near-target residues.....	8
2	Historical development of continuum reactions.....	11
2.1	The role of pre-equilibrium emission in nuclear reactions.....	11
2.2	Reactions induced by composite projectiles.....	15
3	Theoretical background.....	17
3.1	Overview.....	17
3.2	The reaction cross section and classical relationships.....	17
3.3	Entrance-channel critical angular momentum.....	20
3.4	Reaction cross section and angular momentum for ^{12}C and $^{16}\text{O} + ^{103}\text{Rh}$	24
3.5	The initial-state friction dissipative interaction.....	27
3.6	Importance of α -particle re-emission in ^8Be and α -particle incomplete fusion.....	32
3.7	Thermalization of the intermediate nuclei.....	33
3.7.1	The Boltzmann Master Equation theory of pre-equilibrium emission.....	34
3.7.2	Initial nucleon energy distribution in the BME theory.....	36
3.7.3	Mean-field effects.....	37
3.7.4	Effective Coulomb barrier.....	40
3.8	The BME in Monte Carlo calculations.....	40
3.9	Evaluation of evaporation chains in the Monte Carlo calculations.....	42
4	Experimental procedures.....	45
4.1	Overview.....	45

4.2	Delivery of beam.....	45
4.3	The irradiation chamber.....	46
4.4	Beam focusing and monitoring.....	48
4.5	Target preparation and irradiations.....	50
4.6	Radiochemical separations.....	53
4.7	Preparation of counting sources.....	54
4.8	Radionuclide assays.....	55
5	Data analysis.....	57
5.1	Overview.....	57
5.2	Experimental cross sections.....	57
5.3	Comparison with theoretical cross sections.....	58
5.4	Detector calibrations.....	61
5.5	Error analysis.....	62
5.6	Radionuclide identification.....	62
5.7	Other aspects.....	67
6	Results and discussion.....	69
6.1	Overview.....	69
6.2	Radiochemical separations.....	69
6.3	Cross sections and isobaric yields.....	72
6.4	Excitation functions and recoil range distributions.....	80
6.5	Mean excitation energy distributions.....	98
7	Summary and conclusion.....	101
	Appendix 1 Theoretical model input parameters.....	104
A1.1	Overview.....	104
A1.2	Parameters used in the BME calculations.....	105
A1.3	Parameters used in the Monte Carlo calculations.....	108

A1.3.1	Input parameters for $^{12}\text{C} + ^{103}\text{Rh}$	108
A1.3.2	Input parameters for $^{16}\text{O} + ^{103}\text{Rh}$	115

Appendix 2 Alternative radiochemical procedures.....122

A2.1	Overview.....	122
A2.2	Literature survey.....	122
A2.3	Experimental.....	125
A2.3.1	Method 1: Cationic exchange resins in hydrobromide acid-thiourea media	125
A2.3.2	Method 2: Microporous cation exchange resin in HCl media.....	126
A2.3.3	Method 3: Weakly basic anionic exchange resin in 6 M HCl medium.....	127
A2.3.4	Method 4: Strongly basic anionic exchanger in nitric acid media.....	128
A2.3.5	Method 5: Strongly basic anion exchanger in 6 M HCl.....	129

Appendix 3 Beam current integration tests.....131

A3.1	Overview.....	131
A3.2	Test irradiations.....	131

**Appendix 4 Determination of production cross sections from
activation data: constant beam intensity.....132**

A4.1	Overview.....	132
A4.2	Definitions and times.....	132
A4.3	Activity built-up during bombardment.....	134
A4.4	Decay before and during counting period.....	134
A4.5	The cross section expression.....	135

**Appendix 5 Determination of production cross sections from
activation data: fluctuating beam intensity.....136**

A5.1	Overview.....	136
A5.2	Derivation of an expression for the cross section.....	136

A5.3 The correction factor.....137

Appendix 6 Cumulative cross sections.....139

A6.1 Overview.....139

A6.2 The case of one precursor.....139

A6.3 Generalization to more than one precursor.....141

Appendix 7 Experimental cross sections of heavy residues.....142

REFERENCES.....148

LIST OF FIGURES

1.1	Comparison of the predicted isobaric yields of residues produced in the interaction of ^{12}C with ^{103}Rh	5
3.1	Contribution of different reaction mechanisms to the reaction cross section in $^{12}\text{C} + ^{103}\text{Rh}$ and $^{16}\text{O} + ^{103}\text{Rh}$ as a function of projectile energy.....	26
4.1	The dedicated irradiation chamber used for the activation of samples, mounted at the end of beamline N at iThemba LABS.....	46
4.2	Another view of the irradiation chamber with the door in an open position.....	47
4.3	Schematic diagram showing a cross-sectional view of the irradiation chamber and the position of the collimator assembly.....	49
4.4	Schematic diagram showing a cross-sectional view of the collimator assembly.....	49
4.5	Schematic diagram of the punch-and-die set used for target manufacturing.....	52
4.6	The water-cooled target holder.....	52
4.7	Cross-sectional view of a PVC counting-source holder.....	54
5.1	Accumulated charge versus time for an experimental bombardment during which the ^{16}O beam intensity remained quite constant.....	59
5.2	Accumulated charge versus time for an experimental bombardment during which the ^{16}O beam intensity fluctuated significantly.....	60
5.3	A typical x -ray spectrum of a source prepared from the mother solution, i.e.before any radiochemistry (a), and after the radiochemical separation (b).....	68
6.1	Experimental and theoretical isobaric yields obtained in the present study.....	76
6.2	Total isobaric yield predictions according to this study as well as a phenomenological prediction based of the formalism of Rudstam.....	78
6.3	Excitation functions of silver residues produced in the interaction of ^{12}C and ^{16}O with ^{103}Rh at incident energies varying from threshold to 400 MeV.....	84
6.4	Excitation functions of palladium residues produced in the interaction of ^{12}C and ^{16}O with ^{103}Rh at incident energies varying from threshold to 400 MeV.....	85
6.5	Excitation functions of palladium and rhodium residues produced in the interaction of ^{12}C and ^{16}O with ^{103}Rh at incident energies varying from threshold to 400 MeV....	86

6.6	Excitation functions of rhodium residues produced in the interaction of ^{12}C and ^{16}O with ^{103}Rh at incident energies varying from threshold to 400 MeV.....	87
6.7	Excitation functions of rhodium residues produced in the interaction of ^{12}C and ^{16}O with ^{103}Rh at incident energies varying from threshold to 400 MeV.....	88
6.8	Excitation functions of ruthenium residues produced in the interaction of ^{12}C and ^{16}O with ^{103}Rh at incident energies varying from threshold to 400 MeV.....	89
6.9	Excitation functions of technitium residues produced in the interaction of ^{12}C and ^{16}O with ^{103}Rh at incident energies varying from threshold to 400 MeV.....	90
6.10	Excitation functions of technitium and molybdenum residues produced in the interaction of ^{12}C and ^{16}O with ^{103}Rh at incident energies varying from threshold to 400 MeV.....	91
6.11	Excitation functions of niobium and zirconium residues produced in the interaction of ^{12}C and ^{16}O with ^{103}Rh at incident energies varying from threshold to 400 MeV.....	92
6.12	Excitation functions of yttrium residues produced in the interaction of ^{12}C and ^{16}O with ^{103}Rh at incident energies varying from threshold to 400 MeV.....	93
6.13	Excitation functions of tin residues produced in the interaction of ^{12}C and ^{16}O with ^{103}Rh at incident energies varying from threshold to 400 MeV.....	94
6.14	Excitation functions of indium residues produced in the interaction of ^{12}C and ^{16}O with ^{103}Rh at incident energies varying from threshold to 400 MeV.....	95
6.15	Excitation functions of indium and silver residues produced in the interaction of ^{12}C and ^{16}O with ^{103}Rh at incident energies varying from threshold to 400 MeV.....	96
6.16	Forward recoil range distributions for residues formed in the interaction of ^{12}C with ^{103}Rh at an incident energy of nominally 400 MeV.....	99
6.17	Predicted mean excitation energy distributions of IEN produced in the interaction of ^{12}C with ^{103}Rh at an incident energy of nominally 400 MeV for each of the contributing mechanisms considered in this study.....	100

LIST OF TABLES

5.1	Radionuclides identified in the interaction of ^{16}O and ^{12}C with ^{103}Rh	63
6.1	Comparison of extracted production cross sections for selected radionuclides obtained in the bombardment of metallic Rh foils and $\text{RhCl}_3 \cdot x\text{H}_2\text{O}$ disks.....	72
6.2	Measured cross sections for the production of residues in the reaction $^{12}\text{C} + ^{103}\text{Rh}$	74
6.3	Measured cross sections for the production of residues in the reaction $^{16}\text{O} + ^{103}\text{Rh}$	75
6.4	Parameters obtained from a least-squares fit of equations (6.2) and (6.3) [modified Rudstam formalism] to the measured data.....	78
6.5	Predicted cross sections of all contributing reaction mechanisms for $A = 103$ isobars produced in $^{12}\text{C} + ^{103}\text{Rh}$ at a nominal energy of 380 MeV.....	79
6.6	Predicted cross sections of all contributing reaction mechanisms for $A = 103$ isobars produced in $^{16}\text{O} + ^{103}\text{Rh}$ at a nominal energy of 350 MeV.....	80
A1.1	Parameters used in the BME calculations.....	105
↓		↓
A1.3		108
A1.4	Parameters used in the Monte Carlo calculations.....	109
↓		↓
A1.30		121
A3.1	Production rates of ^{48}V induced in test irradiations of Ti monitor foils.....	131
A7.1	Measured cross sections for residues produced in $^{12}\text{C} + ^{103}\text{Rh}$	142
A7.2	Measured cross sections for residues produced in $^{16}\text{O} + ^{103}\text{Rh}$	145

CHAPTER 1

INTRODUCTION

1.1 Motivation

As a point of departure for a discussion on the reactions to the continuum induced by ^{12}C and ^{16}O projectiles, the work of Britt and Quinton [Bri61] seems most appropriate. As part of their experimental study, these authors measured angular distributions of α particles emitted in the bombardment of targets of ^{197}Au and ^{209}Bi with ^{12}C and ^{16}O beams at incident energies of 10.5 MeV/nucleon. They could separate the contribution due to evaporation and thus obtain a component of the spectrum which they attributed to a direct reaction mechanism. This forwardly peaked component corresponded with a velocity close to that of the beam, from which they deduced that the principal direct process involved is the break-up of the incident projectile in a peripheral interaction with the surface of the target nucleus. At that time it was impossible to do any thorough theoretical predictions, however, it was speculated that the partner fragments from the break-up interactions which produce the fast α -particle ejectiles may be absorbed by the target nucleus in close nuclear collisions. Thus it was speculated that *incomplete fusion* processes may be important in these reactions.

It is appropriate for the present discussion to jump forward in time by many years to the study of Parker *et al.* [Par84], a paper which from the perspective of the present study is a seminal work. These authors studied the reaction $^{12}\text{C} + ^{51}\text{V}$ at several incident ^{12}C energies up to 157 MeV. First, they measured the excitation functions of 18 radionuclides (target-like residues) from threshold up to 157 MeV by means of the stacked-foil technique, using primary beams of nominally 72, 96 and 152 MeV. They also measured extensive recoil range distributions of the major residues identified in the excitation function study at ^{12}C energies of 36, 51, 72, 88, 100, 118 and 157 MeV, using stacks of thin aluminium catchers behind a thin vanadium target. Lastly, they measured inclusive continuum spectra of double differential cross sections of protons and α particles emitted at angles ranging from 10° to 150° degrees at all the above incident energies between 51 and 157 MeV. This constituted quite a comprehensive data set for that reaction. The proton emission spectra could be reasonably well reproduced by considering only the evaporation from the equilibrated compound nucleus (^{63}Cu) formed in the complete fusion of the projectile and target nucleus. Thus it was concluded that there was no evidence of any significant yield of protons originating from break-up of the ^{12}C projectile. In contrast, while the α -particle spectra at

INTRODUCTION

angles larger than 45° were consistent with evaporation, a strong second component consistent with projectile break-up was observed towards the smaller angles, a result which was in fact expected and in agreement with previous work. From these results the conclusion was made that when ^{12}C breaks up, it fragments predominantly into α particles. One of the main questions of that study was to what extent the projectile break-up is accompanied by fusion of break-up fragments. This was revealed by the recoil range data. At the lowest incident energy (i.e. 36 MeV) the recoil range distributions of observed residues show broad symmetrical peaks with widths reflecting the perturbing effect of the evaporation of a few particles combined with the effects of straggling and finite target thickness. As the incident energy increases, however, some of these distributions become skew and more complex. At the higher incident energies some of the residues, e.g. ^{54}Mn and ^{51}Cr , show more than one local maximum, an indication of the presence of more than one dominant reaction mechanism. By assuming a model in which there is competition between complete fusion and incomplete fusion of either one break-up α particle or two α particles (constituting the unbound ^8Be fragment), a mostly satisfactory overall description of the data could be obtained. Their theoretical implementation was rather crude, however, neglecting both pre-equilibrium emission as well as evaporation from the ^{55}Mn and ^{59}Co intermediates formed by the incomplete fusion processes. The authors recognized this and stated that a more comprehensive description was required especially at the higher incident energies. Their work, however, indicated that a comprehensive description of the reaction could be obtained by taking only relatively few dominant reaction mechanisms into account.

The success of the simple model by Parker and co-workers [Par84] amongst other reasons prompted further work, both experimentally and theoretically, by a collaboration consisting initially of researchers from the University of Milan, the University of the Witwatersrand (WITS) and iThemba LABS. There were several questions and objectives: Firstly, will this simple model which essentially considers a ^{12}C projectile as a three-alpha cluster survive towards higher incident energies? Will such a model, which is expected to eventually break down as the incident energy is increased, be successful also for heavier projectiles such as ^{16}O ? Can some of the concepts derived from the analysis of light-ion induced reactions be extended to heavy-ion induced reactions, at least to the more simple ones such as the interactions of ^{12}C and ^{16}O with nuclei? The following paragraphs give a summary of some of the previous work by that collaboration which ultimately led to the present study.

INTRODUCTION

In the first number of experiments by the Milan-WITS–iThemba collaboration, excitation functions, recoil range distributions and angular distributions of heavy residues were measured up to incident energies of 400 MeV in ^{12}C and ^{16}O induced reactions on ^{103}Rh [Bir96, Gad97a, Gad97b, Gad98a, Gad98b]. Since a mono-isotopic target with mass close to $A = 100$ was considered to be the ideal choice, ^{103}Rh became the target for these and many subsequent investigations. In the choice of the target it was deemed wise to avoid as far as possible the fission process which would have complicated the interpretation of the results, thus precluding very heavy targets. The target should also not be too light as a too-low Coulomb barrier would have led to excessive evaporation. Various combinations of foil stacks were irradiated and the results were extracted from spectra measured by means of off-line γ -ray spectroscopy of the activated foils.

As in the study by Parker *et al.* [Par84] discussed above, the dominant interaction mechanisms taken into consideration in the theoretical analysis of $^{12}\text{C} + ^{103}\text{Rh}$ were the complete fusion of the projectile and incomplete fusion of break-up α particles and ^8Be fragments with the target nucleus. It was also found that single-nucleon transfer from the projectile to the target nucleus becomes important towards higher incident energies. The mean-field interaction (one-body dissipation mechanism) is mainly responsible for these interactions. The break-up of the projectile was evaluated using a generalisation of the Serber approximation [Ser47, Gad00], which was initially developed to explain the break-up of the deuteron. The cross sections for complete and incomplete fusion were evaluated within the framework of the *entrance channel critical angular momentum* model. According to this model the fusion processes, which are in statistical competition, will only contribute (and consequently dominate) within particular windows of angular momentum. The intranuclear interaction cascade by means of which the composite nuclei formed thermalise was evaluated within the framework of the Boltzmann Master Equation (BME) theory. This theory was first proposed by Harp, Miller and Berne [Har68]. The particular implementation used has been developed by the University of Milan over many years and has been generalized to include the emission of both nucleons and clusters. The pre-equilibrium emission has thus been properly accounted for as well as evaporation after the remaining composite nuclei have attained a state of statistical equilibrium. Since these theories also form the basis of the theoretical analysis of the present study, they will be described in more detail in a subsequent chapter.

An interesting result that emerged from the above-mentioned experiments is that a significant fraction of break-up α particles which initially fuse with the target (as single units

INTRODUCTION

or as component units of ^8Be fragments) are re-emitted with most of their initial energy. This kind of re-emission has also been observed in α -particle induced reactions but with much smaller probability. While roughly one third of α particles are re-emitted in α -particle induced reactions, re-emission probabilities of 0.8 and 0.95 were inferred in the case of ^{12}C and ^{16}O induced reactions, respectively [Gad98b]. The higher re-emission probabilities in the case of the heavier projectiles can be ascribed to the different geometry of the fragment-nucleus system, where on average the participant break-up α particles interact in a more peripheral region of the nucleus. It was also found that residues with mass and charge equal to or close to that of the target are produced copiously with a very small forward range. This was interpreted as a main consequence of the dominant contributions of the incomplete fusion channels followed by the re-emission of α particles with most of their initial energy. However, this finding was primarily based on the theoretical predictions as the data in this mass region were rather sparse, as will be discussed later. In Fig. 1.1 the predicted isobaric yields (i.e. the total cross sections for production of residues with a particular mass – also sometimes called the mass-yield curve) at ^{12}C incident energies of 280 and 400 MeV are presented (as reproduced from [Gad98a]). These values are compared with the results obtained from a phenomenological prescription by Chung *et al.* [Chu91] for the reaction $^{12}\text{C} + ^{\text{nat}}\text{Ag}$. The method of Chung *et al.* is based on a well-known empirical method originally formulated by Rudstam [Rud66]. In order to account for the different mass of the target nucleus in the study by these authors, the masses of the distribution for $^{12}\text{C} + ^{\text{nat}}\text{Ag}$ were reduced by 5 mass units. Although this was a rather crude thing to do, the comparison is nevertheless interesting. Figure 1.1 shows that the agreement between the two distributions is quite good at all masses except for the residues near to that of the target. The predictions by Gadioli *et al.* seem to indicate an enhanced isobaric yield in the near-target mass region with a maximum at $A = 103$, i.e. the target mass. In contrast, the phenomenological prediction shows no such effect. This result is important for the present study, which endeavours to investigate the near-target mass region more closely. The same applies to the assumed correlation between the α -particle re-emission process and the enhanced production of near-target residues.

In both the ^{12}C and ^{16}O induced reactions an overall satisfactory agreement could be obtained between the experimental and calculated excitation functions and recoil ranges by only considering fragmentation into α -like fragments (i.e. single α particles, ^8Be fragments, and in the case of ^{16}O projectiles also ^{12}C fragments) and their role in incomplete fusion processes.

INTRODUCTION

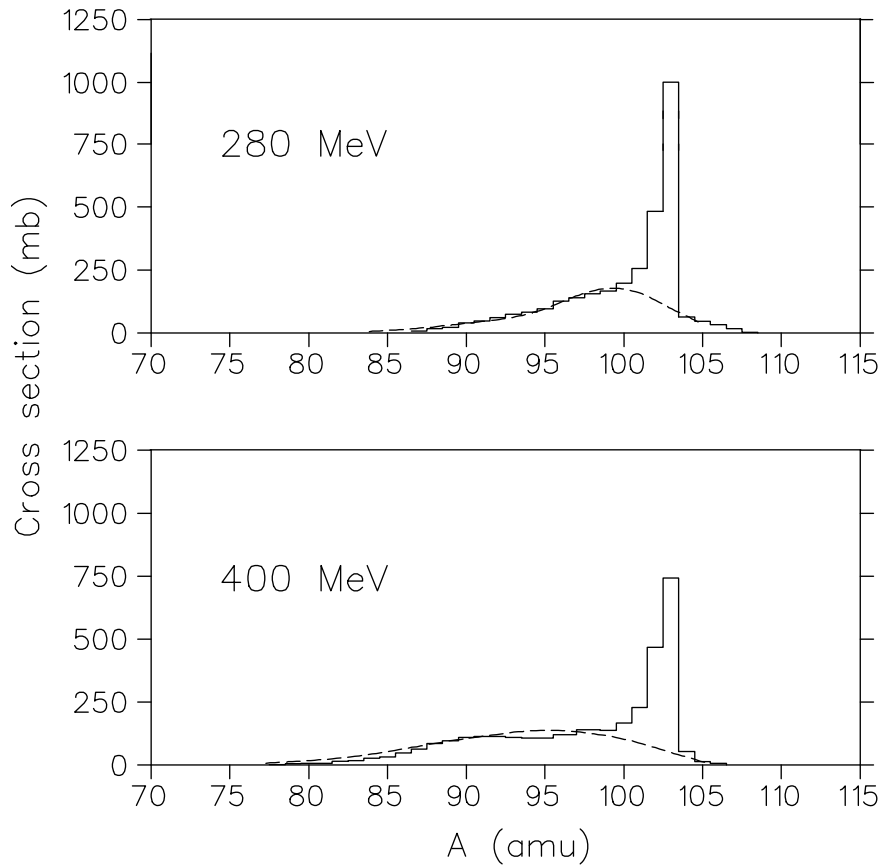


Figure 1.1 Comparison of the predicted isobaric yields of residues produced in the interaction of ^{12}C with ^{103}Rh according to Gadioli et al. [Gad98a] (histograms) and a phenomenological prescription by Chung et al. [Chu91] for the similar reaction $^{12}\text{C} + ^{\text{nat}}\text{Ag}$, shifted by 5 units of mass to account for the difference in target mass (see text). The figure has been reproduced from Gadioli et al. [Gad98a]

As a further test of the assumptions of the model, several subsequent experiments focused on the measurement of double-differential continuum cross sections (i.e. energy and angular distributions) of ejectiles. In the first of these, an extensive set of inclusive α -particle spectra was measured for the reactions $^{12}\text{C} + ^{59}\text{Co}$ and $^{12}\text{C} + ^{93}\text{Nb}$ [Gad99]. The different choice of targets was as a result of an inability to produce thin ^{103}Rh targets due to the brittleness of rhodium. Because the particular target choice was not considered to be of crucial importance, ^{93}Nb (also a target reasonably close to $A = 100$) was chosen as well as ^{59}Co as a consistency check in case of an unexpected mass dependence. These spectra were reproduced satisfactorily by summing the following contributions incoherently: (1) spectator α particles from ^{12}C break-up, (2) α particles re-emitted after incomplete fusion, (3) pre-equilibrium α particles, and (4) evaporated α particles. There was some overestimation of the

INTRODUCTION

cross sections at the most forward angles which became less with increasing incident energy. This was explained at that time as possibly due to final-state interactions, which were neglected in the theoretical analysis. However, the overall good agreement between the experimental data and the theoretical predictions was considered to be strong additional evidence of the presence of the α particle re-emission process and an assurance that the main ingredients of the model were correctly identified and implemented.

In a subsequent experiment the double-differential cross sections of ^8Be fragments produced in their ground state were measured in ^{12}C induced reactions on targets of ^{59}Co , ^{93}Nb and ^{197}Au [Gad01]. The analysis of these spectra at the most forward angles, however, revealed two aspects that have hitherto not been taken into consideration:

- Firstly, it became evident that at incident energies above 200 MeV, the ^{12}C projectile may suffer a considerable energy loss in an initial-state interaction with the target nucleus before breaking up. At the higher incident energies the average $^8\text{Be}_{\text{gs}}$ emission energy was found to be notably smaller than that corresponding to the beam velocity and the spectrum width, which should reflect the momentum distribution of the fragment within the projectile, was distinctly larger than expected. This can be described by introducing a friction dissipative interaction of the projectile with the target nucleus and included in the model by introducing the concept of a survival probability for the projectile. (This will be discussed in detail in a subsequent chapter.) The assumption that the observed softening of the $^8\text{Be}_{\text{gs}}$ emission spectra is due to an initial-state interaction of the projectile, rather than final-state interactions of the emitted fragments, is because it is considered most unlikely for a ^8Be fragment to survive any such final-state interactions. Since ^8Be is unbound, such a final-state interaction will destroy the correlation between its two components α particles, by which it is detected and identified. Interestingly, the inclusion of the friction interaction in the model resulted in a minor but noticeable improvement of the theoretical predictions for the inclusive α -particle spectra.
- Secondly, a surprising amount of ^7Be and ^9Be fragments were observed in the raw singles spectra, leading to further experimental work to measure these intermediate mass fragments (IMF) comprehensively [Bec03]. Since it has been accepted for a long time that ^{12}C break-up will preferentially lead to the formation of α -like fragments or aggregates, the initial expectation was that these ^7Be and ^9Be fragments probably originated in final-state interactions of ^8Be (i.e. projectile break-up followed by pickup

INTRODUCTION

or stripping of a neutron by a ^8Be fragment). However, it was found that all the observed IMF, and $^{7,9}\text{Be}$ in particular, exhibited the same qualitative features as ^8Be in their measured spectra. It was therefore concluded that even if final-state interactions may be partly responsible for the softening of the IMF spectra, the initial-state interaction is by far the dominant contributing mechanism. Furthermore, similar to the analysis of the ^8Be spectra, a good quantitative description of the other measured IMF spectra could be obtained by only taking the initial-state interaction into account [Bec03]. Thus it was concluded that the dominant reaction mechanism for the formation of IMF in the higher emission-energy regime is the binary fragmentation of the projectile with possibly a reduced energy as a consequence of a dissipative interaction with the target nucleus.

Quite extensive measurements of inclusive IMF spectra were performed for both ^{12}C and ^{16}O induced reactions. Due to the absence of ^8Be in the ΔE - E particle identification spectra obtained in the measurements of the other IMFs (because it dissociates into its two α -particle constituents before reaching the detector), ^7Be and ^9Be could be completely resolved. For many of the other IMFs, however, mass separation could not be achieved and the results include the sum of all the produced isotopes of a given charge (i.e. Z). Good Z separation was always achieved. For the ^{12}C induced reactions, spectra of Li, $^{7,9}\text{Be}$ and B fragments were extracted [Bec03]. For the ^{16}O induced reactions, spectra of ^8Be , B, C and N fragments were extracted [Gad02a, Gad02b, Gad03]. As for the ^{12}C induced reactions, the ^{16}O results also consistently indicates the importance of an initial-state interaction of the projectile. In agreement with the interpretation suggested for the fragmentation mechanism, the possibility that the projectile may survive the initial-state interaction without breaking up or fusing with the target nucleus, i.e. inelastic scattering, can therefore also be evaluated.

1.2 Objectives of the present study

The main aims of the present study are to find answers for two main questions which arose from the previous investigations discussed above:

- Can the new theoretical description as formulated for the analysis of the IMF emission spectra still reproduce the experimental data of the heavy residues?
- Can the enhanced isobaric yield predicted for the isobars with the mass of the target be verified experimentally?

INTRODUCTION

1.2.1 New theoretical calculations

Extensive new calculations were performed at the University of Milan where the author spent a year as an exchange student for the purposes of this study. As explained above, the main aim was to investigate the effects of the inclusion of the initial-state interaction of the projectile and other modes of incomplete fusion and compare with previous results of the heavy residues produced in ^{12}C and ^{16}O induced reactions. Although a few other studies using somewhat heavier “ α -type” projectiles have indicated that several other modes of incomplete fusion may contribute (e.g. a study by Parker *et al.* [Par87] on the complete and incomplete fusion in the reaction $^{20}\text{Ne} + ^{93}\text{Nb}$), such modes had not yet been taken into consideration in ^{12}C and ^{16}O induced reactions at the time when this project was initiated.

1.2.2 Isobaric yields of near-target residues

The disagreement between the two sets of isobaric yield curves shown in Fig. 1.1 prompted this part of the investigation. As can be seen from the figure, the disagreement is the largest at the target mass, by about an order of magnitude.

Direct, unambiguous experimental evidence for an enhanced isobaric yield in the near-target mass region is curiously lacking. In previous studies of the excitation functions of the heavy residues produced in the interaction of α -cluster-type light nuclei (and in particular ^{12}C and ^{16}O) with nuclei, the fractions of the measured isobaric yields at or near the target mass were invariably small. For example, previous experimental investigations of the $^{12}\text{C} + ^{103}\text{Rh}$ reaction [Gad97a, Gad97b, Gad98a, Gad98b] reported production cross sections for only one $A = 103$ nuclide, namely ^{103}Ag , which constitutes only about 4% of the predicted isobaric yield. This lack of information at or near the target mass appears to be the case also in other studies involving the interaction of a “lighter” projectile with a “heavier” target nucleus.

A lack of isobaric yield data at the target mass is not too surprising since the activation techniques normally employed to measure production cross sections and/or excitation functions (usually by means of stacked-foil irradiations followed by off-line γ -ray spectroscopy) cannot provide data for stable residues, while many precursors often have radiations which are difficult to measure with these techniques (e.g. low photon energies, small branching ratios, small half-lives, etc.). However, if the target nucleus has an isomeric state only slightly above its ground state, with a half-life and radiations which make an

INTRODUCTION

absolute activity measurement possible, then, in principle, one should be able to experimentally determine quite a large fraction of the isobaric yield at the target mass.

The existence of the 39.76 keV $7/2^+$ isomeric state of ^{103}Rh (normally designated as $^{103\text{m}}\text{Rh}$) is therefore advantageous for this particular study. In fact, the measurement of the cumulative cross sections of the relatively long-lived ^{103}Pd (16.96 days) and ^{103}Ru (39.25 days) [Bro86], together with the cross section for the direct production of $^{103\text{m}}\text{Rh}$, should constitute substantially more than 80% of the predicted $A = 103$ isobaric yield. Thus, measured production cross sections for the $A = 103$ radionuclides, even at only one well-chosen incident energy, may be sufficient to either confirm or disprove an enhanced isobaric yield or alternatively, point out a deficiency in the predictive power of the phenomenological models. The relative strengths of these nuclides may also constitute a sensitive test of the predictive power of the theoretical models.

The measurement of production cross sections for ^{103}Pd , $^{103\text{m}}\text{Rh}$ and ^{103}Ru proved to be difficult for various reasons. Both ^{103}Pd and $^{103\text{m}}\text{Rh}$ only have very weak γ -lines, therefore the only feasible way to achieve an absolute determination of their activities was to measure the 20.1 keV K_α x -rays [Bro86] (63.8% and 6.37%, respectively). Since many of the other nuclides produced in these reactions have x -ray lines in the region 19-22 keV which would interfere with these measurements, radiochemical separation of the different atomic species produced proved to be mandatory. Furthermore, $^{103\text{m}}\text{Rh}$ is an isotope of the same species as the target, which therefore requires a comprehensive radiochemical purification of the target material from all the other disturbing radionuclides before an absolute yield measurement for this nuclide can be performed. To complicate matters more, $^{103\text{m}}\text{Rh}$ has a half-life of just under one hour (56.12 minutes), therefore the chemical separation and production of suitable counting sources have to be rapid processes. By contrast, the relatively long-lived ^{103}Ru has strong γ -lines but its production cross sections are small in the reactions induced by ^{12}C and ^{16}O on targets such as ^{103}Rh .

Both ion exchange chromatography and solvent extraction methods have been used for the separation of Pd from Rh and other elements [Str69, Pat74, Mik79, Haa81, Tar81, Lag82a, Lag82b, Hel83, Lag83, Lag84, Men86, Cha90, Lin92, Gai95, Faß99, Aar02, Her02], but none of these have fulfilled the requirements for this particular study, i.e. the isolation of Rh from Ag, Pd, Ru and Tc, followed by the separation of Pd from the rest of the elements. (Note that Ag and Pd are the two nearest atomic species above Rh, while Ru and Tc are the two nearest ones below Rh in the periodic table. These elements, in particular, need to be separated from the Rh target material in order to measure the 20.1 keV K_α x -rays emitted in

INTRODUCTION

the decay of $^{103\text{m}}\text{Rh}$ cleanly.) After studying the distribution coefficients of the elements of interest, it was decided to explore methods based on ion exchange chromatography in order to develop a rapid chemical separation procedure.

In this work, measured cross sections for the cumulative production of ^{103}Ag , ^{103}Pd and ^{103}Ru , and for the direct production of $^{103\text{m}}\text{Rh}$ at an incident energy of nominally 400 MeV are presented. In addition, the values for all other radionuclides which could be identified from their respective γ -lines are presented in an attempt to reconstruct as much of the total isobaric mass-yield curve in as large a mass region as possible. If, indeed, the phenomenological models fail to reproduce the isobaric yields in the near-target mass region, it will nevertheless be interesting to learn to what degree the agreement is better at masses further away from the target. Note that in Fig. 1.1 no experimental data are shown. In this study we add the data. The chemical separation techniques, including a rapid procedure for producing dry counting sources in under 80 minutes from the end of bombardment (EOB), are also discussed in detail.

It should be stressed again that most of the work quoted above as well as the present study mainly concerns the continuum, as characterised by ejectiles having a projectile-like nature and heavy residues having a target-like nature. As such, reactions to discrete states, spallation reactions, processes which only occur above the threshold for pion production, etc., which are very interesting in their own right, do not form part of the present investigation.

A discussion on the historical development of reactions to the continuum is presented in Chapter 2. The theoretical approach of this study is presented in Chapter 3. The experimental methods and procedures are discussed in Chapter 4. Aspects of the data analysis are discussed in Chapter 5. The results are presented in Chapter 6 and finally a summary and conclusion are given in Chapter 7.

CHAPTER 2

HISTORICAL DEVELOPMENT OF CONTINUUM REACTIONS

2.1 The role of pre-equilibrium emission in nuclear reactions

It is well known that when two heavy nuclei interact with just enough incident kinetic energy to overcome the Coulomb barrier, the complete fusion reaction mechanism dominates. For example, at incident energies below about 60 MeV in the interaction of a ^{12}C projectile with a ^{103}Rh target nucleus, the complete fusion process accounts for substantially more than 90% of the reaction cross section [e.g. Bir96]. It is equally well known that after the *first stage* of the encounter when the two nuclei touch and start to merge into a single nuclear system, an equilibration cascade of nucleon-nucleon interactions commences which lead to a statistical redistribution of excitation energy over all the nucleons constituting the final equilibrated compound nucleus. What is perhaps not so well known is that the small but measurable cross sections for the formation of some of the heavy residues (e.g. ^{113}Sb and ^{113g}Sn in the reaction $^{12}\text{C} + ^{103}\text{Rh}$, constituting less than 1% of the reaction cross section) cannot be accounted for by considering only evaporation of particles from an equilibrated compound nucleus [Ver93, Cri94, Cav95]. Even at incident energies barely higher than the Coulomb barrier, pre-equilibrium emission of nucleons during the thermalisation of the composite nucleus has to be taken into consideration in order to reproduce the formation cross sections of these particular residues [Bir96]. Thus any description of a heavy-ion reaction as a purely *fusion-evaporation* process, which is sometimes assumed to be a good approximation at low incident energies, will have certain limitations even at energies very close to the Coulomb barrier.

A striking example of this, which has already been alluded to above, was given by Birattari *et al.* [Bir96] for the complete fusion of ^{12}C with ^{103}Rh . At an incident energy of 60 MeV a purely fusion-evaporation calculation underpredicts the formation cross sections of ^{113}Sb and ^{113g}Sn residues by more than one order of magnitude! These discrepancies, which are already significant just above 40 MeV, could be completely resolved by the inclusion of pre-equilibrium emission.

It is instructive to look at the historical development of theoretical models for pre-equilibrium reactions (sometimes also referred to as pre-compound reactions) in a non-chronological way even though the bulk of the work during a period of approximately 38 years has been on nucleon-induced reactions. Quite often, the ideas which evolve in light-ion induced reactions find application in heavy-ion reactions as well, and vice versa. In

compound (p,n) reactions above about 10 MeV, the fusion-evaporation theories failed to predict the high-energy component of the emitted neutron spectrum by several orders of magnitude. This led to the pioneering work of Griffin and the development of the semi-classical *exciton model* [Gri66]. This model, as well as other semi-classical models which followed at that time, was very successful in describing the angle-integrated spectral shapes but failed to reproduce the angular distributions of particles emitted into the continuum. One such other model is the *hybrid model* or its successor, the *geometry-dependent hybrid model* (GDH) of Blann [Bla71, Bla75], which is a hybrid between the exciton model and the approach of Harp, Miller and Berne [Har68] (to be discussed later) which found wide application in the calculation of excitation functions of target-like residues produced in light-ion induced reactions. Much later, Chadwick and Obložinský [Cha91, Cha94a] showed that by ensuring that linear momentum at each of the numerous intranuclear transitions is conserved, something that the usual formulation lacked, the angular distributions of emitted particles to the continuum can be reproduced quite well.

The inability of theoretical models to reproduce the continuum angular distributions of emitted particles in nucleon-induced reactions persisted throughout the sixties and seventies into the early eighties. A study of the systematics of continuum angular distributions was made by Kalbach and Mann, which became known as the Kalbach-Mann (KM) systematics [Kal81, Kal82]. Although not a formal theory by any means, the KM empirical expressions based on Legendre polynomials are quite successful in reproducing the angular distributions of emitted particles in light-ion induced reactions at incident energies up to 80 MeV and emission energies up to 60 MeV. Kalbach later refined and extended this work to higher incident energies [Kal88], developing the systematics (or parametrisation) into quite a useful tool. Although some effort was made by Kalbach to justify certain aspects of the parametrisation on sound physical grounds, a thorough physical basis for these systematics was only given later by Chadwick *et al.* [Cha94a].

A number of quantum mechanical theories of pre-equilibrium reactions emerged in the early eighties. Very briefly, the three main theories which have evolved seem to be the quantum statistical theories of Feshbach, Kerman and Koonin (FKK) [Fes80, Fes95], Tamura, Udagawa and Lenske (TUL) [Tam82] and Nishioka, Weidenmüller and Yoshida (NWX) [Nis88]. These theories embody the so-called statistical multi-step reaction theories, where the evolution of the reaction proceeds through definite steps from the initial nucleon-nucleon interaction (first step), with each successive step driving the reaction on towards the formation of the compound nucleus.

HISTORICAL DEVELOPMENT OF CONTINUUM REACTIONS

Two kinds of multi-step reactions can be identified. In the statistical multi-step direct (MSD) reactions, the incident particle upon the first interaction loses energy, but not enough to become bound. The first step therefore excites the target nucleus into a one particle-one hole state (1p-1h), equivalent to an initial exciton number of 2. There are obviously many possible 1p-1h states, which in the FKK theory is denoted as the P_1 subspace of the Hilbert space of the reaction. A further nucleon-nucleon interaction can increase the complexity of the nucleus state to a 2p-2h state, all the possible configurations of which belong to the P_2 subspace. This process can continue, driving the nucleus into states of increasing complexity. While it is possible for the reaction to decay into a state of reduced complexity, this is not very probable. Consequently, the *never-come-back* assumption is usually enforced in calculations. A further assumption is usually employed namely the *chaining hypothesis*, which asserts that the interaction constituting any particular step will change the complexity of the nucleus wave function by at most one unit (i.e. equivalent to a change of the exciton number by 2). The *random phase approximation* is also normally applied, which asserts that states of different angular momenta and parity do not interfere. As long as one particle remains in the continuum, the reaction can proceed along the so-called P -chain up to complexities of $np-nh$ constituting the P_n subspace, where n in actual calculations hardly ever exceeds $n = 10$. At each step a particle can be emitted into the continuum. At each transition, a branching occurs between the transition to the subspace of next higher complexity and emission. Generally, emission from subspaces with smaller complexity will yield ejectiles with higher emission energies. The transitions along the P -chain are fast, characteristic of direct reactions. Typically, above about 20 MeV the MSD reactions are dominant in nucleon-induced pre-equilibrium reactions to the continuum.

The second kind of multi-step reaction is the statistical multi-step compound reaction (MSC), which dominates at lower incident energies. A multi-step reaction becomes MSC when as a result of an interaction, the incident nucleon loses sufficient energy so that it becomes bound. The progression along the multi-step chain, which is now called the Q -chain, is according to states of complexity $np-(n-1)h$ belonging to subspace Q_n : $Q_1(2p-1h) \rightarrow Q_2(3p-2h) \rightarrow Q_3(4p-3h) \rightarrow \dots$, equivalent to exciton numbers of 3, 5, 7, etc. Emission from the Q -chain goes via transitions to the P -chain, although such transitions will in practice often be omitted. Intuitively one can see that as a particle in the continuum loses energy in transitions along the P -chain, it will eventually be captured if emission does not occur. When this happens there is a transition from the P -chain to the Q -chain. As the reaction proceeds through successive steps, the branching ratio for emission becomes smaller

until ultimately the branching ratio for transition to the next step becomes close to unity. At this stage the compound nucleus is formed from which the usual evaporation processes will occur as described by e.g. the Hauser-Feshbach theory. The transitions along the Q-chain are slow, characteristic of compound nucleus reactions.

The multi-step reaction theories very beautifully describe the pre-equilibrium regime as somewhere between direct reactions (which in this context can be described as pure one-step processes) and compound nucleus reactions. It has been an active area of research for many researchers over many years and still is. One subsequent development by Akkermans and Koning [Akk90, Kon91] established a quantum statistical framework for the MSD reactions which embodies most of the differences and similarities between the various theories. The details of this work are beyond the scope of the present discussion other than to mention that the MSD theories can be derived formally from two classes of quantum statistics, called *leading-particle* statistics and *residual-system* statistics. The FKK theory belongs to the former, while the TUL and NWY theories belong to the latter. Interestingly, the basic concepts of the exciton model are also contained in the leading-particle statistics and can be regained by further simplification of the derivation which leads to the FKK theory. Of these theories, the FKK theory has probably been employed the most for the evaluation of experimental continuum angular distribution data (i.e. spectra of double-differential cross sections) of ejectiles in light-ion induced reactions. Further developments included various refinements such as multi-particle emission [Cha94b] from individual steps. These quantum mechanical multi-step theories, however, have not yet in any significant way impacted on heavy-ion reaction dynamics because of the increased complexity but it provides a great measure of insight. In light-ion reactions they have had a major impact in the medium-energy region, up to about a few hundred MeV, during the last 20 years.

During this time, other approaches have also been pursued. Various models have been proposed and applied to the analysis of experimental data. The so-called microscopic simulation methods based on quantum molecular dynamics (QMD) [Aic86] and antisymmetrized molecular dynamics (AMD) [Ono92] are Monte Carlo implementations in which the individual nucleons are represented as Gaussian wave packets, interacting via effective two-body nucleon-nucleon interactions, during which nucleon correlations are tracked from the initial non-equilibrium penetration stage throughout the relaxation stage of the reaction. Originally developed to describe heavy-ion collisions and in particular to study clustering and fragmentation phenomena, the microscopic simulation methods also found application in nucleon-induced reactions at medium energies. For example, Tanaka *et al.*

[Tan95] showed that QMD calculations very successfully reproduce the continuum double-differential cross sections of emitted protons in inclusive (p,p') reactions on various targets at incident energies between 90 and 200 MeV. In another case, Watanabe *et al.* [Wat99] compared calculations based on their semi-classical distorted wave (SCDW) model (developed to include processes up to three steps) with QMD, AMD and FKK predictions as well as measured data for the inclusive $^{58}\text{Ni}(p,p')$ and $^{90}\text{Zr}(p,p')$ reactions at incident energies of 120 and 160 MeV, respectively. They found reasonable agreement between the different predictions except at very forward and very backward angles.

2.2 Reactions induced by composite projectiles

Of the reactions induced by complex particles to the continuum, α particles are amongst the most thoroughly investigated. Earlier calculations based on the exciton and hybrid models were aimed mainly to reproduce the excitation functions of residues and the spectra of emitted protons [Gad76] but did not seriously attempt to reproduce the emitted α -particle spectra or attempt to make a comprehensive analysis of the whole reaction process. The results were not always satisfactory. Generally, a theoretical description of a reaction induced by a complex particle becomes more complicated (at least in principle) compared with nucleon-induced reactions because of processes which compete with complete fusion, leading to different routes for the production of intermediate excited nuclei (IEN). These various IEN will in the usual way emit pre-equilibrium particles, leading eventually to equilibrated nuclei which will further de-excite through evaporation. In the case of α -particle induced reactions the break-up of the α particle in the nuclear field by means of binary fragmentation may lead to the emission of deuterons, tritons and helions [e.g. Wu79], as well as incomplete fusion of any of these fragments. The α particle may also completely dissolve into its four nucleon constituents, a process called α fragmentation. According to Gadioli *et al.* [Gad92], a comprehensive model must include interactions with single nucleons of the target, starting a cascade of binary α -nucleon interactions. In a similar chaining scheme as described earlier, the main decay modes of the composite nucleus at the i 'th stage of this cascade are (1) α particle re-emission into the continuum, (2) a further α -nucleon elastic scattering, and (3) a further α -nucleon interaction leading to α fragmentation. Another process which contributes but not to a large extent is single-nucleon capture before fragmentation, i.e. the formation and break-up of ^5He and ^5Li . Thus in reactions induced by complex projectiles, incomplete fusion channels (which can be described as *break-up-fusion*

HISTORICAL DEVELOPMENT OF CONTINUUM REACTIONS

processes) become important even for projectiles as light as α particles. Due mainly to the efforts of the first half of the eighties, a realistic description of the α -nucleus interaction has been achieved, a review of which was published by Gadioli and Hodgson [Gad86].

In the case of interactions by heavier projectiles such as ^{12}C and ^{16}O it should be no surprise to find that several incomplete fusion reactions contribute. On the other hand, the number of such incomplete fusion channels which need to be considered for a comprehensive description of the reaction and the reproduction of a large body of experimental data is still relatively small. Nevertheless, due to the complexity of the various competing processes that occur, there is not yet a comprehensive and rigorous quantum mechanical theory which can be applied to the theoretical analysis of the data. A semi-classical description of the individual processes therefore seems to be the most appropriate at the present time.

A major step in the understanding of nuclear dynamics was when it was realised that the two types of reactions, direct and compound nucleus, are in fact related: The initial mean-field interaction or the interaction of the projectile with only one or at most a few nucleons of the target may create a simple state (also called a doorway state) with only a small number of excited particles and holes. As already explained earlier, this state may either decay into the continuum or decay to a more complex state by means of intranuclear interactions. Likewise, the new state may decay into the continuum or to a more complex state, etc. Ultimately the remaining excitation energy is distributed randomly among many nucleons, none of which has sufficient energy to go directly into the continuum. Thus some of the orderly kinetic energy at the onset of the reaction is transformed into random thermal energy of the compound nucleus, with pre-equilibrium particles and/or spectator fragments carrying away the rest. The theoretical models developed to describe this sequence of processes have successfully been applied to give a comprehensive description of large sets of experimental cross section data [Gad92] in the case of light-ion reactions while in continuum heavy-ion reactions the same level of comprehensive understanding still has to be achieved.

To conclude, it is interesting to note that in nucleon-induced reactions to the continuum above a few tens of MeV and below a few hundreds of MeV, the reaction can be described as a “pure” sequential pre-equilibrium reaction chain followed by evaporation. The initial interaction between the projectile and a target nucleon is merely the first step in a multi-step direct process. In the case of complex projectiles, the designation of a reaction as a “pre-equilibrium reaction” is no longer sensible as both the formation and decay of intermediate nuclei have to be described as separate but inseparable processes.

CHAPTER 3

THEORETICAL BACKGROUND

3.1 Overview

In heavy-ion reactions a complex series of processes can occur due to the relatively large number of nucleons as well as a large amount of angular momentum that a projectile can transfer to the target nucleus. These processes include the initial mean-field interaction, the formation of an excited intermediate nucleus in a state far from statistical equilibrium, its equilibration by means of intranuclear interactions, pre-equilibrium emission and finally the formation of an intermediate equilibrated nucleus (IEN) which further evaporates particles and particle aggregates, emits γ -rays and/or fissions. There is a statistical competition between these different reaction mechanisms, which all contribute to the reaction cross section and inter alia to the formation of specific heavy residues.

In this chapter, a description is given of all the reaction processes that are presently included in the theoretical model used in this study for the analysis of the cross sections of heavy residues produced in the interaction of ^{12}C and ^{16}O with ^{103}Rh , i.e. the sequence of events that may occur during the formation of the residual nuclei. Briefly, the cross sections for complete fusion and various contributing incomplete fusion mechanisms are evaluated within the framework of the Critical Angular Momentum model [Wil73, Gla75]. The break-up of the projectile is described by a generalization of the Serber Approximation [Ser47, Gad00]. In the present analysis the energy loss suffered by the projectile due to initial-state interactions is taken into consideration. The intranuclear interaction cascade and pre-equilibrium emission is described within the framework of the Boltzmann Master Equation (BME) theory [Cav96, Cav01], generalized to include the emission of clusters. Evaporation of particles after statistical equilibrium has been attained is based on the Weisskopf-Ewing formalism (e.g. [Hod97]) modified to consider average variation of the angular momentum of the nuclei of the decay chain [Ver93]. The entire time evolution of the reaction following the initial mean-field interaction is simulated using a Monte Carlo approach.

3.2 The reaction cross section and classical relationships

The reaction cross section is semi-classically defined in terms of the distance of closest approach, R_{int} , of the interacting ions and the angular momentum, L , [Hod97] by means of the

THEORETICAL BACKGROUND

quantum mechanical expression

$$\sigma_R = \pi \tilde{\lambda}^2 \sum_0^{\infty} (2l+1) T_l. \quad (3.1)$$

T_l is defined as the transmission coefficient for a reaction of a complex projectile with a complex target with an angular momentum l and may have values between 0 and 1. The reduced wavelength, $\tilde{\lambda}$, is given by

$$\tilde{\lambda}^2 = \frac{\hbar^2}{2\mu E_{CM}}, \quad (3.2)$$

with

$$\mu = \frac{m_p m_T}{m_p + m_T} \quad (3.3)$$

the reduced mass and E_{CM} the center-of-mass incident energy given by

$$E_{cm} = E_{lab} \cdot \frac{m_T}{m_p + m_T}, \quad (3.4)$$

where m_p and m_T are the respective masses of the projectile and the target. The transmission coefficient represents the fraction of incident particles with angular momentum l that penetrate within the range of the nuclear force. In a sharp cut-off approximation where all trajectories with angular momenta up to a maximum L_{int} lead to absorption, the transmission coefficient is given by

$$T_l = \begin{cases} 1 & \text{for } l \leq L_{int} \\ 0 & \text{for } l > L_{int} \end{cases}. \quad (3.5)$$

The reaction cross section can thus be written as

$$\begin{aligned} \sigma_R &= \pi \tilde{\lambda}^2 \sum_{l=0}^{L_{int}} (2l+1) \\ &= \pi \tilde{\lambda}^2 (L_{int} + 1)^2 \\ &\approx \pi \tilde{\lambda}^2 L_{int}^2. \end{aligned} \quad (3.6)$$

THEORETICAL BACKGROUND

The limiting angular momentum (for an interaction to take place), L_{int} , can be related to the corresponding distance of closest approach, R_{int} , if the interaction between the interacting ions is described by a conservative two-body potential $V(R_{int})$:

$$\frac{\hbar^2}{2\mu R_{int}^2} L_{int}^2 = E_{CM} - V(R_{int}). \quad (3.7)$$

Combining Eqs. (3.6) and (3.7) leads to the the well-known classical formula for the reaction cross section:

$$\sigma_R = \pi R_{int}^2 \left[1 - \frac{V(R_{int})}{E_{CM}} \right]. \quad (3.8)$$

By rearranging Eq. (3.8) one gets

$$E_{CM} \sigma_R = \pi R_{int}^2 (E_{CM} - V(R_{int})). \quad (3.9)$$

From expression (3.9) one can plot the product of $E_{CM} \sigma_R$ against E_{CM} and these should result in a straight line which intersects the abscissa at $E_{CM} = V(R_{int})$ and has a slope πR_{int}^2 . Bass [Bas80] has experimentally shown that $\sigma_R E_{CM}$ indeed has a linear dependency on the centre-of-mass energy by presenting fission cross sections in the interactions of ^{11}B , ^{12}C , ^{14}N , ^{16}O and ^{20}Ne with ^{238}U (amongst other reactions) where in this case the fission cross section comprised the major contribution to the reaction cross section.

From experimental reaction cross section values the interaction radius and interaction barrier are found to be approximately given by

$$R_{int} = R_1 + R_2 + 3.2 \text{ fm} \quad (3.10)$$

and

$$V(R_{int}) = 1.44 \frac{Z_1 Z_2}{R_{int}} - b \frac{R_1 R_2}{R_1 + R_2} \text{ MeV}, \quad (3.11)$$

where the half-density radii R_1 and R_2 of the interacting ions are given by

$$R_i = 1.12 A_i^{1/3} - 0.94 A_i^{-1/3}, \quad (3.12)$$

$b \approx 1 \text{ MeV}\cdot\text{fm}^{-1}$, and Z_1 and Z_2 are the charges of the interacting ions.

In the present work, the dominant contributions to the reaction cross section comprise the complete and incomplete fusion reactions, single-nucleon transfer from the projectile to the target as well as the inelastic scattering of the projectile.

3.3 Entrance-channel critical angular momentum

In the preceding section it was shown that there is a close relation between the reaction cross section and the angular momentum. In this section we are further exploring this relationship by putting the angular momentum into context.

In 1973, Gutbrod *et al.* [Gut73] showed that at energies close to the Coulomb barrier, the reaction cross section, σ_R , is almost entirely composed of the fusion cross section, σ_F . Hence, the fusion cross section was reproduced by the same formalism as that of the reaction cross section:

$$\sigma_F = \pi \tilde{\lambda}^2 (l_{cr} + 1)^2 \approx \pi \tilde{\lambda}^2 l_{cr}^2 \approx \pi R_B^2 \left[1 - \frac{V(R_B)}{E_{CM}} \right], \quad (3.13)$$

where l_{cr} denotes a so-called *critical angular momentum*, while $V(R_B)$ and R_B are the interaction barrier and the interaction distance, respectively. The interaction distance is given to a good approximation by

$$R_B = 1.4 (A_1^{1/3} + A_2^{1/3}). \quad (3.14)$$

At energies well above the Coulomb barrier, however, it has been found [Nat70a, Nat70b, Püh72] that the fusion cross section decreases while the reaction cross section increases with increasing energy. This feature has been widely considered [Bla72] to be a consequence of the critical angular momentum for the compound system. At angular momenta higher than the *critical* value the fission barrier vanishes and the compound system cannot be formed. The limitation to the formation of the composite nucleus is due to the absence of states below the yrast line (i.e. the minimum excitation energy that a nucleus may have as a function of the total angular momentum).

It was suggested by Wilczyński [Wil73] that the limitation to the fusion cross section could be described on the basis of a two-body contact configuration, where the nucleus-

THEORETICAL BACKGROUND

nucleus force is described from surface energy considerations. The derivative of the surface energy represents the force acting between the two spherical liquid drops if the diffuseness of the nuclear surface is ignored. The critical angular momentum, l_{cr} , is obtained from the condition of force equilibrium (i.e. when the maximum attractive nuclear force is exactly balanced by the sum of the repulsive Coulomb and centrifugal forces):

$$\frac{2\pi(\gamma_1 + \gamma_2)R_1R_2}{R_1 + R_2} = \frac{Z_1Z_2e^2}{(R_1 + R_2)^2} + \frac{l_{cr}(l_{cr} + 1)\hbar^2}{\mu(R_1 + R_2)^3}, \quad (3.15)$$

where μ is the reduced mass, while γ_1 and γ_2 are the surface tension coefficients for drop 1 and 2 in the liquid drop model respectively. In order to deduce $l_{cr}\hbar$ from Eq. (3.15) it is necessary to choose the distance $R_1 + R_2$ *a priori* at the value at which the derivative of the potential is equal to 0. The quantities R_1 and R_2 are taken as those values where the matter density in both drops becomes equal to $\rho_{max}/2$ where ρ_{max} is the nuclear density at the core. Since this method does not take into account the dependence of the critical angular momentum on the entrance channel [Zeb73], which has in fact also been shown to be energy dependent [Bas80], this model fell short and was in disagreement with experimental data [e.g. Gut73]. However, this deficiency can easily be rectified.

The critical distance model has subsequently been modified to take into account the dependency on the entrance channel and the incident kinetic energy [Gal74, Gla75]. In the *critical distance* approach the interaction potential between the two colliding ions, $V(r)$, is given as a function of the critical distance, R_{cr} (defined as the distance at which the interacting ions with $l = l_{cr}$ can reach each other at an energy E_{CM}). The potential is composed of the Coulomb potential, the nuclear potential and the centrifugal potential. From the expression of the energy balance given below the angular momentum can be deduced:

$$E_{CM} = V_{nucl}(R_{cr}) + V_{Coul}(R_{cr}) + \frac{\hbar^2 l_{cr}(l_{cr} + 1)}{2\mu R_{cr}^2}. \quad (3.16)$$

The critical distance is well given by

$$R_{cr} \approx r_{cr} \left(A_1^{1/3} + A_2^{1/3} \right), \quad (3.17)$$

THEORETICAL BACKGROUND

where $r_{cr} \approx 1.0 \pm 0.07$ fm. R_{cr} is approximately equal to the sum of the two half-density radii. The existence of such a critical distance has been experimentally confirmed [e.g. Gla75] in heavy-ion collisions where a large part of the kinetic energy is converted into heat when the shell structure of the individual colliding ions is destroyed and a composite system with re-arranged shell structure is formed.

When the ions approach each other up to a point of no return, they stick together due to the loss of kinetic energy long enough to establish a common nuclear structure leading to fusion. From Eq. (3.1) and the preceding arguments one can therefore write down an expression for the fusion cross section as follows:

$$\sigma_F = \pi \tilde{\lambda}^2 \sum_{l=0}^{\infty} (2l+1) T_l, \quad (3.18)$$

where

$$T_l = \begin{cases} 1 & \text{for } l \leq l_{cr} \\ 0 & \text{for } l > l_{cr} \end{cases}. \quad (3.19)$$

A similar sharp cut-off approximation as Eq. (3.5) has therefore been adopted. Analogous to Eqs. (3.6) and (3.8), the fusion cross section is approximately given by:

$$\sigma_F \approx \pi \tilde{\lambda}^2 l_{cr}^2 = \pi R_F^2 \left[1 - \frac{V(R_F)}{E_{CM}} \right], \quad (3.20)$$

where R_F is the distance of closest approach which is logically taken as the critical distance of Eq. (3.17), or in practice by values which may be marginally smaller. It was shown that R_F may in fact be somewhat smaller than the sum of the interacting half-density radii in order to get a best agreement with experimental data. At higher energies the cross section decreases as $1/E_{CM}$ since l cannot exceed l_{cr} .

The critical angular momentum model can be generalized to also describe incomplete fusion processes and refined by relaxing the sharp cut-off approximation [Wil80, Wil82]. According to the *entrance-channel critical angular momentum model*, incomplete fusion reactions are localized in successive angular momentum windows above the critical angular momentum for complete fusion. The fusion of projectile fragments can be described in a similar way as the complete fusion. For every fusion reaction channel i , a limiting angular

THEORETICAL BACKGROUND

momentum $l_{\text{lim}}(i)$ can be determined, above which that particular channel will no longer be open. In this model it is assumed that

$$l_{\text{lim}}(i) = \frac{A_{\text{tar}}}{A_{\text{frag}}(i)} \times l_{\text{cr}}(A_{\text{tar}}, A_{\text{frag}}(i)), \quad (3.21)$$

where A_{tar} is the target mass, $A_{\text{frag}}(i)$ the fragment mass relevant to channel i , and $l_{\text{cr}}(A_{\text{tar}}, A_{\text{frag}}(i))$ the critical angular momentum for a two-ion system with masses A_{tar} and $A_{\text{frag}}(i)$. A smooth cut-off in the distribution of the transmission coefficient $T_l(i)$ is given by

$$T_l(i) = \left[1 + \exp\left(\frac{l - l_{\text{lim}}(i)}{\Delta_l}\right) \right]^{-1}, \quad (3.22)$$

where Δ_l describes the diffuseness of the cut-off in the T_l distribution.

As already mentioned, a further constraint is the maximum angular momentum that can be supported by the composite system. For higher relative angular momenta, the interacting ions are unable to fuse because they cannot provide to a composite nucleus sufficient energy to be formed since a nucleus with a given angular momentum cannot have an energy below a minimum value, E_J^{min} [Bas73, Hod97], given by

$$E_J^{\text{min}} \approx J(J+1) \frac{\hbar^2}{2\mathfrak{I}}, \quad (3.23)$$

where \mathfrak{I} is the moment of inertia of the composite nucleus and J is its angular momentum. The composite nucleus is formed with an energy $E_{\text{CN}} = E_{\text{CM}} + Q$, with Q the fusion Q -value. There is a maximum angular momentum, l_{max} , which can be brought into the system depending on the total energy of the composite nucleus, as given by

$$E_{\text{CN}}^{\text{Tot}} = E_{\text{CM}} + Q = l_{\text{max}}(l_{\text{max}} + 1) \frac{\hbar^2}{2\mathfrak{I}}. \quad (3.24)$$

If $l_{\text{max}} < l_{\text{cr}}$, the fusion cross section can be written as

$$\sigma_F = \pi \lambda^2 l_{\text{max}}(l_{\text{max}} + 1). \quad (3.25)$$

If $l_{\text{max}} \gg 1$ the fusion cross section is given by

THEORETICAL BACKGROUND

$$\sigma_F = \frac{\pi \mathfrak{I}}{\mu} \left(1 + \frac{Q}{E_{CM}} \right). \quad (3.26)$$

Equation (3.26) should be slightly modified to take into account that the composite nucleus may have some intrinsic excitation energy ΔQ in addition to the rotation energy, hence

$$\sigma_F = \frac{\pi \mathfrak{I}}{\mu} \left(1 + \frac{Q - \Delta Q}{E_{CM}} \right). \quad (3.27)$$

The value for the limiting angular momentum used in fusion reaction calculations should be the lower of l_{cr} and l_{max} as described above.

3.4 Reaction cross section and angular momentum for ^{12}C and $^{16}\text{O} + ^{103}\text{Rh}$

The reaction cross sections for the interaction of ^{12}C and ^{16}O with ^{103}Rh were calculated according to the critical angular momentum model by taking into account that the mechanisms taking place in the interaction of ^{12}C and ^{16}O dominate in windows of angular momentum, which increase with decreasing mass of the fusing fragment. In our calculations, the angular momentum windows were estimated by the consideration that the complete fusion reaction occurs for angular momentum

$$l_i \leq l_{CF}, \quad (3.28)$$

where l_{CF} denotes the limiting angular momentum for complete fusion. Extending the critical angular momentum further to incomplete fusion and other reactions, we had to view the projectile as consisting of two loosely bound fragments. During the collision with the target one of the fragments gets absorbed by the target nucleus and the other escapes virtually undisturbed. The probability that the projectile breaks-up into two fragments has an exponential decrease [Gad98b, Pou91] where the break-up Q-value can be expressed as

$$P(Q) = \exp(-kQ). \quad (3.29)$$

Guided by Eq. (3.29), only a few break-up modes had been considered in previous studies. For example, in the case of $^{12}\text{C} + ^{103}\text{Rh}$ the projectile was considered to break up into $\alpha + ^8\text{Be}$, $p + ^{11}\text{B}$ and $n + ^{11}\text{C}$ [Gad97a, Gad97b, Gad98a, Gad98b, Gad99] while in $^{16}\text{O} + ^{103}\text{Rh}$

THEORETICAL BACKGROUND

the modes considered were $\alpha + {}^{12}\text{C}$, ${}^8\text{Be} + {}^8\text{Be}$, $p + {}^{14}\text{N}$ and $n + {}^{15}\text{O}$ [Gad98a, Gad98b, Gad99]. However, further experiments in which emission spectra of intermediate mass fragments (IMF) were measured [Gad03, Bec03] revealed that several other break-up modes which have hitherto not been taken into consideration also have a non-negligible contribution to the reaction cross section and thus have to be considered. These additional break-up modes are ${}^7\text{Li} + {}^5\text{Li}$, ${}^6\text{Li} + {}^6\text{Li}$, ${}^5\text{He} + {}^7\text{Be}$ and ${}^3\text{He} + {}^9\text{Be}$ (for ${}^{12}\text{C}$ induced reactions) as well as ${}^{11}\text{B} + {}^5\text{Li}$, ${}^{10}\text{B} + {}^6\text{Li}$, $d + {}^{14}\text{N}$ and ${}^7\text{Be} + {}^9\text{Be}$ (for ${}^{16}\text{O}$ induced reactions). These incomplete fusion reactions are considered to take place at angular momenta

$$l_{CF} < l_i < l_{ICF}, \quad (3.30)$$

where l_{ICF} is the highest limiting angular momentum for such a reaction to occur. Since the incomplete fusion channels close at angular momenta higher than l_{ICF} , inelastic scattering can be expected to become one of the dominant processes at $l_i > l_{ICF}$. The reaction cross sections corresponding to these angular momentum windows are approximately given by an expression analogous to Eq. (3.18):

$$\sigma_i \approx \pi \lambda^2 \sum_{l=l_i}^{l_{i+1}} (2l+1) \approx \pi \lambda^2 (l_{i+1}^2 - l_i^2), \quad (3.31)$$

where l_i and l_{i+1} are the extremes of the angular momentum window for the i^{th} mechanism. The reaction cross sections for all the contributing mechanisms considered in this work are shown as a function of projectile energy in Fig. 3.1. The values of σ_R , σ_{CF} , and incomplete fusion of ${}^{7+8+9}\text{Be}$ adopted in this work were obtained by means Eq (3.31). In the cases of the incomplete fusion of ${}^{5,6,7}\text{Li}$, ${}^{3,5}\text{He}$ and deuterons, transfer reactions and inelastic scattering the values were derived from previous experimental data [Bec03, Bir96, Gad97, Gad98, Ste03]. As for the incomplete fusion of the α -particle, the values were obtained by subtracting from σ_R the contributions of all other reaction mechanisms. (Although the results of Fig. 3.1 are somewhat pre-empted by presenting them here as the results and discussion of this work only follows in a later chapter, it is convenient to introduce them here for purposes of the present discussion.) The upper limit of the angular momentum for a particular incomplete fusion reaction can be estimated by analogy with Eq. (3.25) if sufficient knowledge of the magnitude of the cross section exist, yielding the following expression as a good approximation:

THEORETICAL BACKGROUND

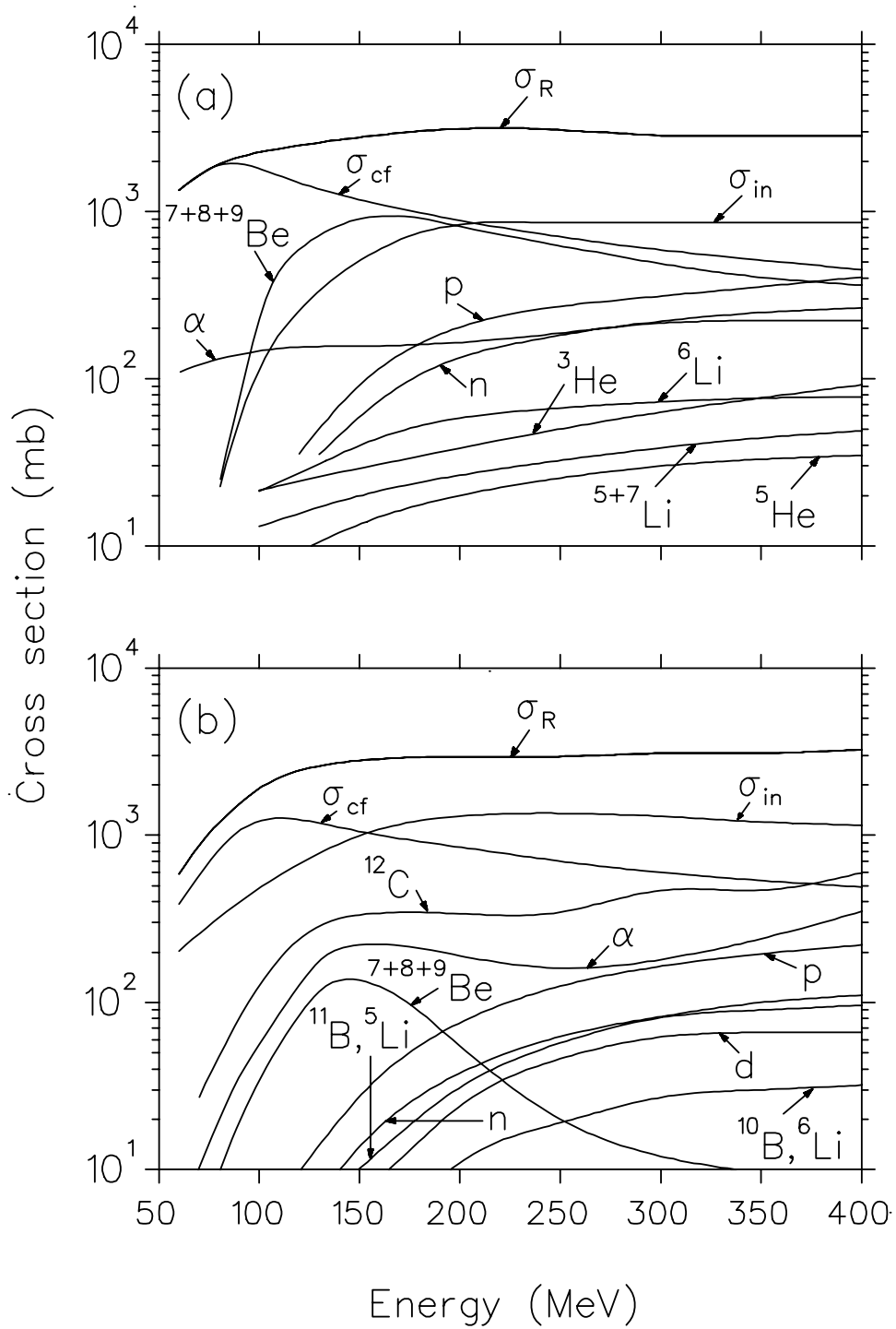


Figure 3.1 Contributions of different reaction mechanisms to the reaction cross section in (a) $^{12}\text{C} + ^{103}\text{Rh}$ and (b) $^{16}\text{O} + ^{103}\text{Rh}$ as a function of projectile energy. The subscripts cf, in and R denote the complete fusion, inelastic scattering and reaction cross sections, respectively. The incomplete fusion contributions are denoted by the fragment type (e.g. ^3He , ^5He , ^6Li , etc.) while p and n denotes the single-nucleon transfer from the projectile to the target.

$$l_{\max} \approx \sqrt{\frac{\sigma_i}{\pi\lambda^2}} - 1. \quad (3.32)$$

The angular momentum values which were adopted in the final calculations of this work, based in part on the goodness of fit with a large body of experimental data and in part on results of previous studies, are presented in Appendix 1. This will be discussed in more detail later.

3.5 The initial-state friction dissipative interaction

A lot of effort has been put into the interpretation of the continuum spectra of the intermediate mass fragments (IMF) emitted in the interaction of medium-mass projectiles (of masses typically less than or equal to 20) with various target nuclei at incident energies of typically a few tens of MeV/amu, since about the late seventies. Of particular interest to the present study is the emission to the continuum of fragments produced in the transfer of one α particle from the projectile to the target. Most of those investigations concentrated on the emission to the continuum of stable projectile fragments (e.g. [Frö79, Uda79, McV80, Hus81, Mar85, Möh88, Möh91, Fuc94], amongst others). A perusal of these previous studies is, to say the least, fascinating, in view of the wide range of interpretations suggested to explain the results.

Two dominant features can usually be identified in the continuum emission spectra of IMFs: (1) A broad break-up peak which is strongest at the most forward emission angles and decreases rather rapidly with increasing emission angle. We will refer to this peak as the *first component*. (2) A *second component* is evident towards lower emission energies. This component also decreases with increasing emission angle but much more slowly than the first component, to the extent that it becomes the dominant feature towards the higher emission angles. At sufficiently large angles where the first component has all but disappeared, the second component also displays the features of a distinct broad peak.

While there is reasonable consensus that the first component originates from a direct break-up of the projectile in a peripheral interaction with the target nucleus, widely different interpretations were given to explain the second component. Here we will not dwell on all these different interpretations, which have been summarised by Gadioli *et al.* [Gad02], but rather point out that in the most recent work the second component has been described successfully as a *coalescence* process [Gad00, Gad01, Gad02a, Gad02b, Gad03, Bec03].

THEORETICAL BACKGROUND

In an investigation of the emission of ^8Be fragments in ^{12}C induced reactions on ^{59}Co [Gad00] and ^{59}Co , ^{93}Nb and ^{197}Au [Gad01] it was found that similar to the case of stable fragments, the first component has a maximum centered at a value corresponding to the beam velocity at the most forward emission angles. Also, again in agreement with the case of stable fragments, the break-up peak has a width considerably larger than expected on the basis of a perturbative far break-up mechanism as described by a perturbative Serber approximation [McV80, Gad99]. This broadening can be explained by introducing either an initial-state interaction of the projectile with the target nucleus before breaking up, or final-state interactions of the emitted fragments with the residual nucleus, or both. In the case of ^8Be emission, however, one can discard mechanisms which describe final-state interactions of the ejectiles. Since ^8Be is unbound, it is unlikely that it will survive a violent final-state interaction without destroying the correlation between its two component α particles, by which it is detected and identified. In this case it is sufficient to only consider the energy loss of the ^{12}C projectile before breaking up, which can be described by a *friction dissipative interaction* and included in the model by introducing the concept of a *survival probability* of the projectile.

Another interesting result was found when investigating the continuum spectra of ^7Be and ^9Be fragments in the ^{12}C induced reactions [Bec03]. Firstly, a surprisingly large number of these fragments are emitted. Since it has been accepted for a long time that ^{12}C break-up will preferentially lead to the formation of α -like fragments or aggregates (see e.g. [Brit61, Siw79a, Siw79b]), the initial expectation was that these ^7Be and ^9Be fragments probably originated in final-state interactions of ^8Be (i.e. projectile break-up followed by pickup or stripping of a neutron by a ^8Be fragment). However, it was found that the observed ^7Be and ^9Be spectra exhibited the same qualitative features as ^8Be . It was therefore concluded that even if final-state interactions may be partly responsible for the softening and broadening of the IMF spectra, the initial-state interaction is by far the dominant contributing mechanism. Furthermore, similar to the analysis of the inclusive ^8Be spectra, a good quantitative description could be obtained by only taking the initial-state interaction into consideration [Bec03]. This was also found for boron and nitrogen fragments emitted in ^{16}O induced reactions [Gad03]. Thus it was concluded that the dominant reaction mechanism for the formation of IMF in the higher emission-energy regime is the binary fragmentation of the projectile with possibly a reduced energy as a consequence of a dissipative interaction with the target nucleus.

THEORETICAL BACKGROUND

When moving in the field of the target nucleus, the projectile loses energy in a continuous way by means of a kind of “nuclear friction” (slowing down) mechanism [Mar85] thereby exciting the target, with the possibility of breaking up or transferring nucleons to the target nucleus in the course of this interaction. This may lead to a considerable reduction of the kinetic energy of the projectile prior to other interactions in which it does not survive. However, the trajectories of the surviving projectile ions are not significantly altered by the friction process.

The spectra of the emitted IMF are evaluated by folding the local plane wave approximation (LPWA) cross section [Ser47, McV80] with an exponential survival probability $P(E_l)$ [Gad00, Gad02a, Gad02b] where E_l is the kinetic energy of the projectile in the CM system. In the calculation the break-up is considered to occur only above a certain minimum energy-loss value $E_{l,min}$. Consequently below this limit the break-up cross section should be zero. The double differential cross section of a fragment emitted at an emission angle θ with an energy E' in the break-up of a projectile with incident energy E_0 is then given by

$$\frac{d^2\sigma}{dE'd\Omega}(E_0, E', \theta) = \sigma_{bu} \frac{\int_{E_{l,min}}^{E_0} P(E_l) S(E, E', \theta) dE_l}{\int_{E_{l,min}}^{E_0} P(E_l) dE_l}, \quad (3.33)$$

where σ_{bu} is the angle and energy integrated break-up cross section and E_l is the energy lost by the projectile before break-up. The survival probability is given by

$$P(E_l) = \begin{cases} \exp[-kk'(E_l - E_{l,min})], & \text{for } E_{l,min} \leq E_l \leq E_0, \\ 1, & \text{for } E_l < E_{l,min}, \end{cases} \quad (3.34)$$

where k' is a constant break-up and mass transfer probability per unit length, while k is related to the energy loss per unit length according to $-dE_l/dx = 1/k$. The values for kk' were obtained from fits to the experimental data. The cross section for producing a fragment of energy E' at an angle θ in the break-up of a projectile of energy $E = E_0 - E_l$ is given by

$$S(E, E', \theta) = \begin{cases} 0, & \text{for } E_l < E_{l,min}, \\ \frac{d^2\sigma^S(E, E', \theta)}{dE'd\Omega}, & \text{for } E_l \geq E_{l,min}. \end{cases} \quad (3.35)$$

THEORETICAL BACKGROUND

The cross section is evaluated in the LPWA by

$$\frac{d^2\sigma^S(E, E', \theta)}{dE'd\Omega} \propto P'P'' |\psi(\mathbf{p})|^2, \quad (3.36)$$

where the function $\psi(\mathbf{p})$ is the Fourier transform of the wave function, $\psi(r)$, describing the relative motion of the fragment within the projectile, given by

$$\psi(\mathbf{p}) = \frac{1}{(2\pi\hbar)^{3/2}} \int \psi(r) \exp\left[-\frac{i}{\hbar}(\mathbf{p} \cdot \mathbf{r})\right] d\mathbf{r}. \quad (3.37)$$

The internal momentum of the fragment within the projectile is given by

$$\mathbf{p} = \mathbf{P}' - \left(\frac{m_f}{m_p}\right) \mathbf{P}, \quad (3.38)$$

where \mathbf{P} is the momentum of the projectile when it breaks up (after the energy loss) and \mathbf{P}' is the momentum of the observed fragment (and p' its modulus) just after break up. This momentum differs from the observed momentum since the fragment is boosted by the Coulomb repulsion after being produced. P'' is the modulus of the momentum of the unobserved fragment and m_f and m_p are the respective masses of the observed fragment and projectile. The folding procedure is the same as that used by Hussein *et al.* [Hus81] in order to account for the final-state inelastic interactions of the observed fragment. The Fourier transform (equation 3.37) is evaluated using the deuteron-like expression

$$\psi(r) = \frac{R(r)}{r}, \quad (3.39)$$

where

$$R(r) = \begin{cases} Ar^2, & \text{for } 0 \leq r \leq b+f, \\ B \sin K(r-b), & \text{for } b+f < r \leq b+R, \\ C \exp(-r/R_0), & \text{for } r > b+R. \end{cases} \quad (3.40)$$

For known $K = \frac{\sqrt{2\mu(V_0 - B)}}{\hbar}$ the quantities f and R_0 are free parameters while

$$b = (2 \tan Kf - Kf) / K \quad \text{and} \quad R = \frac{1}{K} \arctan(-KR_0).$$

THEORETICAL BACKGROUND

The constants A , B and C are given by the matching and normalization conditions, with the values given by

$$A = B \frac{\sin Kf}{(b+f)^2}, \quad (3.41)$$

$$B = \frac{1}{2\sqrt{\pi}} \sqrt{\frac{1}{\frac{b+f}{5} \sin^2 Kf + \frac{1}{2}(R-f) - \frac{1}{4K}(\sin 2KR - \sin 2Kf) + \frac{R_0}{2} \sin^2 KR}} \quad (3.42)$$

and

$$C = B \exp\left(\frac{b+R}{R_0}\right) \sin KR. \quad (3.43)$$

The corresponding Fourier transform is then given by

$$\begin{aligned} \psi(p) = & \frac{4\pi B(\hbar c)^2}{(2\pi\hbar)^{3/2}} \frac{1}{pc} \left\{ \frac{\sin Kf}{pc} \left[\frac{2(\hbar c)^2}{(pc)^2 (b+f)^2} \left(\cos \frac{pc(b+f)}{\hbar c} \right) - 1 \right. \right. \\ & \left. \left. - \cos \frac{pc(b+f)}{\hbar c} + \frac{2\hbar c}{pc(b+f)} \sin \frac{pc(b+f)}{\hbar c} \right] \right. \\ & + \frac{1}{(\hbar Kc)^2 - (pc)^2} \left[pc \sin KR \cos \frac{pc(b+R)}{\hbar c} - \hbar Kc \cos KR \sin \frac{pc(b+R)}{\hbar c} \right. \\ & \left. - pc \sin Kf \cos \frac{pc(b+f)}{\hbar c} + \hbar c K \cos Kf \sin \frac{pc(b+f)}{\hbar c} \right] \\ & \left. \frac{\sin KR}{(\hbar c/R_0)^2 + (pc)^2} \left[pc \cos \frac{pc(R+b)}{\hbar c} + \frac{\hbar c}{R_0} \sin \frac{pc(R+b)}{\hbar c} \right] \right\}, \quad (3.44) \end{aligned}$$

where $p = p_S - \left(\frac{M_S}{M_P}\right) p_P$ while p_S , p_P , M_S and M_P are the momenta and the masses of the spectator fragment and projectile, respectively. The wave function for the relative motion of each fragment pair constituting the projectile (which is considered to be similar to the deuteron) is evaluated for $L = 0$ with a square-well interaction potential. This is the most common occurrence. For $L \geq 1$ the relative motion wave function is evaluated in the cluster approximation using a Saxon-Woods potential.

THEORETICAL BACKGROUND

The energy and angular distribution of the emitted spectator and, therefore, the angular and energy distribution of the intermediate excited system (composite nucleus) formed when the complementary fragment fuses with the target can be evaluated [Par91, Ver93] by assuming (i) that the incident projectile is slowed by the Coulomb barrier between the projectile and the target and (ii) the remaining projectile energy is divided between the two fragments as predicted by the Serber approximation [Ser47], generalizing the later expression thereof as given by Matsuoka *et al.* [Mat78]:

$$\frac{d^2\sigma}{dE_S d\Omega_S} \propto \frac{\sqrt{E_S E_P}}{\left[2\mu B_{proj} + \frac{2m_S^2 E_{proj}}{m_{proj}} + 2m_S E_S - 4 \left(\frac{m_S^3 E_{proj}}{m_{proj}} \right)^{1/2} \cos(\theta) \right]^2}. \quad (3.45)$$

The subscripts s , p and $proj$ represent the spectator, participant and projectile, respectively. E_S and E_P are the corresponding fragment kinetic energies, B_{proj} the binding energy of the spectator and participant inside the projectile, μ is the reduced mass and m_S , m_P and m_{proj} are the respective masses, while θ is the emission angle of the spectator with respect to the projectile. After break-up the emitted fragment is accelerated by the Coulomb field of the composite nucleus created in the absorption of the participant fragment by the target nucleus.

3.6 Importance of α -particle re-emission in ^8Be and α -particle incomplete fusion

In the analysis of the inclusive spectra of α particles emitted in ^{12}C induced reactions on ^{59}Co and ^{93}Nb at energies of 300 and 400 MeV, it was found that the incomplete fusion reactions do not only play an increasingly important role with increasing incident energy, but also that most of the energy transferred to the target nucleus has to be rapidly dissipated without warming the nucleus [Gad99]. In addition to the usual pre-equilibrium emission of particles which occurs during the intranuclear cascade, most of the participant α particles are re-emitted with retention of a large fraction of their initial energy. This re-emission has a weak dependence on the mass of the target nucleus. Re-emission of α -particles is also expected to occur in the incomplete fusion of ^8Be (since it essentially consists of two α particles). Thus one can expect that only those α particles that, after absorption by the target nucleus, are directed toward the denser nuclear core will distribute their energy among the nucleons of the

absorbing nucleus while those that are directed to the low density nuclear surface region will have a rather large probability of escape. Since these incomplete fusion interactions occur in very peripheral regions of the nucleus, the latter process is very likely.

In this work the probability for the re-emission of α particles was set to 0.4 for the incomplete fusion of ^8Be fragments and 0.5 for the incomplete fusion of break-up α particles, for both the ^{12}C and ^{16}O induced reactions (see Appendix 1).

3.7 Thermalization of the intermediate nuclei formed in fusion and incomplete fusion reactions.

When two heavy ions fuse they normally form a composite nucleus which is far from statistical equilibrium since a large fraction of its energy is in the form of an orderly collective translational motion of the nucleons of the projectile and the target. This orderly motion transforms into chaotic thermal motion through a cascade of nucleon-nucleon interactions (i.e. a two-body dissipative interaction mechanism) during the thermalization of the composite nucleus. This process takes some time but before reaching thermal equilibrium, some nucleons and clusters, which still have an energy higher than their equilibrium thermal energy, may be emitted into the continuum. Hence, this pre-equilibrium emission must be taken into account to reproduce the multiplicity spectra of the ejectiles measured in heavy ion interactions. In this work, the thermalization stage is described by means of the Boltzmann Master Equation (BME) theory [Fab89, Fab90, Fab91, Cer92, Fab93, Cav95, Bru95, Cav96, Cav97, Cav98], generalized to also describe the emission of clusters.

3.7.1 Boltzmann Master Equation theory of pre-equilibrium emission

In the BME theory the evolution of the excited system toward equilibrium is simulated by a set of coupled master equations. In this theory, an azimuthal symmetry with respect to the beam direction is adopted, thus one can reduce the momentum description to only two independent variables, p^2 and p_z , which are the square of the momentum of a nucleon and the component of the momentum along the beam axis, respectively. The nucleon states are classified according to their energy, ε_i , and divided into bins of width $\Delta\varepsilon$. The bins are further characterised by constant values of Δp^2 and Δp_z . The number of occupied states, $N(\varepsilon, \theta, t)$ within each bin is equal to the product of the total number of states for that bin, g_i , evaluated

THEORETICAL BACKGROUND

in the framework of the Fermi gas model, times an occupation number $0 \leq n_i \leq 1$. Nucleon states in bin i and j may interact and scatter to states in bins l and m provided that the energy and momentum are conserved and that unoccupied states in bins l and m are available. Unbound nucleons are allowed to escape from the nucleus with an energy

$$\varepsilon_i' = \varepsilon_i - \varepsilon_F - B_i, \quad (3.46)$$

thus contributing to the pre-equilibrium emission. The notations ε_F and B_i denote the respective Fermi energy and the binding energy of a nucleon in the composite nucleus. The subsequent evolution of the nucleus, which is considered to be a two-fermion gas, is described by a set of coupled master equations for the proton and neutron gases. The expression for the proton gas (the neutron gas has an analogous form) is given by

$$\begin{aligned} \frac{d(n_i g_i)^\pi}{dt} = & \sum_{jlm} \left[\omega_{lm \rightarrow ij}^{\pi\pi} g_l^\pi n_l^\pi g_m^\pi n_m^\pi (1 - n_i^\pi) (1 - n_j^\pi) - \omega_{ij \rightarrow lm}^{\pi\pi} g_i^\pi n_i^\pi g_j^\pi n_j^\pi (1 - n_l^\pi) (1 - n_m^\pi) \right] \\ & + \sum_{jlm} \left[\omega_{lm \rightarrow ij}^{\pi\nu} g_l^\pi n_l^\pi g_m^\nu n_m^\nu (1 - n_i^\pi) (1 - n_j^\nu) - \omega_{ij \rightarrow lm}^{\pi\nu} g_i^\pi n_i^\pi g_j^\nu n_j^\nu (1 - n_l^\pi) (1 - n_m^\nu) \right] \\ & - n_i^\pi g_i^\pi \omega_{i \rightarrow i'}^\pi g_{i'}^\pi \delta(\varepsilon_i^\pi - \varepsilon_F^\pi - B_i^\pi - \varepsilon_{i'}^\pi) - \frac{dD_i^\pi}{dt}, \end{aligned} \quad (3.47)$$

where π and ν stand, respectively, for the proton and the neutron. The quantities $\omega_{ij \rightarrow lm}$, $\omega_{i \rightarrow i'}$ and $\frac{dD_i}{dt}$ are the respective internal transition decay rate, the decay rate for emission of single protons of the i^{th} bin into the continuum and the depletion term which accounts for the emission of the protons of the i^{th} bin which are part of a cluster. The internal transition rates are given by

$$\omega_{ij \rightarrow lm} = \frac{1}{2\pi} \int_0^{2\pi} \omega_{ij \rightarrow lm} d\phi_j, \quad (3.48)$$

due to axial symmetry where

$$\omega_{ij \rightarrow lm} = \frac{\sigma_{ij} \nu_{ij} \Pi_{ij \rightarrow lm}}{V}. \quad (3.49)$$

Here V is the nuclear volume, σ_{ij} is the two-nucleon interaction cross section and ν_{ij} their relative velocity. The indexes i, j, l, m stands for the momenta p_i, p_j, p_l, p_m and ϕ_j is the

THEORETICAL BACKGROUND

azimuthal angle of p_j , where $\phi_i = 0$. The quantity $\Pi_{ij \rightarrow lm}$ represents the probability of reaching bins l and m if the interacting nucleons have momenta p_i and p_j belonging to bins i and j . The decay rates $\omega_{i \rightarrow i'}$ are given by

$$\omega_{i \rightarrow i'} = \frac{\sigma_{inv} \mathcal{V}_i'}{g_i V'}, \quad (3.50)$$

where σ_{inv} is the inverse process cross section, \mathcal{V}_i' is the relative velocity between the nucleon and the residual nucleus and V' is the laboratory volume which cancels with a similar factor appearing in the expression of g_i' in Eq. (3.47).

The multiplicity spectrum of nucleons emitted at an angle θ with an energy $\varepsilon - \varepsilon_F - B$, where ε_F and B are respectively the nucleon binding and Fermi energies, is given by

$$\frac{d^2 M_n(\varepsilon', \theta)}{d\varepsilon' d\Omega} = \frac{1}{2\pi \sin \theta} \int n(\varepsilon', \theta, t) \frac{\sigma_{inv, n} \mathcal{V}_n}{V} \rho_n(\varepsilon', \theta) dt, \quad (3.51)$$

where the subscript n indicates nucleon emission and

$$\rho_n(\varepsilon', \theta) = \frac{\sin \theta}{2} \rho_n(\varepsilon') \quad (3.52)$$

represents the density of particle states $\rho_n(\varepsilon')$ in the continuum [Gad02a]. In the case of clusters formed by means of the nuclear coalescence process, very similar expressions can be adopted. The multiplicity spectrum of clusters emitted is given by

$$\frac{d^2 M_c(E'_c, \theta_c)}{dE'_c d\Omega} = \frac{R_c}{2\pi \sin \theta} \int N_c(E'_c, \theta_c, t) \frac{\sigma_{inv, c} \mathcal{V}_c}{V} \rho_c(E'_c, \theta_c) dt, \quad (3.53)$$

where R_c is a survival probability of the cluster, i.e. the probability for emission of the cluster before dissolving again into its constituent nucleons, while the other quantities are defined analogously to the nucleon case. The continuum energy of the cluster is given by

$$E'_c = E_c - S_c - A_c (E_{CN, F} - E_{C, F}), \quad (3.54)$$

THEORETICAL BACKGROUND

where S_C is the cluster separation energy and $E_{C,N,F}$ and $E_{C,F}$ are, respectively, the composite nucleus and the cluster Fermi energies [Cav94]. The cluster state occupation probability $N_C(\varepsilon_C, \theta_C, t)$ is a function of the state occupation probabilities $n(E, \theta, t)$ of the individual nucleons constituting the cluster. For a cluster having Z_C protons and N_C neutrons, the cluster state occupation probability is given by

$$N_C(\varepsilon_C, \theta_C, t) = \prod_i [n_i^\pi(\varepsilon, \theta, t)]^{P_i(E_C, \theta_C)Z_C} \cdot \prod_i [n_i^\nu(\varepsilon, \theta, t)]^{P_i(E_C, \theta_C)Z_C}, \quad (3.55)$$

where the index i runs over all the bins which the states of the protons and neutrons of the cluster may occupy and $P_i(E_C, \theta_C)$ is the fraction of bin i which falls within the Fermi sphere of the cluster C .

3.7.2 Initial nucleon energy distribution in the BME theory

In the Boltzmann Master Equation theory of pre-equilibrium reactions the initial nucleon energy distribution of the di-nuclear system is important. The nucleon momentum distribution depends on the kinetic energy which the nucleons either lose or gain. The energy loss is due to Coulomb repulsion and the gain is due to the difference of the nucleon Fermi energy to that of the composite nucleus. The Fermi energy of an emitted cluster

$$E_{C,F} = \frac{p_{C,F}^2}{2m} \quad (3.56)$$

is not expected to vary in a regular way with its proton and neutron numbers Z and N of the cluster. However, to evaluate the Fermi energies of the isotopes of a given elemental fragment, the liquid drop model was used [Bru95]. The model provides parametrization of the nuclear Fermi energies which depends on the nuclear mass A as well as on the proton-neutron asymmetry and takes into account surface effects. This Fermi energy is given by

$$E_{C,F} = \frac{1}{A} [ZE_{C,F}^\pi + NE_{C,F}^\nu], \quad (3.57)$$

where $E_{C,F}^\pi$ and $E_{C,F}^\nu$ are the respective Fermi energies of the cluster's protons and neutrons given by

THEORETICAL BACKGROUND

$$E_{C,F}^{\pi} = E_F \left(\frac{2Z}{A} \right)^{2/3} \left(1 - 0.387 A^{-1/3} \right)^2 \quad (3.58)$$

and

$$E_{C,F}^{\nu} = E_F \left(\frac{2N}{A} \right)^{2/3} \left(1 - 0.387 A^{-1/3} \right)^2. \quad (3.59)$$

The nuclear matter Fermi energy is represented by E_F with $A=N+Z$ the mass number of the cluster.

The internal nucleon momentum density distributions for the projectile and the target were evaluated using the Saxon-Wood (SW) distribution as well as the Guassian-like (G) distribution [Bru95]. The Saxon-Wood distribution is expressed by

$$\rho(p) = \left[1 + \exp\left((p - p_0) / \Delta p \right) \right]^{-1} \quad (3.60)$$

and the Guassian distribution is given by

$$\rho(p) = \exp\left[-\left((p - p_0) / \Delta p \right)^2 \right]. \quad (3.61)$$

The parameters of both the SW and G distributions were fixed so that the normalization of the proton/neutron momentum distributions gave the correct proton/neutron number. The choice of SW or G is based on the target mass, where for relatively medium-heavy nuclei (e.g. the target of this study) we used the SW distributions and for the light nuclei we took either the G form fitted to the shell model calculations or the SW forms whose parameters are obtained from those of the heavier nuclei through an extrapolation procedure. The values used are listed in Appendix 1.

3.7.3 Mean-field effects

At energies below about 10 MeV/nucleon, heavy-ion collisions are dominated by the nuclear mean field (i.e. a one-body dissipation mechanism). As the beam energy increases, there is a relaxation of the Pauli blocking and the mean-field interaction becomes less dominant while two-body nucleon-nucleon collisions become more important. At energies of about 100 MeV/nucleon and higher the two-body interaction mechanism dominates strongly. In the

THEORETICAL BACKGROUND

intermediate-energy regime (i.e. about 10 – 100 MeV/nucleon) there is a competition between one-body and two-body dynamics.

In order to take both the one-body and two-body reaction dynamics into account in intermediate-energy heavy-ion reactions, a phase-space approach based on the Vlasov-Uehling-Uhlenbeck (VUU) [Fuc92] equation in its Vlasov limit [Mol91, Bon94] is employed. In addition, according to an approach first described by Cassing [Cas87, Cas88] the action of the mean field and nucleon-nucleon interactions can be separated in time. The mean field is dominant in the first stage of the reaction up to a point in time which is of the order of the contact time plus the primary collision time, whereafter the further evolution of the reaction dynamics is mainly governed by two-body nucleon-nucleon interactions.

In the Vlasov limit, the time dependence of the mean values of the projectile translational momentum, $\langle p_p^t \rangle$, and the target translational momentum, $\langle p_T^t \rangle$, are evaluated at the time of contact ($t = 0$) of the two interacting ions at a relative distance z between the centres of mass of the two nuclei, approximately equal to the sum of their radii, $z(t = 0) \approx r_0 (A_p^{1/3} + A_T^{1/3})$. The nuclear mean field is assumed to act until a collision time, t_{coll} , which is needed (on average) by the two nucleons to interact. At this time the window between the two nuclei is large enough to allow nucleons to pass from one nucleus to the other, so that at times greater or equal to t_{coll} they can start to have two-body nucleon-nucleon collisions.

Introducing the mean field at the very beginning of the reaction ($t < t_{coll}$), the mean values of the Vlasov predictions for $\langle p_p^t \rangle$ and $\langle p_T^t \rangle$ at $t = t_{coll}$ are compared with their kinematical momentum values given by

$$p_P^t = \left[\frac{2m \left(E_{lab} + \frac{A_C}{A_T} Q \right)}{A_p} \right]^{1/2} \frac{A_T}{A_C}, \quad (3.62)$$

and

$$p_T^t = \left[\frac{2m \left(E_{lab} + \frac{A_C}{A_T} Q \right)}{A_p} \right]^{1/2} \frac{A_p}{A_C}, \quad (3.63)$$

THEORETICAL BACKGROUND

where A_C denotes the mass of the composite nucleus, E_{lab} is the beam energy in the laboratory system, m is the nucleon mass and Q denotes the fusion Q-value. It was found [Bru95] that the Vlasov predictions ($\langle p_p^t \rangle$ and $\langle p_T^t \rangle$) are consistently somewhat higher than the kinematical values of the individual colliding nuclei (p_p^t and p_T^t). Thus, during the overlap phase of the one-body Vlasov dynamics, the total kinetic energy of the nucleons of both the projectile and the target nucleus increases. A dynamical change happens as the potential wells of the two interacting nuclei merge into the common well of the compound nucleus, leading to a deeper potential well and to nucleon acceleration.

One way to describe the increase of the total nucleon kinetic energy is to replace the incident energy in Eqs. (3.62) and (3.63) by an effective incident energy given by

$$E_{lan}^{eff} = E_{lab} + S, \quad (3.64)$$

where S takes into account the acceleration due to the change of the potential well. Brusati *et al.* presented a phenomenological expression for S :

$$S = \frac{A_C}{A_T} \left[\frac{3}{5} A_p (\bar{\epsilon}_{f_C} - \bar{\epsilon}_{f_p}) + \frac{3}{5} A_T (\bar{\epsilon}_{f_C} - \bar{\epsilon}_{f_T}) \right]. \quad (3.65)$$

Here the subscripts P , T and C stand for the projectile, target and composite nucleus, respectively and the Fermi energy, $\bar{\epsilon}_f$, is given by Eq. (3.57) above. S in Eq. (3.65) has a positive value because the combined system has a larger Fermi energy. Brusati *et al.* [Bru95] showed that the Vlasov predictions of the mean values for the translational momenta of the projectile and the target are in good agreement with the values obtained from Eqs. (3.62) and (3.63) by increasing the incident energy according to Eq. (3.64), over a wide range of masses and energies. The latter approximation is much more convenient to include in a comprehensive computational scheme than the VUU formalism.

Brusati *et al.* also investigated another way to introduce the nucleon acceleration at the beginning of the reaction process in which the composite nucleus is given the additional energy as thermal kinetic energy. The initial momentum distribution is constructed by coupling the modified translational momenta with the Saxon-Wood type (equation (3.60)) internal distributions assuming for both the colliding ions the internal momentum distribution

THEORETICAL BACKGROUND

with the same Fermi energy as the composite nucleus, $\bar{\epsilon}_{f_p} = \bar{\epsilon}_{f_r} = \bar{\epsilon}_{f_c}$. The two prescriptions give essentially the same results for all practical purposes.

3.7.4 Effective Coulomb barrier

Upon their emission, the clusters produced by means of coalescence feel an effective Coulomb barrier V_C which is indicated by the energy that the emitted cluster has. If the cluster is emitted with low energy it indicates a low effective Coulomb barrier and vice versa. In addition, it is possible to ascertain whether the clusters were emitted from a recoiling spherical nucleus or from a deformed nucleus by the dependence of the Coulomb barrier on the angle of emission. The Coulomb barrier $V_C(\theta)$ in the recoiling nucleus reference frame due to nuclear deformations depends on the cluster's emission. The relationship is defined by the emitted cluster inverse cross section, $\sigma_{inv,c}$, the geometrical cross section, $\sigma_{geo}(\theta)$, and the centre-of-mass channel energy, E_{ch} , as given by the semi-classical expression

$$\sigma_{inv,c} = \sigma_{geo}(\theta) \left(1 - \frac{V_c(\theta)}{E_{ch}} \right). \quad (3.66)$$

In order to avoid the sharp and unrealistic low energy edge of this semi-classical expression and to take into account the possibility of cluster emission below the barrier, we used for the $\sigma_{inv,c}$ at emission energies slightly below and around the Coulomb barrier an expression evaluated with the Hill and Wheeler parabolic approximation [Hil53].

3.8 The BME in Monte Carlo calculations

The BME theory of pre-equilibrium reactions is only able to predict the average multiplicity of the particles emitted during thermalization, their average energy and angular distribution. However, it is not sufficient in evaluating excitation functions for a particular reaction which may occur because in this case one actually needs to evaluate the probability of a sequence of events which take place leading to the emission of a particular number of particles. The probability of a sequence of decays which may take place is obtained by recognizing that in the limit of a very short time interval, the multiplicity of the emitted particles in that short interval coincides with their emission probability. Thus the probability of a particular sequence of decays which may take place in a much longer time interval, can be reduced to a

THEORETICAL BACKGROUND

joint probability calculation of a sequence of decays which occurs in these small time intervals. This may be done with a Monte Carlo technique as proposed by Dostrovsky *et al.* [Dos59]. The Monte Carlo calculation simulates a large number of sequences of decays [Cav96, Cav01] and uses as input the partial differential multiplicities of the particles emitted during the cascade of nucleon-nucleon interactions as discussed in section 3.7 above.

Following equation (3.47), the multiplicity spectrum $\frac{dn_i^C}{d\varepsilon_i}$ of protons emitted into the continuum from bin i is given by

$$\frac{dn_i^C}{d\varepsilon_i} = n_i^\pi g_i^\pi \omega_{i \rightarrow i'}^\pi g_{i'}^\pi \delta(\varepsilon_i^\pi - \varepsilon_F^\pi - B_i^\pi - \varepsilon_{i'}^\pi) dt, \quad (3.67)$$

where the decay rates for the emitted particles are given by Eq. (3.47). In each cascade, if one considers a sufficiently short time interval, Δt_j , the differential multiplicity [Cav01] for a particle ν is given by

$$\frac{d^2 N'_\nu(E_\nu, \theta, \Delta t_j)}{dE_\nu d\theta} = \frac{d^2 N'_\nu(E_\nu, \theta, t_j + \Delta t_j)}{dE_\nu d\theta} - \frac{d^2 N'_\nu(E_\nu, \theta, t_j)}{dE_\nu d\theta}. \quad (3.68)$$

These differential multiplicities are saved at time intervals corresponding to a *constant increment of the multiplicity* of all emitted particles integrated over the energy and the solid angle. This leads to time intervals increasing with increasing time since the particle emission probability per unit time decreases with increasing time during the course of the cascade. The Monte Carlo cascade goes through the same procedure at each step, sampling if an emission occurs from the integrated multiplicity distribution. For every emission, the possible energy and direction of particles are chosen randomly. The event is accepted if the energy is conserved, otherwise it is rejected and the next step is analysed. At the end of each Δt_j the centre-of-mass charge, mass and excitation energy of the residual nucleus are calculated and used as those of the new composite nucleus.

The change that the angular momentum, \mathbf{J} , of the composite nucleus undergoes due to pre-equilibrium emission of particles is evaluated as described by Vergani *et al.* [Ver93]. When a nucleon is emitted in a plane with an azimuthal angle ϕ , the modulus of the angular momentum left to the residual nucleus, \mathbf{J}_r , is approximately given

THEORETICAL BACKGROUND

$$J_r^2 = J^2 + \bar{l}_{out}^2 - \frac{2J\bar{l}_{out} \cos \theta}{\sqrt{\cos^2 \theta + \sin^2 \theta \cos^2 \phi}}, \quad (3.69)$$

where

$$\bar{l}_{out} = \frac{1}{\sqrt{2}} \left[\left(\frac{\sigma_{inv}(\varepsilon)}{\pi \tilde{\lambda}^2} \right)^{1/2} - 1 \right] \quad (3.70)$$

is the modulus of the average momentum of the emitted nucleon. At the end of the thermalization cascade, an intermediate equilibrated nucleus (IEN) with a given Z , N and excitation energy E_r is formed that has a total angular momentum J_r . This nucleus may further decay by evaporation.

3.9 Evaluation of evaporation chains in the Monte Carlo calculations

The theoretical approaches which are most often employed to evaluate the decay of an equilibrated nucleus by means of evaporation are based on either the Hauser-Feshbach or the Weisskopf-Ewing theories [Gad92, Hod97]. The simpler Weisskopf-Ewing theory depends only on the nuclear level density and on the formation cross section of the compound nucleus. It does not explicitly consider the conservation of angular momentum and cannot give the angular distributions of emitted particles. The Hauser-Feshbach theory takes into account the formation of the compound nucleus in states of different angular momentum and parity and adds these individual contributions incoherently.

In the following discussion the decaying nucleus is referred to as the compound nucleus with energy E and angular momentum J . The emission from the compound nucleus leads to the residual nucleus with energy U and angular momentum J_r . The decay of the compound nucleus in a state of statistical equilibrium proceeds via a chain of sequential emissions. For the evaporation chain to be incorporated into a Monte Carlo calculation, the emission probabilities of the different particles ν and the probability of exciting residual nucleus states of a given angular momentum J_r can be evaluated using J -dependent decay widths [Ver93]:

$$\Gamma_{\nu(E,J,\varepsilon_\nu J_r)} d\varepsilon_\nu = \frac{1}{2\pi\omega_{CN}(E,J)} \times \sum_{S'=|J_r-i_\nu|}^{S'=J_r+i_\nu} \omega_r(U, J_r) \sum_{l'_\nu=|J-S'|}^{J+S'} T_{l'_\nu}(\varepsilon_\nu) d\varepsilon_\nu, \quad (3.71)$$

THEORETICAL BACKGROUND

where $\omega_{CN}(E, J)$ and $\omega_r(U, J_r)$ are the compound nucleus and residual nucleus level densities, and the $T'_v(\varepsilon_v)$ are the emitted particle transmission coefficients. The spin of the decay channel is given by $\mathbf{S}' = \mathbf{J}_r + \mathbf{i}_v$, where \mathbf{i}_v is the spin of the emitted particle. The spin of the decaying compound nucleus \mathbf{J} , the decay-channel spin \mathbf{S}' and the emitted particle orbital angular momentum \mathbf{I}'_v are related by $\mathbf{J} = \mathbf{I}'_v + \mathbf{S}'$.

For high values of the angular momentum \mathbf{J} , the nucleus may be considerably deformed. A few simplifying assumptions concerning this deformation have been made, namely that it is axially symmetric and symmetric under rotation about an axis orthogonal to the symmetry axis. The level density for the compound nucleus is then given by

$$\omega(E, J) = \omega(E) F(J) = \omega(E) \frac{1}{2} \sum_{K=-J}^{K=J} \exp \left[-\frac{K^2 \hbar^2}{2\mathfrak{I}_{\square} T} - \frac{[J(J+1) - K^2] \hbar^2}{2\mathfrak{I}_{\perp} T} \right]. \quad (3.72)$$

$F(J)$ is sometimes called the spin distribution function. Here T is the residual nucleus temperature and K is the projection of \mathbf{J} along the symmetry axis, while \mathfrak{I}_{\square} and \mathfrak{I}_{\perp} are the nucleus moments of inertia for rotation around the symmetry axis and an axis perpendicular to the symmetry axis, respectively. These moments of inertia have to be evaluated for all sets of values of A , Z , and J along the evaporation chain, which makes the calculation very time consuming.

In order to alleviate the calculational load, the probability of emission of a given particle, v and its energy ε_v , are evaluated using \mathbf{J} -independent decay widths [Dos59]

$$\Gamma_v(E_{CN}, \varepsilon_v) = \frac{1}{\omega_{CN}(E)} \frac{(2i_v + 1) \mu_v \varepsilon_v}{\pi^2 \hbar^2} \sigma_{inv,v}(\varepsilon_v) \omega_r(U). \quad (3.73)$$

The angular momentum of the residual nucleus is then estimated from the spin distribution function as a weighted average of the values

$$J - \bar{l}_{out} \leq J_r \leq J + \bar{l}_{out} \quad (3.74)$$

where the quantity \bar{l}_{out} is the average value of the emitted particle orbital angular momentum as given before in Eq. (3.70), ignoring the intrinsic spin of the particle. In this procedure it is assumed that E and J are independent variables, which is a good approximation for energies

THEORETICAL BACKGROUND

well above the yrast energy. It is found that the angular momentum of the compound nucleus never changes significantly along the evaporation chain except at the very end of the chain when little excitation energy remains. At this stage the yrast energy may permit only decays to states with sufficiently low angular momentum, which may mean that the emission of another particle may even be forbidden.

In this study, the emitted particle inverse cross sections were calculated from the expressions given by Dostrovsky [Dos59] with parameters suggested in [Gad92]. The level density was assumed to have an equidistant spacing as characterized by the usual level density parameter a , for which a value of $a = A/8 \text{ MeV}^{-1}$ was used. Binding energies were taken from the compilation by Audi and Wapstra [Aud95].

CHAPTER 4

EXPERIMENTAL PROCEDURES

4.1 Overview

Several activation experiments were performed in this study. The primary objective was to measure the cumulative production cross sections of ^{103g}Ag , ^{103}Pd and ^{103}Ru , as well as the cross section for the direct production of the short-lived ^{103m}Rh in the interaction of ^{12}C and ^{16}O with ^{103}Rh . However, cross sections for the production of all the other heavy residues observed were also extracted. In cases where radiochemical procedures were applied, several different radiochemical methods were investigated for their suitability. This chapter is devoted to the specific procedures that were finally adopted for the separation of silver, palladium and rhodium from the original target matrices in the irradiations which yielded the experimental data. Details of the other radiochemical methods investigated are discussed in Appendix 2.

4.2 Delivery of beam

The separated sector cyclotron (SSC) of iThemba LABS is capable of accelerating carbon and oxygen ions up to several tens of MeV/nucleon. Beams of ^{12}C and ^{16}O ions with incident energies of nominally 400 MeV were used in this study. Briefly, beam formation starts with an external electron cyclotron resonance (ECR) ion source, which produces the ions and accelerates them to a few tens of keV. The ions are then injected axially and further accelerated to a few MeV by means of a solid pole cyclotron, SPC2, which is one of two injector cyclotrons and the one used to pre-accelerate heavy ions at the SSC facility of iThemba LABS. The SSC provides the final acceleration to the desired energy. After extraction from the SSC, the beam is transported via about 45 m of high-energy beamline to the so-called *N*-line vault when experimental irradiations for activation studies with heavy ions are performed. This beamline ends in a small rectangular irradiation chamber, which will be described in more detail below. The final focusing of the beam onto the samples (targets) to be activated is achieved with a triplet of quadrupoles. A photograph of the final section of beamline and the irradiation chamber inside the *N*-line vault is shown in Fig. 4.1.

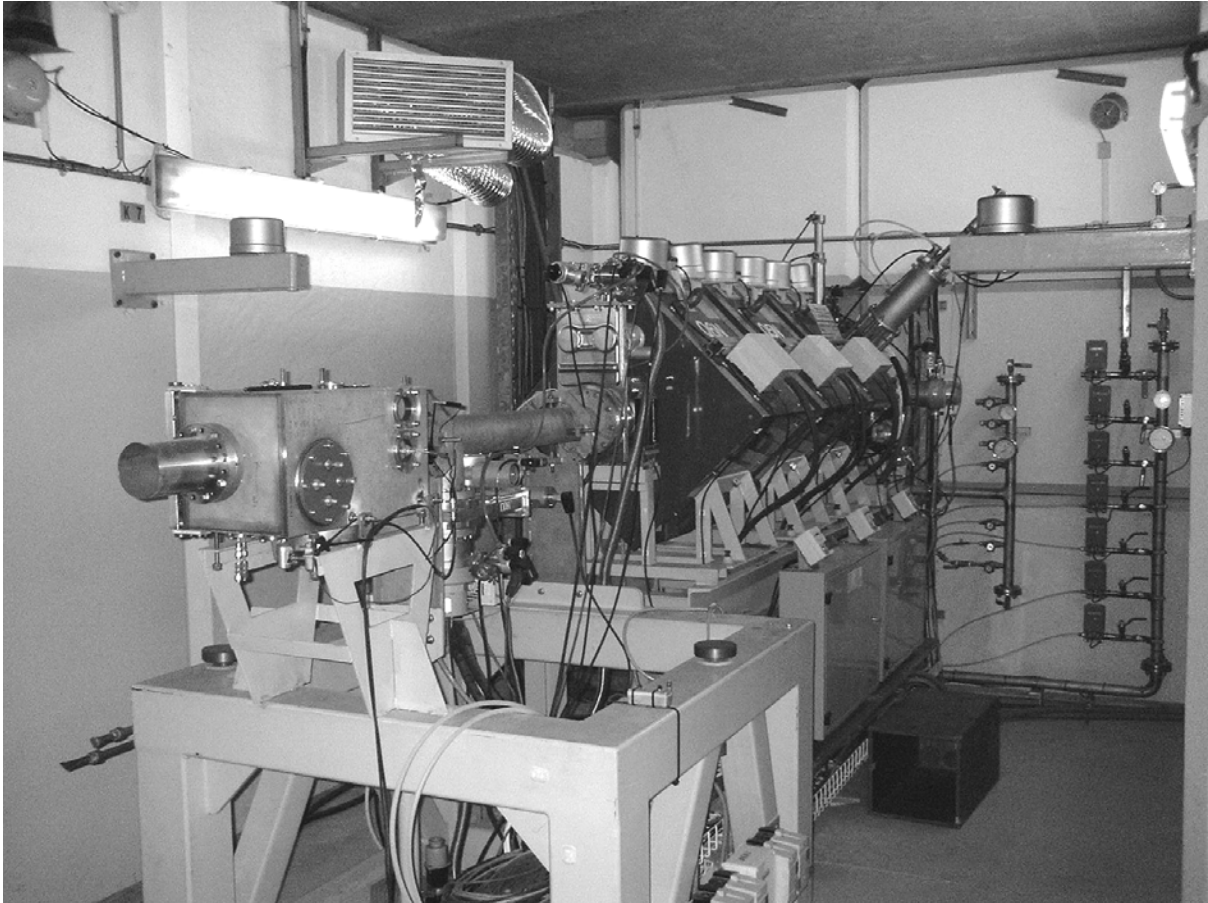


Figure 4.1 The dedicated irradiation chamber used for activation of samples, mounted at the end of beamline N at iThemba LABS. The quadrupole triplet upstream of the chamber is used for the final focusing of the beam.

4.3 The irradiation chamber

The irradiation chamber (see Fig. 4.1) has a rectangular shape and is constructed from stainless steel and aluminium [Fan94]. It can be visualized as consisting of the following main parts: (1) a vacuum-tight outer body, (2) a large door on hinges to gain entrance into the chamber, (3) an accurate mobile vice on guide rods for holding the samples/targets in the irradiation position, (4) a collimator assembly upstream of the target, and (5) a vacuum system. It is also possible to mount a water-cooled beam stop inside the chamber.

The mechanism for holding the targets in the irradiation position and the collimator assembly are mounted on the door of the chamber. A novel feature is that the door can be opened and turned through 180°, thus bringing parts which are normally inside the chamber outside. This allows for rapid and easy insertion and removal of targets. The door is also

fitted with a rotatable handle which controls the opening and closing of the jaws of the vice, allowing for samples or foil stacks of different thicknesses to be accommodated. A photograph of the door, showing the vice and collimator mechanisms, is shown in Fig. 4.2.



Figure 4.2 Another view of the irradiation chamber with the door in an open position. The collimator and vice assemblies are mounted on the door. To ensure positional accuracy, the jaws of the vice move on guide rods.

The chamber is also equipped with insulated feed-throughs for electrical connections, vacuum connections and a transparent port for viewing a beam monitor with a TV camera. A beryllium oxide (BeO) viewer can be placed in the target position, which is useful for the initial focusing when the beam is first brought into the chamber. The entire chamber is electrically insulated and is provided with electron suppression at the beam entrance. It is therefore a Faraday chamber and allows for accurate measurement of the integrated beam current. During irradiations, the beam current to the chamber and also the fraction of the

beam which gets intercepted by the collimator are monitored continuously. This will be discussed in more detail later.

The vacuum system of the chamber is completely independent because it has to be periodically isolated from the beamline to insert or remove targets. A rotary pump provides pre-vacuum ($\sim 10^{-3}$ mbar) and a turbo-molecular pump the high vacuum ($\sim 10^{-7}$ mbar).

Figure 4.3 is a simplified diagram of the irradiation chamber, showing the position of the collimator relative to the beam entrance to the chamber. Figure 4.4 shows the detail of the collimator assembly. This assembly serves two purposes: (1) to prevent electrons stripped from the beam projectiles and/or emitted from materials hit by the beam from escaping, and (2) to define the beam spot on target. This allows for accurate positioning of a well-defined beam, a useful feature for irradiating small, expensive targets. (Rhodium, the target material of the present study, is one of the rarest metals on Earth, with an abundance of only 2×10^{-4} ppm. As a result, it is also one of the most expensive, with a cost similar to that of many highly enriched elements). The design of the collimator is such that the accumulated charge of beam particles which it intercepts can be measured accurately, i.e. it has its own electron suppression. Permanent samarium-cobalt magnets are used in a geometry which makes it impossible for secondary electrons to escape from the collimator to the target and chamber or from the target to the collimator. The collimator side and target side of the assembly are separated by a section of glass-ceramic (Macor) insulator, while the permanent magnets provide strong magnetic fields which very effectively trap all secondary and delta electrons. The collimator inside the assembly is interchangeable. For this work, an aluminium collimator of 2 mm thickness with a 6 mm circular aperture was selected.

4.4 Beam focusing and monitoring

The procedure adopted for the focusing of the beam evolved as a result of previous experiments at iThemba LABS where the experimentalists managed to destroy their very expensive Rh foils. A too-sharp focus should be avoided! When beam is first brought into the irradiation chamber, the collimator is removed and a BeO viewer is placed in the irradiation position. The final sets of quadrupoles in the beamline are then adjusted until a well-defined beam spot is obtained on the viewer. The viewer is then removed and the collimator replaced. At this stage we would normally also mount a dummy target. The quadrupoles are then adjusted in a way which would *defocus* the beam, until about 50% of the beam intensity is measured on the collimator and 50% on the target. The beam spot on

EXPERIMENTAL PROCEDURES

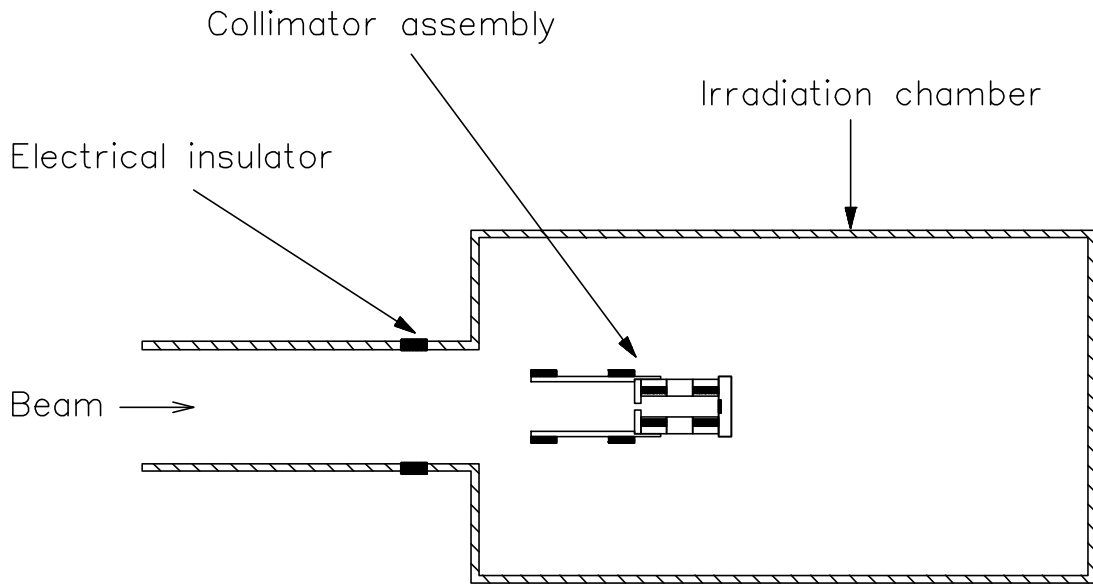


Figure 4.3 Schematic diagram showing a cross-sectional view of the irradiation chamber and the position of the collimator assembly.

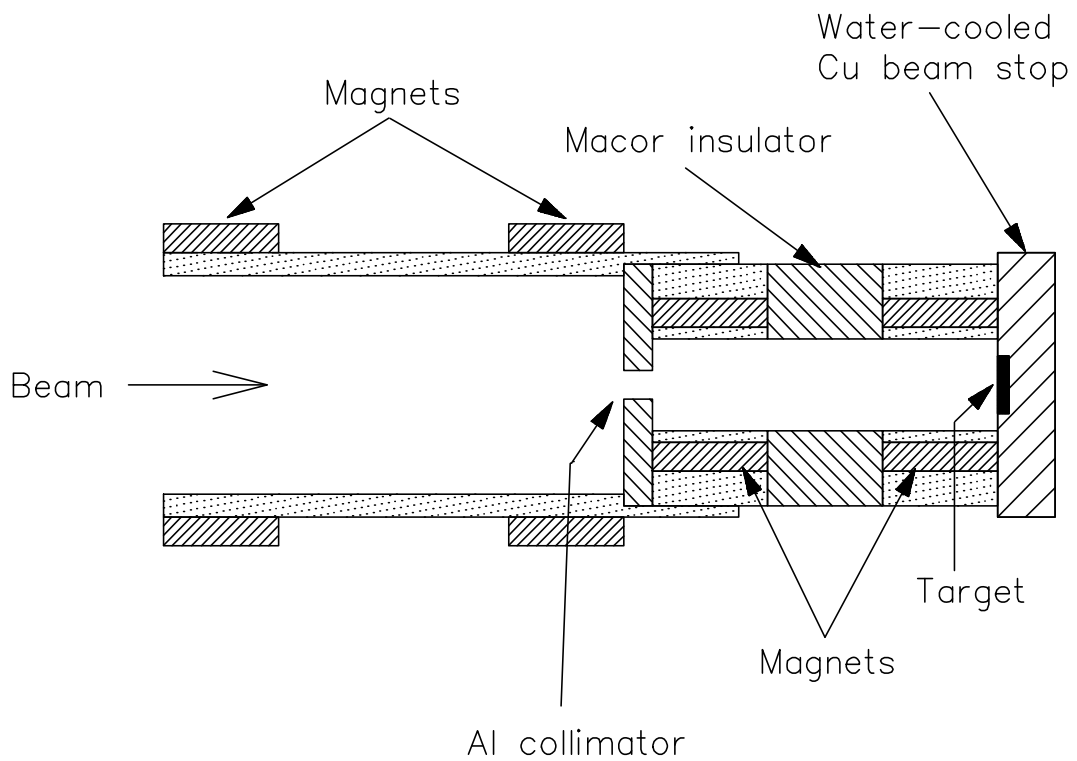


Figure 4.4 Schematic diagram showing a cross-sectional view of the collimator assembly.

target is then assured to be well-defined, with an intensity profile which was found to be more suitable for these kinds of activation studies.

The beam current intercepted by the target and beam stop was measured with a Brookhaven Instruments model 1000C current integrator. The accumulated charge was also logged in 10 second intervals by means of the data acquisition system XSYS. In this way the beam intensity fluctuations during bombardments were monitored. This was done because beam fluctuations may yield inaccuracies in the results, especially in the case of radionuclides with half-lives shorter than or of the same order of magnitude as the bombardment time, if not properly corrected for.

There was some concern that our accumulated charge measurements may be affected by the collimation as well as by the water cooling of the beam stop. A series of activation measurements were performed under different conditions of collimation, with and without cooling, to investigate this. Details of these measurements are presented in Appendix 3.

4.5 Target preparation and irradiations

Suitable target materials were used for the preparation of the target samples. Metallic Rh foils were chosen for the measurement of production cross sections for ^{103}Ru and many other residues produced in the interaction of ^{12}C and ^{16}O with ^{103}Rh . However, metallic Rh could not be employed for the measurement of cross sections for $^{103\text{m}}\text{Rh}$ and ^{103}Pd because in these cases radiochemical processing of the targets was required after bombardment. The radiochemical procedures required the targets to be brought into a solution. However, metallic Rh is extremely inert, which requires strong acidic conditions in combination with electrolysis to bring into a solution – a process which normally takes many days even for small foils such as those utilised in our experiments. During such a long processing period, most of the $^{103\text{m}}\text{Rh}$ ($T_{1/2} = 56.12$ minutes) would have decayed away. For this reason, rhodium (III) chloride salt was found to be a more suitable choice of target material for the determination of the induced $^{103\text{m}}\text{Rh}$ and ^{103}Pd activities. Whereas the anhydrous salt proved to be difficult to dissolve, probably due to partial oxidation, $\text{RhCl}_3 \cdot 3\text{H}_2\text{O}$ was found to dissolve readily in hydrochloric acid solutions.

Two metallic Rh foil stacks were prepared. Self-supporting foils of 99.99% purity were supplied by Goodfellow Ltd. (Cambridge, UK). One foil stack was prepared for bombardment with ^{12}C and the other for bombardment with ^{16}O . For the ^{12}C irradiation, the

EXPERIMENTAL PROCEDURES

stack consisted of a single 5 μm thick Ti monitor foil, followed by several Rh foils of a nominal thickness of 32.02 mg/cm^2 . The thickness of the stack was such that it stopped the beam. A similar stack was prepared for the ^{16}O irradiation except that the foils were thinner in this case, 15.29 mg/cm^2 , because of the higher stopping powers of the ^{16}O projectiles in the target stack. The foil thicknesses were chosen to give a similar set of energy intervals of the measured excitation functions with the two kinds of beam.

The ^{12}C stack was bombarded for 7 hours at an incident energy of 394.5 MeV and an average beam current of 30 nA. The ^{16}O stack was irradiated for 5 hours at an incident energy of 395.1 MeV and an average beam current of 50 nA. The beam energies were determined from a calibrated 90° analysis magnet with an uncertainty of less than 1 MeV. The stack holder was water cooled during the irradiations.

Two rhodium chloride targets were prepared for the determination of $^{103\text{m}}\text{Rh}$, one for irradiation with ^{12}C and the other for irradiation with ^{16}O . These targets were thin disks of 79.2 mg/cm^2 in thickness and 15 mm in diameter, prepared by powder compaction in a punch-and-die set (see Fig. 4.5) with a hydraulic press operated at a pressure of 20 bar. This resulted in an axial pressure inside the punch-and-die set of 2 tons/cm^2 . Two similar targets were prepared for the ^{103}Pd determinations. The $\text{RhCl}_3 \cdot 3\text{H}_2\text{O}$ salt (38 - 40% Rh content, supplied by Strem Chemicals, Newburyport, MA, USA) was first dried in a freeze-dryer for 48 hours prior to use. The freeze-drying was appropriate in this case because it dried the powder from excess H_2O without altering its chemical structure. (When exposed to the atmosphere, RhCl_3 rapidly absorbs H_2O beyond 3 units of crystal water until it completely dissolves.) Vacuum was applied to the punch-and-die tool during the hydraulic pressing and every effort was made to prevent exposure to the atmosphere.

For irradiation, each rhodium chloride target was tightly sealed inside a small recess machined onto one face of a water-cooled copper target holder, which was specially designed for this particular experiment (see Fig. 4.6). A 5 μm thick Ti foil was used as a window as well as to serve as a beam monitor for a consistency check on the current integration. The monitor reaction used was $^{\text{nat}}\text{Ti}(\text{p},\text{X})^{48}\text{V}$, details of which will be presented later. For the $^{103\text{m}}\text{Rh}$ determinations the targets were irradiated for nominally 1 hour, while 5 hour irradiations were performed for the ^{103}Pd determinations. The beams of $^{12}\text{C}^{5+}$ and $^{16}\text{O}^{6+}$ ions were kept at an average electrical current of 25 nA. Since ^{48}V has a relatively long half-life of 15.97 days, the Ti foils were stored after bombardment and counted at a convenient time after all the other work and radionuclide assays had been completed.

EXPERIMENTAL PROCEDURES

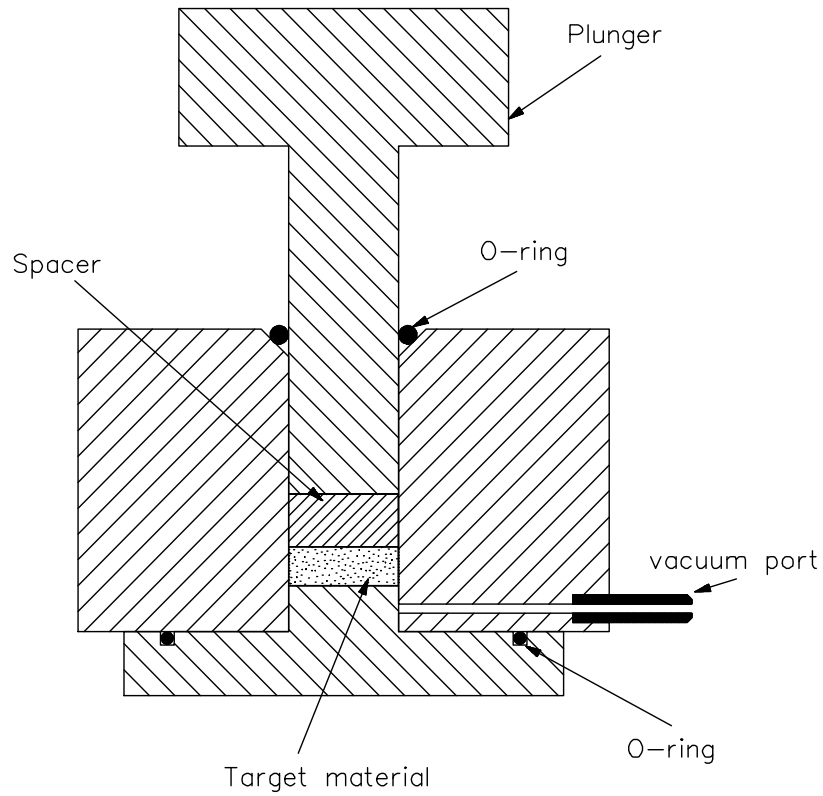


Figure 4.5 Schematic diagram of the punch-and-die set used for target manufacturing.

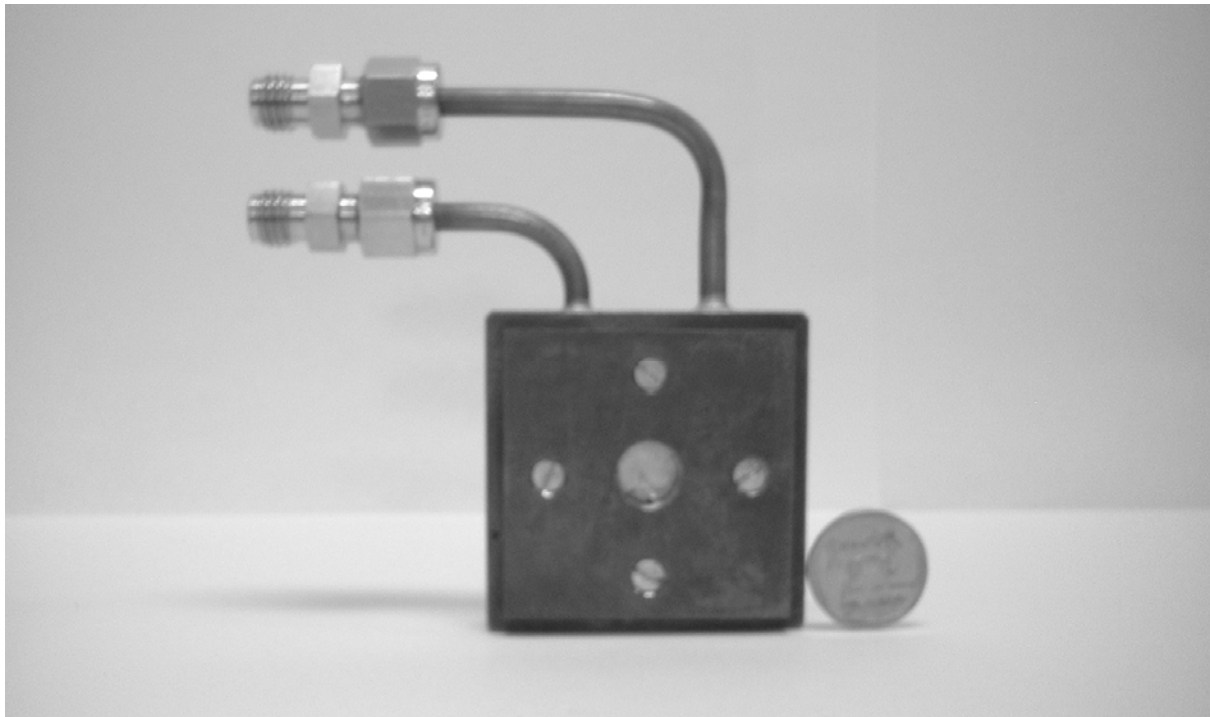


Figure 4.6 The water-cooled target holder. The Swagelok water connections are mounted at the top. A one rand South African coin is shown for scale.

4.6 Radiochemical separations

Several radiochemical techniques were investigated for their suitability to rapidly separate Pd and Ag from a Rh target matrix and to radiochemically purify the Rh so that the induced ^{103m}Rh could be measured. A part of this investigation was indeed to develop the necessary radiochemical procedures. In this section, we will only present the methods which we developed and finally adopted to generate the data of this study. Some of the scientific arguments which guided this development work will be presented in the Results and Discussion chapter. The methods, discussed below, were developed using the facilities of the Radionuclide Production Group at iThemba LABS and are based on ion-exchange chromatography, which is extensively employed in the radionuclide production industry.

The anion exchange resin AG1-X8 with 100-200 mesh particle size, supplied by Bio-Rad Laboratories (Richmond, California), was used in its chloride form. The solutions were prepared with 18 M Ω cm distilled water from a Milli-Q purification system supplied by Microsep (Pty) Ltd. (Tyger Valley, South Africa). All other reagents used were of analytical grade. Columns of 1 cm in diameter were packed with resin to a height of 5 cm and pre-conditioned with 25 ml of 6 M hydrochloric acid solution.

Each irradiated RhCl_3 target was dissolved in 25 ml hot 6 M hydrochloric acid solution, which was then allowed to cool to room temperature by placing the glass beaker in a shallow ice bath. The solution was then filtered through a 0.22 μ Millex filter to ensure that no undissolved residues remained. The volume of the solution was then measured accurately, which nominally was about 21 ml. The preparation of the mother solution in this way took about 5 minutes. A sample of 2 ml of this mother solution was removed for the preparation of “before separation” counting sources (see next section). To the remaining 19 ml of the mother solution, 1.2 ml of 30% hydrogen peroxide (H_2O_2) solution was added as an oxidising agent, the resulting solution stirred for 30 seconds and then pumped through the column with a peristaltic pump at a flow rate of 1.8 ml/min from the bottom of the column to the top. As will be discussed later, the effluent now contained the Ag and Rh, while the Pd, Ru and Tc were retained on the column. The effluent was collected in a beaker on a hot plate to evaporate HCl while the solution was still being pumped through the column. The residual Rh and Ag were eluted from the column by pumping an additional 25 ml of 6 M HCl through the column after the mother solution had passed through.

In order to obtain a solution containing only the Rh, the Ag had to be removed from the effluent. This was accomplished by precipitation of the Ag in the form of AgCl and removal

of the precipitate from the effluent by filtering. First, the effluent was brought to a ~ 1 M HCl solution by evaporating the solution in the beaker until only about 3 ml remained and then adding 20 ml of hot water. A quantity of 60 mg “cold” Ag was then introduced by adding 1 ml AgNO_3 solution dropwise to the hot solution while stirring. The hot saturated solution was then cooled to room temperature and filtered through a 0.45μ Millipore filter which removed the Ag-containing precipitate. Henceforth we will refer to this solution (the filtrate) as the Rh solution.

In order to obtain a solution containing only the Pd, the column was eluted with 50 ml of a 5% ammonia solution. The Ru and Tc remained on the column. Henceforth we will refer to this solution (the eluate) as the Pd solution. Normally, counting sources for radioactive solutions are prepared by sealing small volumes of solution in standard serum or Packard vials. However, since the photon energies of interest extended to the low-energy K x -ray region, self-absorption would have been too severe, therefore dry counting sources were prepared.

4.7 Preparation of counting sources

Counting sources were prepared from the three types of solutions obtained from the radiochemistry of the RhCl_3 target disks, i.e. the mother solution, the Rh-solution and the Pd-solution (see previous section). These sources were prepared by evaporating accurately measured quantities of solution to dryness in PVC holders under an infrared lamp. The PVC source holders (see Fig. 4.7) were specially made for this purpose and were sealed with tight-fitting polyethylene lids after the deposition of the activities.

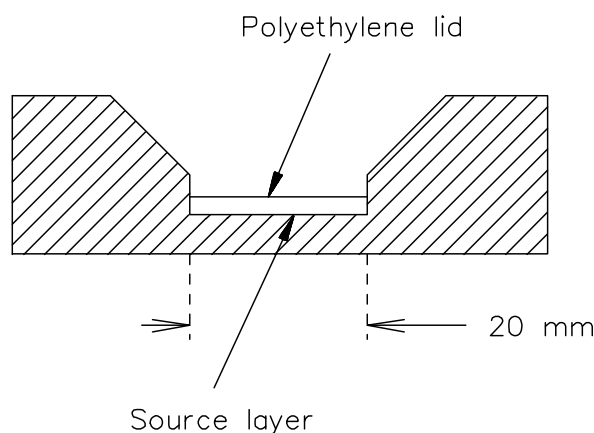


Figure 4.7 Cross-sectional view of a PVC counting-source holder.

After each of the short (1h) irradiations, four sources were prepared: two from the mother solution and two from the Rh-solution. Similarly, four sources were prepared after each of the long (5h) irradiations: two from the mother solution and two from the Pd-solution. In each case, 1 ml of the particular solution was transferred to the source holder and evaporated to dryness. In total, therefore, 16 of these sources were prepared for the experimental measurements.

As already mentioned, the relatively short half-life of $^{103\text{m}}\text{Rh}$ imposed a serious time constraint on the chemical separation procedure and the preparation of the counting sources. For this reason we abandoned the idea of producing point-like sources since the evaporation to such small surface areas would have taken too long. Instead, our sources had flat, circular surfaces of 20 mm in diameter, as shown in Fig. 4.7. An additional reason for this geometry was to keep the thickness of the RhCl_3 salt layer in the sources sufficiently thin so that self-absorption of the rather low energy x -rays remained negligible.

Suitable calibration sources with the same geometry as the experimental sources were prepared from standardised ^{133}Ba , ^{152}Eu and ^{241}Am solutions. These calibration sources were prepared, especially for this experiment, by the CSIR National Metrology Laboratory in Cape Town, South Africa, traceable to the BIPM in Sèvres, France.

4.8 Radionuclide assays

Following each irradiation of a RhCl_3 disk, the mother-solution sources were prepared and counted repeatedly while the chemical separation and preparation of the other sources continued. Two accurately calibrated HPGe detectors, coupled to a 16k channel SILENA multi-channel analyser system, were used. One detector was a standard EG&G ORTEC coaxial intrinsic Ge γ -ray detector with a crystal diameter of 53 mm and 64 mm thickness. The other was an APTEC planar Ge x -ray detector with an active area of 200 mm^2 and a thickness of 10 mm. Both detectors had horizontal configurations and source holders moving on rails to optimise the source-detector distance. The resolution was 1.7 keV FWHM at 122 keV for the γ -ray detector and 0.92 keV FWHM at 21 keV for the x -ray detector. The two detectors were properly separated and shielded from each other. The systematic dead time was kept below 3%.

The reason why two sources of each kind with identical strengths were prepared was to simultaneously collect γ -ray and x -ray spectra in order to optimise our data taking. The counting of the Rh sources started about 80 minutes after EOB and they were counted

EXPERIMENTAL PROCEDURES

repeatedly to follow the decay as a function of time. The Pd sources were counted a few days after EOB since ^{103}Pd has a relatively long half-life (16.96 days). All sources were also re-counted at later times, after the decay of the shorter-lived radionuclides, in order to more accurately assay the longer-lived radionuclides. This provided various cross-checks for the consistency of the data and also served to quantify contaminants in the final solutions obtained from the chemical separations. Although the quantities of radiocontaminants in the final solutions were generally small, they were not negligible and appropriate corrections to the data were subsequently made. Similarly, losses incurred during the chemical separations were carefully quantified and appropriate corrections were made.

Only γ -ray spectra were collected for the metallic Rh foils. Cross sections were calculated from the measured activities for all the radionuclides identified in these spectra. The foils were counted several times during four counting sessions: shortly after EOB, several hours after EOB, two weeks after EOB and again one month after EOB.

All the Ti monitor foils were also counted a few days after EOB and the ^{48}V production rates extracted. As already mentioned, there was some concern that the accumulated charge measurements could have been affected by the cooling water. Very clean de-ionised water was provided to the experimental set-up through relatively long feeding lines (5 m long polyethylene tubes of quarter-inch thickness) from the nearest water manifold, in order to reduce possible conductive losses via these lines. Fortunately, the ^{48}V production rates extracted from all the Ti monitor foils were the same for all practical purposes and no evidence of any conductive losses could be found.

CHAPTER 5

DATA ANALYSIS

5.1 Overview

The collected x -ray and γ -ray spectra were analysed by means of the EMCAPLUS version 2.01 spectrum analysis software provided by Silena, in combination with the spread-sheet program Excel. The EMCAPLUS software was used for photo-peak searches, area and statistical error calculations, background subtraction and, in a few cases, multiplet deconvolution where the photo-peaks overlapped. The data sorting program EVAL of the data acquisition system XSYS was used to extract the current integrator and time scaler values from the event files logged during the experimental bombardments. The radionuclides produced in the interactions of ^{12}C and ^{16}O ions with Rh targets were identified by means of their characteristic x and/or γ -lines which were mainly taken from the *Catalog of Gamma Rays from Radioactive Decay* by Reus and Westmeier [Reu83]. Cross checks were also performed by consulting the *Table of Radioactive Isotopes* by Browne and Firestone [Bro86]. The decay schemes used in this work were adopted from the 8th edition of the *Table of Isotopes* by Firestone *et al.* [Fir96]. In those few cases where there were disagreements between the published decay schemes, the latest decay data were adopted.

5.2 Experimental cross sections

The experimental production cross sections were obtained from the photo-peak areas extracted from the measured photon spectra by means of the following expressions:

$$\sigma(mb) = \frac{A_p T_1 K}{\tau \varepsilon_\gamma \varepsilon_e I_t N_0 \exp(-\lambda(T_m - T_1)) [1 - \exp(-\lambda T_1)] (1 \times 10^{-27})}, \quad (5.1)$$

where A_p is the photo-peak area of a particular x -ray or γ -ray line, T_1 is the duration of the bombardment, K is a correction factor for beam intensity fluctuations, τ is the live counting time, ε_γ is the branching ratio of the photon line, ε_e is the efficiency of the detector, I_t is the total number of beam particles accumulated on the target during bombardment, N_0 is the total number of target nuclei per unit area (cm^{-2}), λ is the decay constant of the particular

DATA ANALYSIS

radionuclide, and T_m is the mean value of the measuring counting interval. All times have units of seconds and the result of Eq. (5.1) is given in units of millibarn (mb). The factor K is given by

$$K = \frac{\left(\sum_{i=1}^n \Delta I_i \right) (\exp(\lambda T_1) - 1)}{\lambda T_1 \sum_{i=1}^n \Delta I_i \exp(\lambda h_i)}, \quad (5.2)$$

where n is the number of current integrator readings logged during the bombardment (scaler values were logged every 10 s), ΔI_i is the beam current integrated (or the number of beam particles on target) during the i^{th} time increment (of 10 s) duration during the bombardment, $1 \leq i \leq n$. Finally, the mean value time is given by

$$T_m = -\frac{1}{\lambda} \ln \left[\frac{\exp(-\lambda(T_3 - T_2))}{-\lambda(T_3 - T_2)} \right], \quad (5.3)$$

where $t = T_2$ denotes the start of the counting period and $t = T_3$ denotes the end of the counting period. These expressions are derived rigorously in Appendices 4 and 5.

The factor K may become important whenever the half-life of a particular radionuclide is shorter than or of the same order of magnitude as the bombardment time. This is illustrated in Figs. 5.1 and 5.2. Although one tried to keep the beam intensity constant during an experimental bombardment, this did not always happen. In Fig. 5.1 an example is shown of a bombardment during which the beam current of 25 nA remained quite constant during the entire period. Consequently, the correction factor K has a value near 1.0 even down to relatively small values of the half-life. The example shown in Fig. 5.2 is of an experimental bombardment where rather large fluctuations in the beam intensity occurred. In this case, corrections of up to 20% are required for the radionuclides with shortest half-lives.

5.3 Comparison with theoretical cross sections

Equation (5.1) is generally applicable in cases where a radionuclide is produced directly (or independently). It is also applicable in cases where a radionuclide is produced via the decay of relatively short-lived precursors (i.e. short lived compared to the half-life of the daughter

DATA ANALYSIS

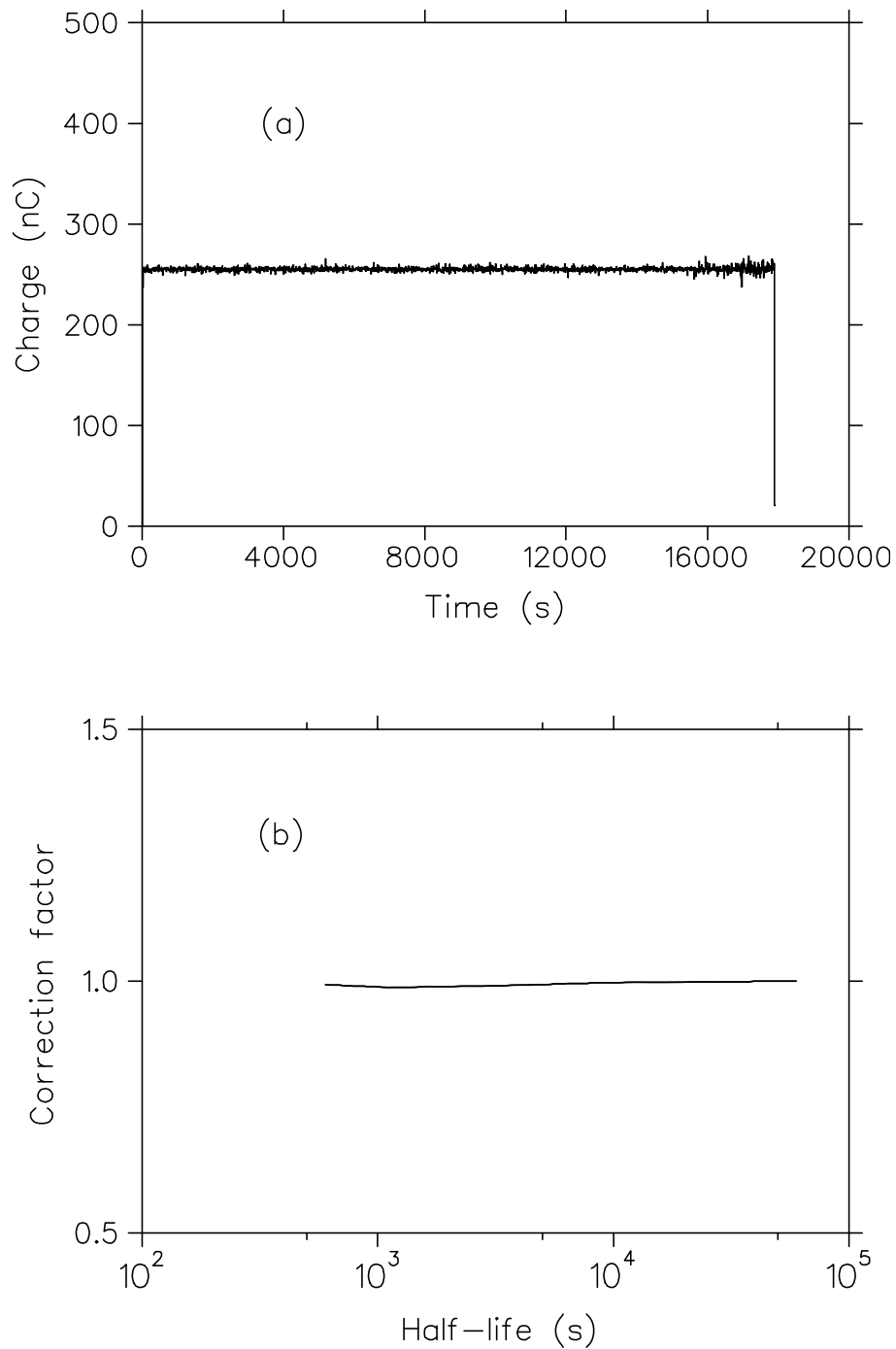


Figure 5.1 The spectrum shown in (a) is the accumulated charge versus time for an experimental bombardment during which the ^{16}O beam of 25 nA intensity remained quite constant. Note that the current integrator scaler values were logged every 10 seconds. In (b) the corresponding correction factor, K , of Eq. (5.2) is shown as a function of the half-life of radioactive decay..

DATA ANALYSIS

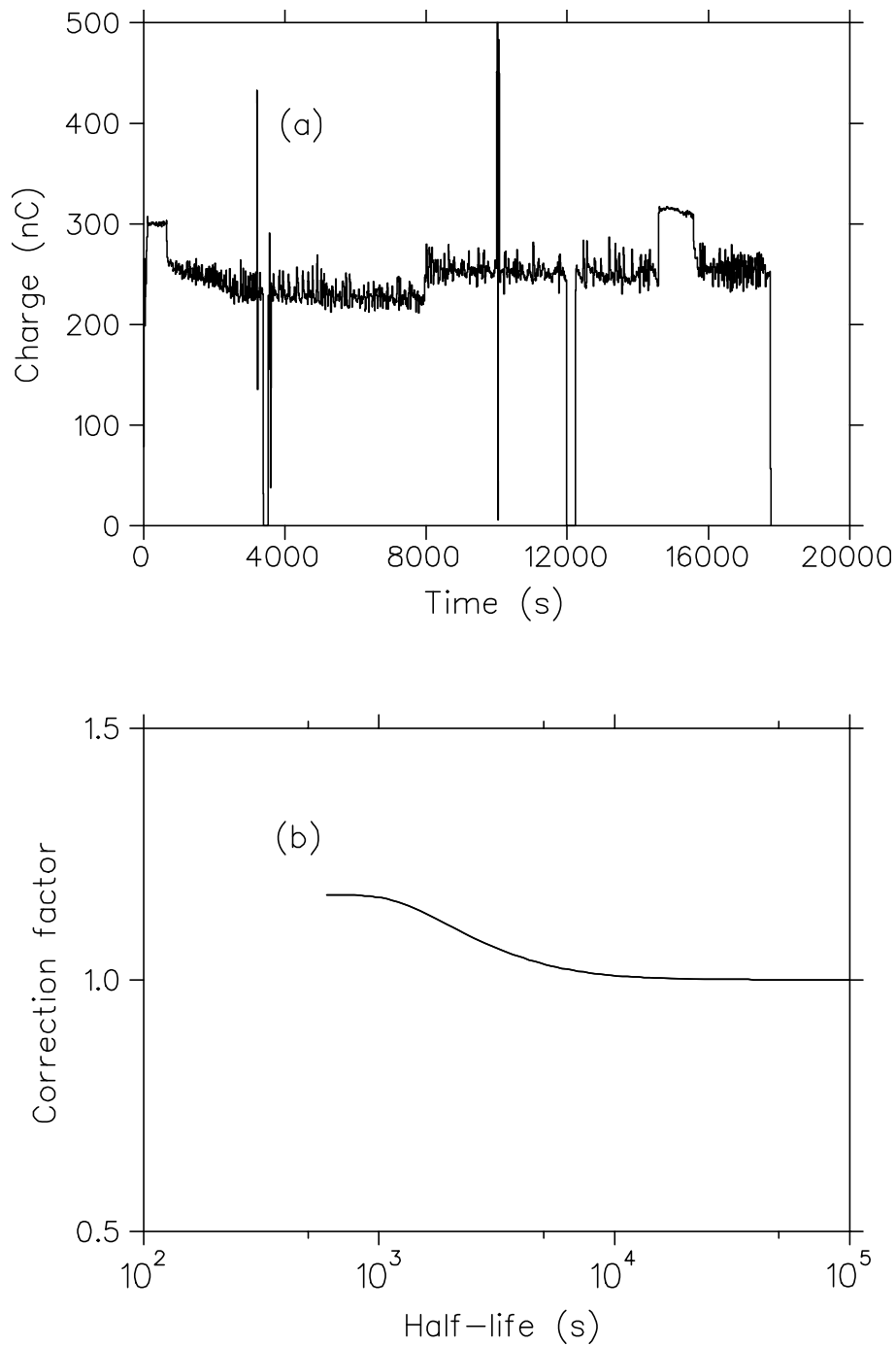


Figure 5.2 The spectrum shown in (a) is the accumulated charge versus time for an experimental bombardment during which the intensity of the ^{16}O beam fluctuated significantly. In (b) the corresponding correction factor, K , of Eq. (5.2) is shown as a function of the half-life of radioactive decay.

nuclide), on condition that the measurements are performed after the decay of the precursors. The experimental cross section is then a *cumulative* cross section. Normally, the theoretical calculations will yield the cross sections for the independent formation of a radionuclide and its precursors. In order to compare with measured cross sections, it is important to know what the relation is between the cumulative cross section and the cross sections for the direct production of these radionuclides. This is given by the following equation:

$$\sigma_c = \sigma_d + \sum_{i=1}^m \left[\prod_{j=1}^i \left(\frac{P_p^{(j)} \lambda_p^{(j)}}{\lambda_p^{(j)} - \lambda_d} \right) \sigma_p^{(j)} \right], \quad (5.4)$$

where σ_c is the cumulative cross section for the production of daughter nuclide d , σ_d is the cross section for the direct production of daughter nuclide d , m is the number of precursors contributing to the production of daughter nuclide, i and j are indices for the precursors with values ranging from 1 to m in such a way that the closest precursor to the daughter nucleus is denoted by index 1 and the one furthest away by index m . $P_p^{(j)}$ and $\lambda_p^{(j)}$ are the branching ratio and decay constant, respectively, of precursor j to the next radionuclide in the decay chain, i.e. to the nuclide with index $j-1$. The cross sections for the direct (or independent) production of the precursors are denoted by $\sigma_p^{(j)}$, where $1 \leq j \leq m$.

Equation (5.4) was used extensively to obtain the theoretical cumulative cross section values in this work. More information on the cumulative cross section and its derivation is presented in Appendix 6.

5.4 Detector calibrations

Both energy and efficiency calibrations were performed using standard sources of ^{133}Ba , ^{152}Eu and ^{241}Am . Barium-133 has a number of strong characteristic x -ray lines at 30.6 keV (34.4%), 31.0 keV (63.5%) and 35.0 keV (18.8%), which were useful for the calibration of the APTEC x -ray detector (see section 4.8). In addition, ^{133}Ba has strong γ -lines at 81.0 keV (32.8%), 302.9 keV (18.6%) and 356.0 keV (62.3%). Europium-152 has strong γ -lines over the entire energy region from 121 keV to 1408 keV. The following ^{152}Eu lines were selected: 121.8 keV (28.4%), 244.7 keV (7.51%), 344.3 keV (26.6%), 444.0 keV (3.12%), 778.9 keV (13.0%), 964.1 keV (14.6%), 1112.1 keV (13.6%), and 1408.0 keV (20.8%). The value of ^{241}Am as a calibration source is that it provides a number of strong x -ray lines at lower

DATA ANALYSIS

photon energies and specifically in the region of interest of the present work: 13.9 keV (13.2%), 17.8 keV (19.3%) and 20.8 keV (4.85%). It also has useful γ -lines at 26.3 keV (2.40%) and 59.5 keV (35.9%), rendering it an indispensable source for the calibration of the *x*-ray detector.

Efficiency calibration curves were prepared for all the relevant source-detector distances by means of smooth spline fits through the calibration points. Detector efficiency values for all other relevant photon energies were obtained by means of interpolation. Although the energy response of both the APTEC *x*-ray and EG&G ORTEC γ -ray detectors were very nearly linear, third-order polynomial fits were used for the energy calibration.

5.5 Error analysis

The uncertainty values of the experimental cross sections were estimated by summing all the contributing uncertainties in quadrature, and were typically between 15% and 20%. This includes the counting statistics, beam loss as a result of non-elastic nuclear interactions (2%), target thickness (10%), accumulated beam charge (2%), detector efficiency (5%), counting geometry (5%), photo-peak integration (2%), branching ratios (2%), and for the data obtained from the RhCl₃ disks, the elimination of contaminant contributions (5% to 12%) and radiochemical losses (5%).

5.6 Radionuclide identification

The radionuclides identified in the measured spectra included several isotopes of silver, palladium, rhodium, ruthenium, technetium, molybdenum, niobium, zirconium and yttrium. In Table 5.1 these radionuclides are listed together with their strongest photon lines and precursors. (A number of precursors were omitted if the theoretical predictions showed their contributions to be insignificant.)

Some of the shorter-lived radionuclides listed in Table 5.1 were only observed in the RhCl₃ targets and not in the metallic targets. One reason for this is that counting of the metallic foils was delayed by the first counting sessions of the sources obtained from the RhCl₃ targets. Also, in order to produce sufficient activity for the determination of ¹⁰³Ru, the bombardment times of the metallic foil-stacks were quite long. Consequently, the photo-peaks of several shorter-lived radionuclides were swamped by the Compton background of the longer-lived radionuclides.

DATA ANALYSIS

Table 5.1 Radionuclides identified in the interaction of ^{16}O and ^{12}C with ^{103}Rh .

Nuclide (half-life)	E_{photon} (keV) (Branching Ratio)	Precursors
^{104}Cd (57.7 m)	709.3 (20.4%)	$1.03(^{104}\text{In} + ^{104}\text{Sn})$
$^{105\text{g}}\text{Ag}$ (41.29 d)	344.57 (41.6%) 280.4 (31.0%)	$1.001(^{105\text{m}}\text{Ag} + ^{105}\text{Cd} + ^{105\text{m}}\text{In} + ^{105\text{g}}\text{In} + ^{105}\text{Sn})$
$^{104\text{g}}\text{Ag}$ (69.2 m)	767.6 (65.9%)	$0.0007(^{104\text{m}}\text{Ag}) + 5.5\text{E-}4(^{104}\text{Cd} + ^{104\text{g}}\text{In}) + 15.38\text{E-}4(^{104\text{m}}\text{In}) + 10.76\text{E-}4(^{104}\text{Sn})$
$^{103\text{g}}\text{Ag}$ (65.7 m)	118.7 (31.1%) 148.2 (28.4%)	$^{103\text{m}}\text{Ag} + 1.13(^{103}\text{Cd}) + 1.15(^{103}\text{In} + ^{103}\text{Sn})$
^{103}Pd (16.96 d)	20.1 (63.8%) 22.8 (13.2%)	$1.007(^{103\text{g}}\text{Ag} + ^{103\text{m}}\text{Ag} + ^{103}\text{Cd} + ^{103}\text{In})$
^{101}Pd (8.47 h)	296.3 (19.2%) 590.4 (12.1%)	$1.022(^{101\text{m}}\text{Ag} + ^{101\text{g}}\text{Ag}) + 1.925(^{101}\text{Cd})$
^{100}Pd (3.63 d)	126.1 (11.0%)	$^{100\text{m}}\text{Ag} + ^{100\text{g}}\text{Ag} + ^{100}\text{Cd} + 1.001(^{100}\text{In} + ^{100}\text{Sn})$
^{99}Pd (21.4 m)	136.0 (72.7%)	$1.12(^{99}\text{Ag} + ^{99}\text{Cd})$
$^{103\text{m}}\text{Rh}$ (56.12 m)	20.1 (6.37%) 22.8 (1.32%)	No precursor
$^{102\text{m}}\text{Rh}$ (2.92 y)	475.1 (94.0%) 631.3 (55.5%) 697.5 (43.2%)	No precursor
$^{102\text{g}}\text{Rh}$ (207 d)	475.1 (44.0%) 628.0 (4.31%) 468.6 (2.77%) 1103.2 (2.77%)	$0.0023(^{102\text{m}}\text{Rh})$
$^{101\text{m}}\text{Rh}$ (4.34 d)	306.9 (86.3%)	$1.085(^{101}\text{Pd}) + 1.087(^{101\text{m}}\text{Ag} + ^{101\text{g}}\text{Ag} + ^{101}\text{Cd})$
$^{100\text{m}+\text{g}}\text{Rh}$ (20.8 h)	539.6 (78.4%) 822.5 (20.1%)	$0.983(^{100\text{m}}\text{Rh})$
$^{99\text{m}}\text{Rh}$ (4.5 h)	340.8 (69.1%) 617.8 (11.8%)	$1.045(^{99}\text{Pd}) + 1.053(^{99\text{m}}\text{Ag} + ^{99\text{g}}\text{Ag} + ^{99}\text{Cd} + ^{99}\text{In} + ^{99}\text{Sn})$
$^{99\text{g}}\text{Rh}$ (16.0 d)	527.7 (40.7%) 353.0 (31.9%)	$0.0016(^{99\text{m}}\text{Rh}) + 0.0366(^{99}\text{Pd} + ^{99\text{m}}\text{Ag} + ^{99\text{g}}\text{Ag} + ^{99}\text{Cd} + ^{99}\text{In} + ^{99}\text{Sn})$
$^{97\text{g}}\text{Rh}$ (31.1 m)	421.5 (75.0%)	$0.54(^{97\text{m}}\text{Rh}) + 1.09(^{97}\text{Pd}) + 1.11(^{97}\text{Ag} + ^{97}\text{Cd})$

DATA ANALYSIS

^{103}Ru (39.25 d)	497.1 (89.5%)	$^{103}\text{Tc} + ^{103}\text{Mo}$
^{97}Ru (2.88 d)	215.7 (85.8%) 324.5 (10.2%)	$1.007(^{97g}\text{Rh}) + 1.012(^{97m}\text{Rh}) + 1.008(^{97}\text{Pd} + ^{97}\text{Ag} + ^{97}\text{Cd})$
^{95}Ru (1.65 h)	336.4 (70.8%)	$1.05(^{95g}\text{Rh}) + 1.07(^{95m}\text{Rh}) + 0.96(^{95}\text{Pd})$
^{96g}Tc (4.28 d)	778.2 (99.7%) 849.9 (97.8%) 812.5 (82.2%)	$0.988(^{96m}\text{Tc})$
^{95m}Tc (61.0 d)	204.1 (66.5%) 582.1 (31.5%) 835.1 (28.0%)	$0.029(^{95}\text{Ru}) + 0.031(^{95g}\text{Rh}) + 0.0281(^{95}\text{Pd}) + 0.031(^{95}\text{Ag})$
^{95g}Tc (20.8 h)	765.8 (93.9%) 1073.3 (3.75%)	$1.061(^{95}\text{Ru}) + 1.067(^{95g}\text{Rh}) + 1.0066(^{95m}\text{Rh})$
^{94g}Tc (4.88 h)	871.0 (100%) 702.7 (99.8%)	No precursor
^{93g}Tc (2.75 h)	1363.0 (65.8%)	$1.04(^{93m}\text{Tc} + ^{93m}\text{Ru}) + ^{93g}\text{Ru} + ^{93g}\text{Rh})$
^{93m}Mo (6.85 h)	684.7 (99.7%) 263.1 (56.7%)	No precursor
^{90}Mo (5.67 h)	257.3 (77.6%)	$^{90g}\text{Tc} + 1.002(^{90m}\text{Tc})$
^{90g}Nb (14.6 h)	1129.1 (92.0%)	$^{90m}\text{Nb} + 1.635(^{90}\text{Mo}) + 1.636(^{90m}\text{Tc}) + 1.637(^{90g}\text{Tc})$
^{88}Zr (83.4 d)	392.9 (97.3%)	$1.0001(^{88g}\text{Nb} + ^{88m}\text{Nb} + ^{88}\text{Mo})$
^{86}Zr (16.5 h)	242.8 (95.8%)	$1.0015(^{86}\text{Nb} + ^{86}\text{Mo})$
^{87m}Y (12.9 h)	381.1 (78.1%)	$1.143(^{87g}\text{Zr} + ^{87m}\text{Zr}) + 1.146(^{87}\text{Nb})$
^{87g}Y (3.35 d)	484.9 (92.2%)	$1.182(^{87m}\text{Y}) + 1.143(^{87g}\text{Zr})$
^{86g}Y (14.74 h)	1076.6 (82.5%) 627.7 (32.6%)	$1.05(^{86m}\text{Y})$
^{85m}Y (4.86 h)	231.7 (23.4%)	$0.918(^{85m}\text{Zr}) + 0.997(^{85g}\text{Zr}) + 0.998(^{85}\text{Nb})$

Continuation of Table 5.1

DATA ANALYSIS

Some expected radionuclides of antimony, tin, indium and cadmium were not identified in this work. Many short-lived radionuclides such as $^{99-104,105m}\text{Ag}$, $^{97-99}\text{Pd}$, $^{95-98}\text{Rh}$, $^{92-94}\text{Ru}$, $^{91,92,93m,94m}\text{Tc}$, $^{88,89,91}\text{Mo}$, $^{86-90m}$, ^{94m}Nb , $^{85,87,89m}\text{Zr}$ and ^{86m}Y were not observed in this work because they had already decayed significantly by the time the measurements were performed. Very long-lived radionuclides such as ^{101g}Rh (3.2 y), ^{97m}Tc (89 d), ^{97g}Tc (2.6×10^6 y), ^{99g}Tc (2.1×10^5 y), ^{93g}Mo (3.5×10^3 y), ^{91g}Nb (680 y), ^{92g}Nb (3.6×10^7 y) and ^{88}Y (106.6 d) were also not observed in this work due to their too low induced activities.

The only neutron-rich radionuclide that was positively identified was ^{103}Ru . It is a relatively long-lived radionuclide with a half-life of 39.25 days. Its precursors are ^{103}Tc (54.2 s), ^{103}Mo (67.5 s) and ^{103}Nb (1.5 s). Ruthenium-103 decays to ^{103m}Rh by emission of 99.75% β^- . The characteristic γ -lines of ^{103}Ru are the 497.1 keV (89.5%) and 610.3 keV (5.64%). In order to get good counting statistics, it was necessary to wait until the Compton background dropped to a sufficiently low level. This was achieved 35 days after EOB. Counts rates of 4000 - 8000 per 24 hours of counting were then obtained for the 497.1 keV photo-peak.

Both ^{102m}Rh and ^{102g}Rh have relatively long half-lives. Rhodium-102m has a half-life of 2.9 years and ^{102g}Rh 207 days. The literature differs widely in the assignment of these two isomers, therefore the assignment according to Firestone *et al.* [Fir96]) was adopted. Rhodium-102m has no precursors, while only 0.23% of ^{102m}Rh decays to ^{102g}Rh . Both these radionuclides can therefore be considered as directly produced for all practical purposes.

The metastable isomer ^{100m}Rh which has a half-life of 4.7 minutes, has no precursors, however it decays to ^{100g}Rh (20.8 h) by 98.3% IT. The other precursor of ^{100g}Rh is ^{100}Pd , which has a half-life of 3.63 days. Since in this case the half-life of the precursor is much longer than that of the daughter, its contribution could be subtracted. Hence the measured ^{100g}Rh is denoted as $^{100m+g}\text{Rh}$ in order to show that it only includes the contribution via the decay of its one independently produced precursor ^{100m}Rh .

The ground state of ^{95}Tc has a half-life of 20.0 hours. It has two precursors, namely, ^{95}Ru (1.65 h) and ^{95m}Tc (61 d). Similarly, since the half-life of the precursor ^{95m}Tc is much longer than that of the daughter ^{95g}Tc , at time of measurement the contribution of this precursor was negligible. This means that the measured ^{95g}Tc only includes the contribution of the other precursor, i.e. ^{95}Ru (97.1%). Ru-95 itself decays to ^{95m}Tc by 2.9% β^+ emission.

In certain cases there were interferences, e.g. in the case of ^{99m}Tc (6.01 h). The characteristic γ -lines of ^{99m}Tc are 140.5 keV (87.7%) and 142.6 keV (0.041%). These lines interfere with the 141.2 keV (69.0%) γ -line of ^{90g}Nb (14.60 h). Since the differences between

DATA ANALYSIS

these lines are less than 3 keV, it was impossible to distinguish whether the measured line belonged to ^{99m}Tc , especially since ^{99m}Tc has no other γ -lines. Fortunately, the other strong line of ^{90g}Nb , 1129.1 keV (92.0%), was clearly identified.

The identification of ^{97}Rh was not simple due to the fact that both isomers have short half-lives that are very close to each other. The half-life of ^{97m}Rh is 44.3 minutes and that of ^{97g}Rh is 31.1 minutes. Both isomers are produced via the decay of ^{97}Pd (3.1 m). Palladium-97 decays to ^{97g}Rh by 98% positron (β^+) emission and to ^{97m}Rh by 2% EC. Also, ^{97m}Rh decays to ^{97g}Rh by 5.6% IT. Both ^{97m}Rh and ^{97g}Rh have their strongest γ -line at 421.5 keV, with branching ratios of 75 % and 13.3%, respectively. Some other lines of ^{97m}Rh such as 188.6 keV (51.2%), 1013.4 keV (5.59%) and 771.1 keV (4.82%) were not present in the spectra, while 839.4 keV (12.4%) and 878.8 keV (9.30%) of ^{97g}Rh were present. Hence, the observed isomer was ^{97g}Rh .

Similarly, the observed isotope of ^{93}Tc was ^{93g}Tc (2.75 h) because the characteristic γ -line of ^{93m}Tc (43.5 m) at 391.8 keV (58.2%) was not present in the spectra, while the characteristic lines of ^{93g}Tc were present.

Silver-104 has two isomers. Silver-104m has a half-life of 33.5 minutes and ^{104g}Ag has a half-life of 69.2 minutes. According to the latest edition of Firestone *et al* [Fir96], ^{104m}Ag has no precursor while ^{104g}Ag is produced via the 100% EC of ^{104}Cd (57.7 m) and via less than 0.07% IT of ^{104m}Ag . The reason why ^{104g}Ag was identified while ^{104m}Ag was not is that although the two isomers share their strongest γ -line, 555.8 keV (which has respective branching ratios of 92.8 and 60.0%) however, all the other lines of ^{104m}Ag (1238.8 keV, 785.7 keV) were not present in the spectra whereas the 767.6 keV, 941.6 keV, 925.9 keV and 857.9 keV γ -lines of ^{104g}Ag were observed.

Silver-103g is a parent nuclide of the relatively long-lived ^{103}Pd (16.96 d). It decays by 100% EC. In turn, ^{103}Pd decays to ^{103m}Rh (56.12 m) by 100% EC. Ag-103g was identified in the γ -ray spectra while ^{103}Pd and ^{103m}Rh could not be because they do not have γ -rays with branching ratios larger than 1%. The only feasible way to identify them was by means of their 20.1 keV x -rays, which has branching ratios of 63.8% and 6.37%, respectively. The other x -rays of ^{103}Pd and ^{103m}Rh are the 22.8 keV line, which has respective branching ratios of 13.2% and 1.32%. Unfortunately, there are other radioisotopes produced in the interaction of ^{12}C and ^{16}O with Rh such as the isotopes of Ag, Ru, Tc, etc. which have x -rays that are very close to the 20.1 keV and 22.8 keV lines. The presence of those other x -rays caused so much interference that before the chemical separation of Rh and Pd, the photo-peaks for the

expected 20.1 keV and 22.8 keV lines could not be resolved (see Fig. 5.3). However, after the separation of Rh and Pd from the target, the 20.1 and 22.8 keV photopeaks were clearly resolved but still contained some residual contamination from Ag and Tc (and also Ru in the case of the ^{12}C irradiation), although in low levels (see Figure 5.3). Appropriate corrections for the contaminants were subsequently made.

5.7 Other aspects

The use of the Excel spreadsheet program proved to be very useful for the book-keeping of all the relevant times since EOB, counting times, etc. At the same time it provided the computational tools to perform all the calculations required for the extraction of the experimental cross sections.

It was important to do accurate volumetric determinations during the chemical separation procedures and the preparation of the counting sources. Proper book-keeping of the volumes of all solutions during each step of the chemistry was an essential part of the task. For each counting source, the exact fraction of the mother solution used in its preparation was determined from these data. Obviously, the radionuclidic yields measured in the sources were then appropriately scaled with the inverse values of these fractions in order to obtain the corresponding yields produced in the original RhCl_3 target disks.

Although the quantities of radiocontaminants in the final Rh and Pd solutions were generally small, they were not negligible. Also, radionuclides of the same species all contributed to the x -ray lines of interest used for the determination of $^{103\text{m}}\text{Rh}$ and ^{103}Pd . These contaminant contributions could be quantified (and subtracted) by calculating the expected contributions to the relevant x -ray photo-peaks based on the measured photo-peak areas of the respective γ -lines listed in Table 5.1. Obviously, contributions from many potential contaminant radionuclides were found to be negligible when their half-lives were either relatively small or much larger than the respective half-lives of $^{103\text{m}}\text{Rh}$ or ^{103}Pd . The relation between the x -ray peak-area contribution from a contaminant as determined from one of its γ -lines is given by

$$A_x = A_\gamma \times \left(\frac{P_x}{P_\gamma} \right) \left(\frac{\varepsilon_x}{\varepsilon_\gamma} \right), \quad (5.5)$$

where A_γ is the photo-peak area of the contaminant during the same counting period, P_x/P_γ the branching ratios and $\varepsilon_x/\varepsilon_\gamma$ the detector efficiencies of the x -ray / γ -ray, respectively.

DATA ANALYSIS

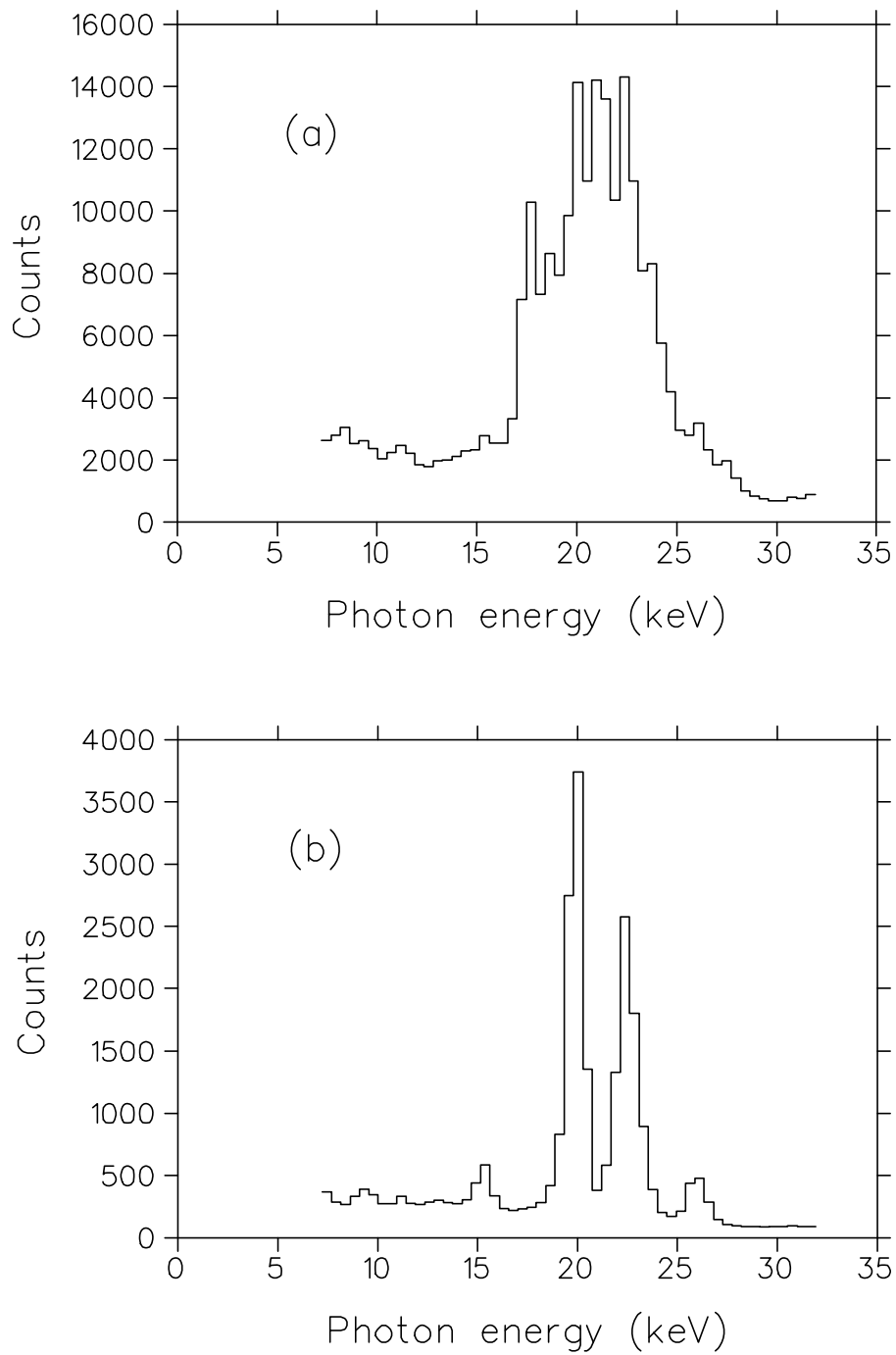


Figure 5.3 A typical x-ray spectrum of a source prepared from the mother solution, i.e. before any radiochemistry, is shown in (a). The corresponding spectrum from the Rh solution, i.e. after the radiochemical separation, is shown in (b). The need for chemical separation is evident.

CHAPTER 6

RESULTS AND DISCUSSION

6.1 Overview

The results of this study are presented in four sections. In section 6.2 some aspects of the radiochemistry investigation are discussed in more detail. In particular, a number of test irradiations with 66 MeV proton beams were performed to test the chemical separations and the procedure for making the counting sources. This was done because 66 MeV protons are conveniently available on a regular weekly basis at iThemba LABS for routine radionuclide production and neutron therapy. The reader who is not so much interested in the chemistry may prefer to proceed directly to section 6.3 where the isobaric yield results are discussed, with particular emphasis on the heavy residues produced in the near-target mass region. In section 6.4 the available excitation function and recoil range distribution data of heavy residues produced in the interaction of ^{12}C and ^{16}O with ^{103}Rh are compared with the new theoretical calculations. For several residues, the new data augment the existing data set, although this was not a main goal of this study. Finally, the calculated mean excitation energy distributions of all contributing reaction mechanisms are presented in section 6.5. Some of these results have already been published or accepted for publication [But03a, But03b, But03c].

6.2 Radiochemical separations

The radiochemical procedure described in Chapter 4 was developed with the aim to achieve a quantitative separation of Rh and Pd from all other nuclides and from each other. In practice, however, some traces of Ag, Ru and Tc contaminants were present in the final solutions. These can be explained by their chemical behaviour in anion chromatographic conditions. Obviously, in order to apply appropriate corrections, the contaminant levels had to be quantified accurately. One of the strengths of off-line γ -ray spectroscopy is that it provides the means to identify and quantify radiocontaminants down to very low levels.

Technetium(VII), which is normally present as pertechnetate ions (i.e. TcO_4^-) is very strongly retained by strong base anion exchange resins, e.g. Dowex 1, from 0 to 12 M hydrochloric acid solutions [Kor89]. The distribution coefficient of Tc decreases from a

RESULTS AND DISCUSSION

value of $> 10^3$ at low acidities (~ 0.1 to 2 M) to *ca.* 10^3 in the range of *ca.* 3 to 12 M acid. In 6 M HCl the distribution coefficients of Ru(IV), Pd(II), Rh(III) and Ag(I) are $\sim 10^2$, $\sim 10^2$, ~ 1 and ~ 2 , respectively. Therefore, as a first step in the chemical separation procedure, a strong base anion exchange resin is ideal to separate Tc, Pd and Ru from the Rh and Ag.

In the first test experiments with 66 MeV proton beams, it was observed that Ru was eluted quantitatively with HCl and collected in the effluent, while the Pd was retained on the column. Since Ru(IV) and Pd have the same distribution coefficient in 6 M HCl, this result showed that only Ru(III) and not Ru(IV) was formed on dissolution of the target. With further study of the chemistry of Ru, it was found that the aqueous solution chemistry of Ru is very complicated and that the species are usually complex and often polynuclear. It shows all oxidation states from (0) to (VIII) and also (-II). Ru(III) is the most stable state [Bur81]. Therefore Ru has to be oxidized to obtain higher oxidation states, especially to (IV). Strong oxidants, such as cerium(IV) in acidic solutions, form ruthenium tetraoxide (RuO_4) but this in turn, in excess hydrochloric acid finally gives a solution of Ru(III) chloro-aquo complexes, such as $\text{Ru}(\text{H}_2\text{O})_3\text{Cl}_3$. The reduction sequence is



If the concentration of the acid is decreased, the reduction proceeds either to Ru(IV) or Ru(VI). When Ce(IV) sulphate was used as an oxidant, however, only about 48.5% of the Ru was retained by the resin. The incomplete oxidation of Ru was probably because most of the Ce(IV) was spent on oxidation of Cl^- to Cl_2 , probably forming a cerium ruthenium complex. It was therefore decided to rather use hydrogen peroxide (H_2O_2) as oxidant. Ru(III), in the presence of H_2O_2 , is usually oxidized to Ru(IV) oxide (RuO_2) as a black precipitate but, in this case, because of a very low concentration of radioactive Ru(III) the RuO_2 was probably dissolved as an oxoanion complex. Ruthenium(IV) is normally present as anionic complexes, many of which are polynuclear. These chloro complexes are readily reduced to Ru(III) species in HCl solutions, as shown in the reaction above.

The results obtained from using H_2O_2 as oxidant showed that Ru, together with Pd and Tc, was quantitatively retained by the resin. To keep Ru in oxidation state (IV) no attempt was made to remove the excess H_2O_2 and, although there were bubbles in the solution during the pumping, it did not cause any problems to the separation process. Typically, more than 99.8% of Rh was recovered in the effluent after subsequent elution with clean 6 M hydrochloric acid.

RESULTS AND DISCUSSION

In the test irradiations with 66 MeV protons no Ag nuclides were produced. However, it was expected that in the ^{12}C and ^{16}O experimental irradiations, contributions of especially ^{103}Ag , ^{104}Ag and ^{105}Ag in the x -ray region of interest would be problematic for accurate measurement of $^{103\text{m}}\text{Rh}$. It was also known that because of the small distribution coefficients of Ag in HCl media on strongly basic anion exchange resins, Ag would not be sorbed on the column. Initially, the modus operandi was to remove the Ag by means of precipitation and filtering from the mother solution and not from the effluent, as was the method adopted later.

In the first experimental irradiation, i.e. $^{16}\text{O} + \text{RhCl}_3 \cdot x\text{H}_2\text{O}$, the separation of Ag from the rest of the nuclides was done by precipitation as AgCl in the 6 M HCl mother solution prior to the ion exchange chromatography. The results from that experiment indicated that only about 74% of the silver was removed from the original solution. Fortunately, corrections for the remaining Ag contaminants in the final solutions could be done in this case. There was, therefore, a strong indication that anionic chloro complexes of produced Ag nuclides (like Ag Cl_2^- , Ag Cl_3^{2-} and Ag Cl_4^{3-}) [Kor89] were not completely dissociated, leading to an incomplete exchange with the added natural silver. Furthermore, when a 1 ml sample of the filtrate was diluted with water to 5 ml for measurement, a colloidal solution was formed, indicating that the solubility of Ag in 6 M HCl is more than that of Ag in 1 M HCl. Considering all the facts mentioned above, it was decided to do the precipitation of Ag in the effluent, rather than the mother solution, in a ~ 1 M HCl solution as described before. This proved to be very successful as only the Rh remained, i.e. no significant activities of Ag radionuclides were detected in the effluent. Subsequently, in all the further experimental work the removal of Ag was done after the ion exchange chromatography was completed.

The radiochemistry was initially planned for the separation of Pd and Rh nuclides from the Ag, Tc and Ru nuclides but, with the reactions of ^{12}C and ^{16}O with ^{103}Rh , nuclides of Mo, Nb, Zr and Y were also produced, although in very low quantities. The results of measurements revealed that the latter four elements were also retained by the resin in 6 M HCl and, on elution of Pd, they still remained on the resin. On elution of the resin with 5% ammonia an average recovery of 91.5% was obtained for Pd (based on the measurements of ^{100}Pd activities). The average amounts of Ru (based on ^{97}Ru measurements) and Tc (based on ^{96}Tc measurements) which co-eluted with Pd were 4.5% and 4.9%, respectively. Many of these contaminant activities were from short-lived radionuclides which decayed away before the measurements of the ^{103}Pd activities were done, and appropriate corrections to the extracted photo-peak areas were made for the contributions from the longer-lived contaminants. Generally, these corrections were small, of the order of only a few percent.

RESULTS AND DISCUSSION

One of the concerns that we had was whether the Rh content of the salt targets was known to the desired accuracy. We used salt labeled as $\text{RhCl}_3 \cdot x\text{H}_2\text{O}$, with x believed to have a value of 3 if care was taken with the handling of the material, which is extremely hygroscopic. Unfortunately, anhydrous RhCl_3 proved to be extremely inert, almost as difficult as the pure metal to dissolve. This made it rather unsuitable as target material because of the requirement for a rapid radiochemical separation procedure. In contrast, hydrous $\text{RhCl}_3 \cdot x\text{H}_2\text{O}$ targets [Lag84] dissolves readily.

One of the reasons why we also irradiated metallic Rh foils was indeed to provide a comparison with the salt targets as a consistency check. For this purpose we selected a few radionuclides, some of which are produced independently and some which are cumulative in nature, for a direct comparison between the two target materials. The extracted production cross sections, averaged over the effective energy windows of the salt targets, are shown in Table 6.1. We do observe some scatter in the data but generally the agreement is satisfactory.

Table 6.1 Comparison of extracted production cross sections for selected radionuclides obtained in the bombardment of metallic Rh foils and $\text{RhCl}_3 \cdot x\text{H}_2\text{O}$ disks.

Isotope	$T_{1/2}$ (hours)	E (keV)	Intensity (%)	Cross-section (mb)	
				metallic Rh	RhCl_3 salt
^{100}Pd	87.12	126.1	11.0	51.99 ± 7.79	50.52 ± 10.0
$^{101\text{m}}\text{Rh}$	104.16	306.9	86.3	222.7 ± 33.4	222.5 ± 44.3
^{97}Ru	69.12	215.6	85.8	162.2 ± 24.3	159.9 ± 31.8
$^{96\text{g}}\text{Tc}$	102.72	778	99.7	46.47 ± 7.65	44.78 ± 8.91
$^{94\text{g}}\text{Tc}$	4.9	702.7	99.8	72.36 ± 10.8	60.03 ± 11.9
$^{93\text{m}}\text{Mo}$	6.9	684.9	99.7	37.00 ± 5.55	34.81 ± 6.91
$^{85\text{m}}\text{Y}$	4.86	231.7	23.4	7.594 ± 1.14	5.740 ± 1.14

6.3 Cross sections and isobaric yields

The measured cross sections for the production of various residues in the interaction of ^{12}C and ^{16}O with ^{103}Rh are presented in Tables 6.2 and 6.3, respectively. These values represent *average* cross sections for the energy windows corresponding to the thicknesses of the rhodium chloride targets used. The majority of these residues were produced cumulatively,

RESULTS AND DISCUSSION

i.e. both directly and via the decay of their precursors, but a few were produced independently as indicated. The cross-section values were derived using the listed half-lives, photon energies and branching ratios, taken from Reus and Westmeier [Reu83] unless otherwise indicated. In many cases cross checks were performed using other γ -lines as well. It should be noted that these values were extracted from rather thick targets. For the ^{12}C beam the energy loss in a RbCl_3 disk was nominally 39 MeV and for the ^{16}O beam nominally 92 MeV. The values listed are *best values*, therefore often derived from the spectra obtained from the metallic stack irradiations. In this case the cross sections were averaged over the above-mentioned energy windows from the corresponding portions of the excitation functions extracted from the metallic stacks. For purposes of comparison with theoretical predictions, a nominal energy of 380 MeV was adopted for the carbon-induced reactions and 350 MeV for the oxygen-induced reactions.

The choice of the RhCl_3 target thickness was a compromise between conflicting requirements. On the one hand, the time constraints allowed for only small volumes to be evaporated to dryness in the preparation of the counting sources. On the other hand, sufficiently strong sources were needed for the radionuclide assays, therefore a relatively large quantity of target material had to be activated (with a rather low beam intensity to avoid damage to the targets) to provide enough activity. The choice of the beam energy of ~ 400 MeV has an important advantage in that it is significantly above the thresholds of most of the contributing reaction mechanisms. In fact, the shapes of the excitation functions of the majority of the observed residues are quite flat and structureless in the energy region 300-400 MeV (see e.g. [Gad97b]), therefore large differences between the average cross sections listed in the tables and the values evaluated at the nominal energies of 380 MeV (for ^{12}C) and 350 MeV (for ^{16}O) are not anticipated.

Figure 6.1 shows for both $^{12}\text{C} + ^{103}\text{Rh}$ (a) and $^{16}\text{O} + ^{103}\text{Rh}$ (b) the comparison between the measured cross sections of this study (solid symbols) and the corresponding theoretical predictions (dotted histogram) for those residues that have the largest cross sections at a particular mass. The open symbols are measured values from previous excitation function experiments by some of the collaborators of the present study and which have only been published or presented in part [Gad97b, Ste03] and which will be published in full in the near future. In a few cases where both the ground state and a metastable state have been measured for the same nuclide and the metastable state does not significantly feed the ground state, the sum of the two contributions were taken. For both reactions the agreement between the measurements and calculations is reasonable except for a possible underprediction below $A =$

RESULTS AND DISCUSSION

Table 6.2 Measured cross sections for the production of residues in the reaction $^{12}\text{C} + ^{103}\text{Rh}$.

Residue	Type ^{a)}	Half-life	E (keV)	Intensity (%)	Experimental cross-section (mb)
^{105}gAg	C	41.29 d	344.5	41.6	8.81 ± 1.38
^{104}gAg	C	69.2 m	555.8	92.8	24.48 ± 4.89
^{103}gAg	C	65.7 m	118.7	31.3	18.31 ± 3.66
^{103}Pd	C	16.96 d	20.1	63.8	109.9 ± 21.9
$^{103\text{m}}\text{Rh}$	I	56.12 m	20.1	6.37	454.9 ± 90.9
^{103}Ru	C	39.25 d	497.1	89.5	1.86 ± 0.26
^{102}gRh ^{b)}	I	207 d	628.0	4.31	129.0 ± 19.4
$^{102\text{m}}\text{Rh}$ ^{b)}	I	2.9 y	631.3	55.5	298.0 ± 44.7
^{101}Pd	C	8.47 h	296.3	19.2	69.97 ± 10.1
$^{101\text{m}}\text{Rh}$	C	4.34 d	306.9	86.3	149.8 ± 22.5
^{100}Pd	C	3.63 d	126.1	11.0	51.99 ± 7.79
$^{100\text{m}+\text{g}}\text{Rh}$ ^{c)}	I	20.8 h	539.6	78.4	88.51 ± 13.3
^{99}Pd	C	21.4 m	136.0	72.7	14.82 ± 2.96
^{99}gRh ^{d)}	I	16.0 d	527.7	40.7	23.64 ± 3.55
$^{99\text{m}}\text{Rh}$	C	4.5 h	340.8	69.1	105.1 ± 15.8
^{97}gRh	C	31.1 m	421.5	75.0	15.89 ± 3.17
^{97}Ru	C	2.9 d	215.7	85.8	135.0 ± 20.2
^{96}gTc	C	4.28 d	778.2	100	46.47 ± 7.65
^{95}Ru	C	1.65 h	336.4	70.8	24.45 ± 4.89
^{95}gTc	C	20.8 h	765.8	93.9	136.8 ± 20.6
$^{95\text{m}}\text{Tc}$ ^{e)}	I	61 d	204.1	66.5	10.36 ± 1.55
^{94}gTc	I	4.88 h	849.7	97.7	83.57 ± 12.5
^{93}gTc	C	2.75 h	1363.0	65.8	29.44 ± 5.89
$^{93\text{m}}\text{Mo}$	I	6.85 h	684.7	99.7	42.77 ± 6.41
^{90}Mo	C	5.67 h	257.3	77.6	24.39 ± 3.66
^{90}gNb	C	14.6 h	1129.1	92.0	86.47 ± 12.9
^{88}Zr	C	83.4 d	392.9	97.3	112.9 ± 16.1
^{87}gY	C	3.35 d	484.9	92.2	101.4 ± 15.2
$^{87\text{m}}\text{Y}$	C	12.9 h	381.1	78.1	50.71 ± 7.60
^{86}Zr	C	16.5 h	242.8	95.8	14.45 ± 2.05
^{86}gY	C	14.74 h	1076.6	82.5	30.04 ± 4.51
$^{85\text{m}}\text{Y}$	C	4.86 h	231.7	23.4	19.65 ± 2.86

- a) C = cumulative production; I = independent production.
- b) Assignments of the ground state and metastable state according to Firestone [Fir96].
- c) The production of ^{100}gRh (20.8 h) is independent of ^{100}Pd due to the long half-life of the precursor (3.63 d). The denotation m+g is used to indicate that the contribution of the independently-produced precursor $^{100\text{m}}\text{Rh}$ to the yield of ^{100}gRh is included.
- d) The production is considered to be independent since only a small percentage of ^{99}Pd (2.6%) and none of the $^{99\text{m}}\text{Rh}$ decay to ^{99}gRh .
- e) The production is considered to be independent since only a small percentage of ^{95}Ru (2.9%) decays to $^{95\text{m}}\text{Tc}$.

RESULTS AND DISCUSSION

Table 6.3 Measured cross sections for the production of residues in the reaction $^{16}\text{O} + ^{103}\text{Rh}$.

Nuclide	Type ^{a)}	Half-life	E (keV)	Intensity (%)	Experimental cross section (mb)
$^{105\text{g}}\text{Ag}$	C	41.29 d	344.5	41.6	77.82 ± 10.9
^{104}Cd	C	57.7 m	709.3	20.4	27.21 ± 5.41
$^{104\text{g}}\text{Ag}$	C	69.2 m	555.8	92.8	62.18 ± 12.4
$^{103\text{g}}\text{Ag}$	C	65.7 m	118.7	31.3	40.15 ± 7.98
^{103}Pd	C	16.96 d	20.1	63.8	116.1 ± 23.2
$^{103\text{m}}\text{Rh}$	I	56.12 m	20.1	6.37	700.1 ± 140
^{103}Ru	C	39.25 d	497.1	89.5	1.59 ± 0.25
$^{102\text{g}}\text{Rh}$ ^{b)}	I	207 d	628.0	4.31	103.1 ± 15.5
$^{102\text{m}}\text{Rh}$ ^{b)}	I	2.9 y	631.3	55.5	215.6 ± 32.2
^{101}Pd	C	8.47 h	296.3	19.2	132.0 ± 19.8
$^{101\text{m}}\text{Rh}$	C	4.34 d	306.9	86.3	222.7 ± 33.4
^{100}Pd	C	3.63 d	126.1	11.0	85.64 ± 12.8
$^{100\text{m}+\text{g}}\text{Rh}$ ^{c)}	I	20.8 h	539.6	78.4	92.43 ± 13.9
^{99}Pd	C	21.4 m	136.0	72.7	35.99 ± 7.16
$^{99\text{g}}\text{Rh}$ ^{d)}	I	16.0 d	527.7	40.7	48.98 ± 6.02
$^{99\text{m}}\text{Rh}$	C	4.5 h	340.9	69.1	161.3 ± 24.2
$^{97\text{g}}\text{Rh}$	C	31.1 m	421.5	75.0	47.38 ± 9.43
^{97}Ru	C	2.9 d	215.7	85.0	162.2 ± 24.3
$^{96\text{g}}\text{Tc}$	C	4.28 d	778.2	100	47.88 ± 7.18
^{95}Ru	C	1.65 h	336.4	70.8	67.98 ± 13.5
$^{95\text{g}}\text{Tc}$	C	20.8 h	765.8	93.9	128.1 ± 19.2
$^{95\text{m}}\text{Tc}$ ^{e)}	I	61 d	204.1	66.5	9.54 ± 1.43
$^{94\text{g}}\text{Tc}$	I	4.88 h	849.7	97.7	72.36 ± 10.8
$^{93\text{g}}\text{Tc}$	C	2.75 h	1363.1	65.8	40.31 ± 8.02
$^{93\text{m}}\text{Mo}$	I	6.85 h	684.7	99.7	37.00 ± 5.55
^{90}Mo	C	5.67 h	257.3	77.6	8.61 ± 1.29
$^{90\text{g}}\text{Nb}$	C	14.6 h	1129.1	92.0	50.0 ± 7.50
^{88}Zr	C	83.4 d	392.9	97.3	60.96 ± 9.14
$^{87\text{g}}\text{Y}$	C	3.35 d	484.9	92.2	54.54 ± 8.18
$^{87\text{m}}\text{Y}$	C	12.9 h	381.1	78.1	26.13 ± 3.92
^{86}Zr	C	16.5 h	242.8	95.8	6.71 ± 1.01
$^{86\text{g}}\text{Y}$	I	14.74 h	1076.6	82.5	16.67 ± 2.44
$^{85\text{m}}\text{Y}$	C	4.86 h	231.7	23.4	7.59 ± 1.14

a) C = cumulative production; I = independent production.

b) Assignments of the ground state and metastable state according to Firestone [Fir96].

c) The production of $^{100\text{g}}\text{Rh}$ (20.8 h) is independent of ^{100}Pd due to the long half-life of the precursor (3.63 d). The denotation m+g is used to indicate that the contribution of the independently-produced precursor $^{100\text{m}}\text{Rh}$ to the yield of $^{100\text{g}}\text{Rh}$ is included.

d) The production is considered to be independent since only a small percentage of ^{99}Pd (2.6%) and none of the $^{99\text{m}}\text{Rh}$ decay to $^{99\text{g}}\text{Rh}$.

e) The production is considered to be independent since only a small percentage of ^{95}Ru (2.9%) decays to $^{95\text{m}}\text{Tc}$.

RESULTS AND DISCUSSION

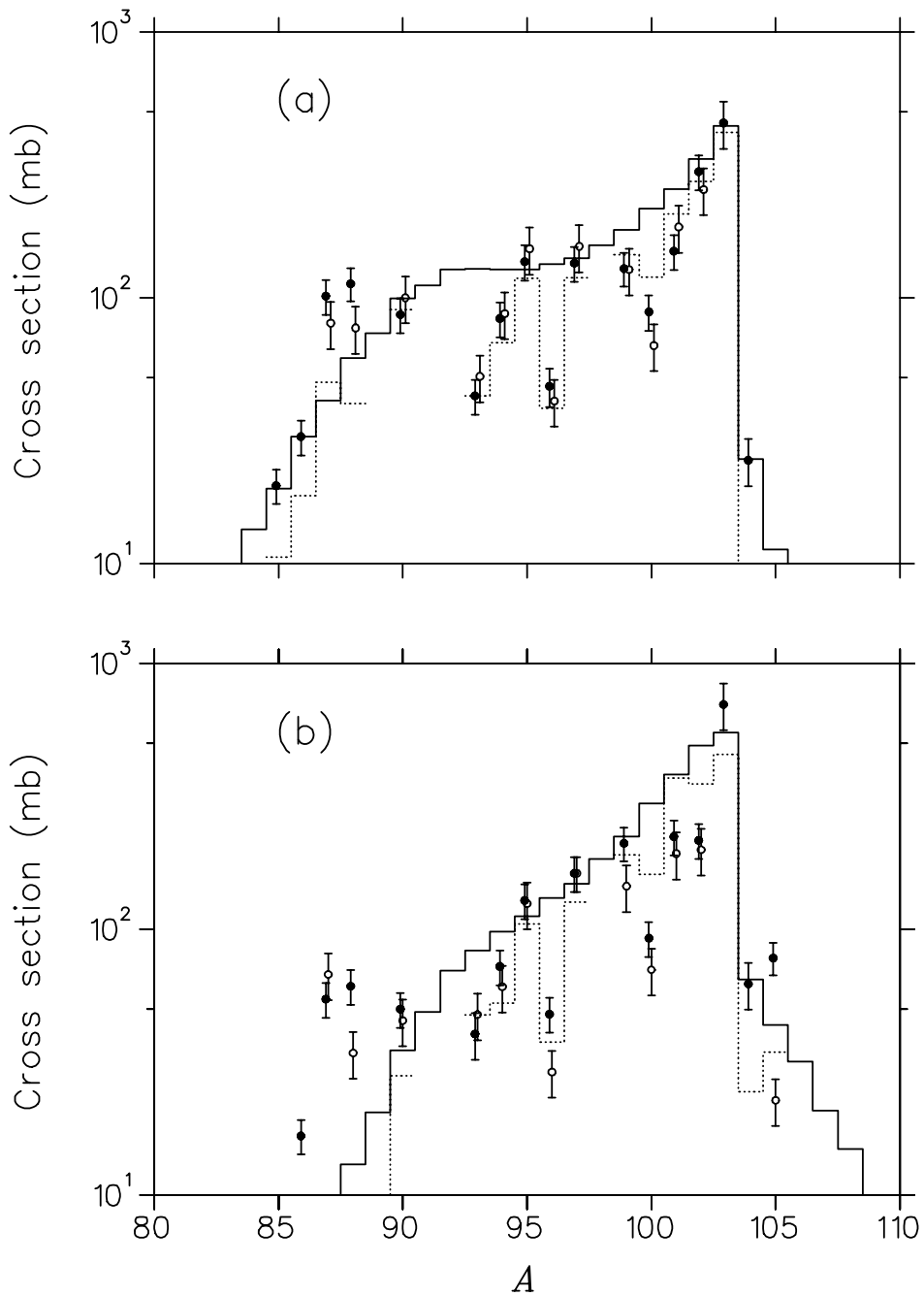


Figure 6.1 The solid symbols are the production cross sections measured in this work for those residues observed with the largest cross section at a particular mass (see Tables 6.2 and 6.3) in the interaction of ^{12}C with ^{103}Rh (a) and ^{16}O with ^{103}Rh (b) at nominal energies of 380 and 350 MeV, respectively. The dotted histograms are the corresponding theoretical predictions. The open symbols are experimental values from our previous excitation function studies [Gad97b, Ste03]. The solid histograms are the respective total isobaric yields predicted by the same theory (see text).

RESULTS AND DISCUSSION

90. Most of the points from the two measured data sets agree to within the experimental uncertainties, with a few more exceptions in the $^{16}\text{O} + ^{103}\text{Rh}$ case than in the $^{12}\text{C} + ^{103}\text{Rh}$ case. Clearly, the experimental data are consistent with an enhanced isobaric yield in the near-target mass region, with a maximum at the target mass. At several masses the observed isobaric yield comprises a significant fraction of the predicted total, as shown by the solid histogram.

Another widely used phenomenological approach which has been used to analyze the isobaric yield distributions in the rather similar reaction $^{12}\text{C} + ^{\text{nat}}\text{Ag}$ is based on a generalization [Chu91, Cho87, Cho89] of the well-known Rudstam formula [Rud66], which utilizes the systematics of the production cross sections of the observed nuclides to estimate the values of the unobserved nuclides. This formalism assumes that the shape of the isobaric charge distribution is independent of the mass, A , and is approximately Gaussian, while the mass-yield distribution can be reproduced with an exponential function. The cross sections of the residues are given by the following ten-parameter formula:

$$\sigma(A, Z) = \exp\left[\alpha_1 + \alpha_2 A + \alpha_3 A^2 + \alpha_4 A^3 + (\alpha_5 + \alpha_6 A + \alpha_7 A^2) |Z_p - Z| \alpha_8\right], \quad (6.1)$$

where

$$Z_p = \alpha_9 A + \alpha_{10} A^2. \quad (6.2)$$

The parameters α_1 through α_4 largely determine the shape of the mass-yield distribution, while α_5 through α_7 determine the width of the isobaric charge distribution. The parameter α_8 determines the shape of the isobaric charge distribution, which corresponds to a Gaussian when $\alpha_8 = 2$. The isobaric charge distribution is assumed to be symmetric about a most-probable charge Z_p , which has a near linear mass dependence (i.e. parameter α_{10} in Eq. 6.2 is generally small). Values for the parameters are found by means of an iterative least-squares fit procedure (see e.g. [Chu91]).

Figure 6.2 compares the isobaric yield distribution for $^{12}\text{C} + ^{103}\text{Rh}$ predicted by our theoretical calculations with a prediction according to the phenomenological expressions given by Eqs. (6.1) and (6.2) with the parameters of Table 6.4. It is evident that the phenomenological prediction underestimates the isobaric mass-yield in the near-target region. In the mass region below about $A = 100$ and above $A = 103$, however, a reasonable agreement could be found. The original Rudstam phenomenological isobaric yield distributions were mainly proposed for proton spallation reactions and a small number of deuteron and alpha

RESULTS AND DISCUSSION

particle spallation reactions. In the case of proton induced reactions, the theoretical justification of such formulae is the hypothesis of a common mechanism for all the observed reactions and the formulae describe the isobaric mass and charge distributions around the mean. In the case of carbon and oxygen induced reactions there is a competition between many different mechanisms which contribute with very different amounts to the production of isobars of different mass. For this reason one cannot expect, as is indeed found, that the same approach may give equally satisfactory results.

Table 6.4 Parameters obtained from a least-squares fit of equations (6.2) and (6.3) to the measured data

Parameter	Value	Parameter	Value
α_1	26.9	α_6	4.25×10^{-3}
α_2	-2.83	α_7	3.54×10^{-5}
α_3	5.2×10^{-2}	α_8	1.85
α_4	-2.6×10^{-4}	α_9	0.49
α_5	-1.56	α_{10}	-4.62×10^{-4}

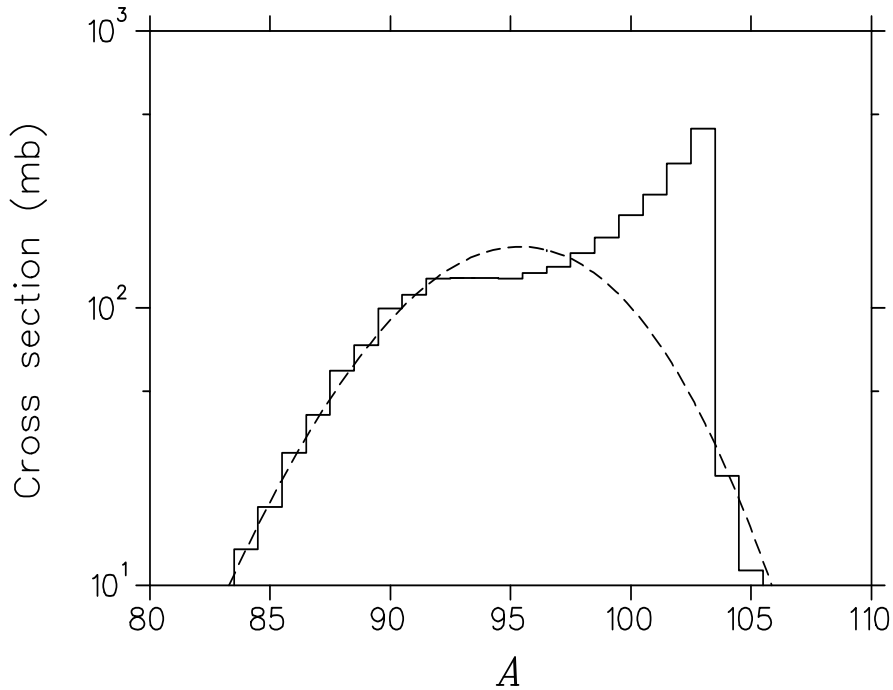


Figure 6.2 The histogram is the total isobaric yield predicted by our theoretical calculations for $^{12}\text{C} + ^{103}\text{Rh}$ at an incident energy of 380 MeV, while the dashed curve is a prediction based on a phenomenological model originally proposed by Rudstam (see text).

RESULTS AND DISCUSSION

The predicted contributions of each reaction mechanism to the cross sections for the formation of all the observed mass $A = 103$ residues (i.e. ^{103g}Ag , ^{103}Pd , ^{103m}Rh and ^{103}Ru) are given in Table 6.5 (for $^{12}\text{C} + ^{103}\text{Rh}$) and Table 6.6 (for $^{16}\text{O} + ^{103}\text{Rh}$). It is clear from the tables that ^{103m}Rh has by far the largest contribution to the total isobaric cross section of $A = 103$ residues ($> 80\%$). As expected, ^{103m}Rh is mostly formed through the inelastic scattering of the projectile whereas its precursors ^{103}Pd and ^{103}Ru are mostly formed through proton and neutron transfer from the projectile to the target, respectively. In contrast, neutron transfer and inelastic scattering mechanisms do not play any significant role in the formation of ^{103}Pd . Similarly, proton transfer and inelastic scattering do not contribute in the formation of ^{103}Ru , while ^{103g}Ag is formed through the complete and incomplete fusion reactions only.

Table 6.5 Predicted cross sections of all contributing reaction mechanisms for $A = 103$ isobars produced in $^{12}\text{C} + ^{103}\text{Rh}$ at a nominal incident energy of 380 MeV.

Mechanism	Cross section (mb)			
	^{103g}Ag	^{103}Pd	^{103m}Rh	^{103}Ru
CF	1.51	2.34	0.48	0.20
^8Be ICF	1.09	2.02	0.52	0.20
^7Li ICF	0.51	1.26	0.58	0.30
^6Li ICF	1.32	3.82	0.82	0.22
^5Li ICF	1.14	2.03	0.31	0.033
^5He ICF	0.19	0.72	0.47	0.21
α ICF	0.56	1.99	0.94	0.21
^3He ICF	2.41	5.71	0.89	0.045
p-transfer	-	12.8	3.75	-
n-transfer	-	-	18.7	3.50
IN	-	-	380	-
Total	8.73	32.7	407	4.92

CF = complete fusion

ICF = incomplete fusion

IN = inelastic scattering

RESULTS AND DISCUSSION

Table 6.6 Predicted cross sections of all contributing reaction mechanisms for $A = 103$ isobars produced in $^{16}\text{O} + ^{103}\text{Rh}$ at a nominal incident energy of 350 MeV.

Mechanism	Cross section (mb)			
	^{103g}Ag	^{103}Pd	^{103m}Rh	^{103}Ru
CF	0.015	4.35	1.72	0.18
^{12}C ICF	0.0065	7.71	0.14	0.38
^{11}B ICF	9.48	2.40	0.0019	0.22
^{10}B ICF	3.76	0.73	0.38	0.036
^8Be ICF	0.39	0.082	9.16×10^{-5}	0.0041
^6Li ICF	2.89	0.73	0.50	0.049
^5Li ICF	5.42	1.08	0.54	0.019
α ICF	10.9	3.76	0.40	0.16
d-transfer	-	3.30	2.19	0.065
p-transfer	-	24.9	6.90	-
n-transfer	-	-	41.3	1.73
IN	-	-	402	-
Total	32.9	49.0	456	2.84

CF = complete fusion

ICF = incomplete fusion

IN = inelastic scattering

6.4 Excitation functions and recoil range distributions

The excitation functions of heavy residues produced in the interaction of ^{12}C and ^{16}O with ^{103}Rh are shown in Figs. 6.3 through 6.12. Most of the experimental data were obtained in previous experiments by members of the collaboration involved in the present study [Bir96, Gad97a, Gad97b, Ste03]. Some of these previous data are still unpublished. The PhD thesis project of Stevens [Ste03] needs a special mention as the present study is in a sense a further investigation prompted in part by the results of that work. The experimental data of the present study are also shown, as well as the theoretical predictions which are displayed as histograms. The new data are presented in Appendix 7. These values are plotted at the energies corresponding to the middle of each energy interval (see Appendix 7) which may lead to some distortion at the lower incident energies in certain cases as these intervals

RESULTS AND DISCUSSION

become quite large in the regions near to the reaction thresholds. It is important to note that most of the excitation function data extracted in the present study was obtained as a by-product of the experimental investigation and not by a need to re-measure the data. The main goals of the new measurements were (1) to obtain data on ^{103}Ru , a residue for which no data existed previously, and (2) a consistency check for the RhCl_3 target activations. As such, it is useful to compare the new data with the previously measured excitation functions for all the residues observed. Also, one would not normally measure excitation functions in these reactions by means of a single irradiation in which the 400 MeV beam is stopped in the foil stack – this would normally constitute a bad experimental practice. However, we did so deliberately in the present study because (1) the main interest was in the higher energy region corresponding to the energy window of the RhCl_3 targets, (2) an extensive set of experimental excitation functions already existed, which (3) gave us the opportunity to see how well (or badly) the data extracted from a single-stack irradiation will compare with the measurements from a conventional foil-stack experiment. However, the single-stack irradiations does have merit for a few other reasons:

- All the foils in a stack were Rh foils with the exception of the first Ti monitor foil. There were no degraders and catcher foils of different materials. The Rh foils (which were about 100 times thicker than the thin foils used in the previous measurements which provided the original set of excitation functions) acted as their own degraders. These thicker foils were in fact necessary to induce sufficient activities for the measurement of ^{103}Ru since the production cross sections are quite small (albeit at the price of averaging the extracted cross sections over larger energy intervals). This also allowed us to also extract data for a few other radionuclides with relatively small cross sections for which either no data or very sparse data existed previously, e.g. $^{87\text{m}}\text{Y}$, $^{86\text{g}}\text{Y}$ and $^{85\text{m}}\text{Y}$ (see Figs. 6.8 and 6.12).
- The use of only Rh foils made it easier to interpolate for the activity in any specific energy window (e.g. that corresponding to the RhCl_3 targets) as such measurements automatically provide the thick-target production rate curve for any observed residue without the need to integrate over its excitation function (which is the usual practice). In principle, at least, this should reduce the experimental uncertainty since the numerical integration step is eliminated.

RESULTS AND DISCUSSION

- Although in a conventional foil-stack experiment where several primary beam energies will normally be used to obtain the full excitation curve (the more primary energies the better), the effects of straggling may still be a matter of concern (especially at the relatively high beam energies of the present study). In principle, it adds to the overall uncertainty in a way which is difficult to exactly quantify. The calculated energy-losses of heavy ions also have much larger uncertainties as compared to protons, by up to an order of magnitude in some cases. This is another justification for comparing the extracted excitation functions from a single thick stack and only one primary energy, with the corresponding data generated from several thinner stacks and several primary energies. (Four primary beam energies were used in the previous experiments - 100, 200, 300 and 400 MeV.) A good agreement, which we hoped to find, will give us a clear indication that the calculated energy values from published stopping power expressions and parameters can be trusted, and that the energy straggling which increases with increasing beam-energy degradation do not affect the data in any unacceptable way. In fact, a single-stack experiment which stops the beam constitutes the best case as a test of this nature.

Perusal of Figs. 6.3 through 6.12 shows that there are many cases where the agreement between the new and the previous data is quite good (e.g. ^{101}Pd and ^{100}Pd in Fig. 6.4, $^{102\text{m}}\text{Rh}$ in Fig. 6.5 (a), $^{101\text{m}}\text{Rh}$ in Fig. 6.6, $^{99\text{m}}\text{Rh}$ in Fig. 6.7, ^{97}Ru in Fig. 6.8 (a), $^{95\text{g}}\text{Tc}$ and $^{94\text{g}}\text{Tc}$ in Fig. 6.9, $^{93\text{m}}\text{Mo}$ and ^{90}Mo in Fig. 6.10, $^{90\text{g}}\text{Nb}$ and ^{86}Zr in Fig. 6.11, ^{88}Zr in Fig. 6.11 (a), $^{87\text{g}}\text{Y}$, $^{87\text{m}}\text{Y}$ and $^{85\text{m}}\text{Y}$ in Fig. 6.12 (a), etc.) But there are also curious disagreements. One case which may at first seem like a particularly bad case is that of $^{99\text{g}}\text{Rh}$ in both the ^{12}C and ^{16}O induced reactions (see Fig. 6.7). Here the disagreement in shape and absolute value is surprisingly large. On closer investigation it was found that the previous data actually includes the metastable state and should in fact have been labeled as $^{99\text{m}+\text{g}}\text{Rh}$. The new data excludes the metastable state. This case is deliberately left uncorrected to illustrate the preferential population of the isomeric state if it is close to the ground state. There are other similar cases in this mass region, including the target and its isomeric state $^{103\text{m}}\text{Rh}$. Figure 6.11 shows that the new data for ^{88}Zr is higher than the previous data by almost a factor of 3 in the case of the ^{16}O induced reaction, while the agreement in the case of the ^{12}C induced reaction is reasonable. The shapes of the excitation functions, however, are in good agreement. Generally, the overall of agreement is slightly better in the case of the ^{12}C induced reactions.

RESULTS AND DISCUSSION

Figures 6.13 to 6.15 show, as examples, how well the new calculations predict the formation of those residues that were not experimentally observed in this study (Sb, Sn and In). These figures are included because they depict, very convincingly, the contributions of complete fusion (^{113}Sb , $^{113\text{g}}$ and ^{111}In), incomplete fusion of ^8Be fragments ($^{110\text{g}}\text{In}$, $^{109\text{g}}\text{In}$ and $^{108\text{m+g}}\text{In}$) and the incomplete fusion of α -particles (Ag isotopes).

The reason why in certain cases no new data are presented except for one point, e.g. $^{104\text{g}}\text{Ag}$ (see Fig. 6.3), is because the metallic Rh foils could not be counted soon enough after the end of bombardment (EOB). This was dictated by the need to complete the measurements of the sources prepared during the radiochemistry of the RhCl_3 targets first, precluding the measurement of data for the shorter-lived radionuclides from the metallic stacks.

Thus, in spite of some disagreements, one can state that there is a good overall agreement between the previous and the new data sets. Likewise, the cases where the agreement between the theoretical predictions and the measured data is satisfactory are far more numerous than the converse, e.g. cases such as ^{86}Zr , ^{88}Zr (see Fig. 6.11) and most of the yttrium radionuclides (see Fig. 6.12) where the agreement tends to be poor. It does seem, however, that the agreement in shape is generally good even in these last-mentioned cases.

A definitive statement on the overall quality of the agreement between the experimental data and the new theoretical predictions is of crucial importance, though. As stated in the Introduction, it was necessary to introduce the initial-state interaction between the projectile and the target nucleus in order to reproduce the spectra of intermediate mass fragments (IMF). The analysis of measured IMF spectra also revealed that incomplete fusion of various non- α -type fragments should not be neglected. The question to be answered is: what effect does the inclusion of these additional reaction processes have on the predictability of the theoretical model concerning the excitation functions of heavy residues? After all, the previous model was quite successful in its predictions of these excitation functions (e.g. [Bir96, Gad97a, Gad97b, Gad98a, Gad98b, Ste03])!

A definitive statement should therefore only be made after carefully looking at the overall agreement between the data and theoretical predictions previously, and comparing this with the present predictions. Indeed, such a comparison leads us to conclude that the ability of the new calculations in reproducing the data is not significantly different (i.e. better or worse) than the previous predictions.

RESULTS AND DISCUSSION

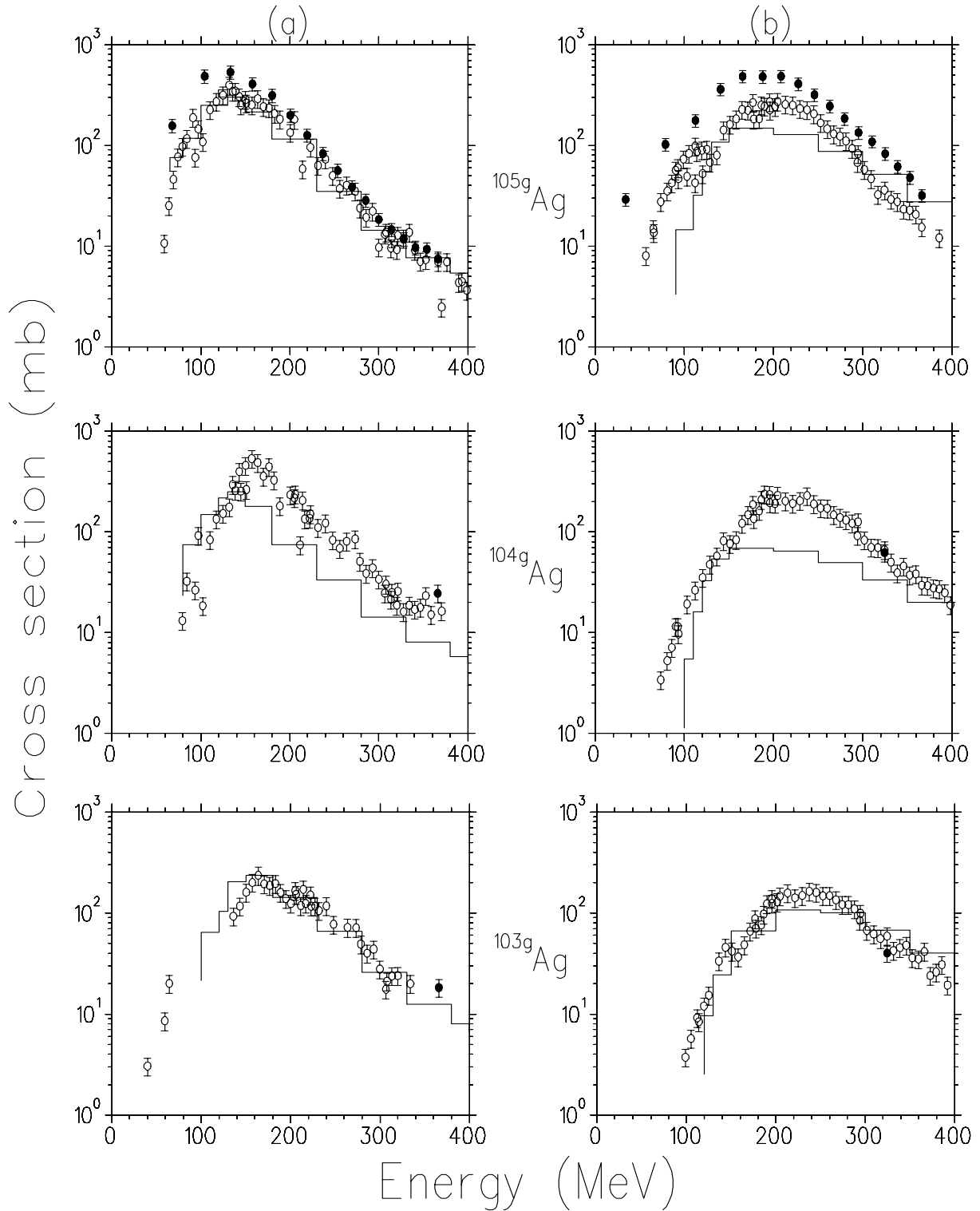


Figure 6.3 Excitation functions of silver residues produced in the interaction of (a) ^{12}C and (b) ^{16}O with ^{103}Rh at incident energies varying from threshold to 400 MeV. The solid points represent the data measured in the present work, the open symbols are the previous data and the histograms are the theoretical predictions of this study.

RESULTS AND DISCUSSION

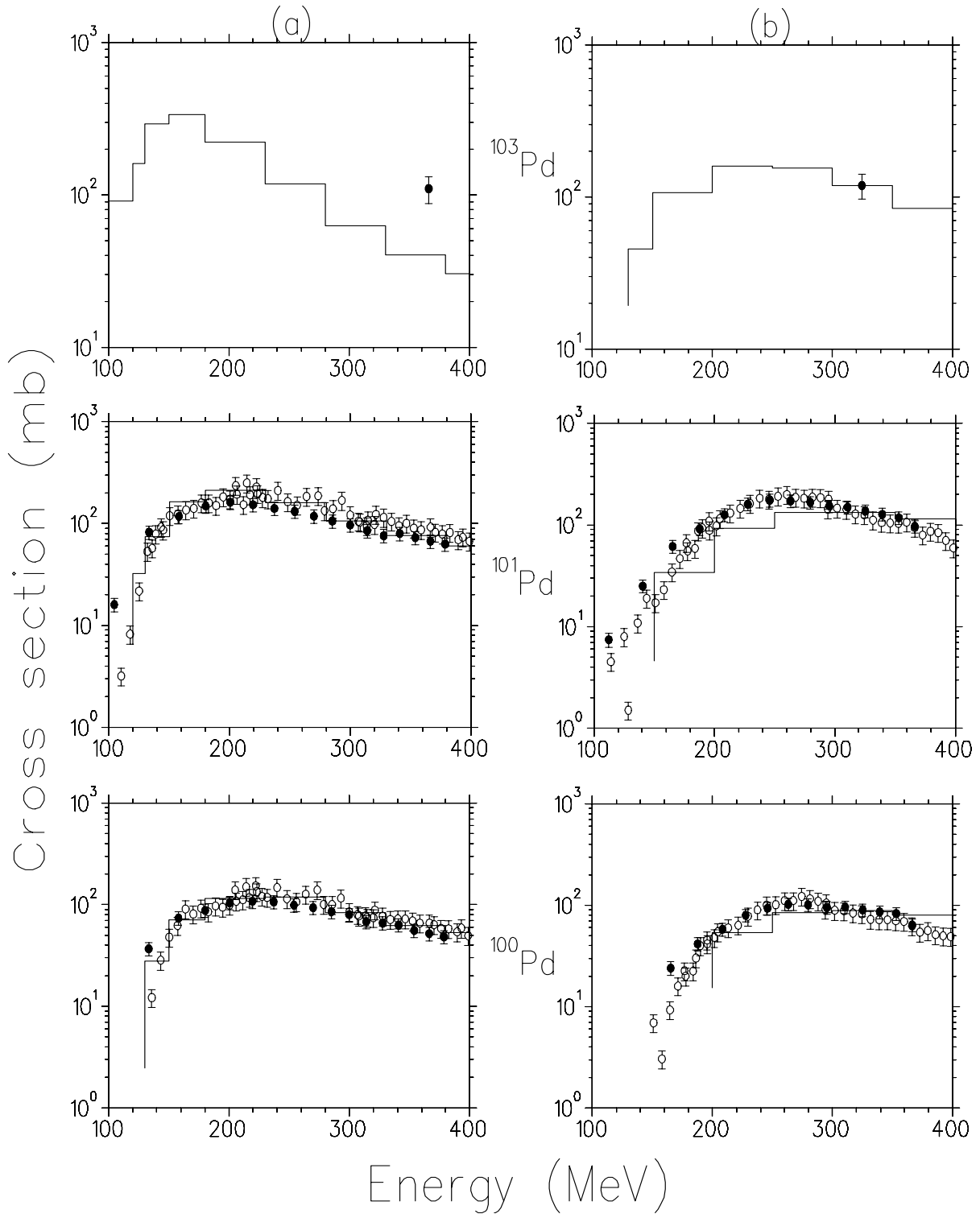


Figure 6.4 Excitation functions of palladium residues produced in the interaction of (a) ^{12}C and (b) ^{16}O with ^{103}Rh at incident energies varying from threshold to 400 MeV. The solid points represent the data measured in the present work, the open symbols are the previous data and the histograms are the theoretical predictions of this study.

RESULTS AND DISCUSSION

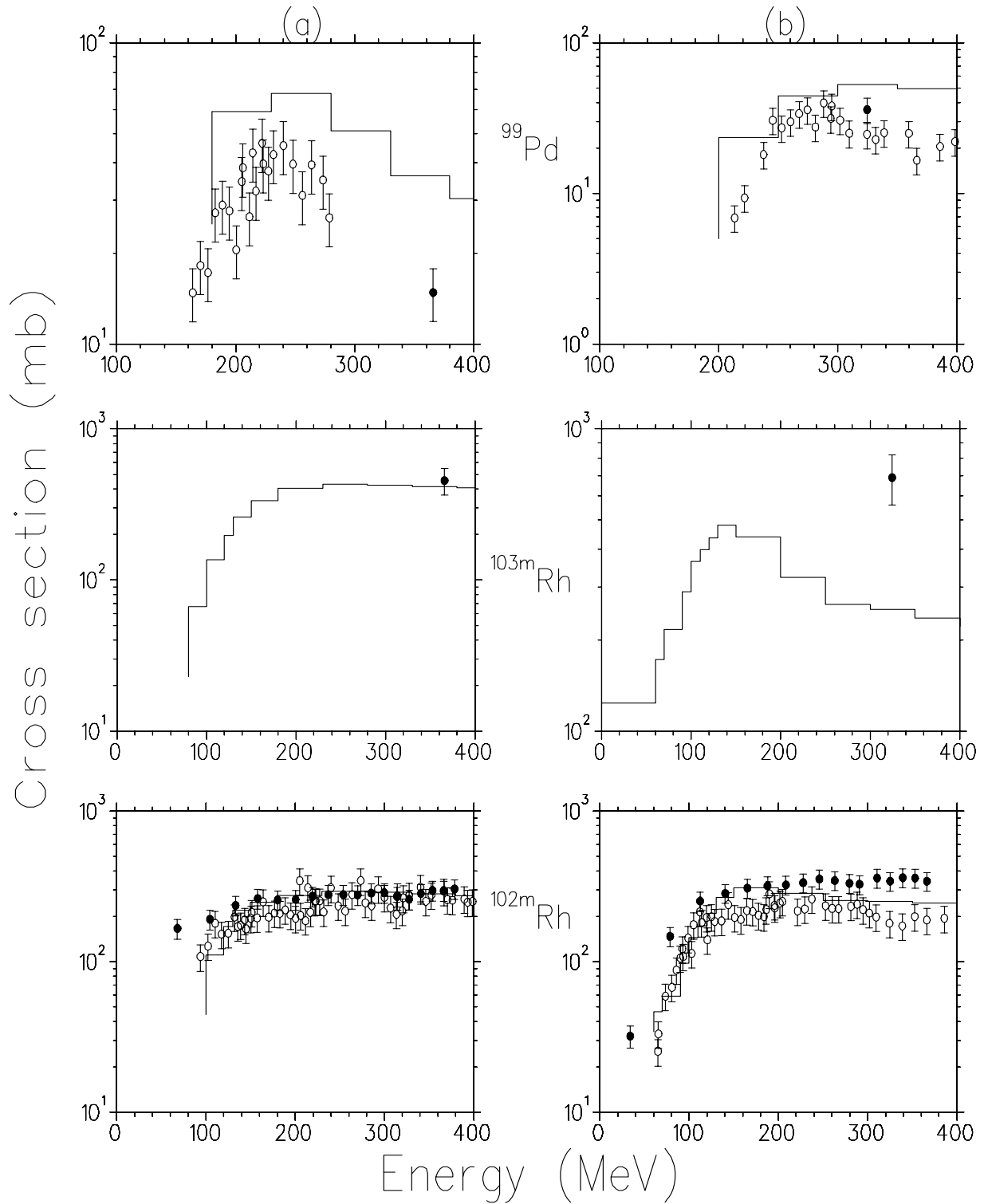


Figure 6.5 Excitation functions of palladium and rhodium residues produced in the interaction of (a) ^{12}C and (b) ^{16}O with ^{103}Rh at incident energies varying threshold to 400 MeV. The solid points represent the data measured in the present work, the open symbols are the previous data and the histograms are the theoretical predictions of this study.

RESULTS AND DISCUSSION

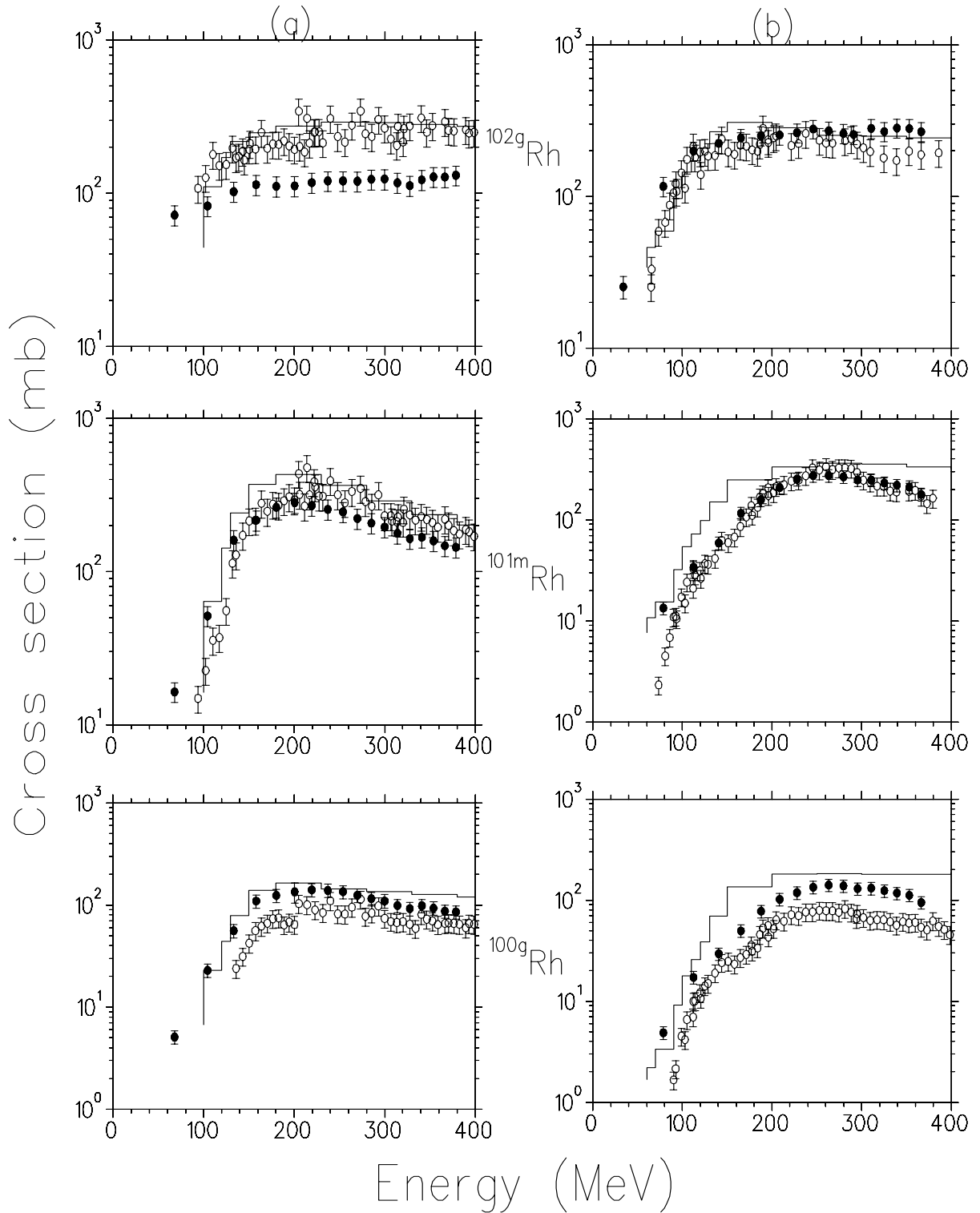


Figure 6.6 Excitation functions of rhodium residues produced in the interaction of (a) ^{12}C and (b) ^{16}O with ^{103}Rh at incident energies varying from threshold to 400 MeV. The solid points represent the data measured in the present work, the open symbols are the previous data and the histograms are the theoretical predictions of this study.

RESULTS AND DISCUSSION

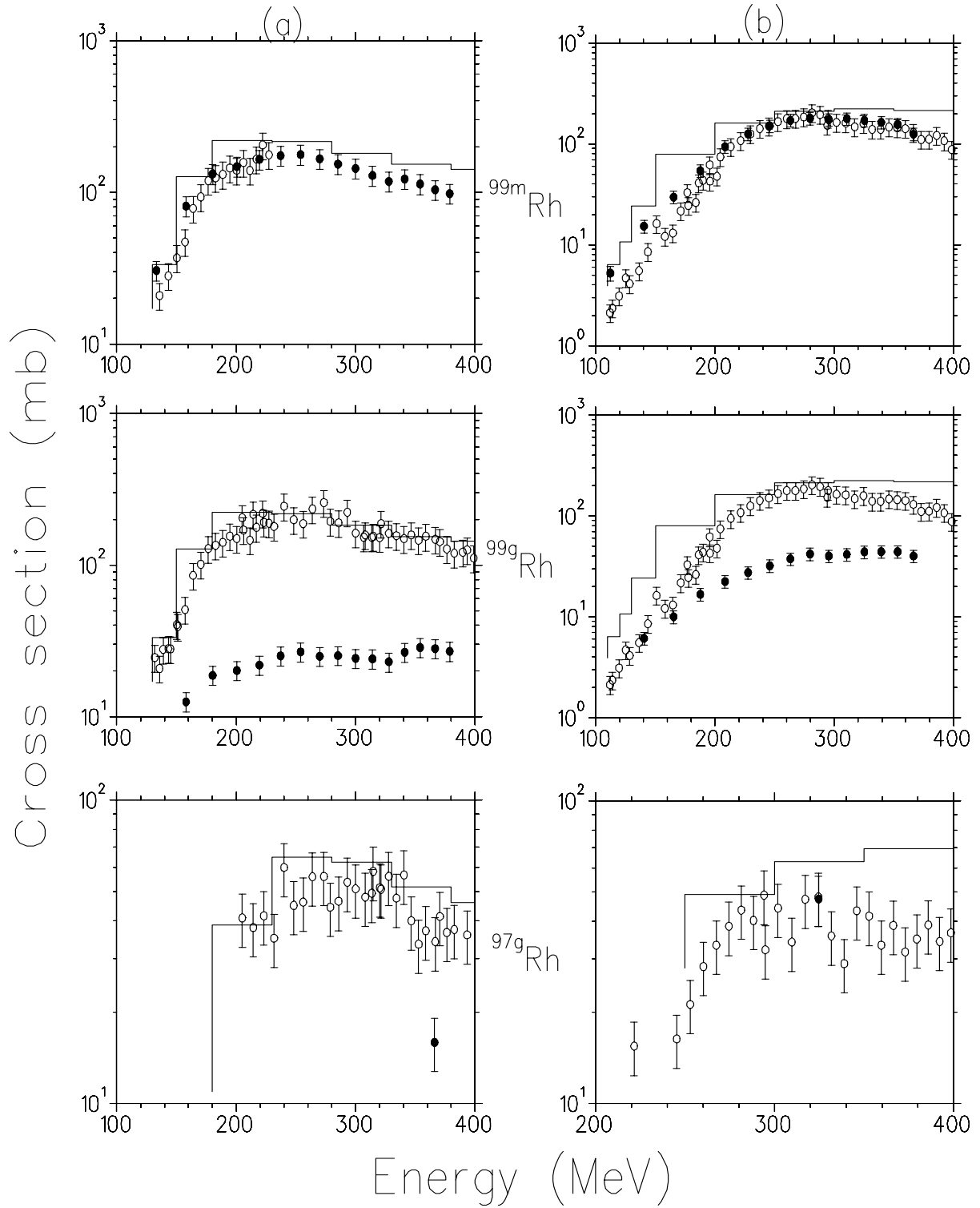


Figure 6.7 Excitation functions of rhodium residues produced in the interaction of (a) ^{12}C and (b) ^{16}O with ^{103}Rh at incident energies varying from threshold to 400 MeV. The solid points represent the data measured in the present work, the open symbols are the previous data and the histograms are the theoretical predictions of this study.

RESULTS AND DISCUSSION

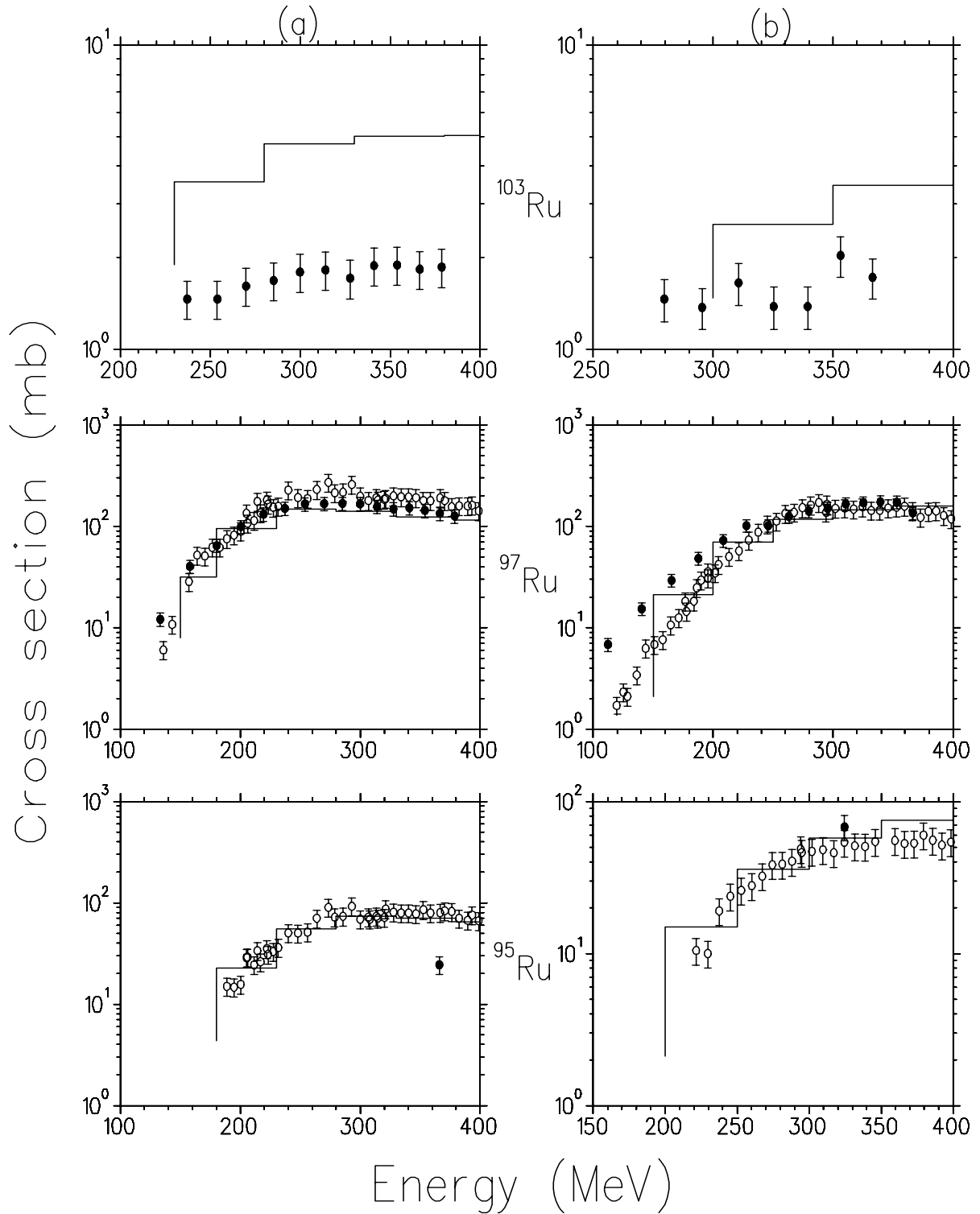


Figure 6.8 Excitation functions of ruthenium residues produced in the interaction of (a) ^{12}C and (b) ^{16}O with ^{103}Rh at incident energies varying from threshold to 400 MeV. The solid points represent the data measured in the present work, the open symbols are the previous data and the histograms are the theoretical predictions of this study.

RESULTS AND DISCUSSION

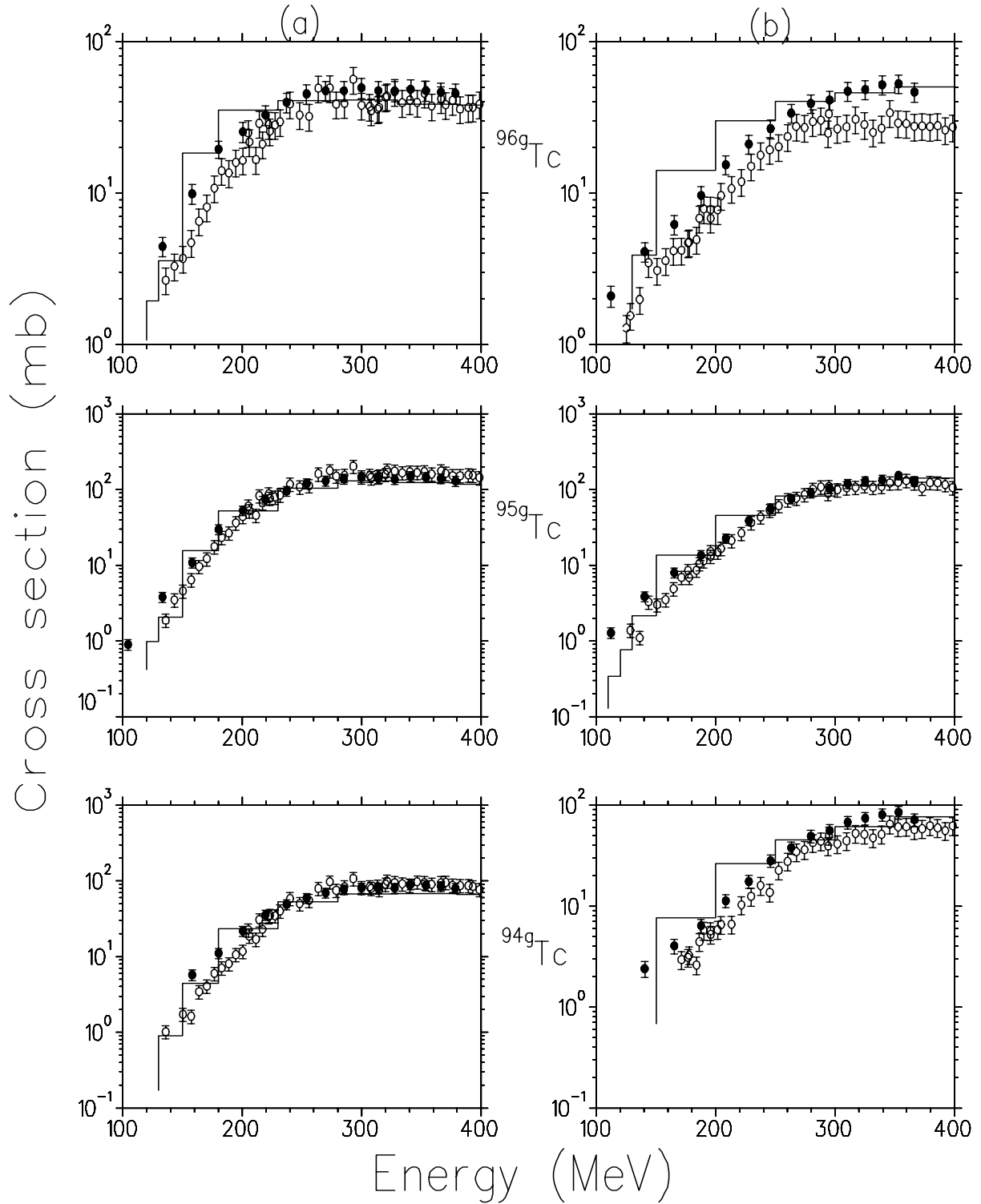


Figure 6.9 Excitation functions of technetium residues produced in the interaction of (a) ^{12}C and (b) ^{16}O with ^{103}Rh at incident energies varying from threshold to 400 MeV. The solid points represent the data measured in the present work, the open symbols are the previous data and the histograms are the theoretical predictions of this study.

RESULTS AND DISCUSSION

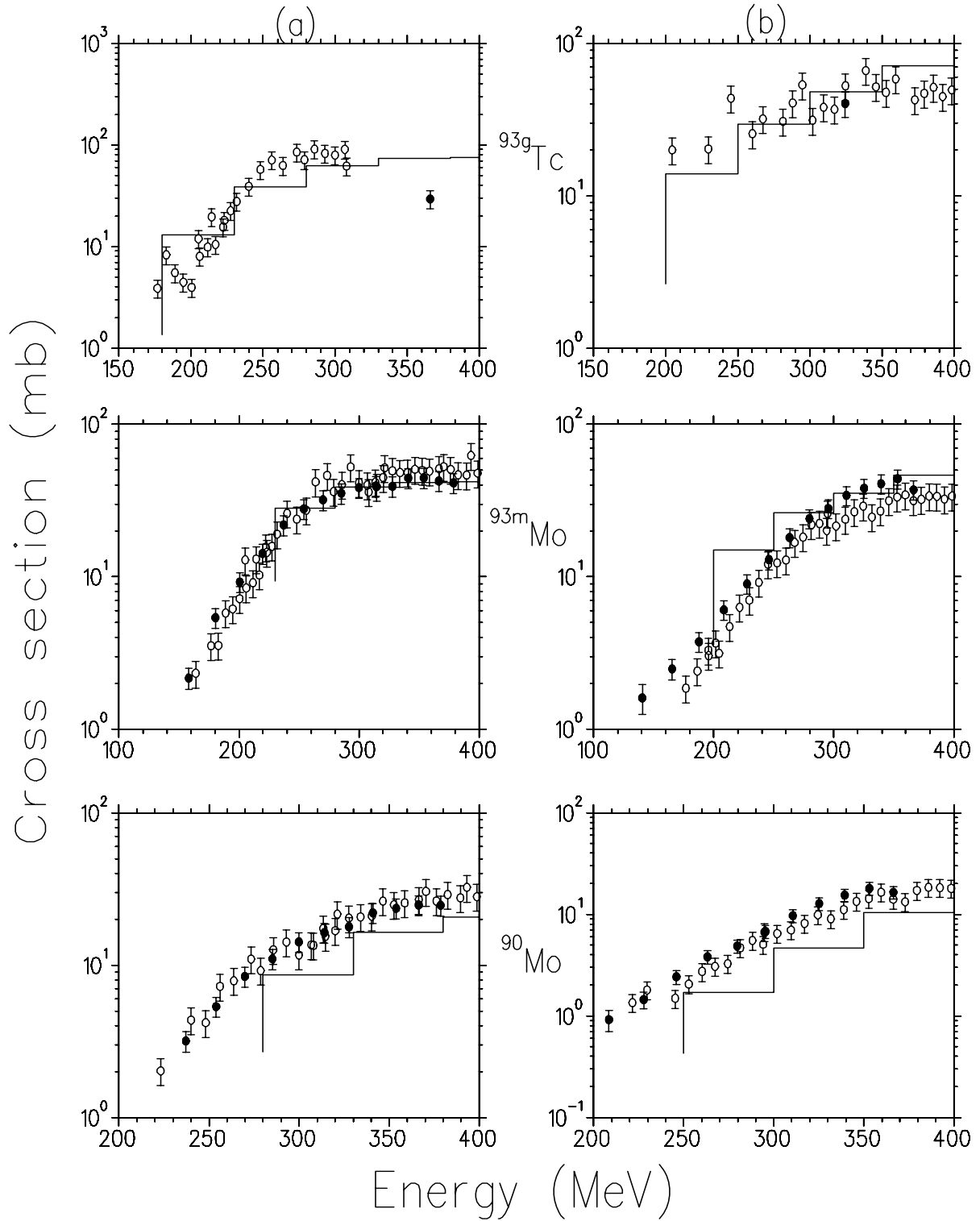


Figure 6.10 Excitation functions of technetium and molybdenum residues produced in the interaction of (a) ^{12}C and (b) ^{16}O with ^{103}Rh at incident energies varying from threshold to 400 MeV. The solid points represent the data measured in the present work, the open symbols are the previous data and the histograms are the theoretical predictions of this study.

RESULTS AND DISCUSSION

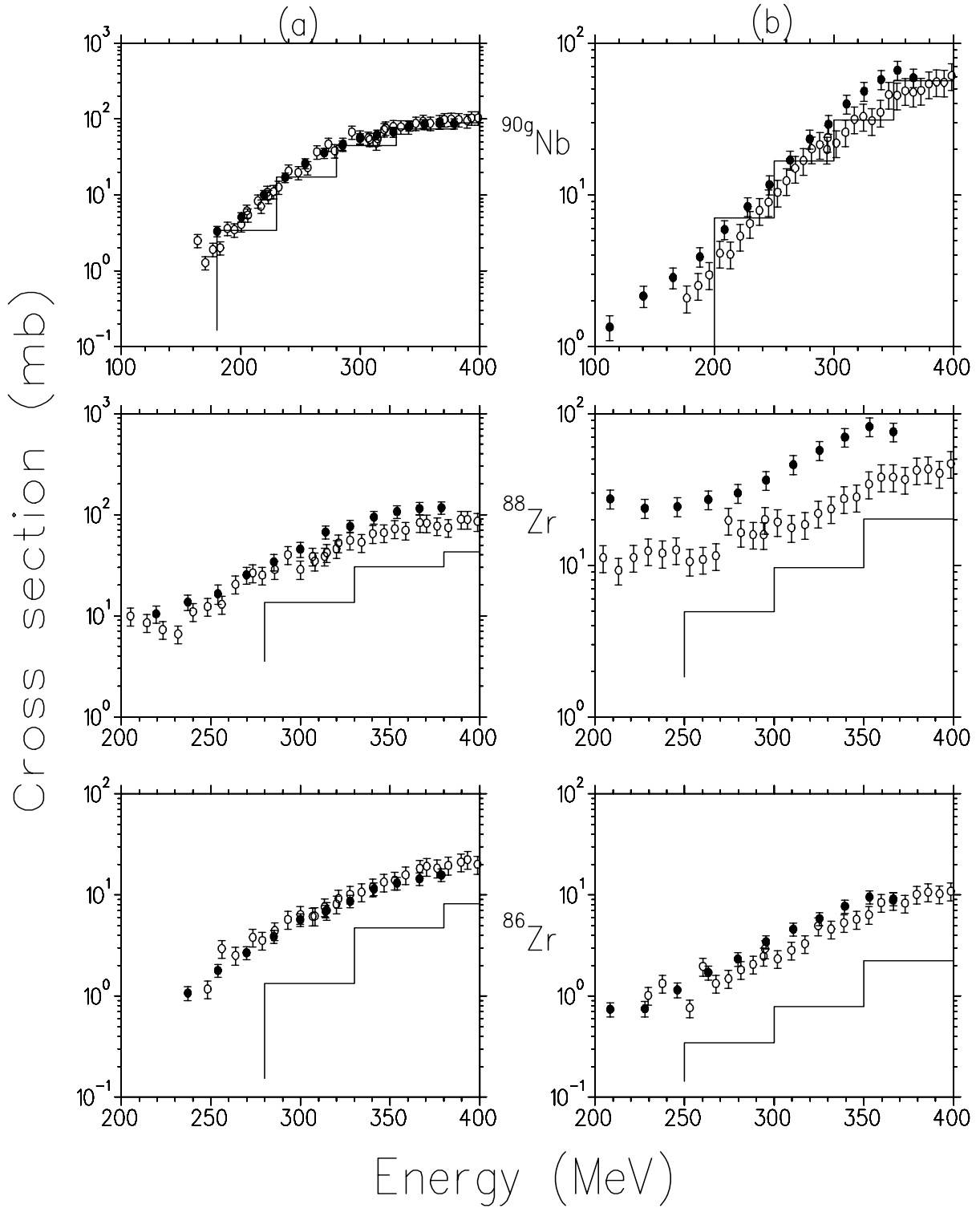


Figure 6.11 Excitation functions of niobium and zirconium residues produced in the interaction of (a) ^{12}C and (b) ^{16}O with ^{103}Rh at incident energies varying from threshold to 400 MeV. The solid points represent the data measured in the present work, the open symbols re the previous data and the histograms are the theoretical predictions of this study.

RESULTS AND DISCUSSION

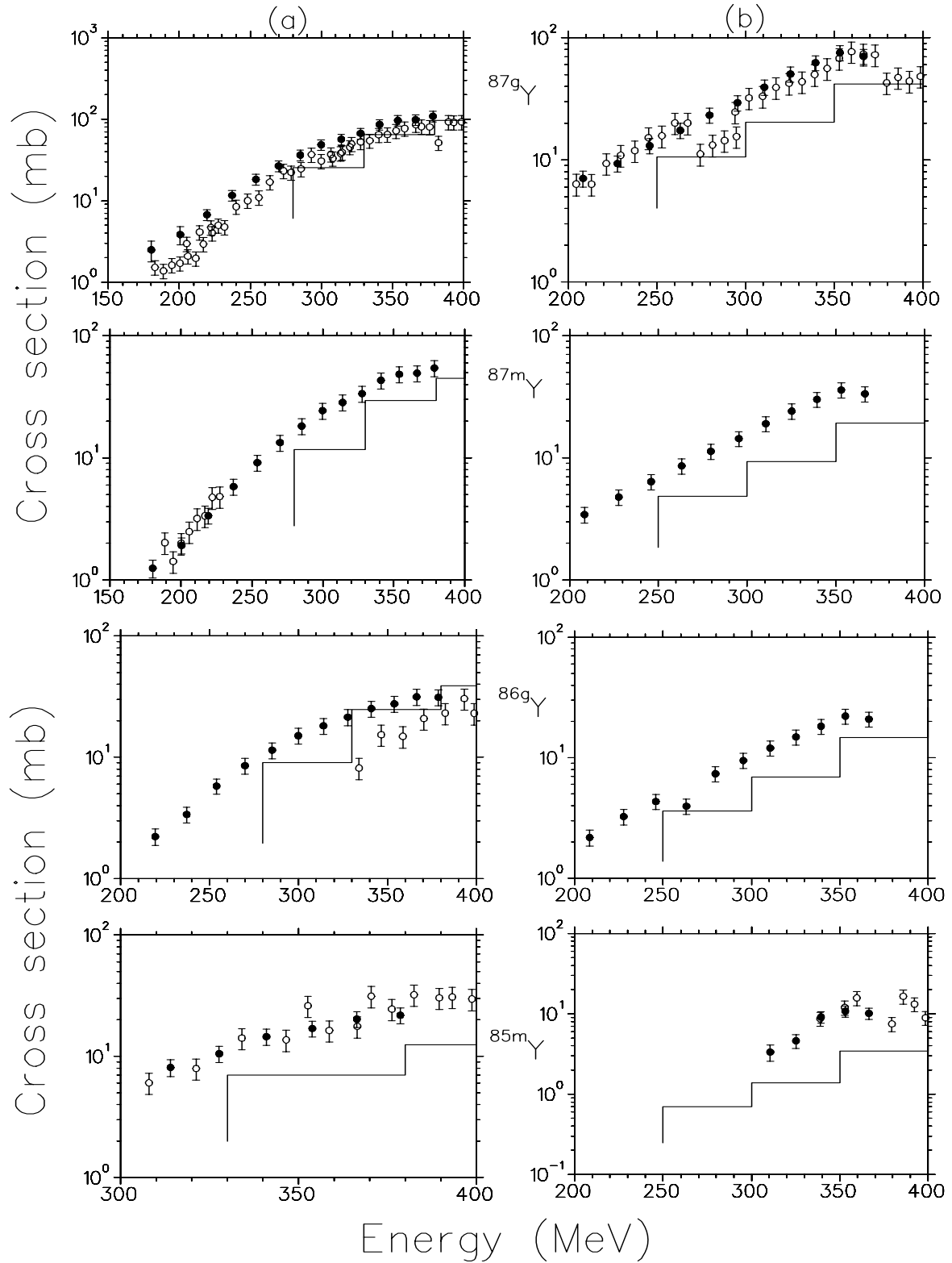


Figure 6.12 Excitation functions of yttrium residues produced in the interaction of (a) ^{12}C and (b) ^{16}O with ^{103}Rh at incident energies varying from threshold to at 400 MeV. The solid points represent the data measured in this work, the open symbols are the previous data and the histograms are the theoretical predictions of this study.

RESULTS AND DISCUSSION

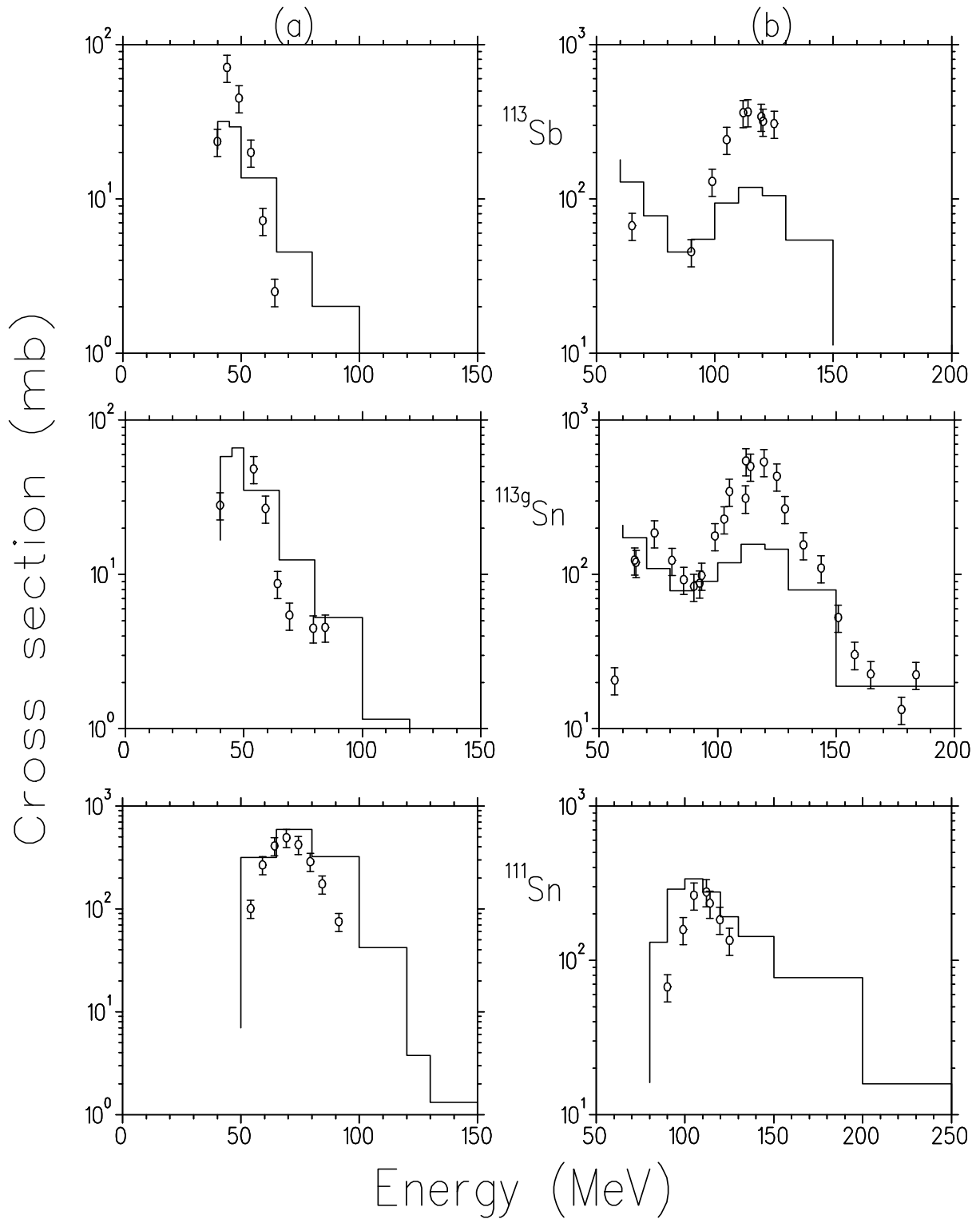


Figure 6.13 Excitation functions of selected tin residues produced in the interaction of (a) ^{12}C and (b) ^{16}O with ^{103}Rh at incident energies varying from threshold to 400 MeV. The open symbols represent the previous data and the histograms are the theoretical predictions of this study.

RESULTS AND DISCUSSION

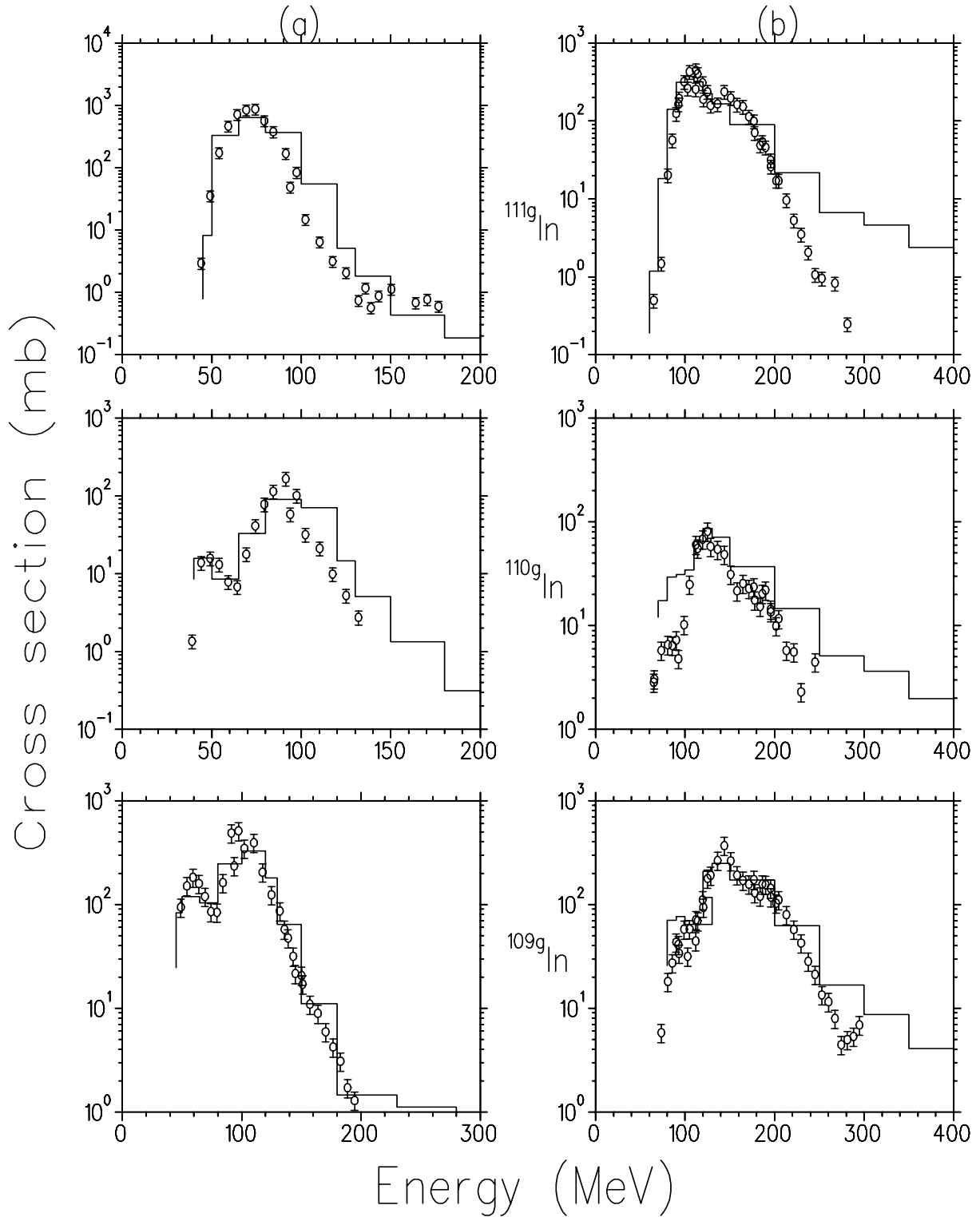


Figure 6.14 Excitation functions of indium residues produced in the interaction of (a) ^{12}C and (b) ^{16}O with ^{103}Rh at incident energies varying from threshold to 400 MeV. The open symbols represent the previous data and the histograms are the theoretical predictions of this study.

RESULTS AND DISCUSSION

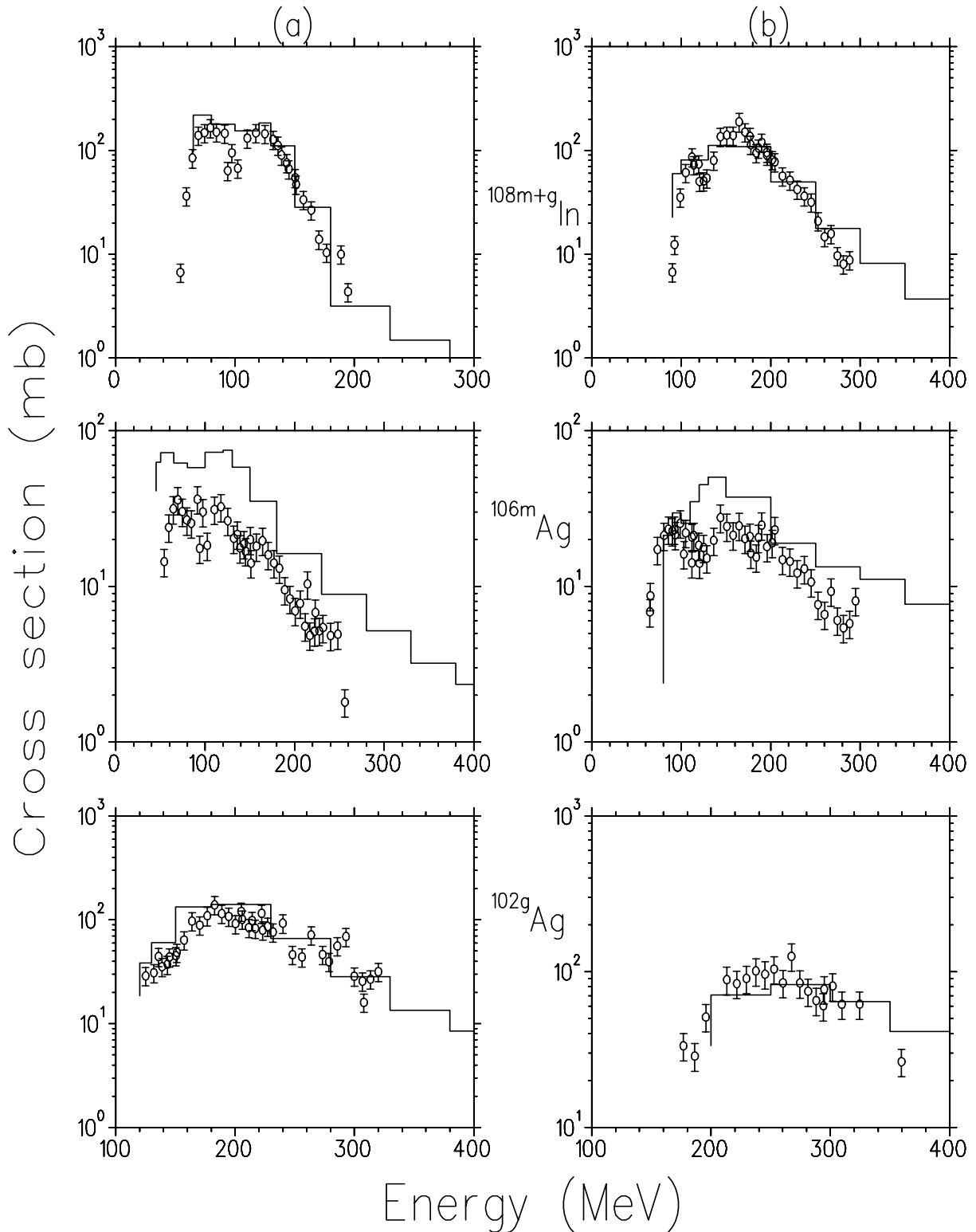


Figure 6.15 Excitation functions of indium and silver residues produced in the interaction of (a) ^{12}C and (b) ^{16}O with ^{103}Rh at incident energies varying from threshold to 400 MeV. The open symbols represent the previous data and the histograms are the theoretical predictions of this study

RESULTS AND DISCUSSION

While this last conclusion may at first sound to be disappointing, it is in fact very reassuring. Not only do the new calculations provide a satisfactory overall prediction of the excitation functions of the heavy residues, but they also provide a satisfactory overall prediction of the spectra of a substantial number of IMFs. The inclusion of the new interaction mechanisms is therefore a meaningful refinement of the theoretical approach. It is also a necessary refinement since without it the IMF spectra could not be satisfactorily reproduced. It is also not merely an empirical adjustment of parameters (as e.g. Rudstam's formalism) but a refinement which can be fully justified from sound physics arguments.

It is instructive to look at the forward recoil range distributions of residues produced in these reactions. For the case of $^{12}\text{C} + ^{103}\text{Rh}$, new calculations were also performed as part of the present study. Since the recoil range distributions were not measured in this particular work, the present theoretical predictions (renormalized to the measured distributions) are therefore compared with the previous data [Gad98a, [Ste03] collected at an incident energy of ~ 402 MeV. The recoil range distributions for selected residues are shown in Fig. 6.16, where the range values were taken as the cumulative thickness in the middle of a particular Al catcher foil in a stack of such catchers placed behind a thin Rh target [Gad98a].

According to Gadioli *et al.* [Gad98a] there are many factors which contribute to larger uncertainties in the case of recoil range measurements using foil stacks than in the case of excitation functions. The calculated forward recoil range distributions depend sensitively on the angular distributions of all emitted particles and clusters (which have no influence on the calculation of the excitation functions). Approximate expressions and/or semi-classical estimates are used for many of these at the present time. There are also large uncertainties associated with the range-energy (or range-momentum) relationship of the heavy residues (as ions with varying effective charge states) in the catcher material. Different versions of the code TRIM [Zie95], for example, give values which differ by more than 20%. The residues themselves have angular distributions which are known only approximately from rather crude measurements. Many of the residues are also produced cumulatively by the decay of precursors, adding more uncertainty as it is most often the precursors which were stopped in the catcher foils before their decay. These are a only a few of the problems, among others. Hence the data as well as the theoretical analysis cannot be expected to be very accurate. Nevertheless, these measurements give an idea of the forward linear momentum of the residues, from which some conclusions can be drawn.

Firstly, as in the case of the excitation functions, it is important to mention that the overall quality of the theoretical predictions shown in Fig. 6.16 is not significantly better or

RESULTS AND DISCUSSION

worse than the previous predictions (i.e. [Gad98a, Gad98b]). In spite of the discrepancies, there is a clear indication that the near-target residues have more skew distributions with mean values shifted towards smaller ranges (see e.g. the palladium and rhodium residues). The larger the difference between the masses of the residue and the target nucleus, the more symmetric the recoil range distribution becomes and the mean of the distribution shifts towards a higher range value (see e.g. the yttrium residues). This is entirely in agreement with the isobaric yield and excitation function results presented above. Residues with mass equal to or near that of the target are produced copiously with a very small mean forward range, i.e. a small forward linear momentum. These nuclei did not get enough energy in the reaction to emit particles to any significant degree. In contrast, a residue such as ^{88}Zr , for example, has a much larger mean forward range, indicating that it was formed in a reaction where a relatively large amount of energy (and momentum) was transferred to the target nucleus. In this case an intermediate nucleus was formed which further decayed by the emission of a substantial number of particles and/or clusters of particles.

6.5 Mean excitation energy distributions

It is also instructive to look at the mean excitation energy distributions of the intermediate equilibrated nuclei (IEN) predicted by the model calculations. This is shown in Fig. 6.17 for the $^{12}\text{C} + ^{103}\text{Rh}$ reaction at an incident energy of 400 MeV. The distributions of all contributing reaction mechanisms in the present model are given as a function of the energy per nucleon of the IEN. If all the projectile energy would be transferred to it, the nucleus would have approximately just over 3 MeV per nucleon. As expected, complete fusion will usually lead to IEN with high excitation energies. The incomplete fusion of a ^8Be fragment can provide an excitation energy exceeding 2.5 MeV per nucleon, although the distribution peaks at a value of about 1.6 MeV. (Note that at this stage of the development of the code, the distribution is inclusive of all the Be fragments considered - i.e. including ^7Be and ^9Be . In other words, ^8Be is considered to represent the average in the range $^7\text{Be} - ^9\text{Be}$.) The incomplete fusion of an α particle can provide about 2 MeV per nucleon to an IEN, however, this distribution is very much skewed towards lower excitation energies. It peaks at a value of about 0.5 MeV per nucleon, an indication of the ability of break-up α particles to escape with a large fraction of their initial energy after their initial fusion with the target nucleus. The incomplete fusion of ^5He , ^5Li , ^6Li and ^7Li provides on average smaller excitation energy to the IEN and these interactions are also less probable. (Note that the y-axis

RESULTS AND DISCUSSION

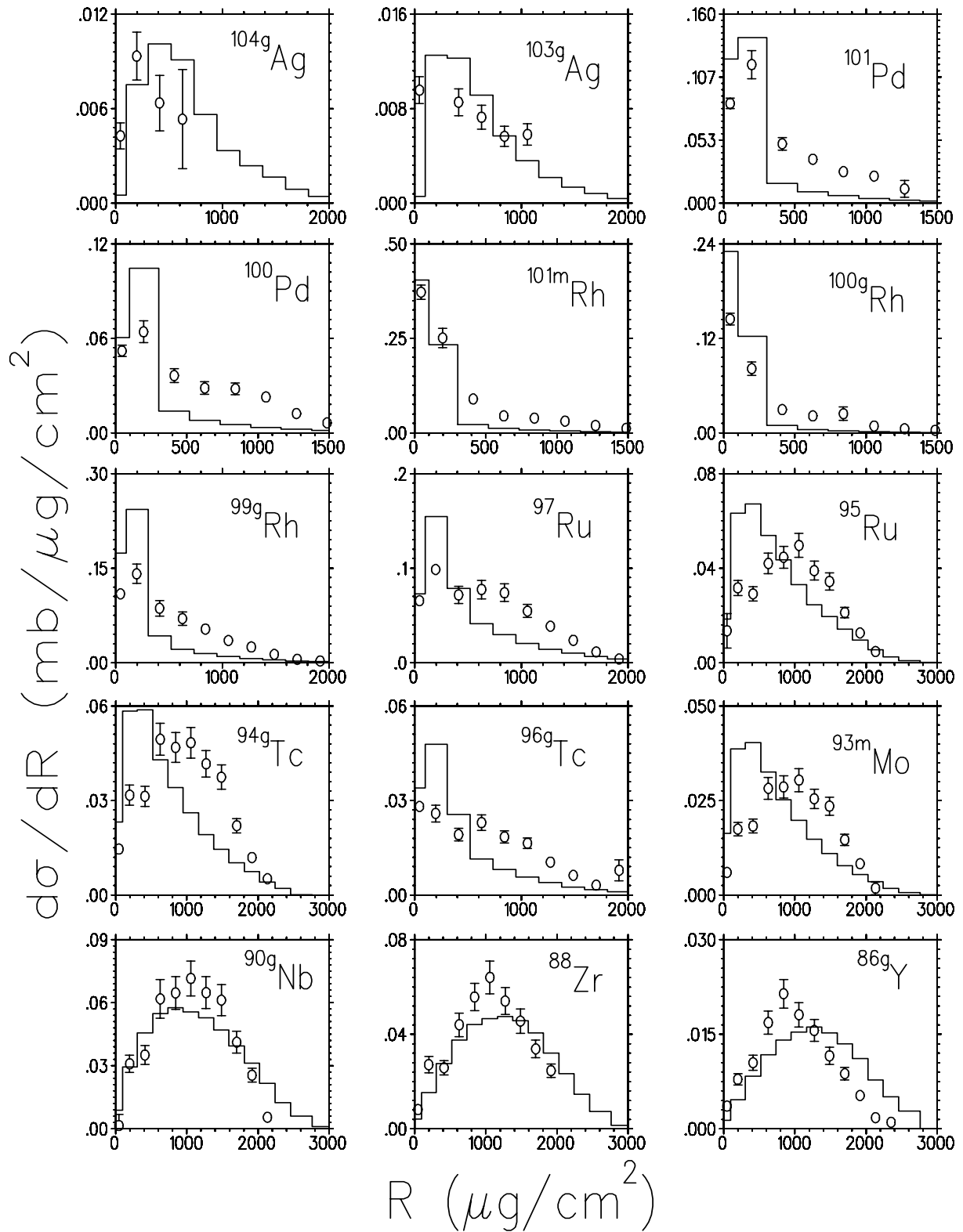


Figure 6.16 Forward recoil range distributions for residues formed in the interaction of ^{12}C with ^{103}Rh at an incident energy of nominally 400 MeV. The open points are the experimental data of Gadioli et al. [Gad98a] and the histograms represent the theoretical predictions of the present study.

RESULTS AND DISCUSSION

has a logarithmic scale.) The incomplete fusion of ${}^3\text{He}$ is about a factor of 5 less probable than the incomplete fusion of an α particle and the amount of excitation energy that it can provide to an IEN is lower, scaling roughly according to the ratio of the masses of ${}^3\text{He}$ and ${}^4\text{He}$. The inelastic scattering distribution decreases exponentially with increasing excitation energy, indicating that this mechanism dominates only at very low values of excitation energy. This mechanism provides on average the least excitation energy to the target nucleus during an interaction, too little excitation to cause emission of particles to any significant degree, thereby mainly feeding the formation of ${}^{103\text{m}}\text{Rh}$ residues.

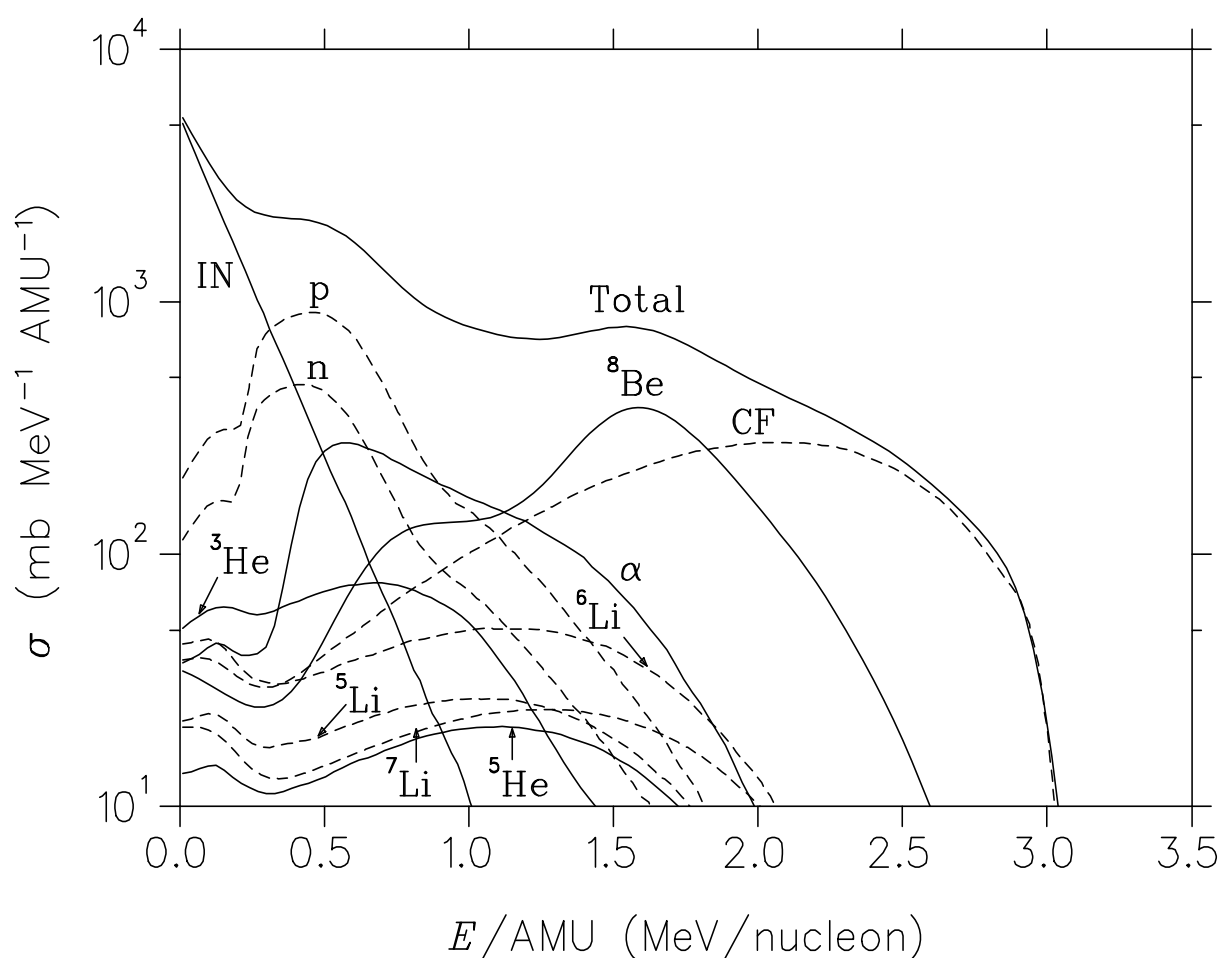


Figure 6.17 Predicted mean excitation energy distributions of IEN produced in the interaction of ${}^{12}\text{C}$ with ${}^{103}\text{Rh}$ at an incident energy of 400 MeV for each of the contributing mechanisms considered in this study. The label CF denotes complete fusion, IN the inelastic scattering of the projectile, p and n the single-nucleon transfer of protons and neutrons, respectively, TOTAL the sum of all the contributing mechanisms, while the remainder of the labels denote the incomplete fusion of projectile break-up fragments, as indicated.

CHAPTER 7

SUMMARY AND CONCLUSION

In this study the activation technique was used to measure formation cross sections of heavy residues produced in the interaction of ^{12}C and ^{16}O with ^{103}Rh at an incident energy of nominally 400 MeV. While the cumulative data sets for these reactions were already extensive before this particular study was initiated, the data for $A = 103$ isobars were nearly non-existent with only ^{103}Ag having been measured in the previous investigations. This project therefore had as a primary objective the measurement of cross sections for the production of ^{103}Pd , $^{103\text{m}}\text{Rh}$ and ^{103}Ru . In order to measure ^{103}Pd and $^{103\text{m}}\text{Rh}$, a fast radiochemical separation procedure and a rapid method of source preparation had to be developed. In this way more than 80% of the $A = 103$ isobaric yield was determined. Since the activation technique inherently yields information on many other residues as well, these cross sections were also extracted and in most cases agreed well with previous values. For a few residues with small production cross sections, e.g. some of the yttrium radionuclides, the values extracted in this work constitute new information. As predicted by a previous theoretical calculation, an enhanced isobaric yield in the near-target mass region was indeed observed, thus the desired experimental verification was obtained.

This study has once again shown that comprehensive experimental data of the heavy residues formed in a nuclear reaction can be obtained by means of the activation technique. Experimentally, these methods are relatively uncomplicated. The data are valuable in the identification of the dominant reaction mechanisms and to infer their relative contributions to the reaction cross sections. However, one particular kind of data, even if quite comprehensive, may nevertheless be insensitive to some of the processes that occur. The importance of the initial-state interaction of the projectile before break-up in ^{12}C and ^{16}O induced reactions, for example, was only realised once the double-differential cross sections of intermediate mass fragments (IMF) were also analysed. The new data generated in this study should therefore be seen as complementary to the larger body of data which also include the emission spectra of IMF and light particles.

In a certain sense, this study completes a full circle of a larger investigation which was initiated about eight years ago by the collaboration between the University of Milan, the University of the Witwatersrand and iThemba LABS. The original model developed to analyse the data of heavy residues worked well, for all intents and purposes, until further

SUMMARY IN CONCLUSION

experiments indicated that IMF spectra cannot be reproduced unless certain modifications are made, most notably the inclusion of the initial-state interaction of the projectile. Such modifications, however, cannot be made in an ad hoc way in order to describe only a subset of the data if the greater objective is to develop a comprehensive theory which will reproduce all the data in an *a priori* calculation. In this study it was therefore considered essential to revisit the heavy fragments and to re-calculate all the excitation functions and recoil ranges. The end result of this exercise is that one can finally state that the present theoretical model, which now includes also several additional modes of incomplete fusion, can still reproduce the heavy residue data satisfactorily. When this study is seen in the context of the larger investigation, it is clear that a deeper understanding of the reactions of a lighter projectile (e.g. ^{12}C and ^{16}O) with a heavier nucleus (e.g. ^{103}Rh) has been achieved. This is the up-side of the present investigation. The down-side is that the relative simplicity of the former model could no longer be retained.

One of the curious properties of nuclei is that single-particle structure and cluster structure can seemingly co-exist. By its very nature this statement implies that a simple model of ^{12}C as a three-alpha cluster is over-simplistic. While in some instances such a simple model may have some merit e.g. at low energies, not very much above the Coulomb barrier it breaks down and at incident energies of a few tens of MeV per nucleon it breaks down rather spectacularly. This is evidenced by binary fragmentation modes such as $^5\text{Li} + ^7\text{Li}$, $^5\text{He} + ^7\text{Be}$, etc., which were incorporated in the model used to analyse the data of this work. The results of the present study supports the observation that the α -cluster structure of the projectile is important in these reactions but also that the overall picture is much more complex than expected from a pure α -cluster model.

One unavoidable aspect of the present calculations is that the model has many parameters. As far as possible the values of these are assigned from the findings and results of other independent studies. Many parameters are constrained to values within narrow limits, e.g. nuclear radii, half-lives and branching ratios, etc. Values for a few other parameters, however, are inferred from fits to the experimental data. The α -particle re-emission probability in a partial fusion process is an example of the latter. The values adopted for the re-emission probabilities in the present theoretical analysis are lower than the values used previously. As mentioned in the Introduction, in some of the previous analyses values of 0.8 and 0.95 were adopted in the case of ^{12}C and ^{16}O induced reactions, respectively. It was these high escape probabilities which were initially thought to be the main cause of an enhanced isobaric yield for residues with mass similar or near to that of the

SUMMARY IN CONCLUSION

target. Clearly, mechanisms which carry substantial energy away from the reaction must be responsible. But mechanisms other than α -particle re-emission can be identified which will also do this. In the new analysis the inelastic scattering of the projectile has been included explicitly and the α -particle re-emission probabilities have been reduced to about half of their previous values (see Appendix 1). It turns out that the inelastic scattering is more important than originally thought. These changes may at first seem to be ad hoc, however, it is important to remember that once a particular set of parameters has been established, it is not changed. There is no fine tuning for individual cases or different parameters for certain subsets of the data. As such, the calculations are *a priori* within the final choice of parameters and other assumptions of the model as seemed most appropriate at the time. As with any theoretical model, one may hope that some of the more “free” parameters such as the α -particle re-emission probabilities will become more constrained with time as more new independent information becomes available.

One avenue which may yield useful new information in the context of the present study will be the measurement of correlations between break-up fragments in ^{12}C and ^{16}O induced reactions. As a first experiment of this nature, one may consider measuring the break-up ^8Be fragments in coincidence with α particles. Such measurements may yield information on both the initial-state interaction of the projectile as well as the re-emission probabilities of α particles if the measurements can be done at several geometries. One may consider a fixed forward angle for the ^8Be arm and a range of emission angles for the α -particle arm in a first experiment. The total energy spectra (i.e. the sum of the ^8Be and α -particle emission energies) generated in this way should show a peak corresponding to the elastic break-up of the projectile close to the beam energy, and a tail towards lower emission energies which will give an indication of the extent of the inelastic processes which excite the target nucleus. One may reasonably expect the cross section to be a maximum close to the geometry where the kinematics of the reaction allows the target nucleus to have zero recoil momentum, therefore measurements at a few angle pairs around this geometry may prove useful. One should certainly also consider measuring the double-differential cross sections of scattered projectiles as a check of the values adopted for the inelastic scattering cross sections in this work. These experiments can all be done with existing equipment in the large scattering chamber at iThemba LABS.

REFERENCES

- [Aar02] Aardenah K. *Separation of ^{103}Pd from Ag and Rh targets for production of ^{103}Pd seeds for prostate cancer brachytherapy*. PhD Thesis, University of Stellenbosch (2002) unpublished.
- [Aic86] Aichelin J. and Stöcker H. *Quantum Molecular Dynamics – a novel approach to N-body correlations in heavy ion collisions*. Phys. Lett. B **176** (1986) 14.
- [Akk90] Akkermans J.M. and Koning A.J. *The quantum statistics of pre-equilibrium phenomenology*. Phys. Lett. B **234** (1990) 417.
- [Aud95] Audi G. and Wapstra A.H. *The 1995 update to the atomic mass evaluation*. Nucl. Phys. A **595** (1995) 409.
- [Bas73] Bass R. *Threshold and angular momentum limit in the complete fusion of heavy ions*. Phys. Lett. B **47** (1973) 139.
- [Bas80] Bass R. *Nuclear Reactions with Heavy Ions*. Springer-Verlag, Berlin, 1980.
- [Bec03] Becker B., Albertini F., Gadioli E., Steyn G.F., Cavinato M., Connell S.H., Cowley A.A., Fabrici E., Förtsch S.V., Gadioli Erba E., Lawrie J.J. and Sideras-Haddad E. *Emission of Li, $^{7,9}\text{Be}$ and B fragments in the interaction of ^{12}C with ^{93}Nb between 200 and 400 MeV*. Eur. Phys. J. **18** (2003) 639.
- [Bir96] Birattari C., Bonardi M., Cavinato M., Fabrici E., Gadioli E., Gadioli-Erba E., Groppi F., Bello M., Bovati C., Di Filippo A., Stevens T.G, Connell S.H., Sellschop J.P.F., Mills S.J., Nortier F.M., Steyn G.F. and Marchetta C. *Preequilibrium processes in the fusion of ^{12}C with ^{103}Rh up to 20 MeV/nucleon*. Phys. Rev. C **54** (1996) 3051.
- [Bla71] Blann M. *Hybrid model for pre-equilibrium decay in nuclear reactions*. Phys. Rev. Lett. **27** (1971) 337.

- [Bla72] Blann M. and Plasil F. *Limits on angular momentum in heavy-ion compound nucleus reactions*. Phys. Rev. Lett. **29** (1972) 303.
- [Bla75] Blann M. *Preequilibrium decay*. Ann. Rev. Nucl. Sci. **25** (1975) 123.
- [Bon94] Bonasera A., Gulminelli F. and Molitoris J. *The Boltzmann equation at the borderline. A decade of Monte Carlo simulations of a quantum kinetic equation*. Phys. Rep. **243** (1994) 1.
- [Bri61] Britt H.C. and Quinton A.R. Alpha particles and protons emitted in the bombardment of ^{197}Au and ^{209}Bi by ^{12}C , ^{14}N and ^{16}O projectiles. Phys. Rev. **124** (1961) 877.
- [Bro86] Browne E. and Firestone R.B. *Table of Radioactive Isotopes*. Ed. Shirley V.S., John Wiley and Sons, U.S., 1986.
- [Bru95] Brusati C., Cavinato M., Fabrici E., Gadioli E. and Gadioli-Erba E. *Nuclear surface, mean field and isospin effects in Boltzmann master equation theory of pre-equilibrium reactions*. Z. Phys. A **353** (1995) 57.
- [Buc63] Buchanan R.F. and Faris J.P. *Adsorption of the elements from nitric acid by ion exchange*. U.S. Atomic Energy Commission Report **ANL-6811** (1963).
- [Bur81] Burns D.T., Townshend A. and Carter A.H. *Inorganic Reaction Chemistry Vol. 2: Reactions of the Elements and their Compound Part B: Osmium to Zirconium*, Ellis Horwood Ltd., Sussex, UK, 1981.
- [But03a] Buthelezi E.Z., Aardenah K., Steyn G.F., Gadioli E., van der Walt T.N., Albertini F., Cerutti F., Connell S.H., Cowley A.A. and Nortier F.M. *Isobaric yields and radiochemistry of near-target residues in the interaction of ^{12}C and ^{16}O with ^{103}Rh at an incident energy of 400 MeV*. J. Radioanal. Nucl. Chem., Vol. 258, No. 3 (2003) 649-658.

- [But03b] Buthelezi E.Z., Aardenah K., Steyn G.F., Gadioli E., van der Walt T.N., Albertini F., Cavinato M., Cerutti F., Connell S.H., Cowley A.A., Fabrici E., Förtsch S.V., Gadioli Erba E. and Nortier F.M. *Isobaric yields of near-target residues in the interaction of ^{12}C with ^{103}Rh at an incident energy of 400 MeV* in Proceedings of the 10th International Conference on Nuclear Reaction Mechanisms, Varenna, (2003) 349, ed. Gadioli E., Ricerca Scientifica, Ed. Educazione Permanente Suppl. N.122.
- [But03c] Buthelezi E.Z., Gadioli E., Steyn G.F., Albertini F., Cerutti F., Birattari C., Cavinato M., Cerutti F., Connell S.H., Cowley A.A., E. Fabrici and E. Gadioli Erba. *Incomplete fusion of projectile fragments in the interaction of ^{12}C with ^{103}Rh up to 33 MeV per nucleon.* Proceedings 8th Int. Conference on Nucleus-Nucleus Collisions, Moscow (2003), in press.
- [Cas87] Cassing W. *Dynamical aspects of intermediate-energy nucleus-nucleus collisions – Quantal single-particle motion in phase space.* Z. Phys. A **327** (1987) 87.
- [Cas88] Cassing W. *Dynamical aspects of intermediate-energy nucleus-nucleus collisions – Nonequilibrium light particle emission.* Z. Phys. A **329** (1988) 471.
- [Cav94] Cavinato M., Fabrici E., Gadioli E., Gadioli-Erba E., Galmarini M. and Gritti A. *Intermediate mass fragments in Boltzmann master equation theory of pre-equilibrium reactions.* Z. Phys. A **347** (1994) 237.
- [Cav95] Cavinato M., Fabrici E., Gadioli E., Gadioli-Erba E., Vergani P., Crippa M., Colombo G., Redaelli I. and Ripamonti M. *Study of the reactions occurring in the fusion of ^{12}C and ^{16}O with heavy nuclei at incident energies below 10 MeV/nucleon.* Phys. Review C **52** (1995) 2577.
- [Cav96] Cavinato M., Fabrici E., Gadioli E., Gadioli-Erba E. and Galbiati E. *Monte Carlo calculations using the Boltzmann Master Equation theory of nuclear reactions.* Phys. Lett. B **382** (1996) 1.

- [Cav97] Cavinato M., Fabrici E., Gadioli E., Gadioli-Erba E. and Risi E. *Ejectile angular distributions in Boltzmann Master Equation theory of nuclear reaction*. Phys. Lett. B **405** (1997) 219.
- [Cav98] Cavinato M., Fabrici E., Gadioli E., Gadioli-Erba E. and Risi E. *Boltzmann Master Equation theory of angular distributions in heavy-ion reactions*. Nucl. Phys. A **643** (1998) 15.
- [Cav01] Cavinato M., Fabrici E., Gadioli E., Gadioli Erba E. and Riva G. *Monte Carlo calculations of heavy ion cross-sections based on the Boltzmann Master Equation theory*. Nucl. Phys. A **679** (2001) 753.
- [Cer92] Cervesato I., Fabrici E., Gadioli E., Gadioli Erba E. and Galmarini M. *Light particle emission in Boltzmann master equation theory of pre-equilibrium reactions*. Phys. Rev. C **45** (1992) 2369.
- [Cha90] Chakkar A.K. and Kakkar L.R. *Micro-separation of palladium by extraction of its complex with o-phenanthroline into chloroform*. Fresenius J. Anal. Chem. **338** (1990) 79.
- [Cha91] Chadwick M.B. and Obložinský P. *Linear momentum in the exciton model: A consistent way to obtain angular distributions*. Phys. Rev. C **44** (1991) R1740.
- [Cha94a] Chadwick M.B. and Obložinský P. *Continuum angular distributions in preequilibrium nuclear reactions: Physical basis for Kalbach systematics*. Phys. Rev. C **50** (1994) 2490.
- [Cha94b] Chadwick M.B., Young P.G., George D.C. and Watanabe Y. *Multiple preequilibrium emission in Feshbach-Kerman-Koonin analyses*. Phys. Rev. C **50** (1994) 996.
- [Cho87] Cho S. Y., Chung Y.H., Porile N.T. and Morrissey D.J. *Target residues from the interaction of copper with 35 MeV/nucleon ^{12}C ions*. Phys. Rev. C **36** (1987) 2349.

- [Cho89] Cho S.Y., Porile N.T. and Morrissey D.J. *Target residues from the interaction of copper with 15-45 MeV/nucleon ^{12}C ions.* Phys. Rev. C. **39** (1989) 2227.
- [Chu91] Chung Y.H., Cho S.Y. and Porile N.T. *Target residues from the interaction of silver with 15-45 MeV/nucleon ^{12}C ions.* Nucl. Phys. A **533** (1991) 170.
- [Cri94] Crippa M., Gadioli E., Vergani P., Ciavola G., Marchetta C. and Bonardi M. *Excitation functions for the production of heavy residues in the interaction of ^{12}C with ^{181}Ta .* Z. Phys. A **345** (1994) 1.
- [Dos59] Dostrovsky I., Fraenkel Z. and Friedlander G. *Monte Carlo calculations of nuclear evaporation processes. III Applications to low-energy reactions.* Phys. Rev. **116** (1959) 683.
- [Fab89] Fabrici E., Gadioli E. and Gadioli Erba E. *Exciton model analysis of neutron spectra from fusion and quasifusion of two heavy ions.* Phys. Rev. C. **40** (1989) 459.
- [Fab90] Fabrici E., Gadioli E., Gadioli Erba E. and Galmarini M. *Hard photon emission in heavy-ion reactions.* Phys. Rev. C. **42** (1990) 2163.
- [Fab91] Fabrici E., Gadioli E., Gadioli Erba E. and Galmarini M. *Fast neutron emission from partial fusion heavy ions reactions.* Z. Phys. A **338** (1991) 17.
- [Fab93] Fabrici E., Gadioli E., Gadioli Erba E., Galmarini M., Gritti A., Vaciago E. and Vergani P. *A unified study of pre-equilibrium emission in heavy ion and nucleon induced reactions* in Proceedings "Perspectives in Heavy Ion Physics" Vol. 38, Eds. Di Toro M and Migneco E., SIF Bologna, 1993, p265.
- [Faß99] Faßbender M., Nortier F.M., Schroeder I. W. and van der Walt T.N. *The production of ^{103}Pd via $^{nat}\text{Ag}(p,x)^{103}\text{Pd}$ nuclear process.* Radiochimica Acta **87** (1999) 87.

- [Fan94] Fantoni R., Fresca, Gadioli E., Guazzoni P., Vergani P., Zetta L., Delleria P.L., Tomasi F., Campagna V., Ciavola G. and Marchetta C. *RERAME: A facility for investigating heavy ion reactions with activation techniques*. Appl. Radiat. Isot. **45** (1994) 325.
- [Fes80] Feshbach H., Kerman A.K. and Koonin S. *Statistical theory of multi-step compound and direct reactions*. Ann. Phys. 125 (1980) 429.
- [Fes95] Feshbach H. *Statistical multistep reactions*. Nuclear Physics News **5** (1995) 17, and references therein.
- [Fir96] Firestone R.B and Shirley V.S. *Table of Isotopes*. 8th Edition., Vol. I, Wiley & Sons Inc., New York (1996).
- [Frö79] Fröhlich H., Shimoda T., Ishihara M., Nagatani K., Udagawa T. and Tamura T. *Alpha-transfer reactions with large energy transfer*. Phys. Rev. Lett. **42** (1979) 1518.
- [Fuc92] Fuchs C., Sehn L. and Wolter H.H. *Relativistic kinetic calculations of heavy ion collisions with phase space dependent fields*. Nucl. Phys. A **545** (1992) 151c.
- [Fuc94] Fucks H. and Möhring K. *Heavy-ion break-up processes in Fermi energy range*. Rep. Prog. Phys. **57** (1994) 231.
- [Gad76] Gadioli E., Gadioli Erba E., Sajo Bohus L. and Tagliaferri G. *An exciton model approach to the analysis of alpha-particle-induced nuclear reactions*. Riv. Nuovo Cim. **6** (1976) 1.
- [Gad86] Gadioli E. and Hodgson P.E. *The interactions of α particles with nuclei*. Rep. Prog. Phys. **49** (1986) 951.
- [Gad92] Gadioli E and Hodgson P. E. *Pre-Equilibrium Nuclear Reactions*. Clarendon Press, Oxford, 1992.

- [Gad97a] Gadioli E., Birattari C., Cavinato M., Fabrici E., Gadioli Erba E., Allori V., Cerutti F., Di Filippo A., Stevens T.G, Connell S.H., Sellschop J.P.F., Steyn G. F., Nortier F.M. and Marchetta C. *A comprehensive study of the interaction of ^{12}C with ^{103}Rh* in Proceedings of the 8th International Conference on Nuclear Reaction Mechanisms, Varenna, (1997), ed. Gadioli E., Ricerca Scientifica, Ed. Educazione Permante, Suppl. No. **111**, p. 271.
- [Gad97b] Gadioli E., Birattari C., Cavinato M., Fabrici E., Gadioli Erba E., Allori V., Bovati C., Cerutti F., Di Filippo A., Galbiati E., Stevens T.G, Connell S.H., Sellschop J.P.F., Mills S.J., Nortier F.M., Steyn G.F. and Marchetta C. *Comprehensive study of the reactions induced by ^{12}C on ^{103}Rh up to 33 MeV/nucleon*. Phys. Lett. B **394** (1997) 29.
- [Gad98a] Gadioli E., Birattari C., Cavinato M., Fabrici E., Gadioli Erba E., Allori V., Cerutti F., Di Filippo A., Vailati S., Stevens T.G., Connell S.H., Sellschop J.P.F. Nortier F.M., Steyn G.F. and Marchetta C. *Angular distributions and forward recoil range distributions of residues created in the interaction of ^{12}C and ^{16}O ions with ^{103}Rh* . Nucl. Phys. A **641**, (1998) 271.
- [Gad98b] Gadioli E., Birattari C., Cavinato M., Fabrici E., Gadioli Erba E., Allori V., Bello G., Cerutti F., Di Filippo A., Vailati S., Stevens T.G., Connell S.H., Sellschop J.P.F. Nortier F.M., Steyn G.F. and Marchetta C. *The interaction of ^{12}C and ^{16}O with ^{103}Rh* . Heavy Ion Physics **7** (1998) 275.
- [Gad99] Gadioli E., Cavinato M., Fabrici E., Gadioli Erba E., Birattari C., Mica I., Solia S., Steyn G.F., Förtsch S.V., Lawrie J.J., Nortier F.M., Stevens T.G., Connell S.H., Sellschop J.P.F. and Cowley A.A. *Alpha particle emission in the interaction of ^{12}C with ^{59}Co and ^{93}Nb at incident energies of 300 and 400 MeV*. Nucl. Phys. A **654** (1999) 523.
- [Gad00] Gadioli E., Cavinato M., Fabrici E., Gadioli Erba E., Bassini R., Birattari C., Crippa S., Steyn G.F., Förtsch S.V., Lawrie J.J., Nortier F.M., Connell S.H., Sideras-Haddad E., Sellschop J.P.F. and Cowley A.A. *Evidence for a dissipative*

friction mechanism based on ^8Be fragments from the interaction of ^{12}C with ^{59}Co . Eur. Phys. J. A **8** (2000) 373.

- [Gad01] Gadioli E., Steyn G.F., Birattari C., Cavinato M., Connell S.H., Cowley A.A., Fabrici E., Förtsch S.V., Gadioli Erba E., Lawrie J.J., Nortier F.M., Sellschop J.P.F. and Sideras-Haddad E. *Emission of $^8\text{Be}_{gs}$ in the interaction of ^{12}C with nuclei at incident energies up to 33 MeV/amu.* Eur. Phys. J. A **11** (2001) 161.
- [Gad02a] Gadioli E., Steyn G.F., Birattari C., Catarisano C., Cavinato M., Connell S.H., Cowley A.A., Fabrici E., Förtsch S.V., Gadioli Erba E., Lawrie J.J., Sellschop J.P.F. and Sideras-Haddad E. *Interplay of mean field and nucleon-nucleon interactions in the production of carbon fragments in ^{16}O induced reactions at incident energies up to 25 MeV/amu.* Nucl. Phys. A **708** (2002) 391.
- [Gad02b] Gadioli E., Steyn G.F., Birattari C., Cavinato M., Connell S.H., Cowley A.A., Fabrici E., Förtsch S. V., Gadioli Erba E., Lawrie J.J., Pigni M., Sellschop J.P.F. and Sideras-Haddad E. *Emission of boron fragments in reactions induced by ^{16}O up to 25 MeV/amu.* Proceedings Rila Conference, Nucl. Theory 21, Ed. Nikolaev V., Heron Press, Sofia, 2002, p223.
- [Gad03] Gadioli E., Steyn G.F., Albertini F. Birattari C., Cavinato M., Connell S.H., Cowley A.A., Fabrici E., Förtsch S.V., Gadioli Erba E., Lawrie J.J., Pigni M., Sellschop J.P.F. and Sideras-Haddad E. *Emission of intermediate-mass fragments in the interaction of ^{16}O with ^{59}Co , ^{93}Nb and ^{197}Au .* Eur. Phys. J. A **17** (2003) 195.
- [Gai95] Gaita R. and Al-Bazi S.J. *An ion exchange method for selective separation of palladium, platinum and rhodium from solutions obtained by leaching automotive catalytic converters.* Talanta **42** (1995) 249.
- [Gal74] Galin J., Guerreau D., Lefort M. and Tarrago X. *Limitation to complete fusion during a collision between two complex nuclei.* Phys. Rev. C **9** (1974) 1018.
- [Gla75] Glas D. and Mosel U. *On the critical distance in fusion reactions.* Nucl. Phys. A **237** (1975) 429.

- [Gri66] Griffin J.J. *Statistical model of intermediate structure*. Phys. Rev. Lett. **17** (1966) 478.
- [Gut73] Gutbrod H.H., Winn W.G. and Blann M. *Measurement and interpretation of heavy ion fusion excitation functions*. Nucl. Phys. A **213** (1973) 267.
- [Haa81] Haasbroek F.J., Strelow F.W.E. and van der Walt T.N. *Separation of carrier free rhodium isotopes from ruthenium cyclotron targets by the extraction of nitrosylruthenium from hydrochloric acid solution*. S. Afr. J. Chem. **34** (1981) 50.
- [Har68] Harp G.D., Miller J.M. and Berne B.J. *Attainment of statistical equilibrium in excited nuclei*. Phys. Rev. **165** (1968) 1166.
- [Hel83] Helus F. *Radionuclide Production*, Vol. I, CRC Press (1983).
- [Her02] Hermanne A., Sonck M., Takacs S., Tarkanyi F. and Shubin Y. *Study on alternative production of ^{103}Pd and characterisation of contaminants in the deuteron irradiation of ^{103}Rh up to 21 MeV*. Nucl. Instr. Meth. B **187** (2002) 3.
- [Hil53] Hill J. and Wheeler J. A. *Nuclear constitution and interpretation of fission phenomena*. Phys. Rev. **89** (1953) 1102.
- [Hod97] Hodgson P.E., Gadioli E. and Gadioli Erba E. *Introductory Nuclear Physics*. Clarendon Press, Oxford, 1997.
- [Hus81] Hussein M.S., McVoy K.W. and Saloner D. *Direct and non-direct contribution to projectile fragmentation at 20 MeV/nucleon*. Nucl. Phys. Lett. B **98** (1981) 162.
- [Kal81] Kalbach C. and Mann F.M. *Phenomenology of continuum angular distributions. I. Systematics and parametrization*. Phys. Rev. C **23** (1981) 112.
- [Kal82] Kalbach C. and Mann F.M. *Possible energy parameters from continuum angular distributions*. Phys. Rev. C **25** (1982) 3197.

- [Kal88] Kalbach C. *Systematics of continuum angular distributions: Extensions to higher energies*. Phys. Rev. C **37** (1988) 2350.
- [Kon91] Koning A.J. and Akkermans J.M. *Randomness in multi-step direct reactions*. Ann. Phys. **208** (1991) 216.
- [Kor89] Korkisch J. *Handbook of Ion Exchange Resins: Their application to Inorganic analytical chemistry*, Vol. III, CRC Press Boca Raton, Florida (1989).
- [Kox87] Kox S., Gamp A., Perrin C., Arvieux J., Bertholet R., Braundet J.F., Buenerd M., Cherkaoui R., Cole A.J., El-Masri Y., Longequeue N., Menet J., Merchez F. and Viano J.B. *Trends of total reaction cross-sections of heavy ion collisions in the intermediate energy range*. Phys. Rev. C **35** (1987) 1678.
- [Lag82a] Lagunas-Solar M.C., Avila M.J., Navarro N.J. and Johnson P.C. *Cyclotron production of Ruthenium-97 (NCA) with 67.5 MeV protons on rhodium targets*. J. Label. Comp. Radiopharm. **XIX** (1982)1436.
- [Lag82b] Lagunas-Solar M.C., Wilkins S.R. and Paulson D.W. *Cyclotron production of rhodium-101m from natural palladium radiochemical methods and preliminary biological studies*. J. Radioanal., Chem. **68** (1982) 245.
- [Lag83] Lagunas-Solar M.C., Avila M.J., Navarro N.J. and Johnson P.C. *Cyclotron production of no-carrier-added ^{97}Ru by proton bombardment of ^{103}Rh targets*. Int. J. Appl. Radiat. Isot. **34** (1983) 915.
- [Lag84] Lagunas-Solar M.C., Avila M.J. and Johnson P.C. *Cyclotron production of ^{101m}Rh via proton-induced reactions on ^{103}Rh targets*. Int. J. Appl. Radiat. Isot. **35** (1984) 743.
- [Lev71] Levin V.I., Kozlova M.D., Malinin A.B. and Zelesskaya A.B. *Production of palladium-103 without a carrier and radioactive colloidal preparation of palladium for medical purpose*. Translated from Radiochimiya **13** (1971) 622.

- [Lin92] Lingen J. and Yan H. *The separation of base metals from platinum metals by ion exchange*. Chinese J. React. Polym. **1** (1992) 54.
- [Mat78] Matsuoka N., Shimizu A., Hosono K., Saito T., Kondo M., Sakaguchi H., Toba Y., Goto A., Ohtani F. and Nakanishi N. *Projectile break-up and the continuum spectra of the ($^3\text{He}, d$) reactions*. Nucl. Phys. A **311** (1978) 173.
- [Mar85] Martinez Guzman F. and Reif F. *Incomplete deep-inelastic heavy-ion collisions*. Nucl. Phys. A **436** (1985) 294.
- [McV80] McVoy K.W. and Nemes Carolina M. *Direct-reaction contribution to projectile-fragment spectra at 10-20 MeV/nucleon*. Z. Phys. A **295** (1980) 177.
- [Men86] Mendes I.A. and Turel Z.R. *A new rapid method for the solvent extraction of Ru/III/ with 1,2,3-benzotriazole into 1-pentanol*. J. Radioanal. Nucl. Chem. Lett., **105** (1986) 201.
- [Mik79] Mikulaj V., Macasek F. and Rajec P. *Simultaneous extraction of palladium and technecium from nitrate solutions with tri-n-octylamine*. J. Radioanal. Chem. **51** (1979) 55.
- [Mye67] Myers W.D. and Swaitecki A.H. *Nuclear masses and deformations*. Nucl. Phys. A **81** (1966) 1 and Akk. Fys. **36** (1967) 343.
- [Mol91] Molitoris J., Bonasera A., Cavinato M. and Gulminelli F. *Mod. Phys. Lett. A* **6** (1991) 3661.
- [Möh88] Möhring K., Srokowski T., Gross D.H.E. and Homeyer H. *A dynamic model for the projectile break-up and incomplete fusion*, Phys. Lett. B **203** (1988) 210.
- [Möh91] Möhring K., Srokowski T. and Gross D.H.E. *Modelling dissipative break-up of heavy ions*, Nucl. Phys. A **533** (1991) 333.

- [Nat70a] Natowitz J.B. *Complete-fusion cross sections for the reactions of heavy ions with Cu, Ag, Au and Bi*. Phys. Rev. C **1** (1970) 623.
- [Nat70b] Natowitz J. B. *Calculated complete-fusion cross sections for 5 to 10.5 MeV/amu ^{64}Ni , ^{86}Kr and ^{136}Xe projectiles*. Phys. Rev. C, Vol.1, **No.6** (1970) 2157,
- [Nis88] Nishioka H., Weidenmüller H.A. and Yoshida S. *Statistical theory of precompound reactions: The multistep direct process*. Ann. Phys. **183** (1988) 166.
- [Ono92] Ono A., Horiuchi H., Muruyama T. and Ohnishi A. *Fragment formation studied with antisymmetrized version of molecular dynamics with two-nucleon collisions*. Phys. Rev. Lett. **68** (1992) 2898.
- [Par76] Paria P.K. and Makundar S.K. *Note on the cation-exchange separation of palladium(II)*. Z. Anal. Chem. **281** (1976) 144.
- [Par84] Parker D.J., Asher J., Conlon T.W. and Naqib I. *Complete and incomplete fusion of $^{12}\text{C} + ^{51}\text{V}$ at $E(^{12}\text{C}) = 36\text{-}100$ MeV from analysis of recoil range and light particle measurements*. Phys. Rev. C **30** (1984) 143.
- [Par87] Parker D.J., Hogan J.J. and Asher J. *Complete and incomplete fusion in $^{20}\text{Ne} + ^{93}\text{Nb}$ reactions*. Phys. Rev. C **35** (1987) 161.
- [Par91] Parker D.J., Vergani P., Gadioli E., Hogan J.J., Vettore F., Gadioli Erba E., Fabrici E. and Galmarini M. *Recoil range study of complete and incomplete fusion of C with Au at 10 MeV/nucleon*. Phys. Rev. C **44** (1991) 1528.
- [Pat74] Patil S.P. and Shinde V.M. *A new method for the solvent extraction separation and photometric determination of palladium*. Mikrochimica Acta (1974) 853.
- [Ple97] Pletcher D. and Urbina R.I. *Electroplating of rhodium. Part 1 and 2: Chloride solutions*. J. Electroanal. Chem. **421** (1997) 137 and 145.

- [Pou91] Pouliot J., Chan Y., DiGregorio D.E., Harmon B.A., Knop R., Moisan C., Roy R. and Stokstad R.G. *Excitation and multiple dissociation of ^{12}C , ^{14}N and ^{16}O projectiles in peripheral collisions at 32.5 MeV/nucleon.* Phys. Rev. C **43** (1991) 735.
- [Püh72] Pühlhofer F. and Diamond R. M. *Enhancement of direct processes in heavy-ion reactions at high angular momenta.* Nucl. Phys., **A191** (1972) 561.
- [Reu83] Reus U. and Westmeier W. *Catalog of Gamma Rays from Radioactive Decay Part II.* At. Data and Nucl. Data Tables, **29** (1983) 193.
- [Rob89] Robert R.V.D. and Graham S.M. Rep.-MINTEK, **M399** (1989) 13.
- [Rud66] Rudstam G. *Systematics of spallation yields.* Z.Naturforsch. **A 21** (1966) 1027.
- [Ser47] Serber R. *The production of high-energy neutrons by stripping.* Phys. Rev. **72** (1947) 1008.
- [Siw79a] Siwek-Wilczyńska K., du Marchie van Voorthuysen E.H., van Popta J., Siemssen R.H. and Wilczyński J. *Incomplete fusion in $^{12}\text{C} + ^{160}\text{Gd}$ collisions interpreted in terms of a generalized concept of critical angular momentum.* Phys. Rev. Lett. **42** (1979) 1599.
- [Siw79b] Siwek-Wilczyńska K., du Marchie van Voorthuysen E.H., van Popta J., Siemssen R.H. and Wilczyński J. *Incomplete fusion in $^{12}\text{C} + ^{160}\text{Gd}$.* Nucl. Phys. A **330** (1979) 150.
- [Ste03] Stevens T.G. *Reaction mechanisms in the complete and partial fusion of ^{12}C with ^{103}Rh .* PhD Thesis, University of the Witwatersrand (2003) unpublished.
- [Str69] Strelow F.W.E., van Zyl C.R and Bothma C.J.C. *Distribution coefficients and the cation-exchange behaviour of elements in hydrochloric acid-ethanol mixtures.* Anal. Chim. Acta **45** (1969) 81.

- [Tam82] Tamura T., Udagawa T. and Lenske H. *Multistep direct reaction analysis of continuum spectra in reactions induced by light ions*. Phys. Rev. C **26** (1982) 379.
- [Tan95] Tanaka E.I., Ono A., Horiuchi H., Maruyama T. and Engel A. *Proton inelastic scattering to continuum studied with antisymmetrized molecular dynamics*. Phys. Rev. C **52** (1995) 316.
- [Tar81] Tarapčik P. and Mikulaj V. *Separation of ^{103}Pd from cyclotron irradiated rhodium targets*. Radiochem. Radioanal. Lett. **48** (1981) 15.
- [Uda79] Udagawa T., Tamura T., Shimoda T., Fröhlich H., Ishihara M. and Negatani K. *Break-up processes in heavy-ion induced reactions*. Phys. Rev C **20** (1979) 1949.
- [Ver93] Vergani P., Gadioli E., Vaciago E., Fabrici E., Gadioli Erba E. and Galmarini M. *Complete and incomplete fusion and emission of preequilibrium nucleons in the interaction of ^{12}C with ^{197}Au below 10 MeV/nucleon*. Phys. Rev. C **48** (1993) 1815 and Report INFN/BE-92/02 18 June 1992.
- [Wat99] Watanabe Y., Kuwata R., Sun Weili, Higashi M., Shinohara H., Kohno M., Ogata K. and Hawai M. *Semiclassical distorted wave model analysis of multistep $(p,p'x)$ and (p,nx) reactions to the continuum*. Phys. Rev. C **59** (1999) 2136.
- [Wil73] Wilczyński J. *Calculation of the critical angular momentum in the entrance reaction channel*. Nucl. Phys. A **216** (1973) 386.
- [Wil80] Wilczyński J., Siwek-Wilczyńska K., van Driel J., Gonggrijp S., Hageman D.C.J.M., Janssen R.V.F., Łukasiak J. and Siemssen R.H. *Incomplete fusion in $^{14}\text{N} + ^{159}\text{Tb}$ system and a “Sum-Rule Model” for fusion and incomplete-fusion reactions*. Phys. Rev. Lett. **45** (1980) 606.
- [Wil82] Wilczyński J., Siwek-Wilczyńska K., van Driel J., Gonggrijp S., Hageman D.C.J.M., Janssen R.V.F., Łukasiak J., Siemssen R.H. and van der Werf S.Y. *Binary l -matched reactions in $^{14}\text{N} + ^{159}\text{Tb}$ collisions*. Nucl. Phys. A **373** (1982) 109.

- [Wu79] Wu J.R., Chang C.C., Holmgren H.D. and Koontz R.W. *Alpha-particle breakup at incident energies of 20 and 40 MeV/nucleon*. Phys. Rev. C **20** (1979) 1284.
- [Zeb73] Zebelman A.M. and Miller J.M. *Role of angular momentum in complete fusion reactions: $^{11}\text{B} + ^{159}\text{Tb}$, $^{12}\text{C} + ^{158}\text{Gd}$, $^{16}\text{O} + ^{154}\text{Sm}$* . Phys. Rev. Lett. **30** (1973) 27.
- [Zie95] Ziegler J.F., Report Code TRIM-95.4 (1995).

APPENDIX 1

THEORETICAL MODEL INPUT PARAMETERS

A1.1 Overview

The most important parameter values that were used in the calculations are given here. The definitions of some parameters are also explained in more detail.

Due to the large amount of information generated and/or used by the theoretical calculations, various parts of the calculations are done in separate codes in such a way that all relevant information can be stored and used by the next code. The occupation probabilities of the compound nucleus states and the multiplicities of the unbound particles (which will be emitted into the continuum) are calculated first, according to the Boltzmann Master Equation Theory which was first proposed by Harp, Miller and Berne [Har68]. (The name of the BME code used, which was developed at the University of Milan, is HMBPZSMD17. HMB is for Harp, Miller & Berne and 17 indicates the version number of the code.) At the end of this calculation, the multiplicities of unbound particles as well as the time evolution of the occupied states are known. This information is then used as input by the Monte Carlo code (CAM14 – version 14 of this code developed at the University of Milan) in order to evaluate all the sequences of cascades that can take place during the relaxation of the compound nucleus.

In each cascade, in a given time interval, a well-known procedure of Dostrovsky *et al.* [Dos59] decides if the particle is emitted and what type of particle is it. This procedure is based on the comparison between an extracted random number and the elements of a vector giving the partial average multiplicities of the particles emitted in the time interval. The generation of a second random number and its comparison with the elements of a vector, giving as a function of energy the multiplicity of the selected ejectile in the time interval Δt_j , fixes the ejectile energy. The event is accepted if and only if the energy is conserved, otherwise it is rejected and the Monte Carlo code analyzes the next step. At the end of each Δt_j step, the charge, mass and excitation energy of the residual is calculated and used as charge, mass and excitation energy of the new composite nucleus. The process is stopped after sufficiently many time intervals to ensure statistical equilibrium has been attained. The incident energies that were taken into account in these calculations were from 40-400 MeV.

A1.2 Parameters used in the BME calculations

The parameters that entered the calculations were the number of integration steps ($nstep$), the time length for each step, Δt_j , ($dtime$) and the start time for time steps ($time_0$), the number protons (Z) and neutrons (N) of the projectile and target as well as the energy of the incident particles. The values for the minimum energy required for the fusion of projectile and target were (Q -value in MeV) -1.019 and -9.093 MeV for $^{12}\text{C} + ^{103}\text{Rh}$ and $^{16}\text{O} + ^{103}\text{Rh}$, respectively. The parameter that accounts for the acceleration of particles during the fusion (called *salto*) was set to 0.0 for $^{12}\text{C} + ^{103}\text{Rh}$ and 0.6 for $^{16}\text{O} + ^{103}\text{Rh}$ and has a proportional relation to the energy increase times the difference between the Fermi energy (E_F) of the projectile and that of the composite nucleus (CN), $E_{F,CN}$. The Fermi values for the CN were 33.86 and 33.91 MeV respectively for ^{12}C and ^{16}O . The binding energies for protons and neutrons entering the calculations were taken from Kox *et al.* [Kox87], if available, else were calculated from the mass formula of Myers and Swiatecki [Mye67]. The values for the maximum energy (E_{max}) for the internal energy distribution, the energy distribution step and the momentum components along the beam axis were 150, 4.0 and 0.5 MeV, respectively.

The parameterization for the reduced radius for the neutron inverse cross sections (R_0) was taken from Dostrovsky *et al.* [Dos59] (= 1.43 fm) and for the proton inverse cross section from Kox *et al.* [Kox87] (= 1.1 fm). In these calculations, the number of complex particles that could be emitted was set to 4 and these were the deuterons (d), tritons (t), ^3He , and α -particles. The parameters for the emitted particles comprised of the mass defect, interaction radius (R_0), Fermi energy (E_F), separation energy (Q_S), and Coulomb repulsion (V_C cluster), as given in Tables A1.1 and A1.2. Table A1.3 contains information pertaining to the projectile and the target. The definitions of some of the parameters given in the tables are presented below. E_{max} for the emitted particles had a value of 200 and 350 MeV for ^{12}C and ^{16}O , respectively.

Table A1.1 The parameters used for the emitted particles in $^{12}\text{C} + ^{103}\text{Rh}$.

Particle	Mass defect (MeV)	R_0 (fm)	E_F (MeV)	Q_S (MeV)	V_C cluster (MeV)
d	13.1	1.45	5.0	11.8	5.91
t	14.9	1.50	9.0	-13.3	5.75
^3He	14.9	1.45	9.0	-13.9	11.2
α	2.42	1.40	17.0	-1.04	11.0

APPENDIX 1

The mass defect, spin, R_0 and E_F are the same for both ^{12}C and ^{16}O . The values for Q_S and V_C , however, are different as given in table below.

Table A1.2 Parameters used for the emitted particles in $^{16}\text{O} + ^{103}\text{Rh}$

Particle	Q_S (MeV)	V_C cluster (MeV)
d	-11.7	5.08
t	-13.3	5.92
^3He	-11.8	11.6
α	0.912	11.0

The Coulomb barrier, momentum distribution and E_F for the target and projectile differed for different incident energy intervals. The values used in these cases are given in the Tables A3.1 below.

Tables A1.3 Coulomb barrier and momentum distribution parameters in the $^{12}\text{C} + ^{103}\text{Rh}$ reactions

200 – 400 MeV						
	$ICOU$ (MeV)	R_0 (fm)	Ff	P_1 (MeV/c)	P_2 (MeV/c)	E_F (MeV)
Projectile	0	1.63	G	63	117	27.4
Target	0	1.63	SW	244.5	12.3	33.7
80 - 180 MeV						
Projectile	1	1.3	SW	202.8	21.3	27.4
Target	1	1.3	SW	244.5	12.3	33.7

In $^{16}\text{O} + ^{103}\text{Rh}$ the parameter values for $ICOU$ and R_0 were the same for the projectile and the target and these were

E_{inc} (MeV)	400 – 90	70	60
$ICOU$	0	1	1
R_0	1.3	1.26	3.1

APPENDIX 1

However, the momentum distribution for the projectile and target differed such that in the energy range 200-400 MeV the values were the following:

	ff	P_1 (MeV/c)	P_2 (MeV/c)	E_F (MeV)
Projectile	G	75	113.9	28.4
Target	SW	244.5	12.3	33.7

At 90-200 MeV the values were

	ff	P_1 (MeV/c)	P_2 (MeV/c)	E_F (MeV)
Projectile	SW	207.3	21.3	28.4
Target	SW	244.5	12.3	33.7

Definitions:

$ICOU$ - describes the slowing down of nuclei by the Coulomb barrier. The units are given in MeV.

R_0 - defines the interaction radius (units of fm), which in the case of the Coulomb potential

appears as follows:
$$V_C = \frac{1}{4\pi\epsilon_0} \frac{Z_p Z_T e^2}{R_0}.$$

Q_S - the separation energy (MeV).

P_1 and P_2 - the momentum distribution components in units of MeV/c.

ff - is the parameter that allows the choice for the wave function which describes the momentum distribution so that if

$ff = 'G'$: the function is Gaussian, with an “average value” equal to P_1 and a standard deviation equal to $P_2 / \sqrt{2}$.

$ff = 'SW'$: the function is the Saxon-Wood, with the “radius” equal to P_1 and the “diffuseness” equal to P_2 .

A1.3 Parameters used in the Monte Carlo calculations

The parameters used in the simulations are given in Tables A10.4 – A10.30 below. The most important parameters that entered the calculation were the break-up Q-value (Q_{rea}), binding energy ($BINDBU$), energy for the projectile break-up (E_{BU}), all given in MeV. The wave function that describes the momentum distribution inside the projectile has parameters of $IFUN$, hh , ff and V_0 , where the wave function takes a particular form for $IFUN = 1, 2, 3, 4$ and 5 . The reaction cross sections for each contributing mechanism, σ_r , is given in units of millibarn (mb), and the corresponding entrance-channel critical angular momentum limits are L_{min} and L_{max} . The energy that the projectile possesses, before break-up C_{bin} $\left(= \frac{e^2}{4\pi\epsilon_0} \frac{Z_p Z_T}{R_{mt}} \right)$ and the energy distribution for the IEN produced in the interactions is given by C_{bin1} and C_{bin2} . The energy-loss step between C_{bin1} and C_{bin2} is given by ΔC_B . The value of C_B takes into account the energy that the fast ejectiles take with after the interactions. All these values are given in MeV. The probability that the absorbed α -particle may be re-emitted ($PROB$) was taken into account only for the incomplete fusions of ${}^8\text{Be}$ fragments and break-up α particles (see section 3.7). The parameter kk' is the constant break-up and mass transfer probability described in section 3.6. The values were adopted from previous experiments [Gad00, Gad02]. The angle θ_{is} is the inelastic scattering angle. A few parameters act as switches in the code. Parameter $Inopre$ controls whether pre-equilibrium emission is considered or not. If $Inopre = 1$, no pre-equilibrium emission is taken into account. Parameter $Iswspe$ controls whether initial-state interactions of the projectile is considered or not. If $Iswspe = 1$, the initial-state interactions are included in the calculation.

A1.3.1 Input parameters for ${}^{12}\text{C} + {}^{103}\text{Rh}$

The reaction cross section consists of contributions from complete fusion (CF), incomplete fusion (ICF) of ${}^8\text{Be}$, ${}^{7,6,5}\text{Li}$, ${}^{5,3}\text{He}$ and α particles, single-nucleon transfer of protons (p) and neutrons (n) as well as inelastic scattering. Projectile energies varied from 40 to 400 MeV.

APPENDIX 1

Table A1.4 Common parameters used at all incident energies

Process	Spectator	Q_{REA} (MeV)	$BINDBU$ (MeV)	$IFUN$	V_0 (MeV)	hh, ff	$PROB$	E_{BU} (MeV)
CF	-	-1.02	-	-	-	-	-	-
ICF (^8Be)	α	-2.06	7.36	1	35	0	0.4	3.2
ICF (^7Li)	^5Li	-9.35	26.6	1	55	0	0	2.2
ICF (^6Li)	^6Li	-13.6	28.2	1	55	0	0	2.2
ICF (^5Li)	^7Li	-13.7	26.6	1	55	0	0	2.2
ICF (^5He)	^7Be	-16.2	27.1	1	70	0	0	1.7
ICF (α)	^8Be	-4.56	7.36	1	35	0	0.5	1.7
ICF (^3He)	^9Be	-12.4	26.9	5	0.0	0	0	1.7
p-transfer	^{11}B	-7.29	15.9	5	0.0	0	0	1
n-transfer	^{11}C	-11.7	18.7	5	0.0	0	0	1
INSC	-			-	-	-	-	-

Table A1.5 Parameters used at 400 MeV

Process	σ_I (mb)	L_{min}	L_{max}	R_{int} (fm)	C_{bin1} (MeV)	C_{bin2} (MeV)	ΔC_B (MeV)	kk'	C_B	$\cos(kk')$	θ_{is}
CF	440	-	-	-	-	-	-	-	-	-	-
^8Be	360	53	71	15	60	300	5	0.04	9.024	-	-
^7Li	49	71	91	11	30	310	5	0.03	17.3	-	-
^6Li	78	71	91	11	30	310	5	0.03	17.3	-	-
^5Li	49	71	91	11	30	290	5	0.03	17.3	-	-
^5He	35	71	91	9	75	300	5	0.06	27.5	-	-
α	225	71	91	9	70	310	5	0.04	27.5	-	-
^3He	92	71	91	10	35	300	5	0.07	25	-	-
p	410	91	139	0	37.2		-	-	22	-	-
n	273	91	139	0	37.2		-	-	22	-	-
INSC	870	91	139	-	-	-	-	-	-	0.06	0.5

APPENDIX 1

Table A1.6 Parameters used at 380 MeV

Process	σ_I (mb)	L_{min}	L_{max}	R_{int} (fm)	C_{bin1} (MeV)	C_{bin2} (MeV)	ΔC_B (MeV)	kk'	C_B	cos (kk')	θ_{is}
CF	470	-	-	-	-	-	-	-	-	-	-
^8Be	375	53	72	15	60	230	5	0.04	9.02	-	-
^7Li	47	72	91	11	30	290	5	0.03	17.3	-	-
^6Li	78	72	91	11	30	290	5	0.03	17.3	-	-
^5Li	47	72	91	11	30	290	5	0.03	17.3	-	-
^5He	34	71	91	9	75	280	5	0.06	27.5	-	-
α	225	72	91	9	70	290	5	0.04	27.5	-	-
^3He	86	72	91	10	35	280	5	0.07	25	-	-
p	390	91	136	0	37.2		-	-	22	-	-
n	260	91	136	0	37.2		-	-	22	-	-
INSC	870	91	136	-	-	-	-	-	-	0.06	0.5

Table A1.7 Parameters used at 330 MeV

Process	σ_I (mb)	L_{min}	L_{max}	R_{int} (fm)	C_{bin1} (MeV)	C_{bin2} (MeV)	ΔC_B (MeV)	kk'	C_B	cos (kk')	θ_{is}
CF	535	-	-	-	-	-	-	-	-	-	-
^8Be	430	53	71	15	60	200	5	0.04	9.02	-	-
^7Li	42	71	87	11	40	250	5	0.05	17.3	-	-
^6Li	75	71	87	11	40	250	5	0.05	17.3	-	-
^5Li	42	71	87	11	40	250	5	0.05	17.3	-	-
^5He	32	71	81	10	60	250	5	0.07	24.8	-	-
α	220	71	87	11	55	270	5	0.06	23.0	-	-
^3He	72	71	87	10	35	255	5	0.1	25	-	-
p	340	87	127	0	37.2		-	-	22	-	-
n	226	87	127	0	37.2		-	-	22	-	-
INSC	884	87	127	-	-	-	-	-	-	0.06	0.5

APPENDIX 1

Table A1.8 Parameters used at 280 MeV

Process	σ_I (mb)	L_{min}	L_{max}	R_{int} (fm)	C_{bin1} (MeV)	C_{bin2} (MeV)	ΔC_B (MeV)	kk'	C_B	cos (kk')	θ_{is}
CF	640	-	-	-	-	-	-	-	-	-	-
^8Be	530	53	71	15	60	150	5	0.04	9.02	-	-
^7Li	36	72	85	11	40	200	5	0.05	17.3	-	-
^6Li	70	72	85	11	40	200	5	0.05	17.3	-	-
^5Li	36	72	85	11	40	200	5	0.05	17.3	-	-
^5He	28	72	85	10	60	200	5	0.07	24.8	-	-
α	205	72	85	11	55	200	5	0.06	23.0	-	-
^3He	65	72	85	10	35	200	5	0.1	25	-	-
p	295	85	117	0	37.2		-	-	22	-	-
n	196	85	117	0	37.2		-	-	22	-	-
INSC	880	85	117	-	-	-	-	-	-	0.06	0.5

Table A1.9 Parameters used at 230 MeV

Process	σ_I (mb)	L_{min}	L_{max}	R_{int} (fm)	C_{bin1} (MeV)	C_{bin2} (MeV)	ΔC_B (MeV)	kk'	C_B	cos (kk')	θ_{is}
CF	780	-	-	-	-	-	-	-	-	-	-
^8Be	680	53	73	15	50	160	5	0.07	9.02	-	-
^7Li	30	73	82	11	30	170	5	0.1	17.3	-	-
^6Li	64	73	82	11	30	170	5	0.1	17.3	-	-
^5Li	30	73	82	11	30	170	5	0.1	17.3	-	-
^5He	23.5	73	82	9	27	170	5	0.1	19	-	-
α	178	73	82	9	50	170	5	0.2	19	-	-
^3He	59	73	82	10	10	160	5	0.07	22.5	-	-
p	245	82	106	0	37.2		-	-	22	-	-
n	163	82	106	0	37.2		-	-	22	-	-
INSC	880	82	106	-	-	-	-	-	-	0.06	0.5

APPENDIX 1

Table A1.10 Parameters used at 180 MeV

Process	σ_I (mb)	L_{min}	L_{max}	R_{int} (fm)	C_{bin1} (MeV)	C_{bin2} (MeV)	ΔC_B (MeV)	kk'	C_B	cos (kk')	θ_{is}
CF	980	-	-	-	-	-	-	-	-	-	-
^8Be	900	53	73	15	50	105	5	0.07	9.02	-	-
^7Li	24	73	79	11	30	120	5	0.1	17.3	-	-
^6Li	52	73	79	11	30	120	5	0.1	17.3	-	-
^5Li	24	73	79	11	30	120	5	0.1	17.3	-	-
α	165	73	79	13	50	135	5	0.2	19	-	-
^3He	52	79	92	10	10	120	5	0.07	22.5	-	-
p	160	79	92	0	37.2		-		22	-	-
n	107	79	92	0	37.2		-		22	-	-
INSC	740	79	92	-	-	-	-	-	-	0.06	0.5

Table A1.11 Parameters used at 150 MeV

Process	σ_I (mb)	L_{min}	L_{max}	R_{int} (fm)	C_{bin1} (MeV)	C_{bin2} (MeV)	ΔC_B (MeV)	kk'	C_B	cos (kk')	θ_{is}
CF	1200	-	-	-	-	-	-	-	-	-	-
^8Be	910	53	71	15	50	105	5	0.07	9.02	-	-
^7Li	20	71	75	11	30	120	5	0.1	17.3	-	-
^6Li	40	71	75	11	30	120	5	0.1	17.3	-	-
^5Li	20	71	75	11	30	120	5	0.1	17.3	-	-
α	160	71	75	13	50	135	5	0.2	19	-	-
^3He	46	75	83	10	10	120	5	0.07	22.5	-	-
p	92	75	83	0	37.2		-	-	22		
n	61	75	83	0	37.2		-	-	22		
INSC	500	75	83	-	-	-	-	-	-	0.06	0.5

The switch I_{swspe} was set to 1 at incident energies of 150-400 MeV and set to 0 for incident energies below 150 MeV.

APPENDIX 1

Table A1.12 Parameters used at 130 MeV

Process	σ_I (mb)	L_{min}	L_{max}	R_{int} (fm)	C_{bin} (MeV)	C_B	E_{BU}	cos (kk')	θ_{is}
CF	1360	-	-	-	-	-	-	-	-
^8Be	730	53	66	15	30	21	1	-	-
^7Li	17	66	69	11	11.9	16	1	-	-
^6Li	30	66	69	11	11.9	16	1	-	-
^5Li	17	66	69	11	11.9	16	1	-	-
α	155	66	66	13	11.9	20.8	1	-	-
^3He	43	69	74	10	11.9	20.8	1	-	-
p	51	69	74	0	37.2	-	-	-	-
n	34	69	74	0	37.2	-	-	-	-
INSC	340	69	74	-	-	-	-	0.06	0.5

Table A1.13 Parameters used at 120 MeV

Process	σ_I (mb)	L_{min}	L_{max}	R_{int} (fm)	C_{bin} (MeV)	C_B	E_{BU}	cos (kk')	θ_{is}
CF	1480	-	-	-	-	-	-	-	-
^8Be	600	53	66	15	30	21	1	-	-
^7Li	16	66	69	11	11.9	16	1	-	-
^6Li	26	66	69	11	11.9	16	1	-	-
^5Li	16	66	69	11	11.9	16	1	-	-
α	152	66	66	13	11.9	20.8	1	-	-
^3He	40	69	74	10	11.9	20.8	1	-	-
INSC	250	69	74	-	-	-	-	0.06	0.5

APPENDIX 1

Table A1.14 Parameters used at 100 MeV

Process	σ_I (mb)	L_{min}	L_{max}	R_{int} (fm)	C_{bin} (MeV)	C_B	E_{BU}	cos (kk')	θ_{is}
CF	1800	-	-	-	-	-	-	-	-
^8Be	250	53	57	15	30	21	1	-	-
^7Li	13	57	60	11	11.9	16	1	-	-
^6Li	17	57	60	11	11.9	16	1	-	-
^5Li	13	57	60	11	11.9	16	1	-	-
α	143	57	60	13	11.9	20.8	1	-	-
^3He	35	57	60	10	11.9	20.8	1	-	-
INSC	110	60	61	-	-	-	-	0.06	0.5

Table A1.15 Parameters used at 80 MeV

Process	σ_I (mb)	L_{min}	L_{max}	R_{int} (fm)	C_{bin} (MeV)	C_B	E_{BU}	cos (kk')	θ_{is}
CF	1940	-	-	-	-	-	-	-	-
^8Be	25	49	50	15	30	21	1	-	-
α	133	50	52	13	11.9	20.8	1	-	-
^3He	28	50	52	10	11.9	20.8	1	-	-
INSC	25	52	53	-	-	-	-	0.06	0.5

As mentioned in section 3.3, at low projectile energies the reaction cross section is composed entirely by the complete fusion cross section. In this calculation this was true for incident energies below 80 MeV.

A1.16 Parameters for the CF at incident energies between 40 and 64 MeV.

E_{inc} (MeV)	σ_I (mb)
65	1414
50	805
45	513
40	135

A1.3.2 Input parameters for $^{16}\text{O} + ^{103}\text{Rh}$

In this case the total reaction cross section is composed of contributions from complete fusion (CF), incomplete fusion of ^{12}C , $^{11,10}\text{B}$, ^8Be , $^6,5\text{Li}$, deuteron (d), single-nucleon transfer of protons (p) and neutrons (n) as well as inelastic scattering (INSC). The projectile incident energies varied from 70 to 400 MeV.

Table A1.17 Common parameters used at all incident energies

Process	Spectator	Q_{REA} (MeV)	$BINDBU$ (MeV)	$IFUN$	V_0 (MeV)	hh, ff	$PROB$	E_{BU} (MeV)
CF	-	-9.093	-	-	-	-	-	-
^{12}C	α	-8.18	7.16	1	100	0	0	0
^{11}B	^5Li	-13.8	25.1	1	100	0	0	0
^{10}B	^6Li	-18.5	30.8	5	0.0	0	0	0
^8Be	^8Be	-9.31	14.6	1	100	0	0.4	2.36
^6Li	^{10}B	-16.3	30.8	5	0.0	0	0	0
^5Li	^{11}B	-12.2	25.1	1	100	0	0	0
α	^{12}C	-4.35	7.16	1	100	0	0.5	1.48
d	^{14}N	-7.21	20.7	1	200	0	0	0
p	^{15}N	-3.47	12.1	5	0.0	0	0	0
n	^{15}O	-8.84	15.6	5	0.0	0	0	0
INSC	-	-	-	-	-	-	-	-

APPENDIX 1

Table A1.18 Parameters used at 400 MeV

Process	σ_I (mb)	L_{min}	L_{max}	R_{int} (fm)	C_{bin1} (MeV)	C_{bin2} (MeV)	ΔC_B (MeV)	kk'	C_B	cos (kk')	θ_{is}
CF	490	-	-	-	-	-	-	-	-	-	-
^{12}C	600	59	88	13	70	300	5	0.02	11.3		
^{11}B	96	88	93	13	70	300	5	0.02	16.6	-	-
^{10}B	32	88	93	13	70	300	5	0.02	16.6	-	-
^8Be	7.5	93	98	13	70	300	5	0.02	21.7	-	-
^6Li	32	93	98	13	70	300	5	0.02	26.6	-	-
^5Li	96	93	98	13	70	300	5	0.02	26.6	-	-
α	350	98	123	11.5	45	320	5	0.02	35.3	-	-
d	66	98	123	12.1	40	300	5	0.02	50.4	-	-
p	220	98	123	9.2	56.4		-	-	50.4	-	-
n	110	98	123	0	56.4		-	-	52.5	-	-
INSC	1150	123	153	-	-	-	-	-	-	0.02	0.5

Table A1.19 Parameters used at 350 MeV

Process	σ_I (mb)	L_{min}	L_{max}	R_{int} (fm)	C_{bin1} (MeV)	C_{bin2} (MeV)	ΔC_B (MeV)	kk'	C_B	cos (kk')	θ_{is}
CF	590	-	-	-	-	-	-	-	-	-	-
^{12}C	460	60	81	13	66	250	5	0.02	11.3		
^{11}B	90	81	85	13	66	250	5	0.02	16.6	-	-
^{10}B	30	81	85	13	66	250	5	0.02	16.6	-	-
^8Be	9.5	85	90	13	66	250	5	0.02	21.7	-	-
^6Li	30	85	90	13	66	250	5	0.02	26.6	-	-
^5Li	90	85	90	13	66	250	5	0.02	26.6	-	-
α	240	90	109	11.5	45	270	5	0.02	35.3	-	-
d	66	90	109	12.1	35	270	5	0.02	50.4	-	-
p	195	90	109	9.2	51.8		-	-	46.4	-	-
n	100	90	109	0	51.8		-	-	51.8	-	-
INSC	1200	109	140	-	-	-	-	-	-	0.02	0.5

APPENDIX 1

Table A1.20 Parameters used at 300 MeV

Process	σ_I (mb)	L_{min}	L_{max}	R_{int} (fm)	C_{bin1} (MeV)	C_{bin2} (MeV)	ΔC_B (MeV)	kk'	C_B	cos (kk')	θ_{is}
CF	600	-	-	-	-	-	-	-	-	-	-
^{12}C	480	56	76	13	59	280	5	0.02	11.3		
^{11}B	81	76	80	13	59	280	5	0.02	16.6	-	-
^{10}B	27	76	80	13	59	280	5	0.02	16.6	-	-
^8Be	12	80	84	13	59	220	5	0.02	21.7	-	-
^6Li	27	80	84	13	59	220	5	0.02	26.6	-	-
^5Li	81	80	84	13	59	220	5	0.02	26.6	-	-
α	180	84	98	11.5	45	240	5	0.02	33.8	-	-
d	62	84	98	12.1	30	180	5	0.02	43.3	-	-
p	164	84	98	9.2	48.4		-	-	43.3	-	-
n	82	84	98	0	48.4		-	-	48.4	-	-
INSC	1300	98	129	-	-	-	-	-	-	0.02	0.5

Table A1.21 Parameters used at 250 MeV

Process	σ_I (mb)	L_{min}	L_{max}	R_{int} (fm)	C_{bin1} (MeV)	C_{bin2} (MeV)	ΔC_B (MeV)	kk'	C_B	cos (kk')	θ_{is}
CF	700	-	-	-	-	-	-	-	-	-	-
^{12}C	340	55	68	13	50	200	5	0.02	11.3		
^{11}B	57	55	70	13	50	200	5	0.02	16.6	-	-
^{10}B	19	68	70	13	50	180	5	0.02	16.6	-	-
^8Be	20	68	73	13	50	170	5	0.02	21.7	-	-
^6Li	19	68	73	13	50	170	5	0.02	26.6	-	-
^5Li	57	68	73	13	50	170	5	0.02	26.6	-	-
α	160	73	85	12	45	190	5	0.02	33.8	-	-
d	46	73	85	11.4	25	180	5	0.02	40.7	-	-
p	125	73	85	11.4	45.5		-	-	40.7	-	-
n	62.5	73	85	0	45.5		-	-	45.5	-	-
INSC	1350	85	115	-	-	-	-	-	-	0.02	0.5

APPENDIX 1

Table A1.22 Parameters used at 200 MeV

Process	σ_I (mb)	L_{min}	L_{max}	R_{int} (fm)	C_{bin1} (MeV)	C_{bin2} (MeV)	ΔC_B (MeV)	kk'	C_B	cos (kk')	θ_{is}
CF	850	-	-	-	-	-	-	-	-	-	-
^{12}C	340	55	65	13	40	150	5	0.032	11.3		
^{11}B	31	65	67	13	40	120	5	0.032	16.6	-	-
^{10}B	11	65	67	13	40	120	5	0.032	16.6	-	-
^8Be	55	67	69	13	40	120	5	0.032	21.7	-	-
^6Li	11	67	69	13	40	130	5	0.032	26.6	-	-
^5Li	31	67	69	13	40	130	5	0.032	26.6	-	-
α	190	69	77	12	37	150	5	0.032	33.8	-	-
d	24	69	77	12.1	20	130	5	0.032	38.3	-	-
p	750	69	77	12.1	42.8		-	-	38.3	-	-
n	37.5	69	77	0	42.8		-	-	42.8	-	-
INSC	1300	77	103	-	-	-	-	-	-	0.032	0.5

Table A1.23 Parameters used at 150 MeV

Process	σ_I (mb)	L_{min}	L_{max}	R_{int} (fm)	C_{bin1} (MeV)	C_{bin2} (MeV)	ΔC_B (MeV)	kk'	C_B	cos (kk')	θ_{is}
CF	1050	-	-	-	-	-	-	-	-	-	-
^{12}C	320	53	60	14	29	50	5	0.058	10.5		
^{11}B	10	53	60	14	29	50	5	0.058	15.4	-	-
^{10}B	3	53	60	14	29	50	5	0.058	15.4	-	-
^8Be	135	60	64	14	29	50	5	0.058	20.16	-	-
^6Li	3	60	64	14	29	50	5	0.058	24.7	-	-
^5Li	10	60	64	14	29	50	5	0.058	24.7	-	-
α	220	64	69	14	28	100	5	0.058	31.2	-	-
d	7	64	69	12.8	15	100	5	0.058	36.2	-	-
p	28	64	69	12.8	40.5		-	-	36.2	-	-
n	14	64	69	0	40.5		-	-	40.8	-	-
INSC	1000	69	103	-	-	-	-	-	-	0.058	0.5

APPENDIX 1

Table A1.24 Parameters used at 130 MeV

Process	σ_I (mb)	L_{min}	L_{max}	R_{int} (fm)	C_{bin1} (MeV)	C_{bin2} (MeV)	ΔC_B (MeV)	kk'	C_B	cos (kk')	θ_{is}
CF	1180	-	-	-	-	-	-	-	-	-	-
^{12}C	300	52	58	14	23	65	5	0.072	10.5	-	-
^{11}B	6	52	58	14	23	65	5	0.072	15.4	-	-
^{10}B	2	52	58	14	23	65	5	0.072	15.4	-	-
^8Be	120	58	61	14	23	60	5	0.072	20.16	-	-
^6Li	2	58	61	14	23	60	5	0.072	24.7	-	-
^5Li	6	58	61	14	23	60	5	0.072	24.7	-	-
α	180	61	65	13	25	80	5	0.072	31.2	-	-
d	4	61	65	12.8	12	95	5	0.072	34.9	-	-
p	14	61	65	12.8	39	-	-	-	34.9	-	-
n	7	61	65	0	39	-	-	-	39	-	-
INSC	780	65	78	-	-	-	-	-	-	0.072	0.5

Table A1.25 Parameters used at 120 MeV

Process	σ_I (mb)	L_{min}	L_{max}	R_{int} (fm)	C_{bin1} (MeV)	C_{bin2} (MeV)	ΔC_B (MeV)	kk'	C_B	cos (kk')	θ_{is}
CF	1230	-	-	-	-	-	-	-	-	-	-
^{12}C	240	51	56	14	21	50	5	0.081	10.5	-	-
^{11}B	4	51	56	14	21	50	5	0.081	15.4	-	-
^{10}B	2	51	56	14	21	50	5	0.081	15.4	-	-
^8Be	82	56	57	14	21	50	5	0.081	20.16	-	-
^6Li	2	56	57	14	21	50	5	0.081	24.7	-	-
^5Li	4	56	57	14	21	50	5	0.081	24.7	-	-
α	1250	57	65	13	23	70	5	0.081	31.2	-	-
D	2	57	65	13.3	12	80	5	0.081	34.9	-	-
P	9.5	57	65	13.3	39	-	-	-	34.9	-	-
N	4.7	57	65	0	39	-	-	-	39	-	-
INSC	650	65	78	-	-	-	-	-	-	0.081	0.5

APPENDIX 1

Table A1.26 Parameters used at 110 MeV

Process	σ_I (mb)	L_{min}	L_{max}	R_{int} (fm)	C_{bin1} (MeV)	C_{bin2} (MeV)	ΔC_B (MeV)	kk'	C_B	cos (kk')	θ_{is}
CF	1280	-	-	-	-	-	-	-	-	-	-
^{12}C	180	50	53	14	18	45	5	0.09	10.5		
^8Be	55	53	54	14	18	45	5	0.09	20.1	-	-
α	85	54	56	13	21	60	5	0.09	31.2	-	-
INSC	600	56	63	-	-	-	-	-	-	0.09	0.5

Table A1.27 Parameters used at 100 MeV

Process	σ_I (mb)	L_{min}	L_{max}	R_{int} (fm)	C_{bin1} (MeV)	C_{bin2} (MeV)	ΔC_B (MeV)	kk'	C_B	cos (kk')	θ_{is}
CF	1200	-	-	-	-	-	-	-	-	-	-
^{12}C	130	46	49	14	16	35	5	0.1	10.5		
^8Be	34	46	49	14	16	35	5	0.1	20.1	-	-
α	55	46	49	13	19	50	5	0.1	31.2	-	-
INSC	510	496	58	-	-	-	-	-	-	0.1	0.5

Table A1.28 Parameters used at 90 MeV

Process	σ_I (mb)	L_{min}	L_{max}	R_{int} (fm)	C_{bin1} (MeV)	C_{bin2} (MeV)	ΔC_B (MeV)	kk'	C_B	cos (kk')	θ_{is}
CF	1100	-	-	-	-	-	-	-	-	-	-
^{12}C	80	41	43	14	13	13	5	0.122	10.5		
^8Be	19	41	43	14	16	50	5	0.122	20.1	-	-
α	36	41	43	13	18	40	5	0.122	31.2	-	-
INSC	290	43	49	-	-	-	-	-	-	0.122	0.5

APPENDIX 1

Table A1.29 Parameters at 70 MeV with $Inopre = 1$

Process	σ_I (mb)	L_{min}	L_{max}	R_{int} (fm)	C_{bin1} (MeV)	C_{bin2} (MeV)	ΔC_B (MeV)	kk'	C_B	cos (kk')	θ_{is}
CF	575	-	-	-	-	-	-	-	-	-	-
^{12}C	26	25	26	14	7	40	5	0.125	10.5	-	-
^8Be	4.5	25	26	14	7	30	5	0.125	20.1	-	-
α	10	25	26	13	15	40	5	0.125	31.2	-	-
INSC	260	25	32	-	-	-	-	-	-	0.125	0.5

Table A1.30 Parameters at 60 MeV with $Inopre = 1$

Process	σ_I (mb)	L_{min}	L_{max}	R_{int} (fm)	C_{bin1} (MeV)	C_{bin2} (MeV)	ΔC_B (MeV)	kk'	C_B	cos (kk')	θ_{is}
CF	380	-	-	-	-	-	-	-	-	-	-
INSC	200	196	24	-	-	-	-	-	-	0.155	0.5

APPENDIX 2

ALTERNATIVE RADIOCHEMICAL PROCEDURES INVESTIGATED IN THIS STUDY

A2.1 Overview

In addition to the procedure described in Chapter 4, five alternative routes for the radiochemical separations were also investigated. The final choice between the six methods investigated was strongly influenced by the time constraint imposed by the short half-life of $^{103\text{m}}\text{Rh}$ and that a rapid method was therefore required. All the methods have their advantages and disadvantages. This appendix describe the alternative methods and present the results obtained with these methods. For completeness, a summary of an extensive literature survey is also included.

A2.2 Literature survey

Solvent extraction methods

Most of the reported papers on the production of ^{103}Pd in the bombardment of Rh targets make use of solvent extraction techniques for the separation and purification thereof. A method based on the extraction of Pd with α -furyldioxime into chloroform from acidic solutions was developed by Tarapčik *et al.* [Tar81]. This method is suitable for the separation of Pd with high yields from large quantities of Rh target material and also for the preparation of carrier-free ^{103}Pd . It employs several extractions, back extraction, evaporation and mineralization methods and is very tedious. In the same work, dimethylglyoxime (DMG) complexation has also been utilized for the extraction of Pd into chloroform. The low yield obtained with this method, however, could probably be due to a large quantity of Rh forming water-soluble complexes with the DMG. According to Lagunas-Solar *et al.* [Lag84], DMG can be used to produce carrier-free ^{103}Pd from Rh targets. DMG-chloroform was also successfully utilized by Levin *et al.* [Lev71] to separate Pd from Rh, Ru and Tc in a hydrochloric-sulphuric acid system ($\text{HCl-H}_2\text{SO}_4$). Meanwhile, Robert *et al.* [Rob89] used DMG for the separation (or purification) of Pd from trace amounts of noble and base metals.

Solvent extraction studies of Pd with tributylphosphate (TBP) from hydrobromic acid (HBr) solutions were performed for the separation of Pd from platinum (Pt) metals and some base metals [Pat74]. An average recovery of more than 99% is reported. Pd, together with Rh and traces of base metal were extracted into 10 ml TBP from a 3 M HBr solution. Palladium was then stripped from the organic phase with 2% ammonia solution (NH₃). The amounts of Pd, Rh and base metal present in the process were 210 µg, 5 mg and 2 mg, respectively.

O-phenantroline as an extracting solvent, was employed by Kumar *et al.* [Cha90] for micro-separation of Pd from Rh and some other metal ions into chloroform. To recover the metal ions from the solvent, combined organic layers were extracted thrice with equal volumes of 25% NH₃ containing 1-2 ml 30% H₂O₂. The method was reported to be very selective for the separation of Pd (40-1000 µg) in the presence of Rh and other ions not exceeding 1 mg.

Rapid and effective separation and determination of Pd in the presence of large amounts of Rh by extraction with dibenzylidithiooxamide (D₅DO) in chloroform has also been reported [Bur81].

Ion exchange methods

Separations of Pt group elements including Pd, Rh and Ru by means of ion exchange resins are carried out routinely for the determination of these metals in geological samples, industrial products and synthetic mixtures containing many other elements. Anion exchange resin in HCl systems can be effectively used to separate the Pt metals, not only from practically all other elements, but also from one another. Such separations on anion exchange resins are more versatile than those effected by the use of cation exchangers of the sulphonic acid type. The latter, however, can be employed for the very effective isolation of the Pt metals, as a group in very dilute HCl media [Kor89]. It is evident that the Pt metals show only very weak or negligible sorption on strongly acidic cation exchange resins from 0.1 to 3 M HCl solutions [Kor89, Str69]. In these previous studies, Pt metals were reported to be predominantly present as anionic chloro-complexes in the HCl solutions.

The behaviour of Pd(II) and other Pt metals on cationic exchangers was investigated by Paria *et al.* [Par76]. In that case they used Dowex 50W-X8 and investigated several eluting agents. Rh and other metals are not retained by this cation resin while Pd and base metals are

adsorbed. An average recovery of 99% Pd was reported when using 4 M ammonium acetate or 0.4 M HCl as eluting agents, however the media in which the sorption occurred was not mentioned.

A decade ago, Lingen *et al.* [Lin92] developed a two-step ion exchange method for the separation of base metals from Pt metals followed by the separation of Rh from the rest of the Pt metals. This method was used for the recovery of Rh from Ni minerals and employs a sodium chloride (NaCl) solution. The distribution coefficients of the elements in different concentrations of NaCl at different pH values were also presented.

In HCl systems, most of the Pt group metals are present as stable anionic chloro-complexes and are retained by strong base anion exchange resins. The high selectivity shown by strongly basic anion exchange resins towards anionic chloro-complexes of Pd and Rh represents a favourable condition for their separation from associated base metals and many other elements. The most undesirable feature common to all methods utilizing the sorption principle, however, is that the elution of the Pt metals is complicated and not always complete. Incomplete recovery may also be the result of reduction of the metal ions to lower oxidation states or to the non-ionic metallic states while in contact with resin. In addition, ion exchange separations are also affected by the manner in which the individual elements are dissolved and complications may also arise due to differences in behaviour between fresh and aged solutions caused by partial hydrolysis of the chloro-complexes, especially in the case of Rh. All these negative effects may impact on the elution of Pt metals. In these cases, only approximate distribution data are usually available [Kor89]. As is the usually the case, these approximate data served as a guideline to the interpretation and explanation of the procedures presented in this particular investigation.

In a study of the separation of Pd from Rh, Pt and other base metals conducted by Gaita *et al.* [Gai95], three ion exchange resins viz. Amberlite IRA-68, IRA-93 and Amberlite IRA-400 in their chloride forms were used and compared to each other. IRA-68 and IRA-93 are both weakly basic anion exchangers, whereas IRA-400 is strongly basic. It is reported in that study that Pd could be completely recovered from a 4 M HCl solution containing 10 ml of a synthetic mixture of 250 parts per million (ppm = mg/l) of each metal, by elution with different concentrations of NH₃. Amberlite IRA-93 exhibited more favourable results in the elution of Pd.

A2.3 Experimental

A2.3.1 Method 1: Cationic exchange resins in hydrobromic acid-thiourea media

Reagents and equipment

All chemicals were of analytical grade and water was obtained from a Milli-Q system with 18 M Ω /cm resistance. AG 50-X4 resin was supplied by Bio-Rad Laboratories (Richmond, California).

Two inductively-coupled plasma optical emission spectroscopy (ICP-OES) instruments, namely a Varian P400 and a Jobin Vyon model Ultima were used for the distribution coefficient measurements. The most sensitive emission lines of the elements were selected, i.e. 340.458 nm and 343.489 nm for Pd and Rh, respectively. The other elements do not have any emission lines around the region of Pd, i.e. 340.419 – 340.497 nm.

The radioactivity induced in the targets was measured with well-calibrated HPGe detectors described in Chapter 4.

Separation procedure

A 5 cm x 1 cm column was packed with AG 50-X4 resin, H⁺ form, 200-400 mesh size. It was preconditioned with 25 ml of 0.5M hydrobromic acid (HBr) – 0.1M thiourea (Tu = CS(NH₂)₂) solution. The flow rate was set to 2 ml/minute. The solution containing quantities of 10 mg of Rh and ~10 μ g Pd (dissolved in 6 M HCl) was evaporated to dryness, cooled down and then dissolved in 25 ml of 0.5 M HBr – 0.1 M Tu solution. It was then passed through the column, which retained the Rh and Pd. The column was then washed with another 25 ml of 0.5 M HBr – 0.1 M Tu solution to elute the Rh. Thereafter the column was washed with 25 ml of distilled water to remove the acid-Tu solution. The Pd was eluted with 25 ml of 7 M HCl. ICP-OES was used for the measurement of Pd and Rh in the final samples.

Results and discussion

Palladium is strongly sorbed on strongly acidic cation exchangers such as Dowex 50 if the dilute HCl or HBr media containing thiourea in molar concentrations of 0.1 or 0.2 is used. On the other hand, Rh is less sorbed on the cationic resins under the same conditions. The distribution coefficients of Pd and Rh in concentration of 0.5 M HCl – 0.1 M Tu are >1000 and ~50, respectively [Kor89]. It is reported that this is mainly due to the fact that Tu forms

moderately stable complexes with all Pt group metals, include Rh(III) and Pd(II). Any subsequent exchange of ligands that may occur and/or the formation of the Tu complexes take place at rates that vary considerably. Although the rate of formation of Tu complexes with Pd is very rapid, it is not so in the case of Rh(III), [Kor89, Ple97]. The fact that the chloro-complexes of Pd are stronger retained than the bromo-complexes was exploited for this separation, hence the investigation of the 0.5 M HCl – 0.1 M Tu medium. Radioactive ^{100}Pd (obtained in the bombardment of $^{\text{nat}}\text{Ag}$ with 66 MeV protons) was used as a tracer. From the elution of Pd with 7 M HCl, a recovery of $92.8 \pm 5.6\%$ of Pd was obtained. Traces of Rh were present in the final solution, however, it was less than 2%.

The advantage of this method was that one single column could be used to separate Pd while at the same time recovering Rh as well. The recovered Rh was be re-used. The disadvantages of this procedure were the small amounts of sulphur contained in thiourea as well as in other additional sulphur complexes which formed during the process, and an impervious sulphur layer which formed at the top of the resin column. The traces of sulphur may or may not have a significant effect on the quality of the final ^{103}Pd (or $^{103\text{m}}\text{Rh}$, for that matter). However, this has not yet been investigated. The formation of the sulphur layer was also found to impede on the flow rate of the eluent, a disadvantage for a rapid radiochemical procedure.

A2.3.2 Method 2: Macroporous cation exchange resin in HCl media

Reagents and chemicals

A macroporous sulphonated polystyrene cation resin AG MP-50 (H^+ form and 200-400 mesh size) supplied by Bio-Rad Laboratories (Richmond, California) was used. All the chemicals used were of analytical grade.

Separation procedure

A 10 cm x 1 cm column was packed with the AG MP-50 resin and preconditioned with 25 ml 0.02 M HCl. A sample containing 100 μg of Pd and 10 mg of Rh (dissolved in 6 M HCl) was used. A radioactive ^{100}Pd tracer was added to the sample for γ -spectroscopy measurements. The sample was evaporated to dryness and then dissolved in 0.02 M HCl. The solution was passed down the column at a flow rate of 2 ml/minute. For the elution of Rh, 25 ml of 0.02 M HCl were used. The column was then rinsed with 25 ml of distilled water. This was followed by the elution of Pd with 50 ml of 7 M HCl. In order to calculate the recovery of

Pd, a sample was taken at every step of the separation and measured by means of γ -ray spectroscopy. The amount of Rh present in the final solution was measured by means of the ICP-OES technique.

Results and discussion

It was found that when a synthetic solution containing micrograms of Pd and milligrams of Rh was used, even in 0.02 M HCl, only about 60% of the Pd was adsorbed by the resin whereas Rh was not retained at all. However, the practical separation compared to the published data [Buc63] shows some differences, also in the methods used. For instance, in that publication a batch method was used while in this work we used a column instead. They reported a 90% recovery of Pd, which is much more than we could obtain. Consequently, this method was discarded on the grounds that it was unsuitable for the separation of Rh and the separation efficiency for Pd was too low.

A2.3.3 Method 3: Weakly basic anion exchange resin in 6 M HCl medium

Reagents and equipment

Palladium was used in its nitrate form, Pd(NO₃)₂, and Rh was used in its chloride form, RhCl₃. A stock solution was made up in 6 M HCl.

Amberlite IRA-93 is a micro-reticular polyamine functionality polystyrene (free base, 20-50 mesh size) resin. It was supplied by Sigma-Aldrich Pty Ltd. The resin was packed into a large column of 20 cm x 3 cm dimensions. It was then converted to a chloride form by rinsing it with 200 ml of 4 M HCl followed by de-ionized water. The water was also obtained from the Milli-Q purifying system described above.

Separation

Several experiments were performed at different flow rates: 1, 2 and 3 ml/minute. Three experiments were performed at a flow rate of 3.0 ml/minute, seven at 2.0 ml/minute and three experiments at 1.0 ml/minute. The solution, containing 500 μ g of Pd and 10 mg Rh, was pumped through the column whereafter the Rh was eluted completely from the resin with 25 ml of 6 M HCl. The column was then rinsed with 30 ml of distilled water to remove the acid. The Pd was subsequently eluted with 50 ml of 5% ammonium solution (NH₄). The excess ammonia of the Pd eluate was gently evaporated and the acidity adjusted by the addition of water to obtain a 0.1 M HCl solution (a suitable concentration for measurement). The

concentrations of elements in the aqueous and resin phases were determined by means of the ICP-OES technique.

Results and discussion

The average recovery of Pd was $78.3 \pm 3\%$ with a flow rate of 3.0 ml/minute, $86.0 \pm 5\%$ at 2.0 ml/minute and $94.7 \pm 1\%$ at 1.0 ml/minute. The amount of Rh in the final solution was less than the detection limit of the ICP instrument (Varian P400). The recovery of Pd in these experiments was somewhat less than the 100% previously reported by Gaita *et al.* [Gai95]. This can only be attributed to the length of the column used and the lower quantity of Pd used in this present work.

The experiment was repeated with a sample solution containing 10 μg of natural Pd and radioactive ^{100}Pd as tracer. The recovery obtained was less – about 20% less, even when the volume of the eluent (5% NH_3) was increased from 50 ml to 200 ml. It was then decided to rather pursue other avenues of investigation.

A2.3.4 Method 4: Strongly basic anion exchanger in nitric acid media

Reagents and equipment

The same as in the above case, except that AG 1-X8, Cl^- form 100-200 mesh size resin was used and 3 M HNO_3 solution instead of 6 M HCl . The resin was purchased from Bio-Rad Laboratories (Richmond, California). The targets were prepared from $\text{RhCl}_3 \cdot x(\text{H}_2\text{O})$ salt supplied by Strem Chemicals (Newburyport, MA, USA).

Separation

A 12 cm x 0.8 cm column was packed with the resin, which was converted to the nitrate form by passing 3 M HNO_3 through the column until the eluent contained no chloride. The resin was finally equilibrated with 50 ml of 3 M HNO_3 . The target solution was prepared in the following way: A quantity of 280 mg of cold $\text{RhCl}_3 \cdot x(\text{H}_2\text{O})$ target material was first dissolved in 1 M NaOH while heating the solution gently. A pale yellow hydrate Rh(III) oxide, $\text{Rh}_2\text{O}_3 \cdot x(\text{H}_2\text{O})$ [Bur81] was formed. To this, 15 ml of 3 M HNO_3 were added in order to dissolve the precipitate. Thereafter, 1 mg of Pd was added to the solution and mixed by stirring while heating for a few seconds. The solution was then pumped through the column at a flow rate of 1.8 ml/minute. Rh was eluted with 50 ml of 3 M HNO_3 . The Pd was then

eluted with 50 ml of de-ionized water followed by 100 ml 5% NH₃ solution. Excess NH₃ was gently evaporated to dryness the residue dissolved in 50 ml of 0.1 M HCl.

Results and discussion

Direct dissolution of the Rh chloride target with nitric acid was avoided because the chloro complexes of Rh are very stable and inert [Ple97]. Therefore, the Rh had to be converted to aqua complexes prior to being treated with HNO₃. A qualitative retention of Pd was achieved, however, the recovery of Pd was found to be only $67.3 \pm 11.9\%$ on elution. The concentration of Rh in the final solution was 2.8 ± 1.6 ppm. From the low recovery we could deduce that the elution was incomplete. In addition, the high spread in recovery yields showed that the method was not reproducible and also unreliable. This method was therefore discarded.

A2.3.5 Method 5: Strongly basic anion exchanger in 6 M HCl medium

Reagents and equipment

The same as in the above case, except that 6 M HCl was used to prepare the target solution. The γ -ray spectroscopy measurements were made in the same way as described in Chapter 4.

Separation

A column (5 cm x 1 cm) was packed with resin and then preconditioned with 25 ml of 6 M HCl. The flow rate of the peristaltic pump was set to 1.7 –1.8 ml/minute. The target, 140 mg (79 mg/cm² thickness and 15 mm diameter) disc-shaped RhCl₃·x(H₂O), was first bombarded with 66 MeV protons for one hour and then dissolved in 20 ml of hot 6 M HCl immediately after bombardment. The solution was cooled down to room temperature and then filtered using a 0.45 μ Millipore filter to remove any undissolved material (e.g. Rh oxide). (This step was included as a precaution even though no visible residues were observed.) A 1 ml sample was transferred to a vial and taken for measurement with a γ -ray detector to check the radioactivity induced in the target before separation. The rest of the filtrate was pumped through the column from the top to the bottom. The Rh was eluted with 35 ml of 6 M HCl followed by 25 ml of de-ionized water to remove the acid. Another 1 ml sample was taken to measure the amount of Rh eluted from the column. The Pd was eluted with 50 ml of a 5% NH₃ solution. A 1 ml sample was again taken for measurement with the γ -ray detector.

In addition to the γ -ray spectra taken, ICP-OES measurements with the Perkin-Elmer P400 were performed to determine the concentrations of non-radioactive elements in the various solutions.

Results and discussion

Pd(II) is retained by strongly basic anionic resins in hydrochloric acid media having concentrations ranging from 0.1 to 12M. However, the species that was predominantly retained in our work was a dark-red band of $[\text{PdCl}_6]^{4-}$ which, according to Korkish [Kor89] also predominates in concentrations of 2-12 M HCl. However, in concentrations between 0.5 and 2 M HCl, $[\text{PdCl}_6]^{2-}$ will also exist. The sorption of Pd compared to that of Rh in AG 1-X8 is higher by about 2 orders of magnitude and it decreases with increasing concentration of HCl. Nevertheless, the distribution coefficients of Pd(II) in 0.1-12 M HCl are sufficiently high in order to allow this element to be separated from Rh [Kor89]. For the elution of Rh, 6 M HCl and for the sorption of Pd as $[\text{PdCl}_6]^{4-}$, 12 M HCl can be used provided the distribution coefficient of Pd is low enough to facilitate the elution. The elution can also be effective by using 1M NH_3 [Kor89].

Considering the element behavior on anion resins, AG 1-X8 with 6 M HCl solution was expected to be a good choice for this separation. The method was first tested repeatedly using natural elements of Rh and Pd. Following the bombardments, in addition to ^{103}Pd (20.1 and 22.8 keV photo-peaks) another palladium isotope, ^{100}Pd (126 keV), rhodium isotopes, $^{101\text{m}}\text{Rh}$ (306.9 keV), $^{99\text{m}}\text{Rh}$ (340 keV) and $^{99\text{g}}\text{Rh}$ (527.7 keV), a ruthenium isotope, ^{97}Ru (215 keV) and technetium isotopes, $^{95\text{g}}\text{Tc}$ (765 keV) and $^{96\text{g}}\text{Tc}$ (778 keV), were identified in the target before separation. After separation, i.e. after the elution of Rh, isotopes of Pd and Tc were quantitatively retained by the resin while 99.8% Rh together with Ru isotopes were successfully eluted with 6 M HCl. The recovery of 92% Pd was achieved by elution with 25ml de-ionized water and 50 ml of 5% NH_3 . The time taken from the end of bombardment to the end of elution of Rh from the column was less than 40 minutes.

This experiment was repeated several times and in all those cases an average of 90% recovery for Pd and 99% for Rh were achieved. There was no trace of Pd in the Rh elute. In the eluate of Pd, however, there was ~ 1.6 ppm (0.02%) of Rh and minute traces of Tc impurities. This method was found to be good enough for the separation of Rh and Pd and would also have been a good candidate for the radiochemistry of this study. The method adopted, however, is considered to be marginally better (see Chapter 4).

APPENDIX 3

BEAM CURRENT INTEGRATION TESTS

A3.1 Overview

The experimental setup was designed for irradiating small samples with a well-defined but partially defocused beam. The beam spot should not be too small as this has resulted in damage to the irradiated specimens in a previous experiment. The use of a defining collimator ensures a repeatable beam spot size. Typically, the beam would be tuned for 50% transmission through the collimator. There was, however, some concern that the electron suppression (see Chapter 4) might not be sufficient and also that conductive losses of accumulated charge via the cooling-water lines may occur. A number of test irradiations were therefore performed to establish the integrity of the current integration measurement.

A3.2 Test irradiations

Six test irradiations under different beam and water cooling conditions were performed. In each test a Ti foil was irradiated for 30 minutes at a nominal ^{12}C beam current of 30 nA and the production rate of the induced ^{48}V ($T_{1/2} = 15.97$ d) accurately measured. Three different ratios of the beam-on-target and beam-on-collimator currents were investigated, with and without cooling water to the target holder. The results are shown in Table A3.1. The spread in measured productions rates is smaller than 5%. We were thus reassured that the beam current integration was not seriously affected by the presence of the collimator or by the cooling water.

Table A3.1 Production rates of ^{48}V induced in test irradiations of Ti monitor foils

Test no.	Water cooling conditions	Beam current (nA)		Production rate (Bq/particle-nC) $\times 10^{-2}$
		Target	Collimator	
1	With	25	5	3.52 ± 0.007
2	Without	25	5	3.37 ± 0.028
3	Without	30	<1	3.36 ± 0.031
4	With	30	<1	3.43 ± 0.014
5	With	15	15	3.52 ± 0.015
6	Without	15	15	3.40 ± 0.019

APPENDIX 4

DETERMINATION OF PRODUCTION CROSS SECTIONS FROM ACTIVATION DATA — CONSTANT BEAM INTENSITY

A4.1 Overview

In this appendix, an equation for the production cross section of an individual radionuclide utilizing the activation data obtained from a thin irradiated target specimen (such as a typical foil in a foil stack) is derived. This equation is applicable in activation studies performed with a constant beam intensity for those radionuclides which are directly produced. It may sometimes be appropriate (i.e. a good approximation) in cases where a particular radionuclide is produced directly as well as indirectly via the decay of short-lived precursors. It may also be used with good accuracy in cases where the half-life of a particular radionuclide is long compared to the bombardment time during which the beam intensity did not stay constant. Corrections for beam fluctuations will be treated in a subsequent appendix. It is assumed that at the time when the measurements of the induced activities are performed, all precursors have already decayed completely.

A4.2 Definitions and times

The activity of a radionuclide produced with cross section σ and half-life $T_{1/2}$ at a time equal to the mean value T_m of a measurement period is given by

$$-\left. \frac{dN(t)}{dt} \right|_{t=T_m} = \lambda N(T_m) = \lambda I_t \sigma N_0 f(t) = \frac{A_p}{\tau \varepsilon_\gamma \varepsilon_e}, \quad (\text{A4.1})$$

where

$N(t)$ - total number of nuclei of the produced radionuclide at time t ,

λ - decay constant = $\ln(2)/T_{1/2}$,

I_t - total number of incident beam particles,

σ - production cross section,

N_0 - total number of target nuclei per unit area,

$f(t)$ - a quantity representing the time dependence of radioactive decay,

τ - live counting time,

APPENDIX 4

ε_γ - branching ratio of a specific γ line,

ε_e - efficiency of the detector,

A_p - photo-peak area.

The total number of incident beam particles is given by

$$I_t = \frac{Q \times 10^{-9}}{q_e \times m}, \quad (\text{A4.2})$$

where

Q - total integrated charge on target (in units of nC),

q_e - electron charge (1.602177×10^{-19} C),

m - charge state of the incident beam.

The total number of target nuclei per unit area is given by

$$N_0 = \frac{dx N_A}{A_T}, \quad (\text{A4.3})$$

where

dx - a real thickness of the target sample (in units of g/cm^2),

N_A - Avogadro's number (6.022136×10^{23} mole^{-1}),

A_T - atomic mass of the target material (g/mole).

It is convenient to define the following relevant times:

$t = 0$ start of bombardment,

$t = T_1$ end of bombardment (EOB),

$t = T_2$ start of counting period,

$t = T_3$ end of counting period.

Thus, the decay time between the EOB and the start of counting is $(T_2 - T_1)$ and the counting period is given by $(T_3 - T_2)$. Since the counting period is also defined as the sum of the live time (τ) and dead time ($\Delta\tau$) of the counting system, the following relation holds:

$$T_3 - T_2 = \tau + \Delta\tau. \quad (\text{A4.4})$$

A4.3 Activity built-up during bombardment

For the sake of the mathematics, it is convenient to divide the irradiation time into n small increments of duration Δt . Thus

$$\Delta t = \frac{T_1}{n}.$$

The activity produced in each small incremental period is therefore given by

$$\Delta R = \frac{\lambda I_t \sigma N_0}{n} = \frac{\lambda I_t \sigma N_0 \Delta t}{T_1}.$$

The value of Δt can be chosen sufficiently small so that radioactive decay losses during such a time increment can be neglected. Due to the radioactive decay (Hel83), this activity projected to EOB is given by

$$\Delta A_i = \Delta R \exp(-\lambda(T_1 - i\Delta t)) \quad \text{for } 1 \leq i \leq n.$$

The total activity produced at EOB is therefore obtained by summing or integrating the above equation

$$\begin{aligned} A_{EOB} &= A(T_1) = \lim_{n \rightarrow \infty} \sum_{i=1}^n \Delta A_i \\ &= \frac{\lambda I_t \sigma N_0}{T_1} \lim_{n \rightarrow \infty} \sum_{i=1}^n \exp(-\lambda(T_1 - i\Delta t)) \Delta t \\ &= \frac{\lambda I_t \sigma N_0}{T_1} \int_0^{T_1} \exp(-\lambda(T_1 - t)) dt \\ &= \frac{\lambda I_t \sigma N_0}{T_1} \left[\frac{\exp(-\lambda(T_1 - t))}{\lambda} \right]_0^{T_1} \\ &= \frac{I_t \sigma N_0}{T_1} [1 - \exp(-\lambda T_1)]. \end{aligned} \tag{A4.5}$$

A4.4 Decay before and during the counting period

Firstly, the decay between the EOB and the start of counting period T_2 is given by

$$A(T_2) = A(T_1) \exp(-\lambda(T_2 - T_1)). \tag{A4.6}$$

To compensate for the fact that in some cases it may happen that the half-life of a radionuclide will be comparable to the duration of the counting period, a mean time T_m is

defined. According to the mean value theorem, the time T_m is defined as a point in the counting time interval (T_2 to T_3) where the actual activity equals the average activity over the entire interval. Thus

$$\begin{aligned} A(T_2) \exp(-\lambda T_m) &= \frac{1}{(T_3 - T_2)} \int_{T_2}^{T_3} A(t) dt \\ &= \frac{1}{(T_3 - T_2)} A(T_2) \int_{T_2}^{T_3} \exp(-\lambda t) dt. \end{aligned} \quad (\text{A4.7})$$

By integrating Eq. (A4.7) and rearranging, the expression for T_m is easily found:

$$T_m = -\frac{1}{\lambda} \ln \left[\frac{\exp(-\lambda(T_3 - T_2))}{-\lambda(T_3 - T_2)} \right]. \quad (\text{A4.8})$$

Also, the activity at the mean value T_m is given by

$$A(T_m) = A(T_2) \exp(-\lambda(T_m - T_2)). \quad (\text{A4.9})$$

A4.5 The cross-section expression

Substitution of Eqs. (A4.5 and (A4.7) into (A4.9) yields:

$$A(T_m) = \frac{I_t \sigma N_0}{T_1} [1 - \exp(-\lambda T_1)] \exp(-\lambda(T_m - T_1)) = \frac{A_p}{\tau \varepsilon_\gamma \varepsilon_e}. \quad (\text{A4.10})$$

It is convenient to let all times be in seconds and N_0 be the number of target nuclei per cm^2 . By rearranging Eq. (A4.10) and taking into consideration that $1 \text{ mb} = 1 \times 10^{-27} \text{ cm}^2$, the expression of the cross section is finally obtained:

$$\sigma(\text{mb}) = \frac{A_p T_1}{\tau \varepsilon_\gamma \varepsilon_e I_t N_0 \exp(-\lambda(T_m - T_1)) [1 - \exp(-\lambda T_1)] (1 \times 10^{-27})}. \quad (\text{A4.11})$$

APPENDIX 5

DETERMINATION OF PRODUCTION CROSS SECTIONS FROM ACTIVATION DATA — FLUCTUATING BEAM INTENSITY

A5.1 Overview

Beam intensity fluctuations may significantly affect measured results in cases where the radionuclides have half-lives shorter than or comparable to the bombardment period. It is also impossible to guarantee a constant beam intensity during the full duration of an experimental bombardment. A good approach is therefore to log the current integrator readings at sufficiently small time intervals during the bombardment. In this work the accumulated charge was logged every 10s, which is a much smaller increment of time than the half-life of the shortest-lived radionuclide which we extracted. In this appendix, an expression is derived which utilizes these current integrator readings to correct for beam intensity fluctuations.

A5.2 Derivation of an expression for the cross section

As in Appendix 4, it is convenient to consider time $t = 0$ as the start of the bombardment. The following quantities and variables can then be defined:

- $t = 0$ - start of bombardment,
- ΔT - time increment of current integrator scaler (10 seconds),
- n - total number of 10 second time increments during the bombardment period,
- $t = n\Delta T$ - end of bombardment (EOB).

The end of each time interval is given by

$$h_i = i\Delta T \quad \text{for } 1 \leq i \leq n. \quad (\text{A5.1})$$

For those radionuclides having half-lives which are much longer than 10 seconds, the activity produced in an incremental time interval is given by

$$\Delta A_i^0 = \lambda N_0 i \sigma \Delta I_i \quad \text{for } 1 \leq i \leq n, \quad (\text{A5.2})$$

where λ , N_0 and σ have the same meanings as before (see Appendix 4) and ΔI_i is the total number of incident beam particles on the target in the i^{th} time increment.

APPENDIX 5

This number is given by

$$\Delta I_i = \frac{\Delta Q_i \times 10^{-9}}{q_e \times m}, \quad (\text{A5.3})$$

where ΔQ_i is the charge (in units of nC) accumulated in the i^{th} time increment (the values of which have been recorded with the XSYS data acquisition system during the bombardments), while q_e and m are the electron charge and charge state of the beam, respectively. Therefore, I_t is given by

$$I_t = \sum_{i=1}^n \Delta I_i \quad (\text{A5.4})$$

If we define any time after EOB as a convenient reference time, T_{ref} , the incremental activity at this time will be given by

$$\Delta A_i(T_{ref}) = \Delta A_i^0 \exp(-\lambda(T_{ref} - h_i)) \quad (\text{A5.5})$$

By substituting Eqs. (A5.1) through (A5.3) into (A5.4) and summing over all i , the total activity at $t = T_{ref}$ is given by

$$\begin{aligned} A(T_{ref}) &= \sum_{i=1}^n \Delta A_i(T_{ref}) \\ &= \lambda N_0 \sigma \sum_{i=1}^n \Delta I_i \exp(-\lambda(T_{ref} - h_i)). \end{aligned} \quad (\text{A5.6})$$

By choosing the reference time to be the mean value of the counting interval and substituting Eq. (A4.1) into Eq. (A5.5), the total activity at $t = T_{ref}$ is given by

$$A(T_m) = \lambda N_0 \sigma \sum_{i=1}^n \Delta I_i \exp(-\lambda(T_m - h_i)) = \frac{A_p}{\tau \varepsilon_\lambda \varepsilon_e}, \quad (\text{A5.7})$$

where A_p , ε_λ and ε_e are the photo-peak area, γ -ray branching ratio and detector efficiency, respectively, as defined in Appendix 4. By rearranging Eq. (A5.6) and adopting units of seconds and cm^2 (see also Appendix 4), the expression for the cross section is finally obtained:

$$\sigma(\text{mb}) = \frac{A_p}{\tau \varepsilon_\gamma \varepsilon_e N_0 (1 \times 10^{-27}) \sum_{i=1}^n \Delta I_i \exp(-\lambda(T_m - h_i))}. \quad (\text{A5.8})$$

A5.3 The correction factor

Equations (A4.11) and (A5.7) have been derived for the cross section, the latter being more general by taking beam fluctuations into account. It is, however, useful to retain the simplicity of Eq. (A4.11) by introducing a correction factor for beam intensity fluctuations. In fact, such a factor may be evaluated independently for each experimental irradiation to determine whether a correction for a specific radionuclide will be required or not, or alternatively, to determine a minimum value for the half-life above which this correction can be neglected.

The correction factor, K , is obtained by explicitly introducing it into Eq. (A4.11) and equating the resulting expression to Eq. (A5.7):

$$K \left[\frac{A_p T_1}{\tau \varepsilon_\gamma \varepsilon_e I_t N_0 \exp(-\lambda(T_m - T_1)) [1 - \exp(-\lambda T_1)] (1 \times 10^{-27})} \right] = \frac{A_p}{\tau \varepsilon_\gamma \varepsilon_e N_0 (1 \times 10^{-27}) \sum_{i=1}^n \Delta I_i \exp(-\lambda(T_m - h_i))}.$$

By eliminating common quantities, the above expression simplifies to

$$\frac{K T_1}{I_t (1 - \exp(-\lambda T_1)) \exp(-\lambda(T_m - T_1))} = \frac{1}{\lambda \sum_{i=1}^n \Delta I_i \exp(-\lambda(T_m - h_i))} \quad (\text{A5.9})$$

With a little algebra, T_m can be eliminated and by rearranging K is obtained:

$$K = \frac{\left(\sum_{i=1}^n \Delta I_i \right) (\exp(\lambda T_1) - 1)}{\lambda T_1 \sum_{i=1}^n \Delta I_i \exp(\lambda h_i)}. \quad (\text{A5.10})$$

A convenient way to investigate the correction factor given by Eq. (A5.9), for any given experimental irradiation, is to evaluate K as a function of λ (or $T_{1/2}$). In this work, we compiled a table of K values for a set of appropriately chosen half-lives and used interpolation to obtain the correction for a specific radionuclide, if required.

APPENDIX 6

CUMULATIVE CROSS SECTIONS

A6.1 Overview

The cross-section expressions derived in Appendices 4 and 5 are generally true for the independent (or direct) production of a radionuclide. Those equations are still useful in cases where the decay of precursors also contribute, but have half-lives that are relatively short compared to the half-life of the daughter nuclide. The production cross section of the daughter nuclide is then called a *cumulative* cross section. In this appendix, the relationship between the cumulative cross section and the individual cross sections for the direct production of both the daughter and precursor nuclides are derived.

A6.2 The case of one precursor

A precursor, p , is produced directly during the irradiation with cross section σ_p and decays with a decay constant λ_p and a branching ratio P_p to a daughter nucleus, d . Similarly, the daughter nucleus is produced directly with cross section σ_d and decays with a decay constant λ_d . As in Appendices 4 and 5, the bombardment is assumed to start at time $t=0$. The following equations hold for $t \leq T_1$, where T_1 is the end of bombardment time:

$$\frac{dN_p(t)}{dt} = \sigma_p N_0 \phi(t) - \lambda_p N_p(t), \quad (\text{A6.1})$$

$$\frac{dN_d(t)}{dt} = \sigma_d N_0 \phi(t) + P_p \lambda_p N_p(t) - \lambda_d N_d(t), \quad (\text{A6.2})$$

where

- $N_p(t)$ - total number of precursor nuclei at time t ,
- $N_d(t)$ - total number of daughter nuclei at time t ,
- N_0 - total number of target nuclei per unit area of thin target specimen or foil,
- $\phi(t)$ - flux of incident beam particles per second.

When $t > T_1$ the following equations hold:

$$\frac{dN_p(t)}{dt} = -\lambda_p N_p(t), \quad (\text{A6.3})$$

$$\frac{dN_d(t)}{dt} = -\lambda_d N_d(t) + P_p \lambda_p N_p(t). \quad (\text{A6.4})$$

The four coupled equations (A6.1) through (A6.4) can be solved by multiplying Eqs. (A6.1) and (A6.3) by

$$\frac{P_p \lambda_p}{\lambda_p - \lambda_d}$$

and adding them to, respectively, Eqs. (A6.2) and (A6.4). This leads to a reduction to the following two equations:

For $t \leq T_1$:

$$\begin{aligned} \frac{d}{dt} \left(N_d(t) + \frac{P_p \lambda_p}{\lambda_p - \lambda_d} N_p(t) \right) = \\ \left(\sigma_d(t) + \frac{P_p \lambda_p}{\lambda_p - \lambda_d} \sigma_p(t) \right) \tau \phi(t) - \lambda_d \left(N_d(t) + \frac{P_p \lambda_p}{\lambda_p - \lambda_d} N_p(t) \right), \end{aligned} \quad (\text{A6.5})$$

For $t > T_1$:

$$\frac{d}{dt} \left(N_d(t) + \frac{P_p \lambda_p}{\lambda_p - \lambda_d} N_p(t) \right) = -\lambda_d \left(N_d(t) + \frac{P_p \lambda_p}{\lambda_p - \lambda_d} N_p(t) \right). \quad (\text{A6.6})$$

The quantity

$$C(t) = N_d(t) + \frac{P_p \lambda_p}{\lambda_p - \lambda_d} N_p(t) \quad (\text{A6.7})$$

varies during the irradiation time as if it is produced with cross section

$$\sigma_c = \sigma_d(t) + \frac{P_p \lambda_p}{\lambda_p - \lambda_d} \sigma_p(t). \quad (\text{A6.8})$$

Equations (A6.5) and (A6.6) becomes, respectively, for $t \leq T_1$:

$$\frac{dC(t)}{dt} = \sigma_c N_0 \phi(t) - \lambda_d C(t), \quad (\text{A6.9})$$

and for $t > T_1$:

$$\frac{dC(t)}{dt} = -\lambda_d C(t). \quad (\text{A6.10})$$

Equation (A6.10) shows that for times greater than the bombardment time T_1

$$C(t) = C(T_1) \exp(-\lambda_d t). \quad (\text{A6.11})$$

By substituting Eq. (6.7) and rearranging, one finds an expression for N_d as follows:

$$N_d(t) = C(T_1) \exp(-\lambda_d t) - \frac{P_p \lambda_p}{\lambda_p - \lambda_d} N_p(T_1) \exp(-\lambda_p t). \quad (\text{A6.12})$$

If $\lambda_p \ll \lambda_d$ and $t \rightarrow \infty$, the second term of Eq. (A6.12) becomes negligible compared to the first. Under such conditions one therefore has

$$N_d(t) \rightarrow C(T_1) \exp(-\lambda_d t). \quad (\text{A6.13})$$

Thus, if a measurement of the daughter activity is performed *after* the decay of its precursor, and if the half-life of the daughter is significantly larger than that of the precursor, then the experimental cross section (as determined from the equations derived in Appendices 4 and 5) will be the *cumulative cross section*, and its relationship with the cross sections for the *direct* production of the daughter and precursor nuclides given by Eq. (A6.8). The cumulative cross section is useful to determine the yield of the daughter nucleus when it is produced both from its direct production and via the decay of the precursor. However, such a prediction will only yield a correct result at times after the “complete” decay of the precursor.

Theoretical calculations will usually yield the cross sections for the direct or independent formation of the radionuclides concerned. In order to compare with experimental measurements, Eq. (6.8) should be applied to these theoretical values.

A6.3 Generalisation to more than one precursor

Equation (A6.8) can easily be generalized for the case where a chain of β -decays feeds a particular daughter nuclide. If there are m contributing precursors in the chain, then it is convenient to label them as follows: $\lambda_p^{(i)}$ and $P_p^{(i)}$ are the decay constant and branching ratio, respectively, of precursor i for its decay to nuclide $i-1$. Label $i=1$ denotes the precursor closest to the daughter nuclide and $i=m$ the radionuclide furthest away from the daughter in the decay chain. When $\lambda_p^{(i)} \ll \lambda_d$ for all $1 \leq i \leq m$, the concept of a cumulative cross section is appropriate and given by

$$\sigma_c = \sigma_d + \sum_{i=1}^m \left[\prod_{j=1}^i \left(\frac{P_p^{(j)} \lambda_p^{(j)}}{\lambda_p^{(j)} - \lambda_d} \right) \sigma_p^{(j)} \right]. \quad (\text{A6.14})$$

APPENDIX 7

EXPERIMENTAL CROSS SECTIONS OF HEAVY RESIDUES PRODUCED IN THE REACTIONS

$^{12}\text{C} + ^{103}\text{Rh}$ AND $^{16}\text{O} + ^{103}\text{Rh}$ AT 400 MeV

Table A7.1 Measured cumulative and direct cross sections for residues produced in $^{12}\text{C} + ^{103}\text{Rh}$.

Energy (MeV)		σ (mb)							
In	Out	^{105}gAg	^{101}Pd	^{100}Pd	$^{102}\text{gRh (ind)}$	$^{102}\text{mRh (ind)}$	^{101}mRh	$^{100}\text{gRh(ind)}$	$^{99}\text{gRh (ind)}$
384.66	372.59	7.460 ± 1.21	62.90 ± 9.43	48.33 ± 7.25	131.2 ± 19.7	303.1 ± 45.5	143.8 ± 21.6	85.43 ± 12.8	23.46 ± 3.52
372.59	360.21	9.310 ± 1.45	67.11 ± 10.1	51.89 ± 7.78	127.7 ± 19.2	295.1 ± 44.3	147.4 ± 22.1	87.05 ± 13.1	23.69 ± 3.56
360.21	347.51	9.660 ± 1.49	72.92 ± 10.9	55.76 ± 8.36	128.1 ± 19.2	295.9 ± 44.4	158.1 ± 23.7	93.04 ± 13.9	23.77 ± 3.56
347.51	334.44	11.73 ± 1.76	79.95 ± 11.9	63.09 ± 9.46	122.5 ± 18.4	282.5 ± 42.4	167.5 ± 25.1	98.23 ± 14.7	21.44 ± 3.12
334.44	320.97	14.62 ± 2.19	75.83 ± 11.4	66.02 ± 9.90	112.2 ± 16.8	258.9 ± 38.8	163.8 ± 24.6	92.07 ± 13.8	29.58 ± 4.44
320.97	307.06	18.40 ± 2.76	85.15 ± 12.8	68.02 ± 10.0	117.1 ± 17.6	270.0 ± 40.5	177.4 ± 26.6	98.78 ± 14.8	32.70 ± 4.91
307.06	292.65	28.42 ± 4.26	96.70 ± 14.5	79.80 ± 11.9	124.1 ± 18.6	286.2 ± 42.9	195.0 ± 29.2	109.4 ± 16.4	28.83 ± 4.32
292.65	277.69	38.55 ± 5.78	105.8 ± 15.9	85.41 ± 12.8	123.5 ± 18.5	284.7 ± 42.7	206.6 ± 30.9	115.3 ± 17.3	30.75 ± 4.62
277.69	262.08	56.26 ± 8.44	118.1 ± 17.7	93.54 ± 14.0	119.9 ± 17.9	276.3 ± 41.4	221.7 ± 33.2	124.3 ± 18.6	30.58 ± 4.59
262.08	245.75	82.77 ± 12.4	131.7 ± 19.7	98.98 ± 14.8	120.5 ± 18.1	277.8 ± 41.7	245.0 ± 36.7	134.8 ± 20.2	14.83 ± 2.22
245.75	228.54	126.1 ± 18.9	140.8 ± 21.1	106.5 ± 15.9	120.5 ± 18.1	277.6 ± 41.6	254.8 ± 38.2	138.9 ± 20.8	5.27 ± 0.79
228.54	210.30	199.1 ± 29.8	153.2 ± 22.9	108.1 ± 16.2	117.5 ± 17.6	270.7 ± 40.6	269.5 ± 40.4	140.7 ± 21.1	
210.30	190.79	313.4 ± 47.0	162.0 ± 24.3	104.5 ± 15.7	111.9 ± 16.8	257.7 ± 38.7	281.5 ± 42.2	134.2 ± 30.1	
190.79	169.68	407.2 ± 61.1	148.8 ± 22.3	87.93 ± 13.2	111.2 ± 16.7	256.1 ± 38.4	262.2 ± 39.3	123.9 ± 18.6	
169.68	146.41	533.2 ± 79.9	117.5 ± 17.6	73.78 ± 11.1	113.9 ± 17.1	262.0 ± 39.3	216.0 ± 32.4	109.2 ± 16.4	
146.41	120.07	485.8 ± 72.9	82.27 ± 12.3	36.80 ± 5.52	102.5 ± 15.4	236.0 ± 35.4	160.1 ± 24.0	55.93 ± 8.39	
120.07	88.768	156.7 ± 23.5	16.02 ± 2.40		82.74 ± 12.4	190.5 ± 28.6	51.30 ± 7.96	22.91 ± 3.44	
88.768	47.167				71.99 ± 10.80	165.7 ± 24.8	16.37 ± 2.45	5.090 ± 0.76	

APPENDIX 7

Table A7.1 Measured cumulative and direct cross sections for residues produced in $^{12}\text{C} + ^{103}\text{Rh}$ (continued).

Energy (MeV)		σ (mb)							
In	Out	$^{99\text{m}}\text{Rh}$	^{103}Ru	^{97}Ru	$^{96\text{g}}\text{Tc}$	$^{95\text{g}}\text{Tc}$	$^{95\text{m}}\text{Tc(ind)}$	$^{94\text{g}}\text{Tc(ind)}$	$^{93\text{m}}\text{Mo(ind)}$
384.66	372.59	98.06 ± 14.7	1.86 ± 0.27	126.5 ± 18.9	45.53 ± 6.83	129.4 ± 19.4	9.830 ± 1.47	79.69 ± 11.9	41.31 ± 6.19
372.59	360.21	103.9 ± 15.6	1.83 ± 0.26	134.6 ± 20.2	46.31 ± 8.95	139.9 ± 20.5	10.31 ± 1.55	84.41 ± 12.7	42.47 ± 6.37
360.21	347.51	113.4 ± 17.0	1.89 ± 0.27	143.9 ± 21.6	47.53 ± 7.13	145.0 ± 21.7	10.93 ± 1.63	86.61 ± 12.9	44.54 ± 6.68
347.51	334.44	122.3 ± 18.3	1.88 ± 0.27	152.4 ± 22.8	48.43 ± 7.26	149.5 ± 22.4	11.16 ± 1.67	89.47 ± 13.4	44.41 ± 6.66
334.44	320.97	118.1 ± 17.7	1.71 ± 0.25	148.5 ± 22.3	47.21 ± 7.08	136.7 ± 20.5	10.34 ± 1.55	80.09 ± 12.0	39.16 ± 5.87
320.97	307.06	129.0 ± 19.3	1.82 ± 0.26	157.5 ± 23.6	47.32 ± 7.09	140.8 ± 21.1	10.92 ± 1.64	80.47 ± 12.1	39.45 ± 5.91
307.06	292.65	143.5 ± 21.5	1.79 ± 0.26	167.5 ± 25.1	49.60 ± 7.44	144.9 ± 21.7	10.53 ± 1.57	80.82 ± 12.1	38.40 ± 5.76
292.65	277.69	153.5 ± 23.0	1.68 ± 0.24	168.5 ± 25.3	47.32 ± 7.09	138.4 ± 20.8	9.540 ± 1.43	76.20 ± 11.4	35.30 ± 5.29
277.69	262.08	166.2 ± 24.9	1.61 ± 0.23	167.7 ± 25.1	47.42 ± 7.11	130.6 ± 19.6	9.000 ± 1.35	69.21 ± 10.4	31.94 ± 4.79
262.08	245.75	177.5 ± 26.6	1.46 ± 0.21	150.6 ± 24.6	45.17 ± 6.77	119.9 ± 18.0	7.790 ± 1.16	59.12 ± 8.87	27.82 ± 4.17
245.75	228.54	174.4 ± 26.1	1.46 ± 0.21	132.1 ± 19.8	39.72 ± 5.96	95.45 ± 14.3	6.540 ± 0.98	48.68 ± 7.30	21.84 ± 3.27
228.54	210.30	164.7 ± 24.7	1.15 ± 0.17	99.78 ± 14.9	32.77 ± 4.91	73.72 ± 11.0	3.470 ± 0.56	35.41 ± 5.31	14.19 ± 2.12
210.30	190.79	147.8 ± 22.2	0.92 ± 0.14	67.77 ± 9.71	25.40 ± 3.81	52.95 ± 7.94		21.67 ± 3.25	9.230 ± 1.38
190.79	169.68	132.2 ± 19.8	0.69 ± 0.11	40.23 ± 6.03	19.46 ± 2.46	29.69 ± 4.45		11.04 ± 1.65	5.380 ± 0.81
169.68	146.41	81.04 ± 12.1	0.47 ± 0.08	12.12 ± 1.82	9.880 ± 1.48	10.83 ± 1.62		5.730 ± 0.89	2.160 ± 0.34
146.41	120.07	30.49 ± 4.57	0.16 ± 0.04		4.440 ± 0.66	3.810 ± 0.57			
120.07	88.768	9.390 ± 1.41				0.900 ± 0.14			

APPENDIX 7

Table A7.1 Measured cumulative cross sections for residues produced in $^{12}\text{C} + ^{103}\text{Rh}$ (continued).

Energy (MeV)		σ (mb)							
In	Out	^{90}Mo	^{90g}Nb	^{88}Zr	^{86}Zr	^{87g}Y	^{87m}Y	^{86g}Y	^{85m}Y
384.66	372.59	24.72 ± 3.71	87.38 ± 13.1	118.9 ± 16.8	15.77 ± 2.24	108.8 ± 16.3	54.4 ± 8.16	31.24 ± 4.68	21.80 ± 3.27
372.59	360.21	24.85 ± 3.72	86.62 ± 12.9	114.8 ± 16.3	14.47 ± 2.05	98.69 ± 14.8	49.35 ± 7.40	31.29 ± 4.72	20.21 ± 3.03
360.21	347.51	23.60 ± 3.54	85.41 ± 12.8	106.9 ± 15.2	13.10 ± 1.86	96.74 ± 14.5	48.37 ± 7.25	27.60 ± 4.14	16.93 ± 2.54
347.51	334.44	22.06 ± 3.31	80.58 ± 12.1	94.22 ± 13.4	11.48 ± 1.63	86.24 ± 12.9	43.12 ± 6.47	25.20 ± 3.78	14.50 ± 2.17
334.44	320.97	17.86 ± 2.67	67.27 ± 10.1	76.41 ± 10.8	8.67 ± 1.23	67.09 ± 10.1	33.55 ± 5.03	21.43 ± 3.21	10.50 ± 1.61
320.97	307.06	16.37 ± 2.45	62.27 ± 9.34	67.12 ± 9.54	6.90 ± 0.98	56.84 ± 8.53	28.42 ± 4.26	18.17 ± 2.74	8.09 ± 1.30
307.06	292.65	14.21 ± 2.13	55.47 ± 8.32	45.45 ± 8.01	5.70 ± 0.81	48.70 ± 7.30	24.35 ± 3.65	15.07 ± 2.26	
292.65	277.69	11.01 ± 1.65	44.84 ± 6.23	34.06 ± 6.47	3.88 ± 0.56	36.24 ± 5.46	18.21 ± 2.73	11.46 ± 1.72	
277.69	262.08	8.430 ± 1.26	35.73 ± 5.36	25.32 ± 4.86	2.68 ± 0.39	26.73 ± 4.01	13.36 ± 2.00	8.53 ± 1.28	
262.08	245.75	5.350 ± 0.80	25.92 ± 3.88	16.47 ± 3.62	1.79 ± 0.26	18.28 ± 2.74	9.14 ± 1.37	5.79 ± 0.84	
245.75	228.54	3.180 ± 0.49	16.95 ± 2.54	13.63 ± 2.38	1.07 ± 0.17	11.63 ± 1.74	5.82 ± 0.87	3.38 ± 0.50	
228.54	210.30		9.99 ± 1.49	10.42 ± 1.99		6.73 ± 1.01	3.36 ± 0.49	2.22 ± 0.34	
210.30	190.79		5.09 ± 0.76	13.71 ± 1.54		3.84 ± 0.97	1.92 ± 0.29		
190.79	169.68		3.31 ± 0.58	17.21 ± 2.00		2.49 ± 0.72	1.25 ± 0.21		
169.68	146.41			20.76 ± 2.50					
146.41	120.07			24.83 ± 2.99					
120.07	88.768			31.06 ± 4.60					

APPENDIX 7

Table A7.2 Measured cumulative and direct cross sections for residues produced in $^{16}\text{O} + ^{103}\text{Rh}$.

Energy (MeV)		σ (mb)							
In	Out	^{105g}Ag	^{101}Pd	^{100}Pd	$^{102m}\text{Rh(ind)}$	$^{102g}\text{Rh(ind)}$	^{101m}Rh	$^{100g}\text{Rh(ind)}$	$^{99g}\text{Rh(ind)}$
373.03	359.88	31.65 ± 4.62	97.04 ± 13.8	63.89 ± 9.22	211.3 ± 30.4	101.4 ± 15.1	178.0 ± 25.2	85.43 ± 12.8	40.09 ± 5.71
359.88	346.35	47.73 ± 6.88	117.5 ± 16.7	83.11 ± 11.8	221.8 ± 31.8	106.1 ± 15.9	211.3 ± 29.9	87.05 ± 13.0	44.10 ± 6.28
346.35	332.42	61.19 ± 8.76	127.2 ± 18.1	86.01 ± 13.3	223.5 ± 32.1	106.9 ± 16.0	220.4 ± 31.2	93.05 ± 13.9	44.13 ± 6.29
332.42	318.03	82.21 ± 11.7	137.1 ± 19.9	89.90 ± 12.7	211.8 ± 30.4	101.3 ± 15.1	231.4 ± 32.8	98.23 ± 14.7	43.98 ± 6.26
318.03	303.15	108.2 ± 15.4	149.6 ± 21.3	96.00 ± 13.7	222.3 ± 31.9	106.3 ± 15.9	247.3 ± 34.1	92.07 ± 13.8	40.53 ± 5.91
303.15	278.69	133.3 ± 18.9	153.8 ± 21.8	94.95 ± 13.6	202.6 ± 29.1	96.91 ± 14.5	247.7 ± 35.1	98.78 ± 14.8	40.09 ± 5.70
278.69	271.60	184.2 ± 26.2	166.8 ± 23.7	101.2 ± 14.5	205.9 ± 29.6	98.46 ± 14.7	265.9 ± 37.7	109.4 ± 16.4	41.93 ± 5.97
271.60	254.77	243.9 ± 34.6	172.5 ± 24.5	102.2 ± 14.6	214.5 ± 30.8	102.6 ± 15.4	274.4 ± 38.9	115.3 ± 17.3	37.52 ± 5.34
254.78	237.09	316.5 ± 44.9	175.0 ± 24.8	93.59 ± 13.4	219.9 ± 31.6	105.2 ± 15.7	274.3 ± 38.9	124.3 ± 18.6	32.03 ± 4.56
237.09	218.39	406.0 ± 57.6	160.0 ± 22.7	79.70 ± 11.4	208.0 ± 29.8	99.48 ± 14.9	252.2 ± 35.8	134.8 ± 20.2	27.44 ± 3.91
218.39	198.45	483.0 ± 68.5	125.9 ± 17.9	58.03 ± 8.36	201.1 ± 28.8	96.17 ± 14.4	208.3 ± 29.5	138.9 ± 20.8	22.35 ± 3.19
198.45	176.99	478.8 ± 68.4	61.46 ± 13.0	41.60 ± 6.07	199.0 ± 28.5	95.17 ± 14.3	158.0 ± 22.4	140.7 ± 21.1	16.71 ± 2.40
176.99	153.53	482.0 ± 68.4	25.06 ± 3.59	23.98 ± 4.79	192.2 ± 27.5	91.92 ± 13.8	116.2 ± 16.5	134.2 ± 30.1	10.00 ± 1.47
153.53	127.37	358.4 ± 50.8	7.440 ± 1.17		177.3 ± 25.4	84.80 ± 12.7	59.02 ± 8.38	123.9 ± 18.6	6.11 ± 0.88
127.37	97.180	175.9 ± 24.9			157.6 ± 22.6	75.37 ± 11.3	34.13 ± 4.35	109.2 ± 16.4	
97.180	60.081	101.7 ± 14.5			92.11 ± 13.4	44.05 ± 6.60	13.40 ± 1.91	55.93 ± 8.39	
60.081	7.887	28.85 ± 4.13			20.03 ± 3.36	9.58 ± 1.43		22.91 ± 3.44	

APPENDIX 7

Table A7.2 Measured cumulative and direct cross sections for residues produced in $^{16}\text{O} + ^{103}\text{Rh}$ (continued).

Energy (MeV)		σ (mb)							
In	Out	$^{99\text{m}}\text{Rh}$	^{103}Ru	^{97}Ru	$^{96\text{g}}\text{Tc}$	$^{95\text{g}}\text{Tc}$	$^{95\text{m}}\text{Tc(ind)}$	$^{94\text{g}}\text{Tc(ind)}$	$^{93\text{m}}\text{Mo(ind)}$
373.034	359.880	124.9 ± 17.7	1.72 ± 0.26	135.9 ± 19.3	$40.8 + 6.12$	129.0 ± 18.1	9.105 ± 1.30	71.42 ± 10.2	37.11 ± 5.28
359.880	346.354	155.9 ± 22.1	2.03 ± 0.31	173.4 ± 24.6	48.52 ± 7.28	153.7 ± 18.9	10.68 ± 1.52	84.89 ± 12.1	43.92 ± 6.25
346.354	332.420	163.6 ± 23.2	1.38 ± 0.22	174.9 ± 24.8	47.10 ± 7.06	134.1 ± 20.0	10.49 ± 1.50	80.20 ± 11.4	40.76 ± 5.80
332.420	318.035	171.5 ± 24.3	1.38 ± 0.22	170.8 ± 24.2	46.04 ± 6.91	129.4 ± 18.3	9.642 ± 1.38	74.15 ± 10.5	38.07 ± 8.42
318.035	303.148	178.2 ± 25.3	1.65 ± 0.26	167.2 ± 23.7	44.06 ± 6.61	119.8 ± 16.9	9.668 ± 1.24	67.69 ± 9.64	34.14 ± 4.86
303.148	278.696	174.0 ± 24.7	1.37 ± 0.21	150.9 ± 21.4	44.18 ± 6.63	102.8 ± 14.6	7.632 ± 1.10	55.82 ± 7.95	28.00 ± 3.99
287.696	271.604	179.7 ± 25.5	1.46 ± 0.23	142.2 ± 20.2	39.69 ± 5.95	90.58 ± 12.8	6.611 ± 0.95	49.13 ± 7.00	24.03 ± 3.43
271.604	254.775	170.9 ± 24.2	0.57 ± 0.10	125.4 ± 17.8	37.57 ± 5.64	75.36 ± 10.6	2.442 ± 0.38	37.69 ± 5.38	18.05 ± 2.58
254.775	237.090	150.8 ± 21.4	0.96 ± 0.19	101.6 ± 14.4	32.24 ± 4.84	56.26 ± 7.93	2.247 ± 0.38	28.06 ± 4.01	12.94 ± 1.85
237.090	218.388	125.6 ± 17.8	0.65 ± 0.14	101.5 ± 14.4	26.46 ± 3.97	38.72 ± 4.93	1.368 ± 0.29	17.47 ± 2.52	8.960 ± 1.29
218.388	198.455	93.89 ± 13.3	0.85 ± 0.17	72.78 ± 10.3	20.36 ± 3.05	22.63 ± 3.14	1.159 ± 0.24	11.25 ± 1.34	6.050 ± 0.88
198.455	176.988	54.33 ± 7.73		48.30 ± 6.85	14.56 ± 2.18	13.56 ± 1.93		6.400 ± 0.98	3.740 ± 0.56
176.988	153.535	29.74 ± 4.25		29.30 ± 4.17	10.11 ± 1.52	7.980 ± 1.14		4.030 ± 0.65	2.480 ± 0.39
153.535	127.369	15.31 ± 2.22		15.38 ± 2.19	7.30 ± 1.10	3.870 ± 0.56		2.390 ± 0.44	1.600 ± 0.60
127.369	97.180	5.240 ± 0.86		6.850 ± 0.99	4.30 ± 0.65	1.280 ± 0.20			
97.180	60.081			2.460 ± 0.37					

APPENDIX 7

Table A7.2 Measured cumulative cross sections for residues produced in $^{16}\text{O} + ^{103}\text{Rh}$ (continued).

Energy (MeV)		σ (mb)							
In	Out	^{90}Mo	^{90g}Nb	^{88}Zr	^{86}Zr	^{87g}Y	^{87m}Y	^{86g}Y	^{85m}Y
373.03	359.88	16.49 ± 2.35	59.14 ± 8.40	75.60 ± 10.7	9.16 ± 1.36	70.38 ± 10.01	33.36 ± 4.73	20.90 ± 2.97	10.13 ± 1.58
359.88	346.35	18.02 ± 2.57	66.30 ± 9.41	81.86 ± 11.6	9.53 ± 1.41	75.38 ± 10.72	35.90 ± 5.09	22.13 ± 3.15	10.78 ± 1.69
346.35	332.42	12.79 ± 1.83	57.57 ± 8.17	69.79 ± 9.93	7.73 ± 1.15	62.39 ± 8.88	30.06 ± 4.27	18.23 ± 2.60	9.110 ± 1.48
332.42	318.03	9.710 ± 1.39	48.22 ± 6.85	57.09 ± 8.14	5.83 ± 0.87	50.40 ± 7.18	24.09 ± 3.42	14.87 ± 2.12	4.610 ± 0.91
318.03	303.15	6.790 ± 0.98	39.74 ± 5.65	45.09 ± 6.57	4.59 ± 0.68	39.33 ± 5.61	19.01 ± 2.70	12.02 ± 1.72	3.340 ± 0.76
303.15	278.69	4.880 ± 0.72	29.20 ± 4.15	36.33 ± 5.20	3.44 ± 0.52	29.37 ± 4.20	14.35 ± 2.04	9.480 ± 1.36	
287.69	271.60	3.820 ± 0.57	23.37 ± 3.32	29.87 ± 4.29	2.33 ± 0.36	23.24 ± 3.33	11.29 ± 1.61	7.360 ± 1.06	
271.60	254.77	2.430 ± 0.38	16.94 ± 2.41	24.31 ± 3.90	1.71 ± 0.27	17.43 ± 2.51	8.580 ± 1.22	3.960 ± 0.58	
254.77	237.09	1.450 ± 0.27	11.68 ± 1.67	23.71 ± 3.43	1.15 ± 0.19	13.06 ± 1.89	6.380 ± 0.91	4.330 ± 0.63	
237.09	218.39	0.920 ± 0.22	8.360 ± 1.20	27.32 ± 3.95	0.75 ± 0.13	9.34 ± 1.37	4.770 ± 0.69	3.250 ± 0.48	
218.39	198.45		5.900 ± 0.85	28.00 ± 4.04	0.74 ± 0.12	7.05 ± 1.05	3.430 ± 0.50	2.180 ± 0.33	
198.45	176.99		3.900 ± 0.57	31.01 ± 4.47		4.71 ± 0.72	2.280 ± 0.34	1.460 ± 0.24	
176.99	153.53		2.850 ± 0.44	47.94 ± 6.84		3.48 ± 0.55	1.840 ± 0.28	1.070 ± 0.19	
153.53	127.37		2.150 ± 0.35			0.78 ± 0.14	0.780 ± 0.14	0.450 ± 0.09	
127.37	97.180		1.340 ± 0.25						
97.180	60.081		0.810 ± 0.14						
60.081	7.887		0.340 ± 0.09						